Technische Universität München
Lehrstuhl für Mikrotechnik und Medizingerätetechnik
Univ.-Prof. Dr. rer. nat. Dipl.-Ing. Tim C. Lüth

An Advanced Force Feedback Tool Design for Minimally Invasive Robotic Surgery

Ulrich Stefan Seibold

Vollständiger Abdruck der von der Fakultät für Maschinenwesen der
Technischen Universität München zur Erlangung des akademischen Grades eines

Doktor-Ingenieurs (Dr.-Ing.)

genehmigten Dissertation.

Vorsitzender:		Univ.-Prof. Dr.-Ing. Gunther Reinhart
Prüfer der Dissertation:	1.	Univ.-Prof. Dr. rer. nat. Tim C. Lüth
	2.	Hon.-Prof. Dr.-Ing. Gerhard Hirzinger

Die Dissertation wurde am 15.05.2012 bei der Technischen Universität München eingereicht und durch die Fakultät für Maschinenwesen am 02.10.2012 angenommen.

Abstract

Through the use of minimally invasive robotic surgery (MIRS), the vision of ”virtual open surgery” is coming closer to reality. Robotic systems strive to retain all the advantages of conventional minimally invasive surgery (MIS) for the patient and at the same time restore hand-eye coordination and preserve, even enhance the manual dexterity of open surgery for the surgeon. Still, surgeons are forced to forgo the touch sensitivity of their hands and – instead of receiving haptic feedback – rely solely on visual information from the operation site. Feeling the tension and tightness of a surgical knot, the variations of stiffness in tissue, or the resistance when inserting a needle through true haptic feedback could offer surgeons a more immediate perception of the physical properties of the operation site. However, these properties need to be measured first.

In order to determine whether surgical task performance can be enhanced by the provision of haptic feedback a robotic system integrating instruments with force measurement capabilities is needed. Then comparable experimental results can be gathered from a single robotic surgery setup. Conducting experiments with and without force feedback, with varying force feedback gain settings, with enhanced or restricted dexterity, unimpeded by other usability variations will help to assess the impact of FFB. The novel articulated tool for MIRS presented in this thesis represents an essential building block for such an experiment. It is capable of measuring interaction forces between tool and tissue in 6+1 degrees of freedom (DoF) and is fully integrated into the DLR Robotics and Mechatronics Center *MiroSurge* scenario as part of the dedicated instrument *MICA*.

Individual components for such a tool already exist in literature. A multitude of wrist kinematics and several multi-DoF force sensor designs have been proposed and built by various research groups. This thesis shows, however, that an advanced tool requires more than just a combination of off-the-shelf components. The interaction and interdependence of all components needs to be addressed early in the concept stage. Especially the clear mechanical separation of tissue manipulation and tool actuation forces is vital for high quality manipulation force measurements. The tip mounted 6 DoF force-torque sensor (FTS) is capable of measuring interaction forces between tool tip and environment. The FTS is based on a Stewart platform with flexural joints and is capable of measuring tissue manipulation forces up to 10 N and torques up to 150 Nmm. It is currently the smallest 6 DoF FTS with a measurement range of several Newtons. Grasping forces are measured by an additional 1 DoF gripping force sensor. Manipulation and gripping forces are isolated by mechanical design from the actuation forces articulating the tool tip. The tool contains an intra-corporal 2 DoF wrist based on an universal joint with intersecting axes articulated by stainless steel cables. End effectors can provide one additional DoF and are realized in the shape of a grasper for tissue manipulation, scissors, a needle holder, and a palpation tool. Wrist articulation is fast enough to follow the motion of a stabilized beating heart surface. The performance of the wrist mechanism is evaluated in a series of trajectory tracking experiments

In addition to experiments testing individual components, two system wide palpation experiments utilizing the entire *MiroSurge* system are conducted. In a subjective evaluation of perceived tissue stiffness, a number of users are asked to sort springs according to increasing stiffness. Palpation is performed by touching the springs with a finger, with a plastic rod representing the ideal telemanipulator, using robotic palpation without FFB, and finally using robotic palpation with FFB. Robotic palpation without FFB results in significantly higher error rates than any other modality. In a second, objective palpation experiment, the *MiroSurge* system is used to generate surface stiffness maps of a liver phantom made from silicone and of an ex-vivo porcine liver by palpating a grid of surface points with the palpation tool. The generated maps show stiffness variations in much finer detail than human users are able to identify during robotic palpation.

In conclusion, this thesis proves the feasibility of combining an intra-corporal 6+1 DoF force-torque sensor with a 2 DoF articulated wrist in a MIRS tool of only 10 mm diameter, providing high-quality FFB and dexterity to the surgeon. With this tool experiments evaluating the impact of FFB, and also animal tests evaluating the entire robotic surgery setup can be conducted in the near future.

Keywords

Robotic surgery, Instruments, Force Feedback

Kurzfassung

Durch den Einsatz der minimal invasiven robotergestützten Chirurgie (MIRC) ist die Vision der „virtuell offenen Chirurgie“ näher gerückt. Robotische Systeme zielen darauf ab, alle Vorteile für den Patienten aus der konventionellen minimal invasiven Chirurgie (MIC) zu erhalten und gleichzeitig aus der offenen Chirurgie die Hand-Auge-Koordination zurück zu gewinnen und die Fingerfertigkeit des Chirurgen zu erhalten oder sogar zu verbessern. Nach wie vor sind Chirurgen gezwungen auf ihr Tastgefühl zu verzichten und sich – anstatt haptische Rückkopplung zu erhalten – ausschließlich auf visuelle Informationen vom Operationsgebiet zu verlassen. Haptische Rückkopplung könnte es Chirurgen ermöglichen, das Zuziehen von chirurgischen Knoten, unterschiedliche Gewebesteifigkeiten, den Widerstand beim Einstechen von Nadeln und weitere physikalische Eigenschaften des Operationsgebietes unmittelbar zu spüren. Dafür müssen diese physikalischen Eigenschaften aber gemessen werden.

Um die Auswirkung der Kraftrückkopplung auf die Bewältigung von chirurgischen Aufgaben in der minimal invasiven robotischen Chirurgie zu bewerten, ist ein robotisches System notwendig, das (Manipulations-) Kräfte messen kann. Erst dann können vergleichbare Ergebnisse mit einem einzigen robotischen Chirurgiesystem gewonnen werden. Experimente mit und ohne Kraftrückkopplung, mit variierenden Parametereinstellungen, mit reduzierter und erweiterter Beweglichkeit können unbeeinflusst von anderen Einflussfaktoren durchgeführt werden. Das in dieser Dissertation vorgestellte abwinkelbare Werkzeug für die minimal invasive robotergestützte Chirurgie stellt eine essenzielle Komponente für solche Experimente dar. Es erlaubt die Messung der Manipulationskräfte zwischen Werkzeug und Gewebe in 6+1 Freiheitsgraden (FG), und ist als Teil des vielseitigen Instruments *MICA* vollständig in das *MiroSurge* Szenario am DLR Robotik und Mechatronik Zentrum integriert.

Einzelne Komponenten für ein derartiges Werkzeug wurden bereits in der Literatur beschrieben. Eine Vielzahl von Gelenkskinematiken und Kraftsensoren mit mehreren Freiheitsgraden wurden von Forschergruppen vorgeschlagen und aufgebaut. Diese Dissertation verdeutlicht jedoch, dass für ein hochintegriertes Werkzeug eine einfache Kombination vorhandener Lösungen nicht ausreicht. Die gegenseitige Beeinflussung und Abhängigkeit der Komponenten muß frühzeitig im Entwicklungsstadium adressiert werden. Insbesondere die klare mechanische Trennung der Gewebemanipulationskräfte von den Antriebskräften ist für eine hochqualitative Messung der Manipulationskräfte zwingend erforderlich. Der an der Spitze des Werkzeugs integrierte 6-FG-Kraft-Moment-Sensor (KMS) kann Interaktionskräfte zwischen Werkzeugspitze und Umwelt messen. Der KMS basiert auf einer Stewart Plattform mit Festkörpergelenken und kann Manipulationskräfte bis zu 10 N und Momente bis zu 150 Nmm messen. Er ist aktuell der kleinste 6-FG-KMS mit einem Messbereich von mehreren Newton. Greifkräfte werden von einem zusätzlichen 1-FG-Greifkraftsensor erfasst. Die Manipulations- und Greifkräfte sind mechanisch von den Antriebskräften der Werkzeugspitze entkoppelt. Das Werkzeug beinhaltet außerdem ein intrakorporales 2-FG-Handgelenk, bestehend aus einem durch Edelstahlseile aktuierten Kardangelenk. Verschiedene Endeffektoren können einen weiteren FG zur Verfügung stellen: ein Greifer für die Gewebemanipulation, eine Schere, ein Nadelhalter und ein Palpationswerkzeug.

Über die Tests der Einzelkomponenten hinaus wurden zwei Experimente mit dem gesamten *MiroSurge* Szenario durchgeführt. Um den subjektiven Eindruck von Gewebesteifigkeit zu evaluieren, sollte eine Gruppe von Versuchspersonen Federn durch Betasten nach Steifigkeit ordnen: mit dem Finger, mit einem Plastikstab als idealem Telemanipulator, mit dem Palpationswerkzeug des robotischen Systems ohne- und mit Kraftrückkopplung. Die robotische Palpation ohne Kraftrückkopplung ergab signifikant höhere Fehlerraten als jede andere Modalität. In einem zweiten, objektiven Palpationsexperiment wurde das *MiroSurge* System verwendet, um Oberflächen-Steifigkeitskarten eines Leberphantoms aus Silikon und einer ex-vivo Schweineleber zu generieren. Die Karten wurden durch automatisches Antasten eines Punktegitters auf der Organoberfläche mit Hilfe des Palpationswerkzeuges generiert. Die erzeugten Karten zeigen Steifigkeitsunterschiede mit deutlich höherer Auflösung als menschliche Benutzer während der robotischen Palpation wahrnehmen konnten.

Die vorliegende Dissertation weist die gleichzeitige Realisierbarkeit eines intrakorporalen 6+1-FG-Kraft-Moment-Sensors und eines in 2 Freiheitsgraden abwinkelbaren Handgelenks in ein MIRC Werkzeug mit nur 10 mm Durchmesser nach. Chirurgen wird qualitativ hochwertige Kraftrückkopplung und Beweglichkeit zur Verfügung gestellt.

Schlüsselworte

Robotische Chirurgie, Instrumente, Kraftrückkopplung

Acknowledgements

This thesis summarizes my research in the field of surgical robotic instruments and force sensors, conducted at the German Aerospace Center (DLR), Robotics and Mechatronics Center (RMC). I wish to thank all colleagues for their help, advice, and opinions. In particular, I want to thank Prof. Dr.-Ing. Gerd Hirzinger for his confidence in my work and the extraordinary opportunity to work in the medical robotics group. The distinguished expertise and teamwork culture at his institute are unequaled. This work would not have been possible otherwise. I also want to thank Prof. Dr. rer. nat. Dipl.-Ing. Tim C. Lüth at the Technische Universität München (TUM) for his advice, guidance, and encouragement during the composition of this thesis.

I want to thank all fellow researchers and students of the DLR medical robotics research group for their commitment to the surgical robotics projects. In particular, I thank Georg Passig, Sophie Thielmann, Florian Fröhlich, Robert Haslinger, Bernhard Kübler, Oliver Eiberger, Michael Strohmayr, Andreas Tobergte, Holger Urbanek, Rainer Konietschke, and also Michael Suppa and Tim Bodenmüller for exceptional teamwork and collegiality. Especially, I want to thank Ulrich Hagn for inspiration and guidance and for promoting the medical group, creating the cohesive team it is today.

A special thank you to my parents, for their unwavering support and love, and for teaching me the value of independence.

I dedicate this thesis to my beloved wife Susan, who has patiently endured the uncounted weekends and evenings of work that went into writing this thesis and has, nonetheless, always supported me.

Contents

1

Introduction

> A common mistake people make when trying to design something completely foolproof is to underestimate the ingenuity of complete fools.
>
> Douglas Adams

The goal of this thesis is to develop a novel articulated grasping tool with full force sensing capability for minimally invasive robotic surgery (MIRS), capable of measuring interaction forces between tool and environment, and at the same time providing enhanced dexterity compared to conventional minimally invasive surgery (MIS).

1.1 Background

Minimally invasive surgery (MIS) is an operation technique established in the mid 20th century. The surgeon operates with specially designed surgical tools through a few small incisions of typically only 1 cm on the patient's skin. The patient typically benefits from a reduction of surgical trauma to tissue, decreased pain and shorter hospitalization. Smaller visible scars compared to open surgical procedures yield cosmetic benefits. These advantages for the patient however, are accompanied by disadvantages for the surgeon (as described by Huang et al. [1], Sauerland et al. [2] among others). The loss of direct manual access to the operation site makes it impossible to assess tissue properties by touch. The long instruments are moved about the fixed point of incision, therefore two degrees of freedom (DoF) are lost and a loss of dexterity inside the patient's body results. The direct hand-eye coordination present in open surgery is also lost. The movement of the instrument is subject to scaling and depends on the depth of insertion. These are significant drawbacks of MIS, which make complex tasks like knot tying very time consuming and require intensive training. Today several surgical procedures in the abdominal cavity are routinely performed minimally invasively. These include the removal of the appendix (appendectomy), the gallbladder (cholecystectomy) as well as hernia repair and treatment of gastro-esophageal reflux disease. More complicated procedures, especially cardiac surgery, are difficult to perform effectively (see Wullstein et al. [3]). As a consequence, MIS is performed predominantly for procedures of low to medium complexity.

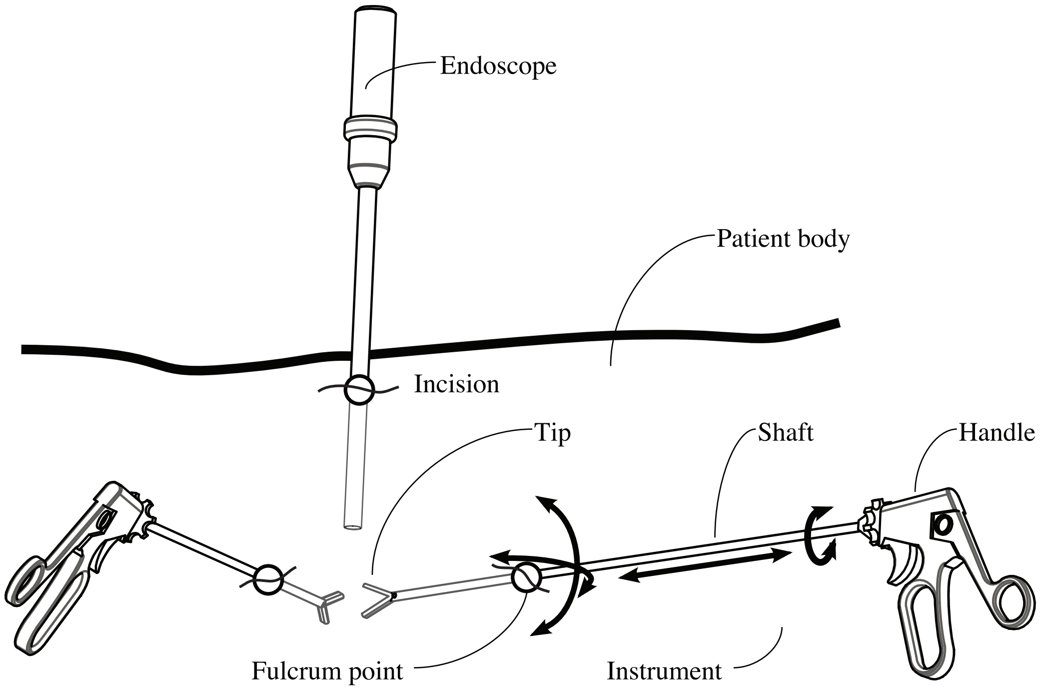

Figure 1.1: Conventional minimally invasive surgery. Long slender instruments are inserted into the patient's body through few small incisions. The incision acts as fulcrum point, restricting instrument motion to 4 DoF (tilting about the fulcrum point, insertion or extraction, and rotation about the instrument shaft). A view of the operation site is provided by an endoscopic camera (Hagn [4]).

In the late 1980s robots were introduced into the operating room (OR) to help overcome some of the disadvantages of MIS. Minimally invasive robotic surgery was born. In this new field of minimally invasive robotic surgery (MIRS), the instruments are not directly held by the surgeon standing at the OR table anymore. Instead, they are remotely commanded by the surgeon who comfortably works in front of an input console while the instruments themselves are moved by specialized robotic arms (Ortmaier et al. [5], Sackier and Wang [6]). Ergonomics becomes an important factor in surgical procedures often lasting several hours. By providing the surgeon with an ergonomic and comfortable work environment, strain and fatigue are reduced. With this telemanipulation approach, undesired reverse hand motion can be avoided and the direct hand eye coordination is reestablished (Ortmaier et al. [7]). The desired downscaling and removal of tremor from the surgeon's hand motion before being transmitted to the robot is another benefit: movements of instruments become more accurate than in open surgery. Actuated instruments with two additional DoFs enable the surgeon to reach every point in the workspace inside the human body with the desired orientation of the tip of the instrument.

Research in the field of MIRS aims to overcome the loss of direct access experienced in MIS and enhance dexterity and sensitivity by using advanced sensors, mechatronic design, control algorithms, augmented reality, and ergonomics.

1.2 Motivation

We use our hands every day for a multitude of intricate tasks. When surgeons learn to perform sophisticated operations, they learn – among many other things – to take advantage of their hand's dexterity during delicate tasks, and to utilize the sensitivity of their fingers to better assess the health of tissue. With respect to dexterity and sensitivity, conventional MIS is actually a step backward. While reduced risk of infection, smaller scars and faster reconvalescence are advantages for the patient, the surgeon's dexterity is reduced and haptic perception is lost almost completely. Surgeons need extensive practice to adapt surgical techniques for this new environment, in order to compensate for the loss of the sense of touch.

Ideally, minimally invasive robotic surgery systems should preserve all the advantages of MIS for the patient, but at the same time enhance rather than restrict the skills of the surgeon. The MIRS system should provide a ”virtual open surgery” environment: The procedure is still performed minimally invasive, but the surgeon is provided with computer enhanced dexterity, a sense of touch and vision quality similar to open surgery. All while comfortably working at an ergonomically designed console that can also provide additional relevant medical information on request.

Today commercially available MIRS systems preserve and extend the dexterity of the surgeon's hands, restore hand-eye coordination, and increase the precision of the human hand through motion scaling and tremor filtering. Still, surgeons are forced to forgo the sensitivity of their hands, and instead rely solely on visual information from the operation site.

The vision of ”virtual open surgery” is coming closer to reality. Research in the field of augmented reality aims to provide additional information in an ubiquitous manner. This ranges from diagnostic information from CT (computer tomography), and MRI (magnet resonance imaging) data to pre-operative planning data. Traditionally, pre-operative CT and MRI data is presented as a 2 D printout over a light box on the OR wall, requiring the surgeon to look up and mentally reorient the image to match the operating site. Augmented reality strives to provide this information directly in the field of view of the surgeon, aligned with, and projected directly over the operating field. The capabilities of the surgeon are enhanced and a wealth of information is provided which is normally inaccessible to the human senses. Tissue manipulation forces and mechanical data on the elasticity of tissue could be presented in a similar way, however, they first need to be obtained.

Aside from the lack of viable commercial solutions, even research groups are still trying to address a number of fundamental questions. The debate on whether task performance can be enhanced by the restoration of haptic feedback – more specific, the feedback of interaction forces and torques between the tool tip and the human body during palpation, grasping and tissue manipulation – is still very much open. Scientific studies weigh in on both sides of the debate. However, no study so far has addressed the combined analysis of *full dexterity* and *simultaneously full haptic feedback* in the context of a *single* robotic surgery system. The reason is simple: An integrated robotic surgery system combining full force measuring and displaying capabilities with dexterity and an ergonomic surgeon console does not exist. Until today researchers are forced to compare the task performance of commercial systems with the performance achievable with prototypic sensorized instruments. In the majority of studies experimental conditions are highly variant and will likely impact the evaluation of the task performance. Comparing experimental results gathered from a single robotic surgery setup – conducting experiments with and without force feedback, with varying force feedback gain settings, with enhanced and restricted dexterity, unimpeded by other usability considerations – will help to assess the impact of force feedback. So far the outcome is unknown.

1.3 Contributions

This thesis describes the development of a novel articulated grasping tool with full force sensing capability for research in the field of minimally invasive robotic surgery. Together with a specialized robotic motor unit the tool constitutes the instrument *MICA*, which is part of the German Aerospace Center's (DLR) *MiroSurge* system. The tool contains an intra-corporal articulated wrist with 2 degrees of freedom, and a 1 DoF end effector. End effectors have been realized in the shape of a grasper for tissue manipulation (Maryland grasper), scissors (Metzenbaum dissector), a needle holder, and a palpation tool. Wrist articulation is fast enough to follow the motion of a stabilized beating heart surface. A custom built, tip mounted 6 DoF force-torque sensor (FTS) is capable of measuring interaction forces between tool and environment. Grasping forces are measured by an additional 1 DoF gripping force sensor (GFS). Manipulation and gripping forces are isolated – by mechanical design – from the actuation forces articulating the tool tip. The force sensor is currently the smallest 6 DoF sensor providing a measurement range of several Newton.

The performance of the tool is evaluated in a series of experiments. Trajectory tracking experiments show performance and accuracy of the tool tip motion. Calibration of the 6+1 DoF force-torque sensor establishes resolution and accuracy of the tip mounted sensor. Palpation experiments using phantom and ex-vivo tissue samples provide proof that the detection of tissue stiffness variations is possible.

This thesis will not attempt to settle the debate on necessity or benefit of force feedback in minimally invasive surgery. In order to find an answer, an entire robotic system, software, infrastructure, the expertise of surgeons, psychologists and engineers is necessary. The novel tool described herein represents an essential piece of hardware. The resulting overall system can be applied as experimental setup for the analysis of the task performance and may help to settle the argument whether or not surgeons – and patients – benefit from haptic feedback during MIRS.

1.4 Outline

The Introduction (Chapter 1) gives a very brief background on the fields of minimally invasive and minimally invasive robotic surgery. A more in-depth treatment of the area of minimally invasive robotic surgery can be found e.g. in Rosen et al. [8]. The introduction further cites the problem statement this thesis is based on and gives an overview over the contributions that are made to the current state of research. Chapter 2 describes the current state of research in more detail. An overview over the surgical robotic system currently developed at the DLR Robotics and Mechatronics Center is followed by a discussion on the availability of both enhanced dexterity and haptic feedback in medical robotic instruments, their impact, and necessary components. The chapter ends with a discussion of the deficiencies of the current state of the art. The design process presented in this thesis (Chapter 3 to Chapter 6) follows the structure laid out in VDI 2221 (see VDI [9], Frei [10]).

Requirements for the proposed tool that were both identified by the deficiencies of the state of the art as well as dictated by the integration into the DLR robotic surgery system are clarified and defined in Chapter 3. This chapter also defines the boundaries of this work and summarizes the key contributions distinguishing this thesis from previous research.

The proposed tool is divided into individual functional modules for force sensing, articulated wrist, tool tip functionality and motor unit with instrument interface. Solution concepts for these functional modules are developed and discussed individually in Chapter 4.

A more detailed layout and the implementation of the individual functional modules are described in Chapter 5. Individual functionality of key modules is demonstrated with module level simulations and experiments.

Chapter 6 discusses experiments aimed to validate the functionality of the entire tool design. The performance of both the force sensor and the articulated wrist is demonstrated in test bench experiments. Furthermore, the functionality of force feedback in palpation tasks is evaluated with a limited user study and with automated palpation experiments.

Chapter 7 concludes this thesis with a discussion of contributions and experimental results, and also provides an outlook towards further research topics.

2

State of the Art

In this chapter a brief overview of the research in the field of minimally invasive robotic surgery, focusing mostly on surgical tools, is given. There is little debate in literature that increased dexterity – which robotic surgery systems and telemanipulation can provide over conventional minimally invasive surgery – produces a benefit to the surgeon. A similar debate on the impact of force feedback, however, is still very much contested. Both debates including some of the key arguments are introduced subsequently, and are followed by an in depth look at existing technical solutions for increasing dexterity and providing force feedback in tools for minimally invasive surgery. However, first of all, research at the DLR Robotics and Mechatronics Center (RMC) in the field of robotic surgery is introduced as it provides the framework this thesis is based on.

2.1 The DLR *MiroSurge* Framework

The research on surgical robotics at the DLR Robotics and Mechatronics Center focuses on versatility and lightweight aspects of robotic components to allow for a wide range of surgical applications and ease of integration into the operating room. Dividing the *MiroSurge* system (concept overview shown in Fig. 2.1 a) into generic building blocks simplifies the development of scenarios for various applications. Major building blocks are the versatile robotic arms (see Fig. 2.1 c), dedicated instruments (see Fig. 2.1 d), configurable user input station (see Fig. 2.1 b), and a modular communication and control infrastructure. Examples for target applications are telemanipulated visceral[1] surgery using *MICA* instruments or semi-autonomous osteotomy using laser ablation or oscillating saws). Extensive details on the development of the DLR *MiroSurge* system can be found in Hagn [4], Ortmaier et al. [11], Hagn et al. [12, 13, 14].

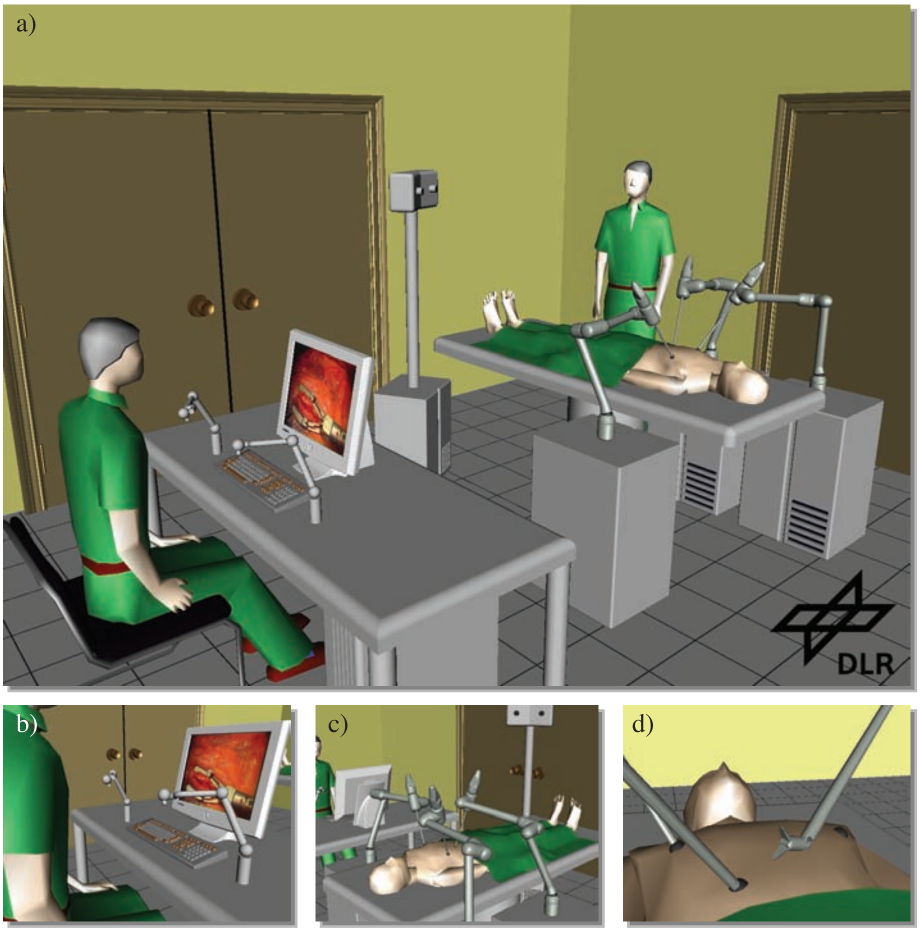

Figure 2.1: Concept of the DLR *MiroSurge* system. Conceptual view of the operating room (a), surgeon input console (b), *MIRO* robotic arms (c), and dedicated instruments (d).

The main component of the DLR *MiroSurge* system is the *MIRO* robot arm. It is based on the robotic technology developed at the Robotics and Mechatronics Center. The *MIRO*

---

[1] pertaining to internal organs

robotic manipulator features 7 actively driven joints, every joint containing a dedicated torque sensor. All joint control and power electronics are integrated into the arm. The dimensions and kinematic structure are similar to the human arm, with a kinematic length of $760\ \mathrm{mm}$ from shoulder to wrist. A low weight of $\leq 10\ \mathrm{kg}$ per arm ensures that the *MIRO* setup can be easily rearranged during surgery. Enhanced control methods and consequent light weight design also increase safety during close interaction with patient and user. A multilayer safety concept implemented in software and hardware aims to avoid collisions, and the reduction of accelerated masses reduces the severity of collisions between man and machine should they occur.

The versatile *MIRO* arm is adapted to specific surgical applications by adding dedicated instruments. The components of the *MiroSurge* system in a typical setup for minimally invasive visceral surgery are shown in Tab. 2.1. The clear separation between versatile robotic platform and dedicated instrument is manifest in the interface between both. It is strictly limited to physical attachment, electrical power and system communication. Instruments, therefore, are considered self-sufficient robots, incorporating all necessary motor control, power, communication, and sensor signal conditioning electronics. The novel articulated grasping tool presented in this thesis is part of the development effort for the dedicated instrument *MICA*. Therefore, the concept and requirements for *MICA* will be discussed in detail in Sec. 3, and Sec. 4.

The *MiroSurge* surgeon input console consists of two Force Dimension sigma.7 hand controllers and a 3D monitor. The sigma.7 was commissioned by DLR and built by Force Dimension [15]. It is the first force feedback input device that combines control of the instrument tip in 7 DoF with the feedback of manipulation forces, torques, and grasping force. The sigma.7 is based on the Force Dimension parallel delta structure which provides a good trade-off between workspace size and stiffness. The proliferation of the 3D display market in recent years offers a wide selection of high definition 3D monitors (either with glasses or autostereoscopic) that can be used as part of the input console.

The communication and control infrastructure of the *MiroSurge* system (see Fig. 2.2) is based on *SpaceWire* [16] bus architecture and Simulink external control models executing on QNX real-time operating system (RTOS) [17]. Each *MIRO* and *MICA* is connected to a dedicated QNX system executing the Simulink external model for joint level control. The two QNX systems corresponding to one *MIRO* / *MICA* manipulator are connected to a mid-level QNX system via *aRDnet* (agile Robot Development net), a real-time communications framework developed at the Robotics and Mechatronics Center by Bäuml and Hirzinger [18]. The mid-level system executes models related to whole arm kinematics and force feedback and also connects to one sigma.7 via USB. A top-level QNX system executes models for the whole system kinematics, also including the 3$^{\text{rd}}$ *MIRO* carrying the stereo endoscope. A number of *Linux* PCs provide a graphical user interface (GUI) for user interaction, 3D video rendering and display, instrument tracking, and virtual system visualization.

This modular infrastructure, while seemingly complex, simplifies the development of scenarios with any number of components, from single arm autonomous camera guidance (as described by Wei et al. [19], Omote et al. [20]) to multi arm telemanipulation setups including surgeon and assistant consoles and instruments.

Table 2.1: Components of the DLR *MiroSurge* system for minimally invasive visceral telesurgery (Hagn et al. [21]).

	Component	Parameters (per single component)
Telemanipulators	3 DLR *MIRO* arms	7 DoF Weight $\leq 10\text{kg}$ Payload 30 N Kinematic length 760 mm (shoulder to tool interface) position, torque and impedance control
Instruments	2 DLR *MICA* instruments (described in this thesis)	2 DoF articulated wrist joint 1 articulated end effector 7 DoF force-torque sensor integrated in tool tip
	WOLF stereo endoscope	endoscopic stereo camera pair
Control interface	2 Force Dimension sigma.7	6+1 DoF force feedback device
Display	SeeFront 3D	Autostereoscopic 3D display

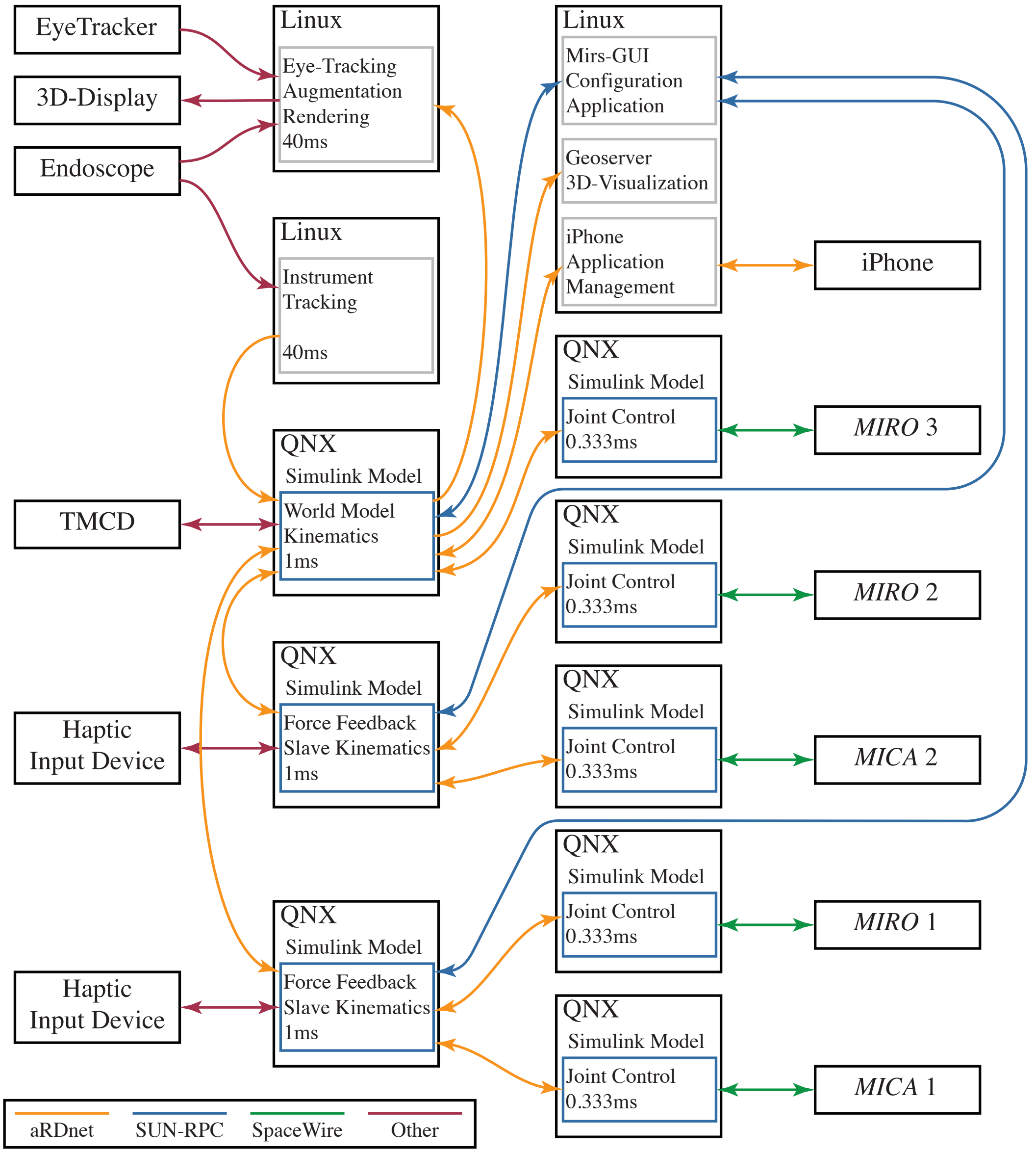

Figure 2.2: Main components and interconnections of DLR *MiroSurge* system. Currently, every *MIRO* and *MICA* is connected to a dedicated real-time QNX PC providing joint level control. Force feedback input control and whole arm (10 DoF) kinematics is provided by a QNX PC for each *MIRO*/*MICA* setup. Top level control for the entire scenario (world model) is provided by one more QNX PC which also provides connectivity for a TMCD (tele-manipulation command device, a remote control and safety stop device). A number of Linux PCs provide a GUI, 3D video rendering and display, instrument tracking, and virtual system visualization (adapted from [22]).

2.2 Robotic Systems in Clinical Applications

Many robotic systems have been available or proposed for the use in surgery. They include assistance systems, programmable automates and telemanipulation systems. Excellent surveys and classification of robotic systems for surgery can be found in Hagn et al. [14], Camarillo et al. [23], Kim and Schulam [24], Dotzel et al. [25] as well as in Sackier and Wang [6], Taylor and Stoianovici [26], Cleary and Nguyen [27], Davies [28].

In the context of the MIRS tools described in this thesis, the field of robotic telemanipulation systems for visceral surgery is most relevant. When considering commercially available MIRS systems for clinical use, two robotic systems are most prominent. The Zeus system by Computer Motion (Ghodousssi et al. [29]) was available until 2003 when Computer Motion was acquired by Intuitive Surgical® after a lengthy patent battle. It consisted of a surgeon's console and three individual robotic arms mounted to the operating table. The center arm held a standard laparoscope which could be controlled by either voice command or a hand-held key pad. Two more robotic arms were used to guide several different minimally invasive instruments. These instruments included a 1 DoF wrist joint at the tip of the tool, actuated by a detachable motor module mounted to the proximal end of the tool. Combining the movements of the robotic arm and the instrument resulted in a total of 5 DoF for articulation and 1 DoF for grasping at the tool tip. The input console closely recreated the kinematics of conventional minimally invasive surgery, simulating the restricted movement about the point of incision. Surgeons skilled in conventional MIS were, therefore, able to readily adapt to this system. The latest version included a 3D vision system, requiring the surgeon to wear shutter glasses.

The only commercial robotic system for minimally invasive visceral surgery currently available is the daVinci® system by Intuitive Surgical® (Intuitive Surgical [30], Guthart and Salisbury [31]). As of June 2011, more than 1900 systems were in clinical use. It consists of three main components: a surgeon console with three-dimensional video display viewer, a robotic manipulator with up to four robotic arms (one arm for the laparoscope and up to three arms for various instruments), and a vision cart. Three-dimensional visualization is possible using two separate optic channels in the stereo laparoscope. 3D video images of the operative situs are displayed on a stereo display in the surgeon console. Camera control is possible directly from the surgeon console through the use of a combination of hand and foot controls.

The daVinci® System uses a kinematic structure different from the Zeus® system. At the input console, the surgeon's hand movements are not constrained by trocar kinematics, instead, surgeons are able to freely move their hands in 6 DoF. This hand motion is translated by the control software to generate the motion of the EndoWrist® instruments. The EndoWrist® instruments contain a 2 DoF wrist and 1 DoF end effector at the tool tip. The surgeon's hand motions are, therefore, more similar to open surgery than to conventional MIS. ”EndoWrist® instruments allow for an impressively complete range of motion of the instrument tips, readily facilitating tissue dissection and optimal needle positioning, comparable to open surgery” (Sung and Gill [32]).

A number of clinical trials compare the performance of one robotic surgery system with conventional laparoscopy (Lee et al. [33], Desgranges et al. [34], Trimlett et al. [35], Prasad et al. [36]), or directly compare the Zeus® and daVinci® systems with each other (Wullstein et al. [3], Sung and Gill [32]). In conventional laparoscopy tip movement is restricted to 4 DoF, the vision system is usually 2 D and tools are manipulated directly, usually by scissor-like handles with thumb and finger rings. A direction reversal and variable scaling between hand and tool tip motion exists. The Zeus® system provided 5 DoF motion, 3D vision and restored hand-eye coordination. The daVinci® system provides 6 DoF motion, immersive 3D vision with restored hand-eye coordination, and hand motion is not restricted. Attributing performance gains to either improved tool tip dexterity, improved user interface, or 3D over 2 D vision, based on the above mentioned studies is difficult. General agreement exists, however, that each of these three factors contributes to an improvement in overall performance. Unfortunately, no technical or performance details are known on the drivetrain of either the Zeus® or daVinci® systems.

2.2.1 The Benefit of Dexterity

The impact of dexterity on task performance in minimally invasive surgery, both conventional and robotic, has been extensively studied, with wide agreement on the benefit. Only a small exemplary selection of research on the impact of tool tip dexterity will be presented in this section. Hodgson et al. [37] evaluated the effect of reversed hand and tool motion resulting from the trocar constraint as well as the effect of 4 DoF, 5 DoF and 6 DoF motion on task performance. Both open surgery tools and conventional laparoscopic surgery tools were used during the evaluation. It was shown, that avoiding the reverse hand and tool motion drastically improved performance in simple pick and place tasks as well as complicated suturing tasks. Full 6 DoF dexterity yielded little improvement over restricted (4 DoF, as in conventional laparoscopy) motion for simple tasks, however substantial benefits could be shown for complicated tasks.

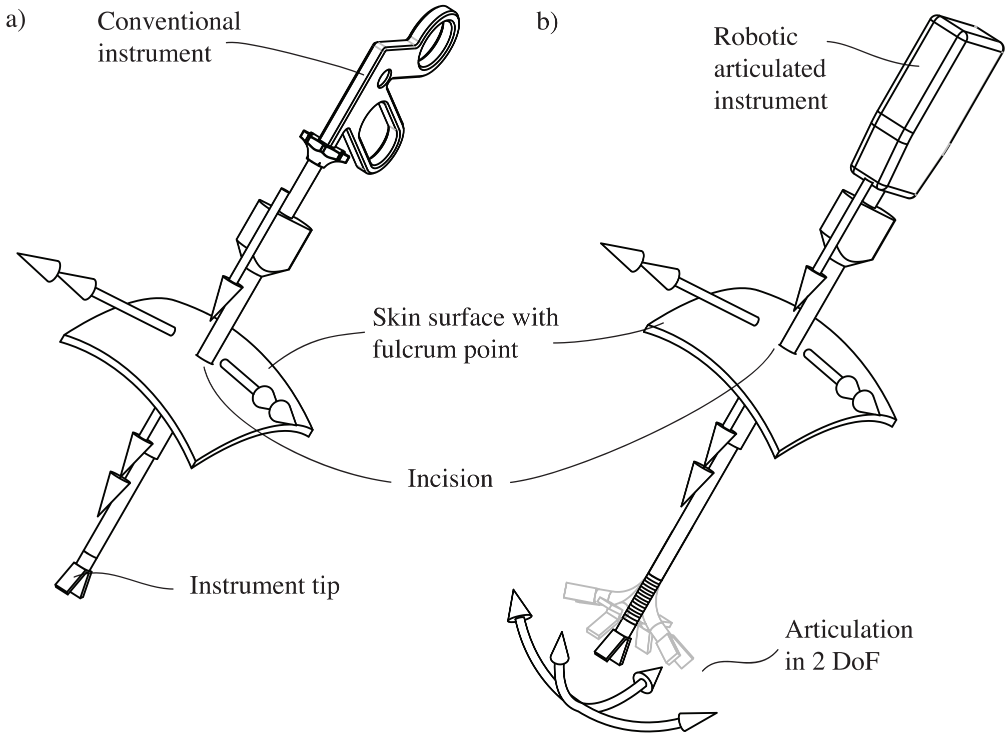

Figure 2.3: Loss of dexterity at the instrument tip. Conventional instrument with four degrees of freedom (DoF) at the distal end (a), and articulated instrument with full (6 DoF) manipulability at the distal end (6 DoF).

Laparoscopic instruments with additional intra-corporal degrees of freedom need not be robotic. One example is the Radius Surgery System® (by Tuebingen Scientific Medical GmbH) [38]. This tool incorporates a deflectable and rotating tip (2 DoF pitch-roll) with an ergonomically designed handle. Due to its close resemblance to a conventional laparoscopic instrument integration in a conventional clinical setting is straight forward with little additional cost. Frede et al. [39] found an accelerated learning curve and improved accuracy for vesicourethral anastomosis[2]. However, the reversal between hand and tool tip motion

---

[2] connecting the urinary bladder and the urethra

remains, and simultaneous movement in 6 DoF is difficult to achieve. This is due to the complicated mapping between hand and tool tip motion, as two additional DoF have to be controlled with each hand, placing high demands on the surgeon's manual dexterity. It was observed that surgeons tend to deflect the wrist to an advantageous approach position and then leave it locked in that position for a majority of manipulation tasks.

The study performed by Dakin et al. [40] compares conventional laparoscopic skill performance to both the Zeus® and daVinci® systems. Surgeons were evaluated for time and accuracy on a number of laparoscopic training tasks of increasing difficulty. The tasks were 'rope passing', 'bead drop' on a pegboard, 'peanut task' of dropping cotton balls into beakers, and 'suturing' with knots and running stitches of various sizes. While the first three tasks evaluate important task primitives such as grasping and instrument positioning, they do not allow for a performance prediction during a complex surgical task. Only suturing is representative of the latter. A reduced number of errors and higher precision, especially during the complex tasks was evident for both robotic systems. The presence of articulated EndoWrist® tools and 3D vision are likely factors contributing to daVinci® outperforming Zeus® regarding speed and accuracy.

Hernandez et al. [41] investigated the effect of training on surgical task performance using a small bowel anastomosis model with the daVinci® system. The model simulated a complex procedure that requires advanced planning and the use of a significant range of skills. Surgeons were evaluated on shape, lumen, and strength of the anastomosis, as well as on time, tool tip path length and number of movements. Surprisingly, after only five training sessions, results did not significantly vary between novice and expert laparoscopic surgeons. The high level of immersion and intuitive handling of the EndoWrist® instruments without motion restrictions likely offer advantages to surgeons who are relatively new to laparoscopic surgery techniques.

As already indicated at the beginning of this section, there is general agreement on the correlation between increased dexterity and increased task performance. The situation is less clear for the impact of haptic feedback on surgical performance.

2.2.2 The Impact of Haptic Feedback

Lederman et al. [42] describes haptics "... as a perceptual system, mediated by two afferent subsystems, *cutaneous* and *kinesthetic*...". Being able to recognize objects by touch relies on a number of receptors: mechanoreceptors and thermoreceptors embedded in the skin (cutaneous), and mechanoreceptrs embedded in muscles, joints and tendons (kinesthetic). The haptic properties of an object can be summarized by the following characteristics: Surface texture relates to the cutaneous system, and is mostly characterized as roughness. Weight relates to the kinesthetic system and can be perceived as an object's resistance to the rotational forces generated by the limbs. Compliance is an object's deformability under external force. An object's geometric properties are determined by size and shape. Thermal quality and orientation are two further haptic properties according to [42]. While weight and texture can be clearly assigned to the kinesthetic and cutaneous domains respectively, the perception of compliance and geometric properties overlaps both domains. The dominance of each domain depends mostly on the scale of the object. Objects smaller than the fingertip are generally perceived through the cutaneous domain, larger objects through the kinesthetic domain.

Many of the studies presented below use the terms *force feedback*, *tactile feedback*, and *haptic feedback* interchangeably. Within this thesis, force feedback is a subset of haptic feedback related to kinesthetic mechanoreceptors and tactile feedback is a subset related to cutaneous mechanoreceptors. Both sets require rather different physical sensors and displays. Tactile feedback most often utilizes an array of pressure sensitive 'taxels' as sensor to provide a simultaneous spatially resolved force distribution. The measurement of cutting, suturing, and dissection forces with a multi DoF force-torque sensor, and also the measuring of tissue stiffness by indentation on the other hand, are considered force sensing.

To visualize the scope of force feedback described in this thesis, the model of haptic exploration with a pen or tweezers can be used. It is possible to recognize an object's size, shape, weight, (point) compliance, and to exert forces and torques, but the recognition of surface textures is limited. The measurement of a compliance distribution is possible, but only by *sequential* palpation of individual points. For the remainder of this thesis, only force feedback relating to the scope defined above will be discussed.

During open surgery surgeons rely strongly on their sense of touch. Recognizing the haptic properties of tissue allows them to assess the health of tissue and locate certain structures (e.g. blood vessels or tumors). In conventional MIS, much of the haptic feedback from the operation site is lost. Bholat et al. [43] assert that haptic feedback is present during MIS and surgeons are still able to determine size, shape and compliance of objects. However, this becomes more difficult with decreasing structure size, though. Tissue manipulation forces cited in literature range from 0.3 N for bypass grafting (Salle et al. [44]) to few Newtons overall (according to Peirs et al. [45], Kitagawa [46], Verner et al. [47], Braun et al. [48], Brouwer et al. [49]). The friction generated within the instrument mechanism and between the instrument and the access port in laparoscopic surgery can, therefore, greatly exceed tissue manipulation forces for small structures (Picod et al. [50]). In MIRS no direct contact between the surgeon's hand and the tool tip exists. Consequently, haptic feedback is lost completely.

Experienced surgeons are able – through experience – to interpret tissue deformation visible in the laparoscopy image as a measure of applied manipulation force. However, tissue properties depend on patient, tissue type, health, and can also vary with time (Wagner et al. [51]). Moreover, stiff or rigid materials such as bones, and suture materials show no perceptible deformation at all. It is, therefore, difficult to guarantee optimal and reliable tightness of a knot, for example, because thread tension cannot be estimated visually (Müller [52]). Kitagawa et al. and Akinbiyi et al. [53, 54] proposed a modified EndoWrist® instrument with 2 DoF strain gauges attached to the tool shaft in order to measure and display knot tying forces directly. This resulted in significantly less broken sutures and loose knots. However, because of the placement of strain gauges on the tool shaft, the force signal suffered from errors due to wrist actuation and friction.

Hagen et al. [55] suggest that haptic feedback is not necessary. During this study, predominantly novice surgeons express major concerns about the lack of haptic feedback in robotic surgery. While surveying three groups of individuals: surgically inexperienced subjects, novice and expert laparoscopic surgeons, it was found that all of the experts perceived purely visual cues that are available in the video image (such as tissue deformation) as analog to haptic feedback, and even half of the novices perceived the visual information as analog to haptic feedback already during the first procedure. Therefore, Hagen et al. [55] concludes that with experience, perception of haptic feedback and the overall level of comfort with robotic surgery increases significantly. According to this study, perceived haptic feedback renders real haptic feedback less important and demonstrates that the importance of haptic feedback is overestimated by novices in robotic surgery.

Wagner et al. [56] motivate the use of force feedback with the example of attempting to move one's hand or tool in a straight line. "A free motion using only information-based forms of feedback, such as visual signals, is difficult and results in an imperfect straight line. However, moving a tool, such as a pencil, in a straight line is trivial when using a ruler as a guide. The ruler constrains the motion of the pencil to lie exactly alongside the ruler. Using a ruler transforms a task requiring precise position control and mental effort into a simple task requiring the user only to push the pencil against the ruler. In a similar manner, force feedback can reduce the mental workload and positioning control accuracy needed when attempting to position a tool alongside an environmental structure" [56]. The force information acting as the constraint might come from the intrinsic stiffness of an organ, however it might also be based on a model.

A previous dissection experiment by Wagner et al. [51] seems to support the 'physical guide' hypothesis. During the experiment, participants were asked to dissect and expose an arterial structure embedded in tissue, simulated by caulking and play-dough, respectively, using a telemanipulator setup consisting of two PHANToM® haptic hand controllers. Tissue manipulation forces were recorded by a 6 DoF force-torque sensor manufactured by ATI Industrial Automation, Inc.. The presence of force feedback reduced the number of errors as well as the level of applied forces, however did not significantly impact the speed of dissection. It is hypothesized that with decreasing levels of force feedback, the force information is transformed from a physical constraint into supplemental information that requires a conscious effort to utilize.

Equally, Deml et al. [57] found a lower error rate but also a lower dissection speed in an experiment similar to Wagner et al. [51], when force feedback was present. They conclude that higher force scaling leads to decreased performance because subjects are fighting the presented forces. Gain levels should be adjusted so that displayed forces are just above the detection threshold of the user.

In another study, Wagner et al. [58] also describe the reduction of applied tissue manipulation forces in the presence of force feedback for all participants, however, only surgically trained experts were able to benefit from the additional information without an increase in trial time. It was also shown that force feedback had the potential to reduce errors without requiring cognitive attention. This implies that processing of force feedback information can occur faster than other stimuli, and that force feedback does not necessarily increase mental workload.

All previously mentioned studies agree, that the presence of force feedback leads to a reduction of the applied force level, however not a reduction in task execution time. Postulating – for the moment – that for selected applications haptic feedback will prove beneficial, the question still exists, whether feedback of all force and torque components is necessary and whether high quality force feedback is needed. Kitagawa et al. [46] indicate that the effect of force feedback limited to 2 DoF – neglecting forces in the direction of the instrument shaft – approximates 3 DoF force feedback. Also, user performance with the 3 DoF force feedback closely approximated performance during manual task execution. Tavakoli et al. [59] hint that the force components which are considered essential during an interaction may change with the type of task being performed. When performing grasping tasks, lateral and axial (with respect to the tool shaft) forces may dominate due to pulling and pushing of tissue, whereas torsional forces may be of greater importance during suturing tasks. Saha et al. [60] attempted to establish a metric to determine which force components are most beneficial for selected surgical tasks. A modified EndoWrist® equipped with a 6 DoF ATI-Nano force-torque sensor was used for suturing and knot tying tasks. It was assumed that the force component showing the largest variations during the experiment would be the most significant one. However, the validity of this assumption has not been proven.

Brouwer [61] hypothesizes, that contrary to common belief, low cost low quality force feedback devices might be just as good as expensive, high quality setups. He used a commercial state of the art surgical training simulator consisting of a trocar based force feedback hand controller and a surgical simulation environment (manufactured by Immersion Corp.), and artificially inserted time delay, friction, and mechanical cogging into the simulation. Decreasing the quality of the force feedback signal did not significantly alter the usability of the test setup and the performance of participants while used in a surgical training environment.

Further reviews on the application of haptic feedback in surgical simulation and training systems can be found in Basdogan et al. [62], Fager [63], van der Meijden and Schijven [64]. Reviews on haptics in MIRS are compiled by Bethea et al. [65], Feller et al. [66], Tavakoli et al. [67]. Obviously, the debate on the benefit and useful extent of force feedback (or more general, haptic feedback) during MIRS is far from over. Should the summary on the impact of haptics given above seem confusing, it successfully conveys the inconclusive state of research in the field.

The conclusion of this review is: for an objective evaluation, a tool is needed combining dexterity and full force feedback. Only then the assessment can be made which components of manipulation forces and torques are required to advantageously utilize force feedback. Wrist actuation forces need to be separated from tissue interaction forces to allow for accurate force feedback. Such a system does not exist so far and will be developed in this thesis. The following sections will take a closer look at the availability of two major functional building blocks required to build such a system: articulated wrists and force-torque sensor.

2.3 Surgical Tools and Components

Some of the motion restrictions imposed on surgical manipulation by the invariant point (trocar point) can be overcome – and thus dexterity improved – by increasing the number of articulated degrees of freedom available at the instrument tip (see Fig. 2.3). This is achieved by introducing one or more articulated joints close to the instrument tip, often referred to as wrist. Similarly, in order to provide force feedback, the interaction forces between instrument tip and surrounding environment (manipulation forces and gripping force) have to be measured. The following sections give an overview of previously reported wrist and force sensor implementations relevant to the field of minimally invasive surgery.

2.3.1 Robotic Wrists in Minimally Invasive Surgery

Only a limited number of surgical tools for MIRS have ever reached the commercial stage. A selection is discussed below. The best known example of articulated tools for MIRS is the EndoWrist® by Intuitive Surgical® as part of the daVinci® robotic surgery system. The tool design is highly integrated with a diameter of 8 mm, is extremely rugged and provides two cable driven DoF in addition to the actuation of the functional end (forceps, scissors and needle holders), thus providing full dexterity inside the body (see Fig. 2.4 a and Madhani and Salisbury [68]). Subsequently, Intuitive Surgical® developed even smaller tools with a diameter of 5 mm, featuring a cable driven spine kinematic for the 2 DoF actuation (see Fig. 2.4 b and Cooper et al. [69]). Sterilizability of the steel cables is still an issue despite a silicone wiper that is supposed to prevent liquids from penetrating the tool shaft, which – aside from commercial considerations – is one of the reasons that tools are only certified for 10 applications. Rotation about the shaft axis causes the actuation cables inside the shaft to twist, greatly increasing mechanical friction.

Other tools that were commercially available as part of a robotic systems were the articulated wrist by endoVia Medical, Inc. (see Lee and Brock [70]) which was very similar in kinematic structure to the EndoWrist®, and the 1 + 1 DoF tool as part of the Zeus® system (see Grace [71]). The Zeus® wrist was extremely compact and was articulated by sliding

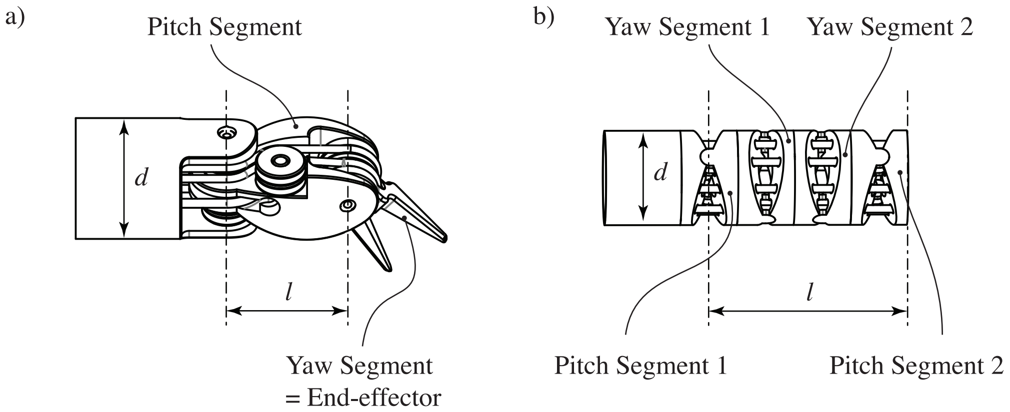

Figure 2.4: Size and segment numbering conventions for the 8 mm EndoWrist® [68] with pitch-differential kinematics (a) and the 5 mm EndoWrist® [69] with pitch-yaw-symmetric kinematics (b).

linkages, however, it could only be articulated towards one side.

One more tool that is currently commercially available, albeit only for conventional laparoscopy, is the Radius Surgery System® (by Tuebingen Scientific Medical GmbH) (see Braun et al. [38]). The tool has a diameter of 10 mm with a roll-pitch-roll wrist kinematic and exchangeable end effector. The wrist is driven by bevel gears with the motion being transmitted by rotating tubes and sliding shaft. In order to allow the surgeon to control the 2 + 1 wrist DoF, the instrument handle has been completely redesigned. Pitch articulation is controlled by tilting of the surgeon's wrist, and tip roll is controlled by a knob rotated with the surgeon's thumb and index finger.

The topic of robotic wrists is not limited to surgical tools. Rather to the contrary, the largest selection of robotic wrist designs and implementations is found in industrial and service robotics. Rosheim [72] compiled an extensive overview of robotic wrist actuators. Due to their complexity, most of these design and component suggestions do not reasonably scale down to the size required in surgical tools. The overview of previously reported wrist designs is, therefore, limited to implementations found in, or suggested for surgical tools. Comprehensive reviews of the state of the art in in this field have been compiled by Cepolina et al. [73] and Catherine et al. [74]. Rather than simply enumerating tools, Catherine et al. [74] have attempted to create normalized reference criteria that allow for a performance comparison of given wrist designs against a postulated ideal reference wrist.

While the definition of the ideal reference will always be somewhat arbitrary, the classification scheme tries to account for the often reciprocal effect of certain design specifications (e.g. increasing the number of degrees of freedom for a wrist of given diameter and length will likely limit the range of motion (RoM)).

Aside from the number of motion degrees of freedom, the range of motion and the achievable force at the tip of the instrument, the motion accuracy and dynamics respectively are two important considerations in robotics, however they have been neglected in previous reviews and are seldom included in the original publication. Therefore, a number of original publications on articulated minimally invasive tools is revisited in order to extract this information where available. Results of this review are summarized in Tab. 2.2. The table is divided into the main categories of manual tools (non-motorized), handheld robotic (handheld but actuated by electric motors), robotic (actuated by electric motors and attached to a robotic arm), and wrist components that have not been integrated into a tool yet. Also included are some specialized tools for endoscopic, single port and NOTES[3] procedures.

The following assumptions have been made during the compilation of Tab. 2.2. Individual data may have been reported differently in the original publication but for the sake of comparability has been transformed to the following scheme:

- *Tool tip motion* is reported as wrist motion plus end effector motion (e.g. 2 + 1).
- *The first 4 DoF are provided by an external fixture*. Pivoting about the point of insertion, movement along the tool shaft and rotation about the shaft axis (as shown in Fig. 2.3 a are assumed to be provided by a robotic manipulator or human operator and are not considered part of the tool wrist motion. Therefore, shaft rotation is always considered as external motion, even if the actual joint location is close to the tool wrist.
- *Wrist diameter and length* are measured from the first wrist joint axis to the end effector axis (see Fig. 2.4 a) and b). If the publication does not include an end effector (see Fig. 2.4 b), the length is measured to the end of the wrist component. Should the length not be reported, a best guess estimate is used.
- *Segments* are defined as components or functional groups that provide the full RoM for one DoF and are driven by a single actuator. In Fig. 2.4 b) the components labeled

---

[3] Natural Orifice Transluminal Endoscopic Surgery

as pitch segments 1 and 2 are driven by a single actuator. The same holds true for yaw segments 1 and 2. Therefore, the wrist is classified as having 2 DoF with 2 segments each. Functional groups driven by independent actuators are counted as individual degrees of freedom (as in Abbott et al. [75]).

- *Kinematics* describes the kinematic layout of wrist and end effector structure. The 8 mm EndoWrist® shown in Fig. 2.4 (a) is a pitch-yaw wrist with the end effector co-located on the yaw axis. Yaw motion is created by uniform jaw movement, whereas end effector motion is created by opposing jaw movement. This type of kinematics is labeled as pitch-differential kinematics. The 5 mm EndoWrist® shown in Fig. 2.4 (b) is described as pitch-yaw-symmetric kinematics, having an independent, symmetrically actuated end effector (Cooper et al. [69]). An end effector with only a single moving jaw is classified as one-sided.

Summary discussion of Tab. 2.2:

- Only two out of 28 wrist designs report force measurement capability. Dario et al. [76] describe a manipulation force sensor integrated into a flexible arthroscope, and Arata et al. [77] report a gripping force sensor as part of the instruments's drive unit.
- The reported manipulation force range extends from 0.5 N to 10 N, with most groups reporting 1.5 N to 5 N. Only five groups reported values for the gripping force with a range of 5 N to 50 N.
- Dynamics of tool tip movement is only quoted in five publications, and is exceedingly slow in three cases with only up to 0.14 Hz. Because of the limited dynamics and limited force range, tiny motors or shape memory alloy (SMA) actors can be used. Those can even be placed directly in the tool tip, allowing for a direct drive mechanism. The one group reporting higher dynamics uses significantly larger motors in their designs (nominal motor power of 19 W in the case of Piccigallo et al. [78] yielding $560°\frac{1}{s}$ and up to 18 W in case of Piccigallo et al. [79] yielding $1\frac{\mathrm{m}}{\mathrm{s}}$ at the tip).
- 13 designs use steel cables to transmit the actuation forces from the drive unit to the tool tip, seven designs use rotating shafts and 6 use sliding linkages. Cables are popular due to their flexibility, high load capability, and relative ease of termination.

The next section will provide a closer look at force sensors that have previously been used within the field of minimally invasive surgery.

Table 2.2: Comparison of tool wrists reported in literature.

Reference	DoF[a] wrist + tip	RoM[b] [°]	Size dxl[c] [mm]	Kinem.[d]	Segm.[e]	Joint[f]	Trans.[g]	Actuation[h]	F_{Tip}[i] [N]	Dynamics[j]	Accuracy [°]	FTS[k]
manual												
Braun [38], . . . Frede [39]	2+1	80, ∞, ns	⌀10x8	pro	1	pin	s,r					0
Melzer [84]	2+1	120, ∞, ns	⌀7x70	prs	m	flex	s					0
handheld robotic												
Dario [76]	1	110	⌀4.2x25	p	m	pin	c	DC			1.1	1
Nakamura [85]	2+1	90, ns	⌀6x20	pyo	2	cyl	c		5, 8		4.3	0
Piccigallo [78], . . . Focacci [86]	2+1	±60,. . . ±180, 60	⌀10x35	pro	1	pin	c	DC 19 W	ns,ns,50	$560° \frac{1}{s}$		0
Yamashita [87]	2+1	±80, ns		pyo	2	pin	r	BLDC	3, 5		9	0
robotic												
Grace [71]	1+1	90, 30	⌀6x3	po	1	pin	r	DC				0
Mueglitz [88]	1+1	±180	⌀9.2x60	po	m	pin	s		5, ns			0
Harada [89]	2	±90	⌀2.4x5	py	2	ball	c	US				0
Arata [77]	2+1	±70, ±50	⌀10x22	pd	1	pin	r	DC				1
Berkelman [90]	2+1	±90	⌀6x20	py	3	ball	c	BLDC	5			0
Madhani[68]	2+1	±90, ±90	⌀8x9	pd	1	pin	c		10, 50			0
Cooper [69]	2+1	±90, ±90	⌀5x15	pys	2	pin	c					0
Ishii [91], . . . Ishii [92]	3+1	±90, ns	⌀10x70	pyro	3	pris	s	DC 2.23 W	4	0.14 Hz	3	0
components												
Kode [93]	0+1	30	⌀5x50	o		pin	d	DC/SMA	5.5			0
Zahraee [94]	1+1	90, ∞, ns	⌀6x40	pro	m	pin	r,s	DC				0
Arata [95]	2	±45	⌀15x14	py	1	flex	r	DC	5		2.3	0
Darbemamieh [96]	2	±90	⌀8x16	py	2	pin	c					0
Peirs [97]	2	±90	⌀4.9x22.5	py	m	flex	c					0
Ho [98]	4	±60	⌀12x92	pyyp	2	pin	d	SMA	1.5	$\frac{1}{20}$-$\frac{1}{35}$ Hz	7	0
Guckert [99]	3	ns, < ±40, < ±20		rpy	1	ball	c					0
Sieklicki [100]	3	±20, ±0.25mm	⌀2.5x7.5	pyl	1	flex	r				$8 \frac{\text{deg}}{\text{mNm}}$	0

Continued on Next Page. . .

Table 2.2 – Continued

Reference	DoF[a] wrist + tip	RoM[b] [°]	Size dxl[c] [mm]	Kinem.[d]	Segm.[e]	Joint[f]	Trans.[g]	Actuation[h]	F_{Tip}[i] [N]	Dynamics[j]	Accuracy [°]	FTS[k]
Salle [44],. . . Morel [101]	5	±90, ±90, . . . ±180,±90, ±180	⌀10x110	pyryr	1	pin	d	BLDC	< 0.15			0
endoscopic												
Kawahara [102]	1+1	±60, ns	⌀2.6x10	ps	1	flex	c		0.5			0
Ikuta [103]	7+1	±40, ±50, ∞, ns	⌀10x90	pypypyrs	1	univ	c	DC		0.1 Hz	5	0
single port												
Piccigallo [79]	6	±90, ±67, ±90, . . . ±180, ±60, ±180	⌀23x142	rpprpr	1	pin	s,d	BLDC,. . . 4-18 W	5,10	$1\frac{\mathrm{m}}{\mathrm{s}}$	8 mm	0
NOTES												
Abbott [75]	8+1	50x50x100mm^3, ns	⌀7.2x75	trpyypyd	1	roll	c	DC			5.3-20, . . . $1.15\frac{\mathrm{deg}}{\mathrm{mNm}}$	0

---

[a] Wrist degrees of freedom + end effector degrees of freedom.

[b] Range of Motion of wrist and end effector in degrees, continuous (∞), not specified (ns). ± denotes symmetric operation, a positive value denotes one-sided operation only.

[c] Diameter, and length of the wrist mechanism from first axis of articulation to end-effector axis.

[d] Tool kinematics: roll (r), pitch (p), yaw (y), linear (l). End effector kinematics: single articulated jaw (o), symmetrically actuated jaws (s), differentially actuated jaws (d).

[e] Every DoF consists of 1-4, or many (m) discrete joint segments actuated in unison.

[f] Joint construction: pin (pin), flexural (flex), cylindrical (cyl), ball (ball), prismatic (pris), universal (univ) and cylindrical surface contact (roll).

[g] Transmission of drive motion: sliding link (s), rotating shaft (r), cable (c), direct-drive (d).

[h] Actuation: DC motor (DC), brushless DC motor (BLDC), ultrasound motor (US), shape memory alloy (SMA).

[i] Tip force in Newtons, grasping force in Newtons.

[j] Tip dynamics. The values stated in Hertz denote the frequency of full range sinusoidal motion.

[k] Degrees of force sensing integrated with the tool.

2.3.2 Multi DoF Force Sensors

Many minimally invasive instruments with force-feedback have been proposed and built in the past. An excellent and comprehensive review of ”force sensing and its application in minimally invasive surgery and therapy”, including experimental studies related to force sensing, and also an overview of commercially available force sensors has been compiled by Trejos et al. [80]. Gathering information on force feedback instruments, this review lists information on tool actuation, sensor technology, sensor location, sensing degrees of freedom, and – if available – sensor resolution. Other extensive reviews have been compiled by Puangmali et al. [81], mainly focusing on the variety of physical principles employed in force sensors and van der Putten et al. [82] focusing on haptics in surgery, training and simulation, including references to some haptics theory and comparative studies. Some additional information can be found in the review on haptics in MIRS by Okamura [83].

Together, the above mentioned reviews cover the current state of the art of force sensing in minimally invasive surgery. However, more detailed information on the sensor performance (measured load components, force and torque range, bandwidth, resolution and accuracy) has not been included in these reviews.

Especially the last three parameters are seldom mentioned in publications at all and have not been included in existing reviews. Therefore, previously published research was revisited in an attempt to extract this information where available. Results of this new review are summarized in Tab. 2.3.

It has to be noted at this point, that commercially available force transducers will not be reviewed separately. A large number of single DoF load cells and load beams are commercially available, a number are mentioned in Trejos et al. [80]. Their application – where appropriate – is straight forward and, therefore, further examples are not discussed in this thesis. The only commercially available multi DoF sensors that exhibit useful sizes and load ranges for the application in MIRS are the ATI Nano and ATI Mini series 6 DoF transducers offered by ATI Industrial Automation, Inc.. These sensors are described in more detail below.

The sensors and tools listed in Tab. 2.3 fall into the following categories and are ordered by increasing number of measured load components. It has to be noted that in this section the terms force and load will be used interchangeably. A more specific definition will be developed in Sec. 4.3.

- *Purely mechanical measurement of forces.* The tool designed by Takaki et al. [104] contains a Moiré fringe pattern that visually displays mechanical deformation in the tool shaft caused by the grasping force.

- *Sensors not designed towards integration in MIS tools* but included in the survey because of interesting design concepts. The 6 DoF sensor presented by Beyeler et al. [105] was fabricated in a multilayer MEMS (microelectromechanical system) process and highlights the almost ideal mechanical properties of silicon as a structural material for force sensors in the Millinewton range. However, when surface faults are present (crack, step, opening), single crystal silicon easily breaks along crystalline lattice directions, which prevents it from being used in sensors for larger forces.

  The 6 DoF Stewart Platform based sensor presented by Dai and Kerr [106] is large with a diameter of 80 mm, assembled from several steel components, but it points to an interesting variation on the Stewart Platform (Stewart [107]). All sensing elements are moved from the legs of the Stewart Platform into the base and are sensitive to bending forces rather than the linear elongation of the legs, which should yield larger signal values and simplifies leg construction.

- *Microsurgery tools.* The tools presented by Berkelman et al. [108] and Iordachita et al. [109] are intended for ocular surgery. Berkelman et al. [108] designed a strain gauge based sensor integrated into the pen-like handle of the tool. Iordachita et al. [109] used FBG sensors directly applied to the tool cannula, which is only 0.5 mm in diameter.

- *EndoWrist® tools modified with attached strain sensors close to the wrist* to measure bending moments in the shaft. The sensor location proximal of the wrist simplifies electrical connection to the sensor. However, three sets of drive cables for wrist and the gripper are connected through the sensor which subject the sensor to actuation forces and errors due to friction. Compensating for these errors is extremely difficult since all cable forces and their locations need to be known. Twisting of cables inside the shaft adds further difficulty. Akinbiyi [110] and Mayer et al. [111] have selected this location and attached strain gauges to the shaft of an EndoWrist® tool, a design for which Larkin et al. [112] submitted a patent application. Akinbiyi [110] and Wagner [56] attached additional strain gauge sensors to custom tips of an EndoWrist® tool and a Laprotek® tool, respectively, and thereby avoided measuring actuation forces and friction. Perreault et al. [113] attached strain gauges directly to the drive cables inside an EndoWrist® tool, measuring the wrist actuation forces rather than the manipulation forces. It was necessary to disable the shaft rotation of the tool to facilitate this placement. Shimachi et al. [114] built a custom interface plate to be inserted between the daVinci® arm and EndoWrist® tool, which allows for a measurement of manipulation forces exerted on the shaft of the tool. Aside from Meer et al. [115] who used capacitive sensors integrated in special jaws, and Tadano and Kawashima [116] who used pressure sensors to control actuation forces in a pneumatically actuated instrument, the modified EndoWrist® tools mentioned above are the only experimental tools to integrate an articulated wrist and force sensing into a single tool.

- *Instrumented tool sleeves or instrumented trocars.* Prasad et al. [117] and Tavakoli et al. [67] built dedicated sleeves supporting the tools inside the trocar equipped with force sensors. Trejos et al. [118] built a sleeve like covering as part of the tool itself. Sleeves help shielding the sensor from friction inside the trocar, but preserve the versatility of using the same sleeve with various tools. Hanna et al. [119] and Shimachi et al. [120] used custom built sensors integrated into trocars.

- *Tools using a commercial ATI 6 DoF force-torque sensor.* Only a few commercially available 6 DoF force-torque sensors provide a useful combination of size and load range. Two are offered by ATI Industrial Automation, Inc.. The ATI Mini40 offers a load range up to 80 N and 4 Nm with a diameter of 40 mm and a height of 12 mm. It offers a through hole with a diameter of 6.35 mm for cables. The ATI Nano43 offers a load range up to 36 N and 500 Nmm with a ring shape of outer diameter of 43 mm and inner diameter of 20 mm and a heigth of 11 mm. Due to its ring shape, the Nano43 is most often used as trocar sensor. Both sensors provide good performance but are far too large to be integrated into the tip of a surgical instrument. The only reference to the use of an ATI Nano17 with its diameter of 17 mm, height of 15 mm and sensing ranges from 12 to 50 N and 120 Nmm to 500 Nmm, was found in a blunt dissection phantom experiment described by Kitagawa [46]. Dubois et al. [121] and Rosen et al. [122, 123] used commercial ATI sensors installed on the split shaft of conventional MIS tools. Measurement of manipulation forces was affected by friction inside the trocar, stiffness of the abdominal wall and most significantly by the large force necessary to actuate the end effector. Zemiti et al. [124] used a commercial sensor inside a modified trocar. A robotic fixture attached to the base of the trocar is pivoting sensor, trocar, and instrument about the point of insertion. Since the trocar is attached to the base of the sensor, parasitic forces caused by trocar movements do not influence the sensor signal. Linear movement of the instrument along the shaft axis and rotation about that axis are provided by the instrument drive unit. The downside of such an arrangement is that instrument movements will change the position of the instrument's center of mass with respect to the sensor, causing large errors that have to be compensated.

Summary discussion of Tab. 2.3:

- 24 out of 33 reviewed tools provide force sensing but do not include articulated degrees of freedom other than the end effector. Out of the nine groups that report on both force sensing and dexterity, six use modified EndoWrist® tools with strain sensors attached to either jaws, shaft, cable, or a modified trocar. Out of the remaining three (Wagner [56], Meer et al. [115], Tadano and Kawashima [116]), two groups use modified tools by endoVia Medical, Inc. (Lee and Brock [70]). Among these, 4 DoF is the highest number of load components reported by Tadano and Kawashima [116] using pressure sensors in a pneumatic drive mechanism. Unfortunately the accuracy is only 1 N. Only Meer et al. [115] reports a dedicated tool design, however with only 2 DoF load measurement capability up to a maximum of 1.7 N.

- The only tool with more than 4 DoF force measurement capability not using an ATI sensor is a dedicated design presented by Trejos et al. [118, 125]. It comprises an instrumented sleeve for use with conventional (manual) handle and tool tips. All other tools with more than 4 DoF force measurement capability use ATI Industrial Automation, Inc. sensors either in a split shaft or trocar location.

- Aside from microsurgical tools, the reported manipulation force range extends from 1.7 N to 25 N, with most groups reporting 5 N to 10 N. Similarly, gripping forces range from 1.7 N to 50 N with most falling within 5 N to 25 N.

- Resolution – reported only by 13 out of 33 groups – falls within a range of 4.8 bit to 16 bit, with most groups reporting within the 5 bit to 8 bit range.

- Accuracy – reported by 17 groups – falls within a range of 3.3 bit to 9.5 bit, with most falling into the 5 bit to 7 bit range.

- Bandwidth is difficult to assess as publications are not always clear whether the reported frequency is filter bandwidth or sampling frequency. Reported values vary

Table 2.3: Comparison of sensors and sensor concepts reported in literature.

Reference	DoF	Load$^\mathrm{a}$	Range$^\mathrm{b}$	Size [mm]	Method$^\mathrm{c}$	Location$^\mathrm{d}$	Bandw.$^\mathrm{e}$ [Hz]	Resolution$^\mathrm{f}$ [eq. bit]	Accuracy$^\mathrm{g}$ [eq. bit]	Wrist DoF$^\mathrm{h}$
mechanical										
Takaki [104]	1	$\mathrm{F_g}$	6 N	⌀10	Moiré	Shaft$_\mathrm{I}$				0
non-medical										
Beyeler [105]	6	F, M	1 mN, 2.6 μNm	10x9x0.5	Cap		30		9.5, 9.5	0
Dai [106]	6	F, M		⌀80x49	SG		<320		0.36 N, . . . 0.89 mNm	0
MIS tools										
Larkin [112]	ns	ns		⌀8		Shaft$_\mathrm{I}$	>10			2
Bicchi [126]	1	$\mathrm{F_g}$		⌀20	SG, HB	Shaft$_\mathrm{O}$				0
De [127]	1	$\mathrm{F_g}$	24.5 N		Futek FR-1010	Drive				0
MacFarlane [128], . . . Hannaford [129]	1	$\mathrm{F_g}$			$\mathrm{i_{Motor}}$	Drive	1000			0
Akinbiyi [110]	2	$\mathrm{F_x}$, $\mathrm{F_y}$		⌀8	SG, FB	Shaft$_\mathrm{I}$				2
Iordachita [109]	2	$\mathrm{F_x}$, $\mathrm{F_y}$	50 mN	⌀0.5	FBG	Tip	>100	7.6		0
Mayer [130], . . . Mayer [131]	2	$\mathrm{F_x}$, $\mathrm{F_y}$		⌀8	SG, FB	Shaft$_\mathrm{I}$	1200			2
Prasad [117]	2	$\mathrm{F_x}$, $\mathrm{F_y}$	10 N	> ⌀5	SG	Sleeve			4.4	
Trejos [132]	2	$\mathrm{F_y}$, $\mathrm{F_z}$	5 N, 5 N	⌀3.7	SG, HB	Tip	100	4.8, 4.8		0
vanMeer [115]	2	$\mathrm{F_z}$, $\mathrm{F_g}$	1.7 N, 1.7 N	3.5x0.7x10	Cap	Jaw				2
Akinbiyi [110]	3	$\mathrm{F_x}$, $\mathrm{F_z}$, $\mathrm{F_g}$	5 N, 5 N, 5 N	5x10.4x1.5	SG, FB	Jaw	29		$R^2 = 0.991$	2
Valdastri [133], . . . Beccai [134]	3	F	1N,20 N	2.3x2.3x1.3	SCSG	Tip	100	8.4, 10	6.6	0
Berkelman [108], . . . Berkelman [135]	3	F	0.5 N	⌀12.5x15	SCSG	Handle	10	16, 15	10	0
Hanna [119]	3	$\mathrm{M_x}$, $\mathrm{M_y}$, $\mathrm{F_g}$			SG, HB	Trocar			3.3	0
Peirs [136]	3	F	1.7 N, 2.5 N	⌀5x8.85	Optical Int.	Shaft$_\mathrm{I}$		5.4		0
Perreault [113]	3	$\mathrm{F_x}$, $\mathrm{F_y}$, $\mathrm{F_g}$	10 N, 10 N	6x1.1 each	SG	on Cable	1000			2
Rausch [137]	3	F	5N	2x1x0.39mm	SCSG, FB	Shaft$_\mathrm{I}$	>390	8	6.6	0
Shimachi [120]	3	F	10 N	⌀40x120	SG	Trocar	2	7.6	5.0	0
Shimachi [114]	3	F	10 N	1.2kg	SG	Sleeve	25		5.1	2
Tavakoli [67]	3	F		⌀10	SG	Sleeve				

Continued on Next Page. . .

Table 2.3 – Continued

Reference	DoF	Load[a]	Range[b]	Size [mm]	Method[c]	Location[d]	Bandw.[e] [Hz]	Resolution[f] [eq. bit]	Accuracy[g] [eq. bit]	Wrist DoF[h]
Tholey [138]	3	$\mathrm{F_x, F_y, F_g}$	25 N, 25 N	13x40x12	SCSG	Jaw		10.3, 7.6	8, ns	0
Tholey [139]	3	$\mathrm{F_x, F_y, F_g}$	10 N, 15 N	5x5x1	SG	Shaft, Jaw		6.6, 7.2		0
Wagner [56]	3	F	5 N	25x6.5x8	SCSG, QB	Jaw	1000	6.2	5.6	2
Stephan [140]	4	F, $\mathrm{F_g}$	5 N, 15 N, 5 N	8x10	SG	Jaw	720	5.6, ns, ns	5.3, 6.2, 6.6	0
Tadano [116]	4	$\mathrm{F_x, F_y, M_z, F_g}$			$\mathrm{p_{Air}}$	Drive	30	0.1 N	1 N	2
Trejos [125], . . .	5	F, . . .	5 N, 25 N, . . .	⌀10	SG	Sleeve	10	7.4, ns, . . .	7.4, ns, . . .	0
Trejos [118]		$\mathrm{M_z, F_g}$	80 mNm, 50 N					5.7, 7.2	4.9, 5	
using ATI										
Dubois [121]	6	F, M			ATI Mini40	$\mathrm{Shaft_O}$	235		$R^2 = 0.94$,. . . $R^2 = 0.97$	0
Zemiti [124]	6	F, M	36 N, 500 mNm		ATI Nano43	Trocar	670		8.5, 7	0
Rosen [122], . . .	7	F, M, $\mathrm{F_g}$			ATI Mini40, . . .	$\mathrm{Shaft_O}$	30			0
Rosen [141]					Futek Fr-1010					

---

[a] Load component measured by the sensor. $\mathrm{F_g}$ is the gripping force. F denotes all force components, similarly M denotes all torque components.

[b] The measurement range for individual load components is given following the order shown in column *Load*. Only one value is given for $\mathrm{F_x}$ and $\mathrm{F_y}$ if equal, same for $\mathrm{M_x}$ and $\mathrm{M_y}$. If the range of all three force or torque components is equal, only one value is given for all three.

[c] Force measurement method: visual Moire pattern (Moire), capacitive (CAP), foil backed strain gauges (SG), and semiconductor strain gauges (SCSG) in quater (QB), half (HB) and full bridge (FB) configurations, fiber Bragg grating (FBG), other optical (Optical), motor current ($\mathrm{i_{Motor}}$), air pressure ($\mathrm{p_{Air}}$) and commercially available sensors.

[d] Sensor location: on the tool shaft outside ($\mathrm{Shaft_O}$) and inside of the trocar ($\mathrm{Shaft_I}$), in the drive unit (Drive), on the tool tip (Tip), in the end-effector jaws (Jaw), on the tool handle (Handle), on the trocar (Trocar), as part of a sleeve located between tool and trocar (Sleeve), on actuation cables (on Cable), and on the connection between robot and tool (TCP).

[e] Sensor readout bandwidth in Hz.

[f] Equivalent bit-count sensor resolution.

[g] Equivalent bit-count sensor accuracy.

[h] Degrees of freedom of a tool wrist, if present.

widely from 2 Hz to 1200 Hz with 12 groups exceeding 100 Hz and only 4 groups exceeding 1000 Hz.

Tab. 2.3 shows that a large number of force-torque sensor sensors integrated into surgical tools have been suggested and built, clearly emphasizing the need for this technology. However, most tools that incorporate a force-torque sensor forgo an articulated wrist. Sensors are mostly limited to a subset of load components. The solutions that do provide full force feedback rely on commercial sensors which – due to their size – need to be placed outside of the patient's body. There they are subject to the influence of trocar forces and are located far from the operation site, reducing the achievable accuracy. Parasitic influences such as articulation forces are considered largely as an afterthought, using software algorithms to compensate for an error that is sometimes several orders of magnitude larger than the desired signal.

2.4 Deficiencies of the State of the Art

Improved dexterity has been proven beneficial in minimally invasive surgery. Many studies have compared conventional MIS to the Zeus® and daVinci® systems and have acknowledged that performance is always affected by a number of factors (tool dexterity, user interface, vision system). A comparison among disparate systems – commercial as well as research – will always introduce variables that are almost impossible to control for. Yet, arguments for and against the benefit of haptic feedback are made based on experiments comparing the daVinci® to a force feedback tool coupled to a PHANToM® (by SensAble Technologies, Inc.) input device. Arguments are also made based on user interviews. This approach is perspicuous but far from ideal. Researchers have to deal with a number of limitations preventing a fair evaluation:

- *Combinations of dexterity and full force feedback do not exist yet.* The overview given in this chapter clearly shows that the measurement of tissue interaction forces and torques, the measurement of the gripping force, and enhanced dexterity are – so far – mutually exclusive.
- *If force feedback is present, it is usually limited to few force and torque components.* Quite a few research groups have retrofitted EndoWrist® instruments with force sensors close to the tip. While this appears to be an easy fix, the rigidity of the tool

shaft and parasitic interactions from tool tip movement severely degrade the quality of measurements. Even at rest, measuring the force and torque in the direction of the shaft axis is virtually impossible. Retrofitting an existing tool or tool design with a force sensor will always yield limited results.

- *Missing system integration*. The daVinci® is a closed system. While it is possible to attach sensors to tools, the information cannot be displayed using the daVinci® surgeon console. The surgeon input console contains motors and can supposedly provide force feedback to the user, however, this capability is not currently implemented. Outside of Intuitive Surgical®, only the Computer Integrated Surgical Systems and Technology Engineering Research Center (CISST-ERC), [142] has access to the daVinci® system interface, yet even there a PHANToM® is used for haptic experiments. Currently there exists no system for robotic surgery that provides tools with full force feedback and dexterity, a surgeon console with full force feedback capability, and 3D vision system.

The review of research in the field of force feedback for minimally invasive surgery shows that the impact of force feedback on the surgeon's task performance is still being debated, while the benefit of dexterity has been established. Components such as dexterous tools and 6 DoF force sensors exist separately, however building a dexterous tool that also provides full force feedback requires more than a combination of off-the-shelf components. Constraints posed by the medical environment, both in terms of tool size and biocompatibility are severe. Still, a tool combining dexterity and full force feedback is necessary to determine if force feedback provides a benefit to surgeon and patient during MIRS.

3

Objectives and Limitations

This thesis presents a generic tool design as part of a novel dedicated instrument for minimally invasive robotic surgery. The dedicated instrument *MICA* and the versatile robotic arm *MIRO* are major components of the DLR's *MiroSurge* scenario (presented in Sec. 2.1 and Hagn et al. [14]). Currently the *MiroSurge* system is used for research related to MIRS, workspace and setup planning, augmentation, ergonomic user interface design, haptic feedback, and autonomy. In the future it will enable surgeons to perform operation techniques that require a high degree of dexterity and precision, such as minimally invasive coronary artery bypass operations on the beating heart (Falk et al. [143]). With its modular and versatile design, applications ranging from autonomous camera guidance or laser osteotomy[1] requiring only one *MIRO*, to complex procedures in visceral surgery requiring multiple arms and tools are currently being developed (as described by Hagn [4]). Aside from strict telemanipulation – the surgeon controlling tools directly – the *MiroSurge* system will allow the implementation of semi-autonomous functionality such as camera guidance (described by Omote et al. [20]) or motion compensation of the beating heart (described by Ortmaier [144]).

3.1 Objectives

For any specific application, the versatile robotic platform consisting of a number of *MIRO* arms and the *MiroSurge* infrastructure described in Sec. 2.1 will be outfitted with dedicated

---

[1] surgical procedure cutting bone

instruments. Fig. 3.1 shows dedicated instruments attached to two *MIRO* arms in a setup for visceral surgery. A third *MIRO* carries a laparoscopic camera. The dedicated instrument is inserted through the hollow *MIRO* wrist with the tool shaft extending towards the patient.

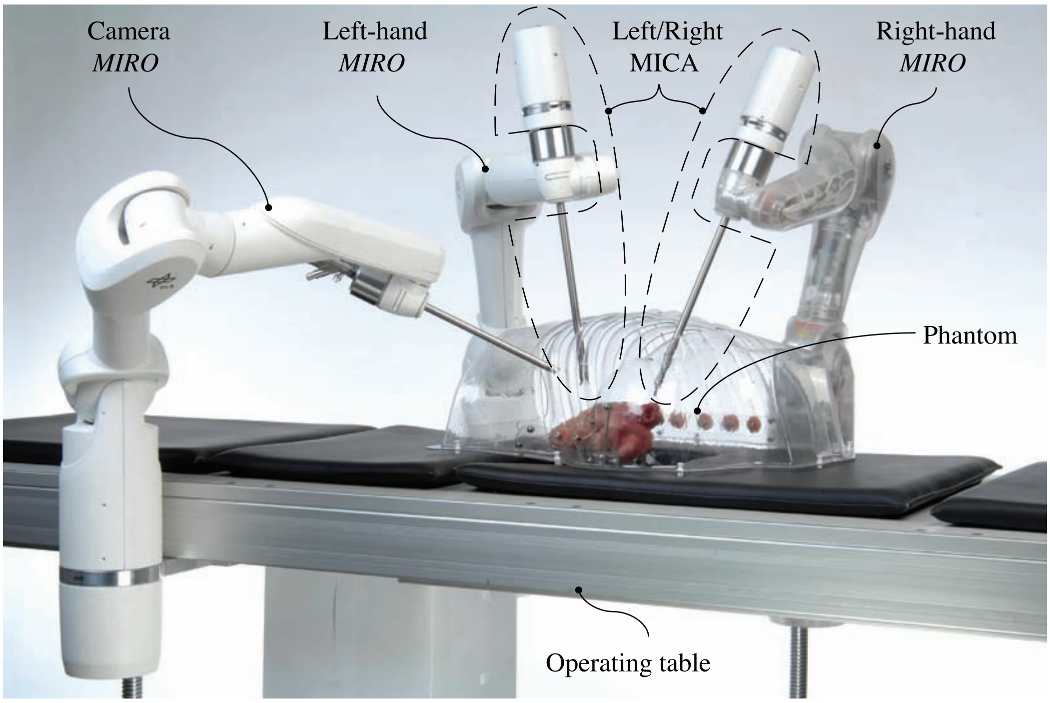

Figure 3.1: Two dedicated instruments coupled to left and right-hand *MIRO* arms in a *MiroSurge* setup for visceral surgery (see Hagn [4]).

3.1.1 Requirements governed by *MIRO*

The clear separation between versatile robotic platform and dedicated instrument is manifest in the interface between both. The instrument interface is strictly limited to a single mechatronic interface. The interface provides physical attachment, an electrical power connection and a high speed digital communication interface. The integration of the dedicated interventional instrument for minimally invasive robotic surgery within the *MiroSurge* setup governs a number of system requirements:

- *Dedicated instruments are self-sufficient robots* incorporating all necessary motor control, power, communication, and sensor signal conditioning electronics.

- *Tool length of between 210 mm and 330 mm.* Konietschke [145], Konietschke et al. [146] conducted a workspace analysis for several cardiac and abdominal laparoscopic procedures. A tool length of between 210 mm and 330 mm measured from the *MIRO* wrist to the tool tip was found to yield optimum manipulability, accuracy and avoidance of joint limits with respect to the *MIRO* kinematics and desired target workspaces.

- *2 DoF intra corporal wrist and 1 DoF end effector* . In order to overcome the kinematic restrictions placed by the insertion of the tool through the patient's skin, the tool has to provide at least two additional intra-corporal wrist degrees of freedom.

- *Distance between tool wrist and tool tip should be 20 mm.* Konietschke [145] also shows that the distance between tool wrist and tool tip has an influence on the optimal kinematic design of the *MIRO*. For current *MIRO* kinematics, this length is suggested to be 20 mm. A shorter distance would not yield a more compact optimal *MIRO* design, however a length exceeding 30 mm would violate *MIRO* optimization constraints. Furthermore, the distance between skin and operative situs places an additional limit on the distance between tool wrist and tool tip. For abdominal procedures this distance can be increased by insufflation[2]. However, this is not an option for cardiac procedures as the rigidity of the rib cage limits the available workspace.

- *Tool diameter of 10 mm or less.* The *MiroSurge* system is ultimately targeted at MIRS at the beating heart. The intercostal space[3] places an upper limit on the tool diameter.

- *Lightweight and compact design.* Added weight at the *MIRO* tool center point (TCP) will adversely affect the dynamic performance of the robotic arm. The *MIRO* is designed to manipulate a load of up to 30 N at the TCP with full dynamics. The weight of the instrument and the desired manipulation forces both contribute towards the maximum load of 30 N. Additionally, the instrument should be compact, particularly in diameter. Multiple robotic arms will be working in close proximity around the operating table. Interference and collisions of instruments have to be avoided.

---

[2] introducing inert gas into a body cavity to expand workroom

[3] space separating two adjacent ribs

- *Quick instrument changes* are necessary during surgical procedures. The connection between *MIRO* and tool is established by a switchable ferromagnetic coupling, that allows removal by extracting the instrument shaft upwards through the hollow *MIRO* wrist – away from the patient – along the line of the trocar. In the event of complete system or power failure the *MIRO* wrist prevents the instrument from dropping towards the patient.

Aside from the requirements dictated by the integration of *MICA* into the *MiroSurge* system, further specifications define the core capabilities of *MICA* as robotic system. Those specifications are tool wrist range of motion and dynamics, and force measurement range and resolution. These requirements will be discussed in the following sections.

3.1.2 Wrist Dynamics

One target application of the *MiroSurge* system is minimally invasive robotic surgery on the beating heart. It is one of the most demanding applications within the *MiroSurge* scenario in terms of tool dynamics, dexterity and sensitivity. A stabilizer is attached to the heart surface either by suction or mechanical pressure, framing the operative situs. While heart motion is reduced within the stabilized region, it is not suppressed completely, and the residual motion renders precise tasks very difficult. The goal within the *MiroSurge* scenario is to capture and track the residual heart motion by laparoscopic camera. This information can be used to virtually stabilize the video image for the surgeon and to follow the captured surface motion with the tool tip. Thereby, the surgeon would see a virtually immobilized heart surface, and the captured surface motion would be superimposed over the surgeon's hand motion.

Using motion and frequency analysis on video sequences captured during minimally invasive bypass surgery on a stabilized beating heart, Ortmaier et al. [7] quantified the residual motion of various points on the heart surface within the stabilized region. Lateral motion (in image coordinates with units of pixel) of one natural landmark is exemplified in Fig. 3.2 (a). Frequency analysis established the dominant frequencies of the non-sinusoidal residual motion to be in the range of 0.24 Hz, 1.2 Hz, 2.4 Hz, and 3.5 Hz. A minimum motion frequency of 5 Hz is therefore stipulated for the dynamics of the tool wrist.

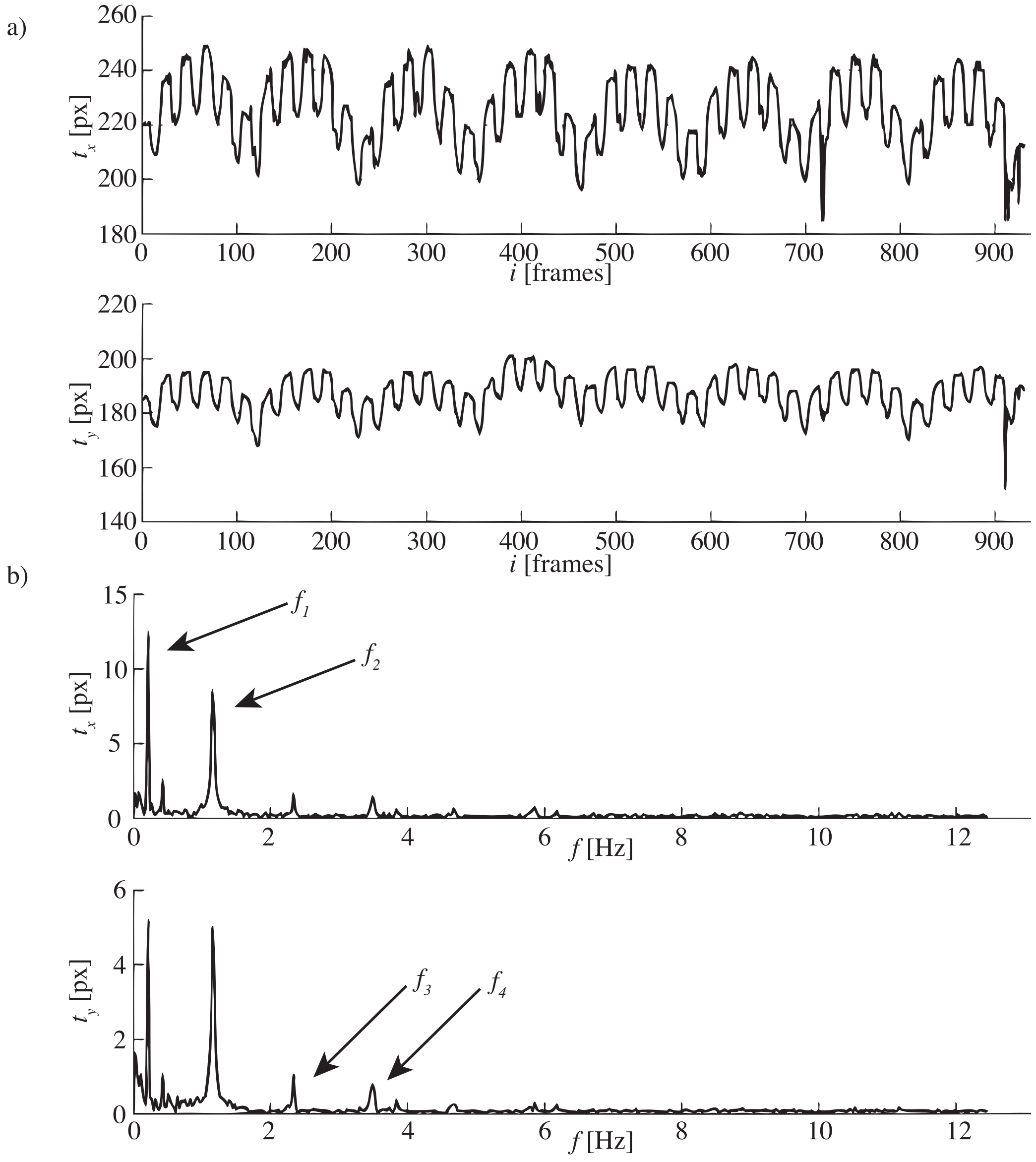

Figure 3.2: Motion of natural landmark on the surface of a stabilized beating heart extracted from endoscope image ($25^{frames}/_{s}$) (a), and frequency distribution of that motion (b) (see [7]).

3.1.3 Range of Motion

The required range of motion and dexterity of the tool wrist depends directly on the selected surgical task. A large number of minimally invasive procedures is possible with conventional, non articulated tools. Konietschke [145] used a tool wrist range of motion limit of ±30° in 2 DoF for the *MIRO* kinematics optimization. According to a study by Dakin and Gagner [40], the Computer Motion® Zeus® system, having one additional degree of freedom at the wrist, did not improve accuracy or speed for basic surgical manipulation tasks. Only for fine suturing tasks some (although inconsistent) accuracy at the cost of significantly increased time was found. In the same study, the daVinci® system by Intuitive Surgical®, having two degrees of freedom at the wrist outperformed Zeus® in all categories and showed increased accuracy but also increased task completion time.

Tools with a larger RoM than the EndoWrist® instruments have also been proposed (see Tab. 2.2). While having a wrist RoM as large as possible is certainly desirable, the feasible RoM is always going to be a trade-off between joint size, joint complexity and the integration of additional functionality such as force sensing.

The instrument wrist and end effector transfer the capability of the human wrist and fingers into the patient's body, so the range of human wrist motion was used as a guideline for the tool wrist. Luttgens and Hamilton [147] report an average range of human wrist motion of 60° for wrist flexion and extension (see Fig. 3.3), however values of up to 80° have been reported (Abdel-Malek et al. [148]). The range of motion in ulnar deviation (adduction) and radial deviation (abduction) is considerably lower, in the range of 20° to 30°. The human wrist range of motion is perfectly adapted for high precision and ergonomic work in front of, and close to the human torso with forearms in a roughly horizontal position. Ergonomic work places are set up so that the work space will coincide with this optimal manipulation region.

Due to the nature and the kinematic restrictions of MIS, it is not always possible to position the tools similar to the optimal human wrist position. Rather than imitating the asymmetric range of motion of the human wrist, a robotic wrist should provide a symmetric, spherical workspace. This provides the greatest versatility in terms of manipulability considerations for all tool placements. Obviously that workspace should be as large as possible. It is expected that an increased RoM will increase task performance, however, no quantifiable data on the relationship between RoM, reachability, and task performance was available for

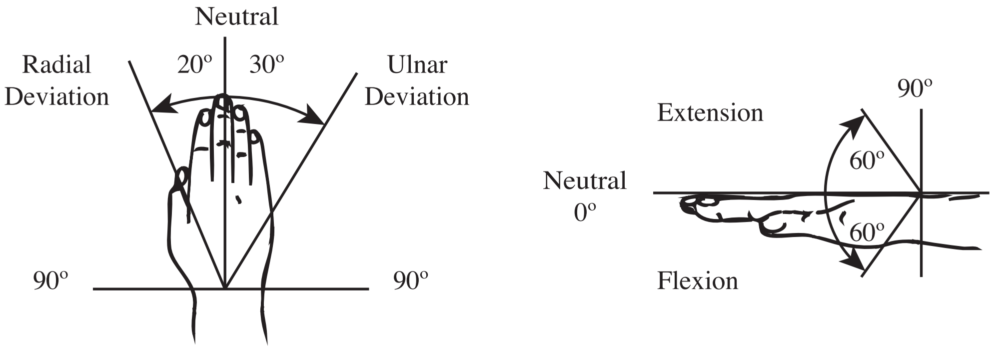

Figure 3.3: Wrist Range of Motion Luttgens and Hamilton [147].

MIRS tools, and a more detailed quantification would have been purely arbitrary[4].

3.1.4 Force Measurement Range and Resolution

The force measurement range is defined separately regarding tissue manipulation forces applying to the force-torque sensor and needle holding forces relating to the grasping force sensor. Tissue manipulation forces have been previously reported ranging from few Newtons overall (according to Peirs et al. [45], Kitagawa [46], Verner et al. [47], Braun et al. [48], Brouwer et al. [49]) up to 67 N in axial (shaft) direction (see Lum et al. [150]). Despite the surprisingly large manipulation forces reported by Lum et al. [150], obtained during suturing and dissection in a porcine model, most reported values fall well below 10 N for the manipulation force. Moreover, most studies commenting on the difference between force feedback and non-force feedback experiments when manipulating tissue or tying sutures, show a decrease in applied force when force feedback is present. Therefore, a force measurement range of up to 10 N is deemed sufficient for the manipulation force measurement range. In terms of the needle holding force (gripping force), tools should have the ability to not only delicately grasp tissue, but also to strongly and securely hold needles in order to limit the number of tool changes between tissue grasper and needle driver.

While the measurement range should be larger than the knot tying and needle holding force, physical constraints, particularly electrical noise necessitate a trade-off between sensor reso-

---

[4] Zacharias [149] established a relationship between wrist RoM and reachability (see Sec. 5.2) in 2011

lution and measurement range. Tissue penetration forces of commonly used suture needles are studied to establish the minimum required resolution of the force-torque sensor. It is stipulated that the FTS should be able to resolve the penetration of a needle into soft tissue and the subsequent relaxation of tissue.

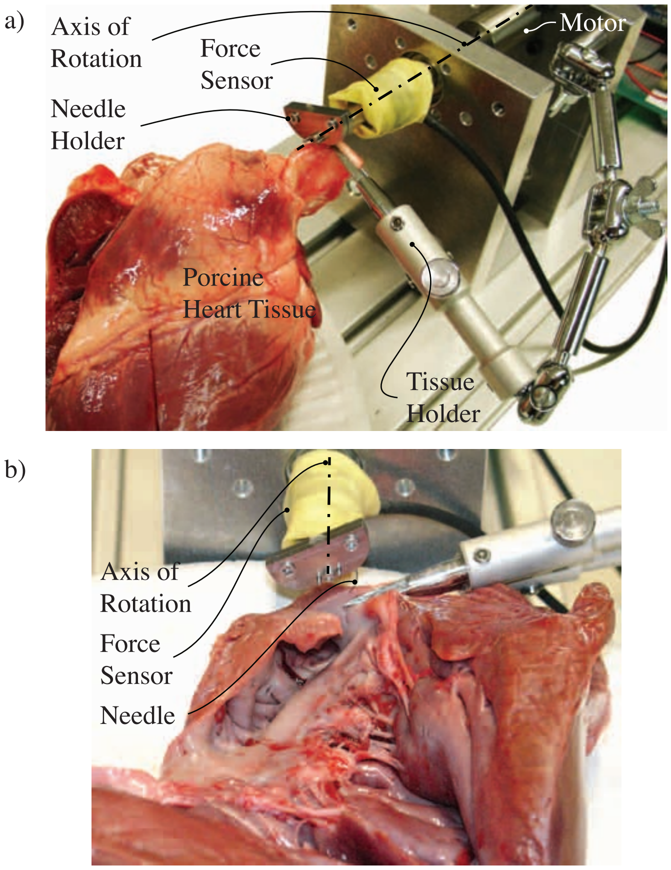

Figure 3.4: Setup for needle insertion trial: Overview (a), and closeup (b).

Penetrating soft tissue is a very complex, nonlinear process, which was analyzed in depth by numerous research groups (Abolhassani et al. [151], Frick et al. [152], Maurin et al. [153], Okamura et al. [154], Podder et al. [155]). The necessary penetration forces depend on the needle geometry, needle trajectory, tissue type, and patient specific tissue characteristics. In order to establish reliable experimental data on needle insertion forces, cadaveric tissue manipulation trials with porcine heart tissue are performed. To achieve repeatable results,

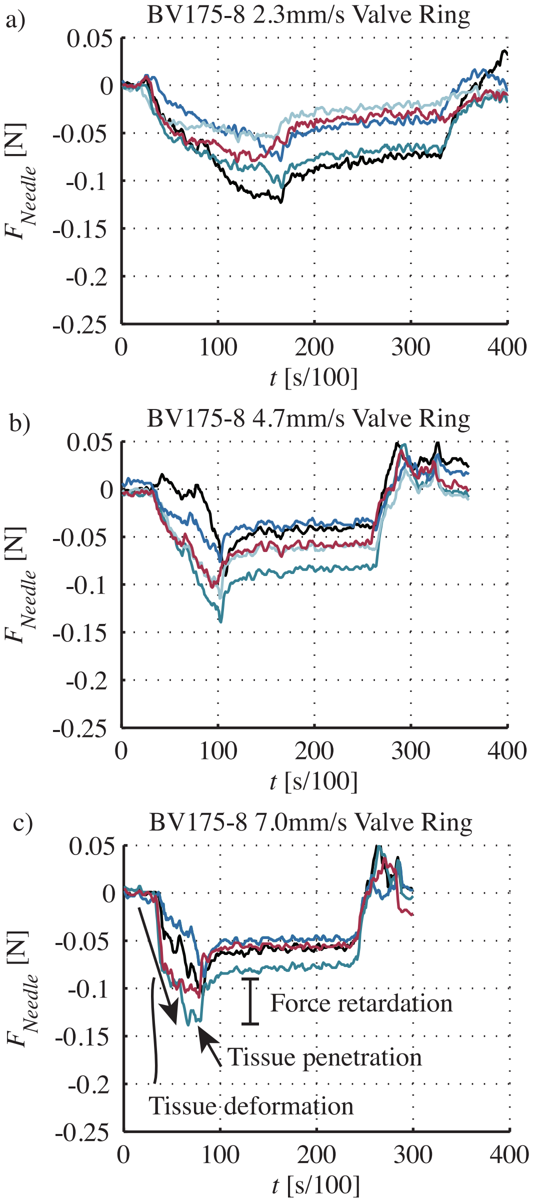

Figure 3.5: Results of needle insertion trial. Penetration forces of aortic valve ring with Ethicon BV175-8, $\frac{3}{8}$-curve, round bodied, 7-0 at 2.3 $\frac{mm}{s}$ (a), 4.7 $\frac{mm}{s}$ (b), and 7.0 $\frac{mm}{s}$ (c).

an automated test set up is used (see Fig. 3.4 (a)): A force/torque-sensor (ATI nano17) mounted to a DC-motor with integrated encoder and gearbox is used to measure forces while moving the needle on a circular trajectory around its center.

Commonly, minimally invasive suturing is performed with curved eyeless needles that are identical to those used in open surgery. Results for an Ethicon BV175-8, $\frac{3}{8}$-curve, round bodied, 7-0, 10 mm long micro-vascular needle, penetrating and retracting from aortic valve ring tissue are shown in Fig. 3.4. The force values measured by the nano17 are then compensated for the needle holder mass, transformed to, and aligned with the needle tip. Measured forces do not differ greatly between insertion velocities of 2.3 to 7 mm/s. The data shows the typical, previously reported pattern of tissue deformation, penetration, tissue relaxation and needle retraction. Measuring the force retardation subsequent to tissue penetration, it is found to be in the 0.05 N range. Combined with the measurement range of ± 10N, the incremental resolution of 0.05 N requires an overall sensor resolution of roughly 10 bit.

3.2 Limitations

- *Limited wrist range of motion* for the sake of the integration of force feedback. RoM is a tradeoff between useful dexterity and mechanical complexity which is further increased by the integration of force feedback.

- *The implementation of electrosurgery* is still to be completed. The application of high frequency electrical current to dissect or coagulate tissue is a basic operation in surgical procedures. The electrical current seals off small blood vessels embedded in the tissue being dissected, thereby limiting blood loss. Surgical procedures on tissue perfused with blood are drastically complicated by the absence of electrosurgery.

- *A biocompatibility evaluation* is still due. Biocompatibility relates to the biological effect of the device and its components on tissue in that any negative effects of the materials used need to be known and prevented. For any medical device there exist certain requirements relating to patient and operator safety that need to be met. The basic requirements of the clinical evaluation of a medical device are set out in the Medical Device Directive [156] and the Active Implantable Medical Device Directive [157]. Checking biocompatibility of a product and/or its components based on ISO 10993 is one way of meeting these requirements. While emphasis was placed on using biocompatible materials, and encapsulating non-biocompatible components, no formal evaluation or risk assessment has been conducted.

- *Sterilizability and cleaning* is still to be assessed. In addition to being biocompatible all components in direct contact with the patient must be able to withstand sterilization, which in clinical applications is often performed by autoclaving according to EN 554. Components that do not require autoclaving are commonly spray sterilized. The requirements of steam sterilization have been considered in concept, material choices and component geometry wherever possible, however sterilizability has not been proven thus far. The Robotics and Mechatronics Center does not have the expertise to conduct biocompatibility and sterilizability testing, furthermore, the steps required to demonstrate conformance to these requirements of such a complex system are not at all clear.

- *System safety aspects* other than relating to biocompatibility and sterilizability have not been consistently implemented yet. The device should not harm patient, operator, itself or other OR systems. This relates to electromagnetic compatibility as well as safety limits implemented on the software, electronics and mechanical hardware level.

- *Involved instrument changes*. Due to the coaxial arrangement of tool shaft, *MIRO* wrist, and instrument body, tool changes during a surgical procedure always involve the removal of the entire instrument, not just the task specific tool.

- *Cost* and design for manufacturability and assembly have not been considered during this project. The advanced tool design serves as a technology prototype, overcoming current limitations of the state of the art.

3.3 Distinguishing Details

Individual components for an articulated, force sensing minimally invasive surgical tool exist. Various wrist kinematics for minimally invasive tools have been proposed and built. Many different multi-DoF force sensor designs have been reported. However building a dexterous tool that also provides full force feedback requires more than a combination of off-the-shelf components. Especially the clear mechanical separation of tissue manipulation and tool actuation forces is vital for high quality manipulation force measurements. While the issue of force isolation has been recognized in literature, no viable solution for medical tools has – so far – been proposed. The force-torque sensor integrated into the present tool is aimed at haptic exploration similar to the capability of gloved fingers or the use of tweezers. Exerting forces and torques is possible as is the recognition of shapes, weight, tension and point compliance of an object. The recognition of surface textures is extremely limited. The articulated tool design for MIRS described in this thesis will, therefore, combine the following details distinguishing it from the state of the art:

- Dedicated, self-contained instrument designed to integrate closely with the DLR *MiroSurge* scenario, requiring only external electrical power and systems communication.
- Combining a generic tool design for a cable driven 2 DoF wrist and 1 DoF end effector that can take the shape of grasper, scissors, and needle holder.
- the currently smallest full 6 DoF manipulation force and 1 DoF grasping force sensor with a measurement range of several Newton, and
- the mechanical isolation of wrist and grasper actuation forces from the tissue manipulation forces.
- The instrument is capable of up to 5 Hz wrist motion frequency under full load, required for motion compensation of the beating heart.

Previous studies aimed at assessing the combined impact of articulation and force feedback were compelled to compare disparate systems or subsets of capabilities. The verdict is still out, however, the proposed tool will bring this evaluation one step closer.

4

Concept

The *MiroSurge* framework defines a clear separation between the *MIRO* as robotic platform and *MICA* as dedicated instrument. Similar to this functional separation, *MICA* itself can be structured into several functional groups. Minimally invasive surgical procedures require a number of different instruments performing distinct functions (holding, cutting, grasping, etc.). Many instruments share common design elements such as the elongated shaft and the requirement for actuation. They mainly differ in the shape and therapeutic function of the tool tip. From a system point of view, therefore, it is reasonable to structure the instrument into a generic system (required for all tools), and interchangeable, task specific systems aimed at a distinct therapeutic functionality. This functional structure is depicted in Fig. 4.1, further broken down into the modules extra-corporal motor unit (EMU), force-torque sensor (FTS), wrist and end effector. Following VDI 2221, solution concepts for these individual modules will be developed in this chapter.

4.1 Extra-corporal Motor Unit

At the highest abstraction level, *MICA* has the task of converting the electrical energy supplied by the *MiroSurge* system into mechanical motion at the tool tip, as shown in Fig. 4.2 (a). Depending on the *conversion principle* from electrical energy to mechanical motion, the *location* of this first energy conversion, and the *form of energy* transmitted through the tool shaft, the instrument actuation system can be characterized.

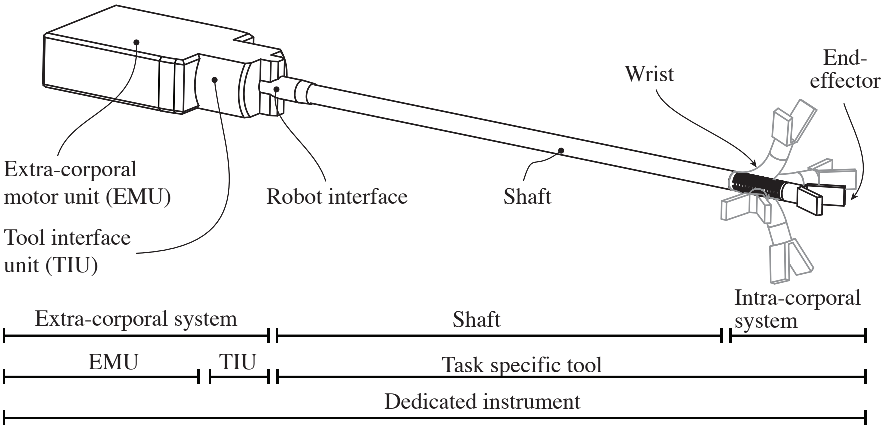

Figure 4.1: Concept and functional groups of the dedicated instrument with extra-corporal motor unit (EMU), and task specific tool.

Form of Energy

The tool shaft can be treated as energy conductor, separating *MICA* into an extra-corporal and intra-corporal robotic system (Fig. 4.2 (b)). Energy is provided by the extra-corporal system, transmitted through the conductor – the tool shaft – to the intra-corporal system, there to actuate the tool tip. Only a limited number of energy forms are available to actuate robotic systems (Chiu et al. [158]) – in the present case – the intra-corporal system. Disregarding chemical and optical energy, which are unsuitable to actuate a MIRS tool, the three remaining forms are electric, fluidic and mechanical energy.

To clarify this concept, a number of examples are shown in Fig. 4.2 (c-e):

- *Electromechanical direct-drive*, Fig. 4.2 (c). Electrical energy is conducted by electrical wires in the tool shaft. The tool tip is actuated by direct-drive in the form of a voice-coil actuator, or shape memory actuator.
- *Cable driven tool*, Fig. 4.2 (d). Mechanical energy is transmitted through the tool shaft by steel cables that are actuated by a rotary electromagnetic motor.
- *Hydraulically driven tool*, Fig. 4.2 (e). Pressure is generated by a hydraulic cylinder actuated by linear electromagnetic motor and transmitted through the tool shaft. The tool is actuated by a second hydraulic cylinder.

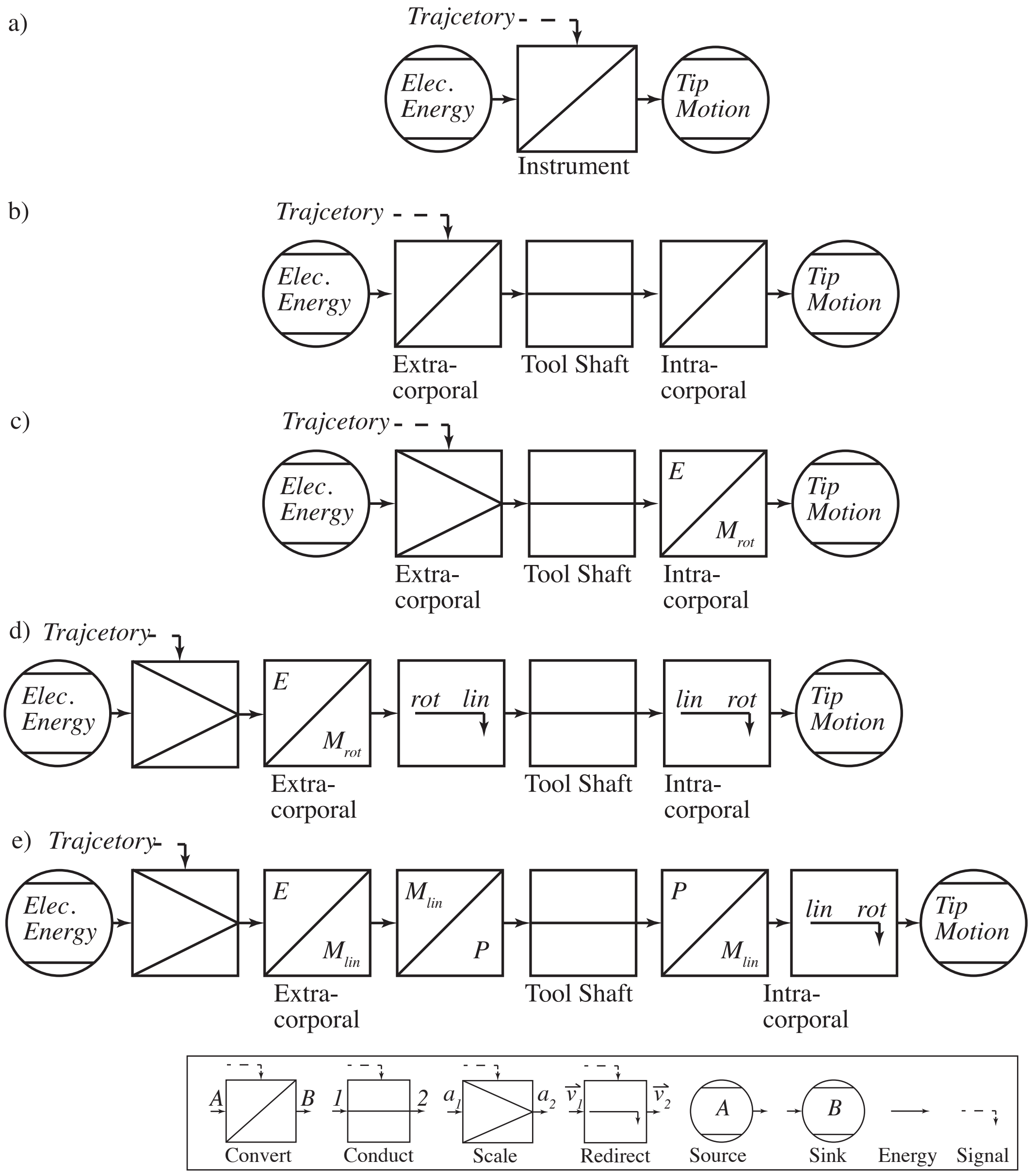

Figure 4.2: At the highest abstraction level, *MICA* converts electrical energy into tool tip motion, controlled by the surgeon's hand movement (a). *MICA* separated into extra-corporal and intra-corporal system connected by the tool shaft (b). Tool actuated by direct-drive electric motors in the wrist (c). Cable driven tool actuated by rotary electromagnetic motor (d). Tool driven by hydraulic cylinder (e). (Elementary function symbols based on Koller and Kastrup [159])

Electromechanical Conversion Location and Principle

The actuation of *MICA* can involve a single or multiple energy conversions (as shown in Fig. 4.2). Because *MICA* is overall electrically powered, the first conversion is always from electrical to mechanical energy (again disregarding chemical and optical energy). This conversion can conceivably be located in either the extra-corporal system or the corporal sub-system. A selection of electromechanical actuator principles is shown in Fig. 4.3 (Chiu et al. [158]). Many of these actuation principles have vastly different force and motion ranges, a comparison based on specific energy and actuation frequency is useful.

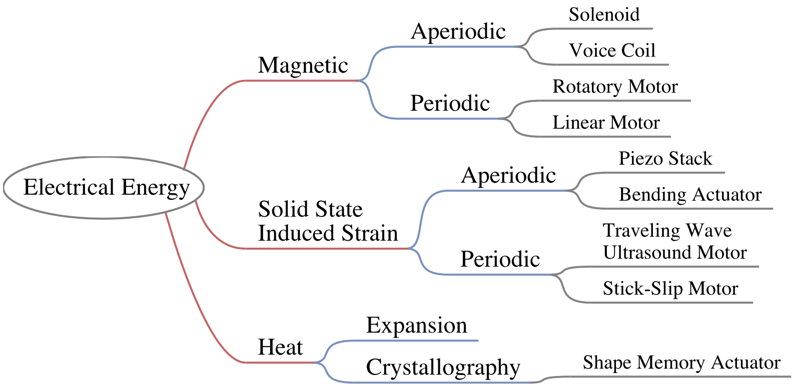

Figure 4.3: Conversion principles from electrical energy to mechanical motion (Chiu et al. [158]).

In order to estimate a lower limit for the work performed while moving the tool tip, the model shown in Fig. 4.4 is used. Inertia and losses due to friction and conversion efficiency are neglected, therefore, the estimate is independent of energy conversion steps. The model is a simplified representation of one possible tool tip mechanism. The cable force F_c is acting on a wrist pulley of radius r_p. A cable travel of s_c is required to move the tool tip about angle θ_9. Length l_d is the distance between last wrist joint axis and length l_g is the effective gripper jaw length. The tissue manipulation force is F_m.

Initially, the effective gripper jaw length was arbitrarily defined as $^2/_3$ of the jaw length, assuming that the maximum manipulation force would not be applied directly at the tool tip. On the original jaw design this equated to an effective jaw length of $l_g = 9.75\mathrm{mm}$. While the jaw length changed with subsequent jaw designs, it was decided to keep the value of parameter l_g constant.

With $\theta_9 = 45°$, $l_d = 18.75$ mm, $l_g = 9.75$ mm, $r_p = 2.95$ mm and $F_m = 10$ N the resulting cable force is $F_c = 96.6$ N and an actuator travel of $s_c = 2.3$ mm is required. The work performed to move the wrist is therefore $W = 0.22$ J.

$$W = F_m \cdot (l_d + l_g) \cdot \pi \frac{\theta_9}{180}$$
$$W = 10\mathrm{N} \cdot (0.01875 + 0.00975)\mathrm{m} \cdot \pi \frac{45°}{180°} = 0.22\mathrm{J}$$

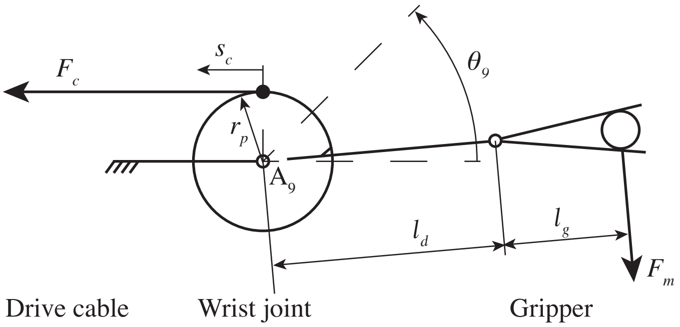

Figure 4.4: Model for estimating the lower limit of the work performed during wrist movement, with $\theta_9 = 45°$, $l_d + l_g = 28.5$ mm, $r_p = 2.95$ mm and $F_m = 10$ N. A resulting cable force of $F_c = 96.6$ N and cable travel of $s_c = 2.3$ mm yield a performed work of $W = 0.22$ J.

Tab. 4.1 gives an overview of specific energy densities for various actuators and a qualitative estimate of achievable actuation frequencies. The specific energy of muscle tissue is shown for reference only. Further information on the selection of electromechanical actuators based on performance indices can be found in (Huber et al. [164]). Hydraulic pressure is not shown as energy conversion principle because the conversion from electrical energy to hydraulic pressure is a multi step process (as shown in Fig. 4.2 (e): electrical energy → mechanical force → hydraulic pressure → mechanical force), with hydraulic pressure serving only as transfer medium. It is a viable option for transmitting energy, if the generation of pressure, e.g. by an electromagnetic actuator is located in the extra-corporal system of the instrument. Leakage and controllability concerns still exist with miniature hydraulic systems, therefore, this principle was not pursued at this time.

It is evident that the space available in the intra-corporal part of the tool (distal of the tool

Table 4.1: Specific energy densities for various actuators. Exclusion criteria for intra-corporal actuation of 2 DoF within the confines of the tool shaft (achievable work within the shaft $\leq 0.22\mathrm{J}$ and Frequency $\leq$5 Hz) are printed in bold font.

Actuator	Volume Specific	Weight Specific	Frequency	Space req'd.
	Energy $[\mathrm{J/cm^3}]$	Energy [J/g]	[Hz]	$[\mathrm{cm^3}]$
Electromagnetic [160]	$\mathbf{0.025}$	0.003	fast	8.8
Electrostatic [160]	$\mathbf{0.0015}$	0.0015	fast	147
Solid State Strain [161–163]	$\mathbf{0.001-0.01}$	$0.001-0.002$	fast	22
SMA [160, 163]	≥ 100	≥ 15	$\leq \mathbf{3}$	≤ 0.002
Thermal Expansion [160]	0.4	0.15	**slow**	0.55
Muscle [160, 163]	0.07	0.07	≤ 5	3.1

shaft) is not sufficient for the use of electromagnetic or solid state induced strain (piezo) actuators. Shape memory alloys could provide the work output, however cycle rate is inversely proportional to cross-section, whereas output force is proportional to cross-section. Even with rapid heating algorithms and immersion cooling, a cycle rate of 5 Hz cannot be achieved with actuators providing the necessary force (Troisfontaine et al. [165]).

Keeping in mind the previously outlined dynamic and load requirements of 10 N and 5 Hz (Sec. 3.1.2 and Sec. 3.1.4), it is not possible to place electromechanic actuators in the intra-corporal section of the tool. Electrical micro motors in the wrist itself (Salle et al. [44], Cepolina and Michelini [73]) or SMAs (Ho and Desai [98]) do not provide sufficient work output and will not be considered any further.

Starting from the premise that motors will be located in the extra-corporal instrument section, Kübler [166] and Thielmann [167] have independently performed a thorough investigation of various motor concepts during their diploma-theses, both arriving at brushless DC (BLDC) motors as preferred actuation solution. The initial design by Kübler [166] was based on commercially available BLDC motors and Harmonic Drive® gearheads, providing three DoF of rotational motion as output from the extra-corporal section. This design was successfully used with the first generation of tools described in Sec. 5.1.3.1. It was superseded by a new, higher dynamic design by Thielmann [167] which uses hollow shaft proprietary BLDC motors (ILM-38) developed at Robotics and Mechatronics Center. Ball screws are mounted within the hollow motor shaft, providing 3 DoF of linear motions as output of the extra-corporal section. This new design of the *MICA* motor unit also contains advanced motor and communication electronics derived from the *MiroSurge* framework. For a more detailed description, refer to Thielmann et al. [168]. All experiments shown in Sec. 6 were performed with the new motor unit.

4.2 Intra-corporal Articulated Wrist

A large number of mechanically actuated wrist designs has previously been devised and discussed in literature. Most of these wrists can be classified by the four parameters shown in Fig. 4.5: wrist kinematics, the number of joint segments being actuated in unison, whether joints are discrete (pin joint) or elastic (flexural joint), and by the direction and type of mechanical actuation. A variety of previous designs has been discussed in Sec. 2.3.1.

Fig. 4.6 shows various options for a serial, single stage, discrete wrist. Fig. 4.6 a) shows a roll-pitch-yaw (RPY) wrist with separate end effector. This is the least complicated joint arrangement as every joint is associated with exactly one DoF. This is also true for roll-pitch-roll (RPR) wrists (Fig. 4.6 (b)). The ability to rotate the end effector about its approach axis allows for a more economic handling of curved needles as most of the movement required to follow the needle's curve is executed by the last roll joint. However, RPR wrists exhibit a singularity in the middle of workspace. The singularity necessitates high joint velocities for trajectories in proximity to the singularity. Cavusoglu et al. [169] performed a manipulability comparison between RPY and RPR kinematics for generalized tasks in robotic surgery. He found that the ”roll-pitch-roll wrist configuration is preferable when there is a steep approach angle to the suturing surface [...], and the roll-pitch-yaw wrist configuration is preferable when the approach angle to the suturing surface is shallow.” Fig. 4.6 (c) shows the kinematics of the EndoWrist® tool. It is a shortened form of the RPY configuration where the yaw and end effector axes coincide. Fig. 4.6 (d) is a universal joint configuration. It is also a shortened RPY configuration, however in this case pitch and yaw axes intersect.

During common telemanipulation tasks, the surgeon is always part of the position control loop, and is able to compensate for small movement inaccuracies of the tool. During semi-autonomous tasks this compensation for errors is not possible anymore, therefore a high degree in trajectory following accuracy is necessary. If possible, distal position sensors measuring the actual wrist position should be avoided as they further complicate the tool design. Therefore, any mechanical play in the wrist or drive mechanism needs to be avoided. Also, any elasticity in the wrist or drive train will have to be compensated for and should be kept to a minimum. In order to satisfy the force and dynamics requirements, the wrist needs to be compact and rugged, avoiding a large number of movable pin or spherical joints in order to keep the number of moving parts low. A limited number of joints and moving parts will also help to keep mechanical play and backlash low.

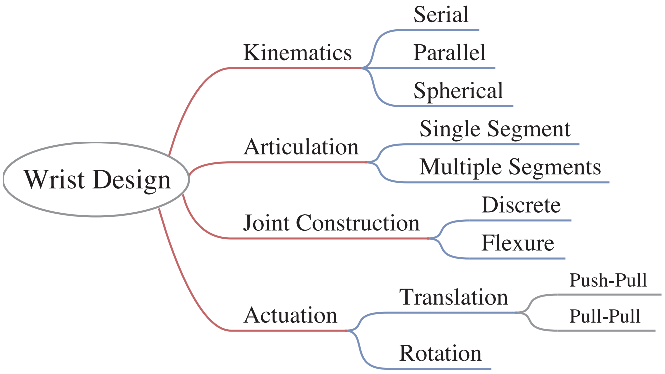

Figure 4.5: Classification of wrist designs for surgical instruments.

The wrist mechanisms based on the examples shown in Fig. 4.7 were considered for this project and will be briefly introduced in the following overview. Actuation is provided by counteracting cables unless otherwise noted. Usually the cable loop is rigidly closed about a rotating drive pulley, creating a continuous cable loop, not an antagonistic mechanism. For antagonistic actuation, each cable tail would be independently actuated by a separate motor. The reason for cables being favored in most wrist designs are low cost, easy handling, and the simple elimination of mechanical play through pretension. The flexibility of the cable allows the elimination of a number of pin joints compared to a rod based mechanism. On the other hand, elastic deformation of the cable when running around pulleys and friction while gliding along surfaces creates mechanical losses. Longitudinal elongation, creep, cable termination, and minimal bending radius are issues that require attention when designing with cables. The biggest disadvantage of open cables is that they consist of an open twisted structure that is potentially penetrated by liquid. Sterilization becomes an issue which is likely one reason for Intuitive Surgical® to limit the use of EndoWrist® tools to 10 operations and issuing comprehensive guidelines for cleaning the tools using mechanical brushes.

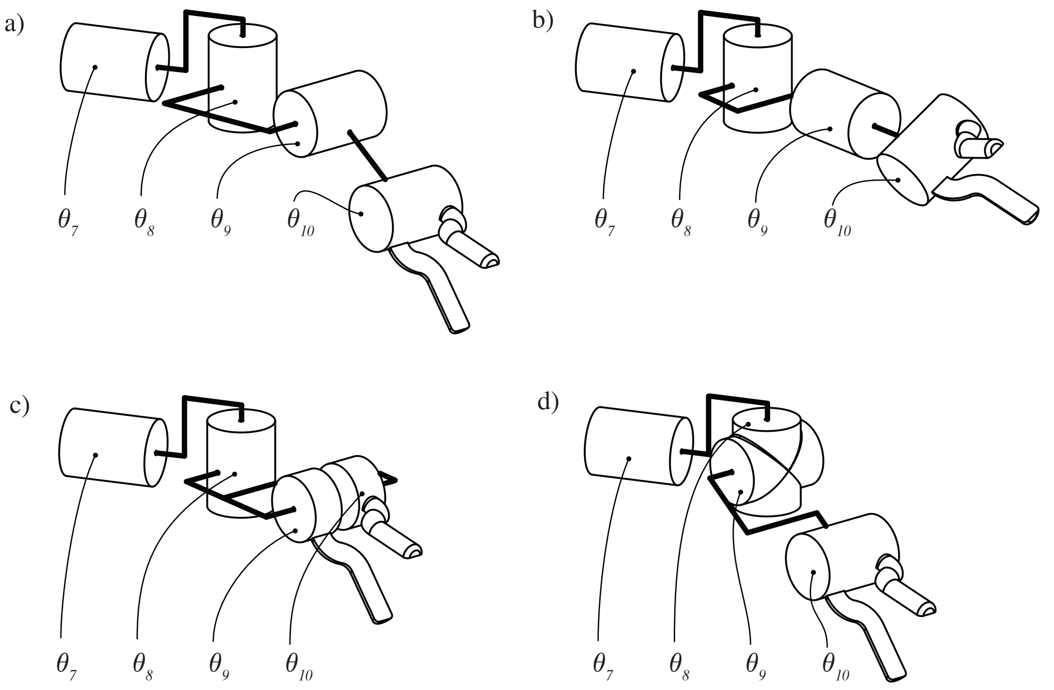

Figure 4.6: Serial single stage discrete wrist kinematics. For all kinematics shown, the first roll axis (here θ_7) is aligned with the tool shaft. Roll-pitch-yaw configuration (a), roll-pitch-roll configuration (b), EndoWrist® as shortened variation of roll-pitch-jaw configuration with coinciding jaw θ_9 and gripper θ_{10} axes (c), and universal joint roll-pitch-yaw configuration with intersecting pitch θ_8 and yaw θ_9 axes (d).

The following wrist concepts were considered:

- The mechanism shown in Fig. 4.7 (a) is based on the *1st generation DLR robotic finger*. It is a serial kinematic, discrete joint design with the two DoFs being separated into two stages. It achieves coupling of the two stages for each DoF by using sections of gearwheels and is therefore not completely free of mechanical play. Coupling can also be achieved by using tensioned cables arranged in a figure-8 loop between each stage instead of gears, thus eliminating play. Enlarged prototypes of both the gear and cable coupling concept were built as rapid prototyping models. The disadvantage of this concept is the relatively large length of the mechanism.

- The *endoscope bending mechanism* shown in Fig. 4.7 (b) is a serial multi stage flexure

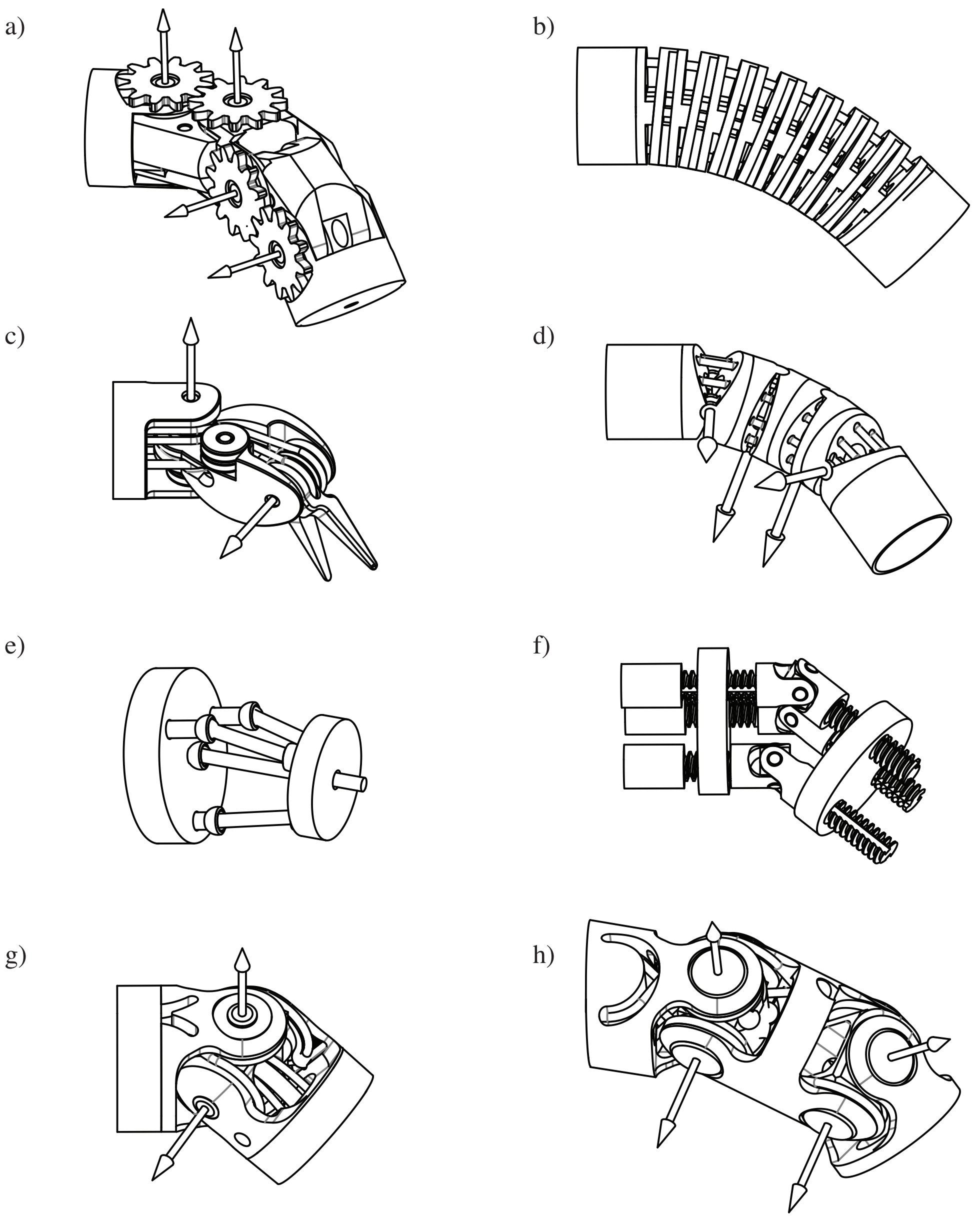

Figure 4.7: Selection of surgical wrist concepts that have been considered for this project: Wrist based on the DLR robotic finger (a), endoscope bending mechanism (b), 8 mm EndoWrist® (c), 5 mm EndoWrist® (d), parallel mechanism (e), rotationally actuated parallel mechanism (f), universal joint (g), coupled double universal joint (f).

based mechanism. Range of motion increases with the length of the mechanism due to limited elastic deformation for each flexure. This concept is most suited for a long tool with large radius of curvature and a low manipulation force requirement (as usually found in flexible endoscopes) and was therefore not considered further.

- The *8 mm EndoWrist*® , Fig. 4.7 (c), is a serial single stage discrete joint mechanism. The wrist is available from Intuitive Surgical® with a large number of different end effector functions and shapes, being mass produced yet still extremely rugged. Distinguishing detail of this design are two independently movable end effector jaws which, when moved in the same direction form the second DoF of the wrist. When moved in opposite directions the end effector is opened and closed. Therefore, the wrist is extremely short considering the available range of motion. However, while many research groups work with force-torque sensor attached to the shaft of an EndoWrist® tool (see Sec. 2.3.2), it does not lend itself to the placement of a force sensor between wrist and end effector, since that placement requires a separation between the axes of second wrist DoF and end effector.

- The *5 mm EndoWrist*® , Fig. 4.7 (d), is a two stage discrete wrist mechanism. It is more closely related to the DLR robotic finger mechanism (a) than the elastic bending mechanism (b). The coupling of the two stages for each DoF, which is performed by gears or cables in (a), is relocated from the wrist itself to the interface unit. This allows for a much more compact wrist design. In contrast to an elastic mechanism each of the four wrist sections are independently actuated using a mechanism similar to a swash plate in the interface unit to generate the required differential cable motions. This mechanism is the smallest in diameter covered here. Surgeons complain about the large deformation of this tool when applying force to the tip. Likely this is caused mostly by the small diameter and the corresponding flexibility of the shaft and drive cables as the mechanism itself seems well designed from a conceptual point of view.

- The *parallel mechanism*, Fig. 4.7 (e), is a single stage parallel kinematic preferably actuated by push-pull rods. A parallel platform actuated by three prismatic links can generally be moved in three DoF, but is usually limited in the achievable range of motion. Either one of the links is of fixed length and is used to transmit the end effector actuation motion, or the movement of the platform in the third DoF with reference to the base is used to actuate the end effector. Parallel platforms rely either on flexural joints which limits the range of motion further, or depend on ball and socket joints which are difficult to manufacture in the required small dimensions. For this reason the parallel platform concept was not followed.

- *Double screw drive mechanism*, Fig. 4.7 (f), proposed by Ishii and Kobayashi [91]. While this is also a parallel platform, in contrast to concept (e), the prismatic links are actuated by a thread mechanism which translates the rotation of motors into an elongation of the links. Only one stage of the original three stage mechanism is shown here. The small diameter of the parallel mechanism compared to its length yields very low stiffness in addition to significant mechanical play caused by the threads and cardanic joints.
- The *universal joint based mechanism*, Fig. 4.7 (g), is a single stage discrete spherical wrist. In its most basic form it consists of 3 structural components and 2 cable loops. Range of motion is limited to a maximum of $\pm 45^\circ$ in both DoF in order to guarantee a spherical workspace. Larger articulation is possible, however direct movement between points might not be possible as great circle (direct) trajectory any more. One major advantage of the universal joint concept is the ability to rotate the end effector about its approach axis without changing the orientation of the tool shaft. This greatly reduces necessary robot motion e.g. when penetrating tissue with a curved needle.
- The *coupled double universal joint*, Fig. 4.7 (h), is a double stage version of the universal joint. The two stages are coupled using pretensioned cable loops as suggested by Thompson [170]. An enlarged prototype of this concept was built using rapid prototyping. While the concept is feasible, complexity is fairly high and the coupling loops generate a noticeable amount of friction. This concept will likely be investigated further in the future.

Although being conceptually highly interesting designs, the wrists by ComputerMotion™ (Grace [71]), Tuebingen Scientific (Braun et al. [38]), and Müglitz et al. [171] were not investigated further for this project as an extension of the original mechanism designs from one DoF to two DoF would be difficult and likely negate their advantages.

Despite its workspace limitation, the universal joint based mechanism (g) was chosen for the wrist. Aside from being compact and rugged, it simplifies the inverse kinematics for the *MIRO*, due to intersecting wrist axes. Inside its workspace it combines the advantages of both RPY and RPR kinematics, limiting robot motion during the common task of suturing. While a larger workspace is certainly desirable, the RoM of $\pm 45^\circ$ will allow a number of proof-of-concept experiments. The universal joint based design also avoids intellectual property issues as no reference to prior art could be found.

4.3 Intra-corporal Force Sensor

A concept for the tool's wrist mechanism has been selected in the previous section. A force-torque sensor concept for the integration into the minimally invasive tool will be developed in the current section. A number of different force and moment components arise from the tool's interaction with the environment. As described in Sec. 2.2.2 the scope of force feedback described in this thesis can be visualized by haptic exploration with a pen or tweezers. It is possible to to exert forces and moments and grasp objects. A distinction will be made between the *gripping force* and *manipulation loads*. The *gripping force* is the normal force exerted by the jaws of the gripper onto tissue or materials located directly between those jaws. The *gripping force* only takes the two distinct forms: gripping (positive value) and spreading (negative value). *Manipulation loads* denote the general 6 DoF force and moment field describing the tool's interaction with the environment and take the form of axial and lateral pushing/pulling, bending, and twisting. The force-torque sensor discussed in the current section is targeted at the *manipulation loads*. The *gripping force* sensor is part of the generic functional tip (see Sec. 4.4).

4.3.1 Sensor Location

The spatially separated arrangement of user input station and robotic manipulator in MIRS prevents any haptic feedback from the operation site. In order to provide direct feedback of tissue manipulation forces to the surgeon, these forces have to be measured at the operation site. The full set of manipulation loads at the tool tip, acting between the tool and tissue include three manipulation force components, three manipulation moment components and the gripping force.

Although Bholat et al. [43] point out that in spite of friction within the trocar and resistance of the abdominal wall, tactile sensations can still be felt at the handle of conventional MIS instruments and van der Putten et al. [82] list several mechanical approaches for transmitting forces to the handle, the force information will contain less errors the closer to the tool tip

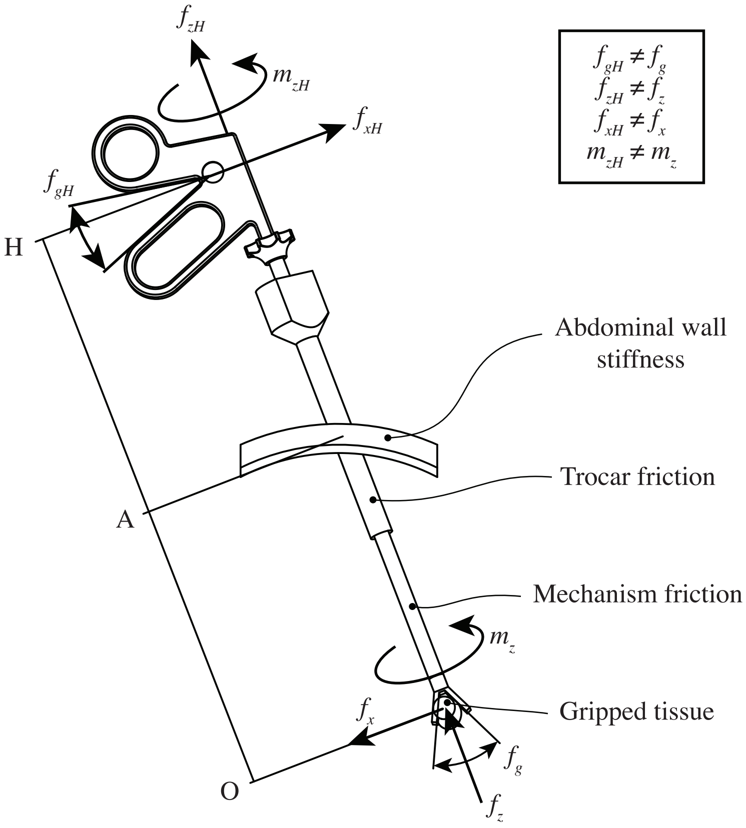

Figure 4.8: Interference factors in conventional minimally invasive surgery. The grip force (f_{gH}) is not equal to the tip force (f_g) due to the instrument's mechanism. The hand force (f_{xH}) is not equal to the organ force (f_x) due to the scaling factor (ideally $f_{xH} = f_x(\overline{\mathrm{OA}}/\overline{\mathrm{AH}})$) and the resistance of the abdominal wall. The pull force at the handle (f_{zH}) is not equal to the pull force at the organ (f_z) due to trocar friction. The torque, applied at the handle (f_{zH}), is influenced by the trocar friction as well. (*Image and force identifiers adapted from van der Putten et al. [82]*).

it is obtained. Even close to the tool tip, the capability of the FTS to distinguish between lateral forces and bending moments decreases with the distance between force sensor and instrument tip. The reason is illustrated in Fig. 4.9.

Fig. 4.9 shows the bending moment induced in the tool shaft (represented as solid beam) by a bending moment m_y (a) and a lateral force f_x (b). Two sensor elements sensitive to bending moments are placed in location S_1 and S_2 along the shaft, separated by the sensor base length s_b. Let the bending moment m_y be equal to $f_x \cdot l$ for this example, the sensor element S_1 will register identical signal magnitudes of $f_x \cdot l$ for both cases (a) and (b). In case (a) the moment distribution is constant, so elements S_1 and S_2 will register the same signal. However, in case (b) lateral force f_x causes a linear increase in beam bending moment, therefore, the moment magnitudes at S_1 and S_2 will be:

$$m_y(\mathrm{S}_1) = f_x \cdot l$$
$$m_y(\mathrm{S}_2) = m(\mathrm{S}_1)(1 - \frac{s_b}{l})$$

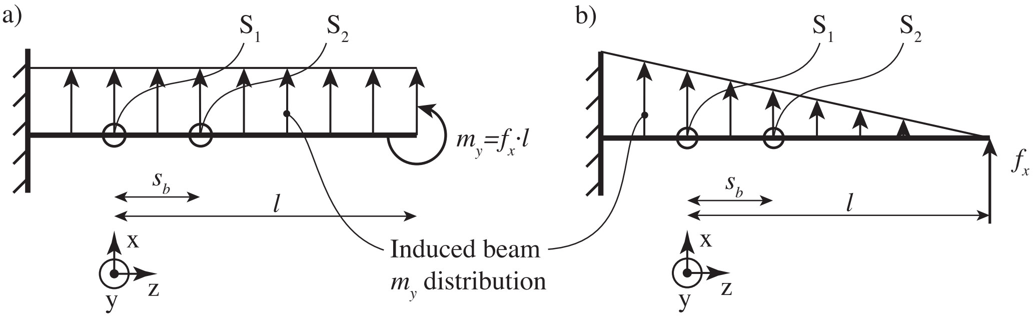

Figure 4.9: Comparison of moment distribution induced in beam by bending moment m_y (a) and lateral force f_x (b) applied to the beam tip. Two bending moment sensor elements are placed at distance l (S_1) and $l - s_b$ (S_2) from the tool tip. In case (a) the moment distribution is constant over the length of the beam, in case (b) a linear increase is observed from the beam tip to fixture.

Increasing the distance l between tool tip and FTS will not only decrease the relative difference between S_1 and S_2, but also lateral forces will cause increasingly large resulting moments acting on the FTS. Designing the sensor to withstand these large moments caused by lateral forces results in decreased sensitivity and resolution for true bending moments. Therefore, the FTS should be placed as close to the tool tip as possible.

Furthermore, similar to the parasitic influence of friction inside the trocar, any friction and backlash in the wrist drive mechanism will affect the FTS performance unless the sensor is decoupled from actuation mechanism.

Placement of a force-torque sensor is possible in several distinct locations:

1. *In the jaws of the end effector* (see Fig. 4.10, location (1)). The jaws entail the most severe size constraints. Additionally, the measurement of manipulation forces also depends on the grasping state, and measured loads depend on the jaw angle. Many tools only differ by the shape and function of the jaws. Placing a sensor here will require the development of specialized sensors for every jaw shape. Many tools for MIRS differ mainly in the jaw design of the functional end. Forceps, needle holders, dissectors, even some mono- and bipolar electro surgery tools consist of two movable jaws that are opened and closed symmetrically by a single actuator. Therefore, a generic tool design is preferred, where a large number of functional variants can be produced without major changes to the overall design. This rules out a placement of the FTS in the jaws of the gripper.

2. *Between functional end and wrist* (see Fig. 4.10, location (2)). Size restrictions are less severe than in the jaws. If the FTS is of roughly cylindrical shape, most of the tool diameter except a central portion for accommodating the gripper actuation mechanism can be utilized. However, the electrical connection to the sensor has to be routed through the joint, requiring highly flexible, isolated, multi-strand wires.

3. *In the shaft between wrist and trocar* (see Fig. 4.10, location (3)). This placement does not require the electrical connection to be routed through the joint, which will prolong the life expectancy of the sensor. The available outer diameter is equal to the diameter of the tool, as above, however more space is required for the integration of wrist and gripper actuation mechanisms. The force flow of actuation forces moving the wrist will be closed through the FTS (compare Fig. 4.19).

4. *As part of a specialized trocar* (see Fig. 4.11, Salle et al. [44]). This placement requires a different approach with the *MIRO* holding and orienting a specialized trocar instead of the instrument. The tool is inserted through a guide tube. Guide tube and trocar are connected through the FTS. Manipulation load measurements are not affected by trocar friction or resistance, however, they have to be compensated for the

effects of the instrument mass. These effects obviously change dependent on orientation of the instrument. Separation of lateral forces and moments is most difficult here due to the large distance between FTS and force application point. However, the distance of load sensing elements will also increase due to the larger possible diameter of the FTS, somewhat increasing the sensitivity of force/moment separation. Due to the requirement for specialized trocars and the dependence of the force measurement on the orientation of the instrument, the placement of a force-torque sensor inside a trocar as shown in Fig. 4.11 will not be considered any further.

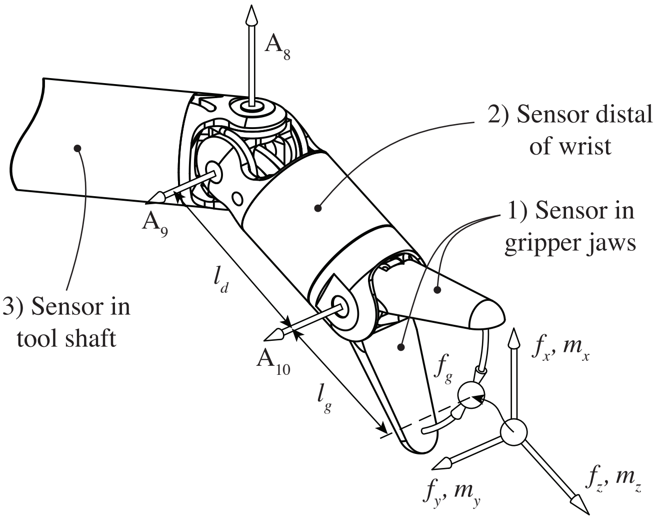

Figure 4.10: Definition of manipulation loads ($f_{x,y,z}$, $m_{x,y,z}$) and gripping force (f_g) acting at the tool tip caused by interaction with the environment. All forces are assumed to be acting on a point located on the tool axis at a distance of l_g distal from the jaw rotation axis A_{10}. The force frame is always aligned to the end effector frame. Also shown are possible locations for the placement of force-torque sensor on the tool: 1) In the jaws of the gripper; 2) Between wrist and gripper; 3) In the tool shaft proximal to the wrist

In the locations immediately distal to the tool wrist (location (2) between wrist and end effector), and proximal to the tool wrist (location (3) in the tool shaft), parts of the tool actuation mechanism need to be routed through or around the sensor. As discussed Fig. 4.4, actuation forces exceed manipulation forces significantly. Placing the force-torque sensor in a location were the actuation force flow is closed through the FTS, requires the sensor to be able to withstand those large actuation forces, greatly reducing resolution for the com-

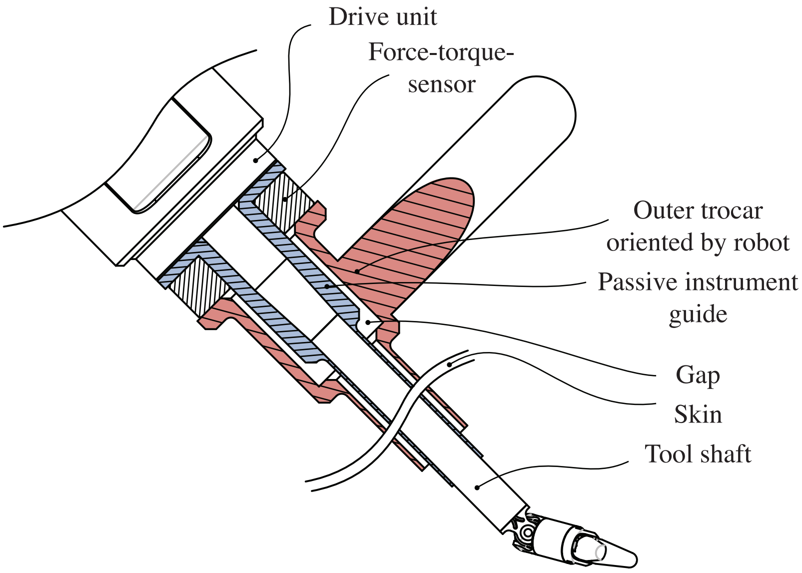

Figure 4.11: Location of manipulation force sensor inside a specialized trocar (*Concept adapted from Salle et al. [44]*).

paratively small manipulation forces. Knowing the exact magnitude and location/direction of actuation forces allows for compensation of the FTS signal, however any remaining parasitic effects (friction in the drive mechanism, stick-slip effects and play) cannot be accounted for, and will introduce considerable errors in the measurement.

In case of a sensor placement between wrist and functional end, only the mechanism actuating the end effector will have to be integrated into the sensor. Measurement of the gripping force is required to provide the user with a complete set of manipulation loads and gripping force. The relationship between the end effector actuation force (which is a parasitic load on the FTS) and the gripping force is known, thus knowledge of the gripping force can be used to compensate the FTS signal for the end effector actuation. A concept for further reducing the parasitic effect of the end effector actuation force will be presented in Sec. 4.4. Finally, if the FTS is located between wrist and end effector, the sensor coordinate system is always aligned with the end effector approach direction and, therefore, inaccuracies of the wrist motion tracking will not introduce a misalignment of manipulation forces. The location between wrist and end effector is chosen for the placement of the force-torque sensor for these reasons.

4.3.2 Force Sensing Concepts

No suitable 6 DoF force-torque sensor is available commercially or has been proposed in previous research that would allow for the integration close to the tool tip of a MIRS instrument. The development of a customized solution, therefore, starts with a review of applicable sensing methods, and the definition of general requirements for the current application.

Many classification schemes for force sensors have been proposed in the past. A broad and representative sensor classification scheme was suggested by White [172], allowing a universal categorization of sensors based on measurands, detection means, conversion phenomena, materials, and applications. The force-torque sensor proposed here would fall into the following categories (category names and descriptions according to White [172]):

- *(A) Measurand*: Mechanical force (A 6.4), strain (A 6.6) or moment (A 6.8)
- *(C) Detection Means*: Electric, magnetic or electromagnetic (C 3) or mechanical displacement (C 5).
- *(D) Physical Sensor Conversion Phenomena*: Magnetoelectric (D 3.4), elastoelectric (D 3.7), photoelastic (D 3.10).

Category *(B)* would detail the technological aspects of the sensor (sensitivity, range, stability, resolution, output, cost, etc.), category *(E)* the sensor material and category *(F)* the field of application. While this classification is most useful for the comparison of existing sensors, it can be used as a template for listing the relevant requirements in the present application.

A similar template for the collection of sensor requirements can be found in Stefanescu [173], listing the following categories:

- Measurand (i.e. force), range (expressed in Newtons), overload, accuracy, frequency response.
- Transduction principle, closely related to measurement method.
- Measurement system capabilities: signal conditioning, data processing (filtering, error compensation), transmission, and display.

- Available space, ambient, and functional/working conditions.
- Economic aspects: performance-cost ration, possibilities of reusing or redesign, periodic verification of technical characteristics.

Force requirements for the proposed MIS tool have been detailed in Sec. 3.1.4. They are 10 N for manipulation forces, and accordingly, 150 Nmm in manipulation moments. While the motion frequency of the proposed tool only reaches up to a few Hz (see Sec. 3.1.2), the human sensitivity to forces and vibrations ranges from static contacts up to over 1 kHz with a peak sensitivity around 250 Hz (Siciliano and Khatib [174]). While the expected loads will mostly be static or of low frequencies, a faster response is still necessary to allow for interactions between the tool and hard materials (bone, needle, other tools). Therefore, the force transducers should be able to operate within the zero to 1 kHz range, however with an emphasis on static forces and low (up to 250 Hz) frequencies.

The transmission of the sensing element output signal, and the available space (for both, transducer, and signal conditioning electronics) are governed by the sensor placement as discussed in the previous section. A review of available sensing principles (Stefanescu [173], Pallàs-Areny and Webster [175], Fraden [176]) reveals that most frequently force is first converted to strain and then in a second stage strain is converted to an electrical or optical signal. Fig. 4.12 shows a summary of electrical and optical properties that strain sensors are commonly based on. Each of these properties in turn can be affected by one or more physical effects, such as:

- *Geometry*: change in width, length, distance or curvature due to a mechanical force.
- *Piezoresistance*: change in semiconductors conductivity due to a mechanical force.
- *Piezoelectricity*: generation of a surface charge due to a mechanical force.
- *Magnetoelasticity*: change in magnetization by a mechanical force.
- *Piezooptics*: change in refractive index due to a mechanical force.
- *Photoelasticity*: generation of double refraction by a mechanical force.

Considering the above detailed force, dynamic, and size requirements, only a small subset of sensor concepts is usable in the present application.

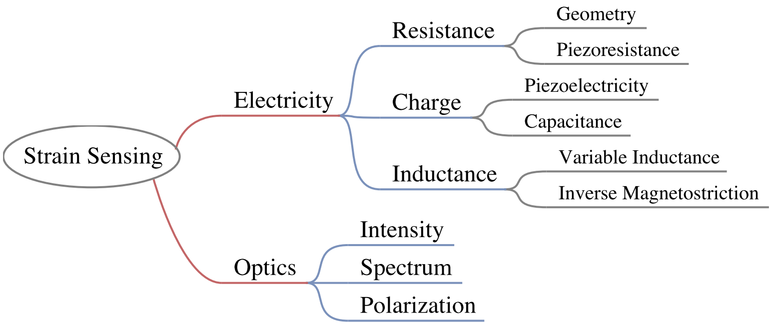

Figure 4.12: Most common physical effects used for measuring strain.

The piezoelectric effect describes how some crystals under compressive loading generate an electrical charge that is directly proportional to the force applied. In order to use this effect for a measurement system, electrical charge is then converted to a proportional output voltage with the aid of a charge amplifier. Piezocrystals (e.g. single crystal quartz, gallium phosphate) generate small charges, but are long term stable and the generated charge does not change with temperature (HBM [177]). Piezoceramics, on the other hand, generate a larger charge, but are pyroelectric (the charge is temperature dependent) and not long term stable. Piezoceramics have the advantage of a high modulus of elasticity which is comparable to metals, leading to a low deflection, high linearity, and a high natural frequency. Sensitivity of piezoelectric transducers is unfortunately often frequency dependent.

The major disadvantage of piezoelectric and other charge based transducers (e.g. capacitive transducers) is that they are unsuitable for true static measurements. A static force results in an invariant amount of charge. Since all charge amplifiers will exhibit some leakage currents, continuous signal decay occurs. Charge based transducers are most suitable for signals at higher frequencies, however, the required dynamic range with an emphasis of static and low frequency signals rules out most charge based transduction principles.

Optical transducer technologies usually require more complicated signal conditioning systems that cannot easily be integrated into a MIRS instrument. However, optical signals are mostly immune to electromagnetic interference and can be transmitted over larger distances than unamplified electrical transducer signals. The necessary signal conditioning system can therefore be placed outside of the instrument (e.g. in a rack alongside the robotic system) without considerable signal loss or degradation. Optical intensity and polarization encoded signals should be avoided, as most optical fibers exhibit a certain amount of losses and change in polarization state related to bending. These parasitic losses could not be distinguished from desired intensity/polarization changes due to the changes in the measurand. Some optical transducers, however, produce a spectrum encoded signal. Fiber Bragg grating (FBG) transducers (see Fig. 4.13) and fiber based Fabry-Perot interferometers produce a spectrum (frequency) encoded signal that is proportional to the applied mechanical strain. These transducers are, therefore, less susceptible to light intensity variations. In white light fiber based Fabry-Perot interferometers a semi-transparent mirror at the end of the fiber reflects a first portion of light back down the fiber. The remaining light traverses a cavity delimited by a second reflective surface which reflects a second portion back down fiber. A spectrometer is used to record the interference spectrum of the reflected light. The distance of adjacent peaks in the interference pattern allows for the determination of the cavity length (Totsu et al. [180]) and, therefore, the amount of mechanical strain acting on the cavity. Fiber Bragg gratings are composed of a periodic variation in the refractive index of the fiber core. Broad spectrum light is sent into the fiber and each index step acts as semitransparent mirror and reflects a tiny amount of light back down the fiber. All reflected

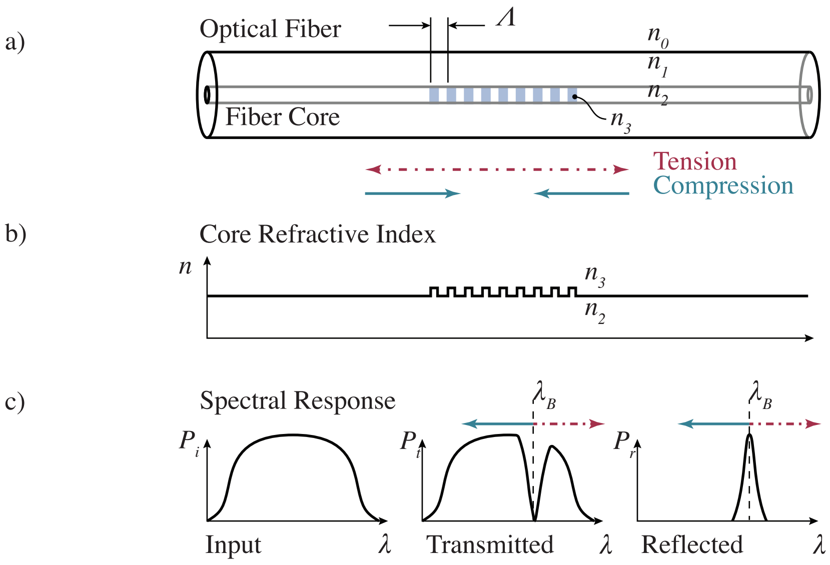

Figure 4.13: Fiber Bragg grating composed of a periodic variation in refractive index (n_2 and n_3) along the core of a single mode fiber core with grating period Δ (a,b). Most of the incident spectrum is transmitted, only a very narrow wavelength peak (λ_B) related to the grating period and refractive index is reflected (c) (*Image adapted from Kersey et al. [178], Wikipedia [179]*).

light portions create interference which extinguishing most of the spectrum except one specific wavelength λ_B, called the Bragg wavelength. The Bragg wavelength is defined by the relationship:

$$\lambda_B = 2n_e\Lambda$$

where n_e is the effective refractive index of the grating in the fiber core, and Λ is the grating period (an example for a typical grating that reflects 1500 nm, the grating period is 500 nm for an effective refractive index of 1.5).

Both transducer principles have successfully been used in the medical field (see Totsu et al. [180], ENDOSENSE [181]) and show great benefits. Signal conditioning systems can be placed in a location where sterilization is not required and the sensor itself and the signal transmission are not susceptible to electromagnetic interference. While system components and sensors for FBG systems are becoming more available and are getting cheaper, there is still a large number of unsolved problems regarding temperature compensation, sensor packaging and application, sufficiently small and reliable fiber connections, and fiber handling, to name a few. In order to investigate FBG sensors in more detail, a substantial investment into fiber optic equipment, handling and measurement systems is necessary, which was not possible at the outset of this project.

Resistive strain gauges convert a mechanical deformation into a change of electrical resistance. They have been invented in 1938 and since discussed and characterized extensively (see Stefanescu [173], Pallàs-Areny and Webster [175], Fraden [176], useful application notes can be found in Hoffmann [182], Measurements Group [183]). Therefore, only a very brief overview will be given here. Two basic types of strain gauges exist:

- *Geometry* based strain gauges rely on the effect that the resistance of a conductor is not only dependent on its specific resistivity, which is a material property of the conductor, but also on the conductor geometry. If a conductor is stretched under tension, both the increase in length and the reduction in cross-section will increase the conductor's resistance. Thin film strain gauges consist of a strip of thin conductive material arranged in a meander shape to multiply the effect of strain on the conductor. Two dual element strain gauge patterns with their typical meander shapes are shown in Fig. 4.14. The sensitivity of the pattern to mechanical strain is the dimensionless gauge factor (K) which is defined as:

$$K = \frac{1}{\varepsilon}\frac{\Delta R}{R} \tag{4.1}$$

with the nominal strain gauge resistance R and the change in resistance ΔR (both in Ω) under *general* mechanical strain ε. The value of the gauge factor depends mostly on the strain gauge resistor material. It is usually slightly larger than two ($k \geq 2$) for metal resistive alloys.

- *Piezoresistance* based strain gauges are manufactured from semiconductor materials that are heavily doped to form a resistor. Here mechanical strain causes a change in inter-atomic spacing, leading to a change in carrier mobility (positive or negative depending on the material). The effect is a relatively large change in resistance resulting in gauge factors commonly in the range of 50-150. Semiconductor strain gauges made from silicon are also not prone to plastic deformation and therefore do not exhibit hysteresis of the gauge material itself (Büttgenbach [184]).

Both technologies show a dependence of the strain gauge resistance on temperature, semiconductor strain gauges, moreover, also show a temperature dependent sensitivity. A comparison of the merits of both technologies can be found in Little [185].

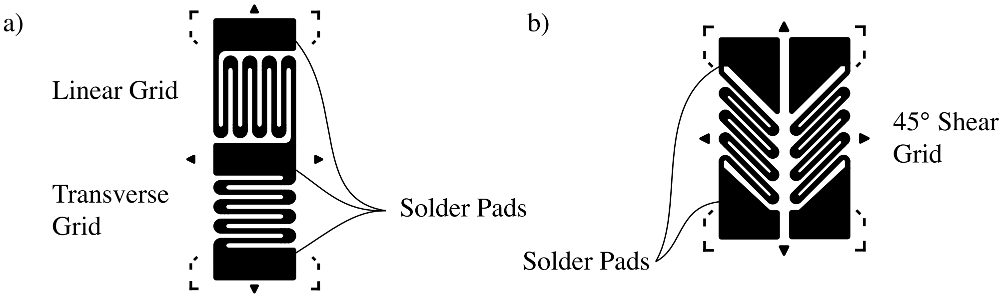

Figure 4.14: Example of two common dual element strain gauge grid patterns. The long axis of the matrix is intended to be aligned with the direction of principal strain. The dual element gauge on the left (a) is designed for linear strain, the gauge pattern on the right (b) is intended for shear strain and can be used in torque transducers for example.

The minute changes in resistance exhibited by strain gauges are difficult to measure accurately on their own, therefore, commonly a Wheatstone bridge network (see Fig. 4.15) is used to derive a voltage output from the resistance change. A large variety of bridge networks exist, depending on the number and alignment of strain gauges: quarter bridge arrangement (one active strain gauge, three passive resistors), half bridge (two active strain gauges, two passive resistors), and full bridge (four active strain gauges). Half and full bridges can be used to compensate for some of the temperature effects on strain and resistance, as an equal change in resistance experienced by all resistors in the bridge will not produce a change in bridge output voltage.

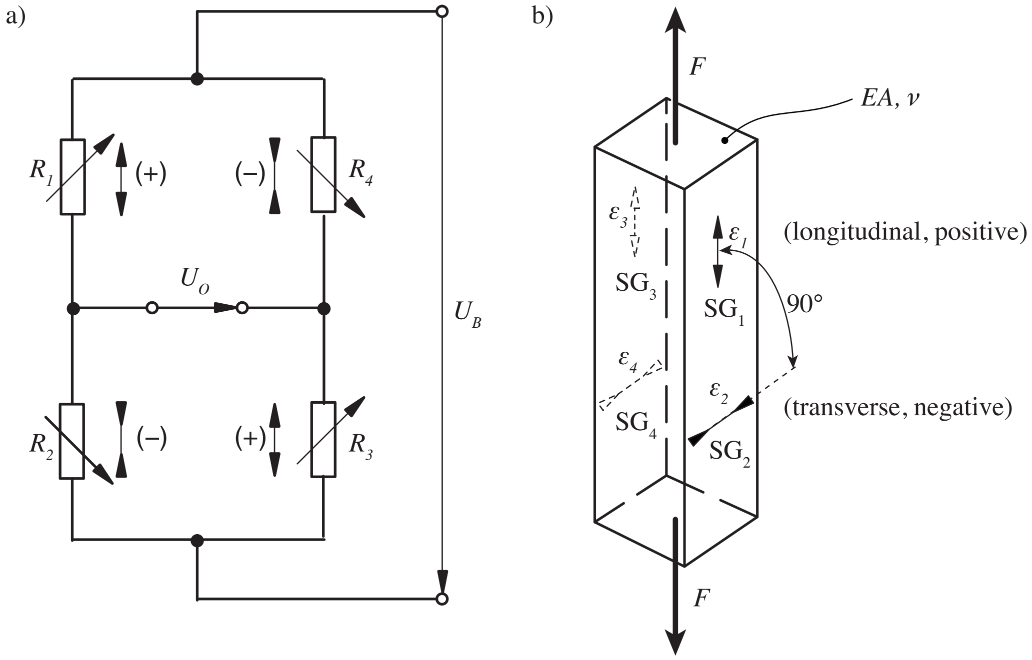

Figure 4.15: Principle of Wheatstone bridge strain gauge network (a) and placement of strain gauges on a beam under tension (b). R_{1-4} and ε_{1-4} are the resistances of, and relative strains experienced by strain gauges SG_{1-4}. In the depicted loadcase, gauges SG_1 and SG_3 experience positive strain (tension) and the resistance of R_1 and R_3 increases. Gauges SG_2 and SG_4 experience negative strain (compression) due to the Poisson effect and the resistance of R_2 and R_4 decreases. U_B is the bridge supply voltage and U_O is the bridge output voltage (*Image from HBM [186]*).

If all bridge resistors are equal and the variation in resistance due to strain is much lower than the base resistance value, the ratiometric bridge output relative to the strain (ε) and the gauge factor (K), can be written as (Measurements Group [183]):

$$\frac{\Delta U_O}{U_B} = \frac{N}{4} \cdot K \cdot \varepsilon \tag{4.2}$$

ΔU_O is the change in Wheatstone bridge output voltage and U_B is the bridge supply voltage. The dimensionless bridge factor N denotes the number of bridge resistors aligned to the *longitudinal* strain $\varepsilon = \frac{F}{EA}$, with F being the tensile/compressive force in Newton, E the Young's Modulus in $\frac{\mathrm{N}}{\mathrm{mm}^2}$ of the beam under tension/compression and A the cross-section of the beam in mm^2. In the case of transverse strain gauges, which are aligned at 90° to the longitudinal strain, N will take fractional values based on the Poisson's coefficient ($\nu = 0.3$ in this example). Therefore, the full bridge shown in Fig. 4.15 (b) will have a bridge factor of $N = 2.6$ based on the top gauges being aligned to the longitudinal strain, the bottom gauges being aligned to transverse strain of the compressed beam. Further examples of bridge factors N based on the bridge layout are given in Measurements Group [183].

The bridge output voltage is fed into a signal conditioning circuit. Many circuit schematics have been used, however in the most basic form the signal conditioning circuit consists of an operational amplifier, filter and analog to digital converter as shown in Fig. 4.16. Strain gauges show good stability for long-term measurements, and exhibit high linearity if fully active Wheatstone bridge arrangements are used (Measurements Group [183]). They are a tried and tested transducer technology and gauges are available in various shapes and sizes, giving a large amount of design freedom for the sensor geometry and will, therefore, be used in the FTS.

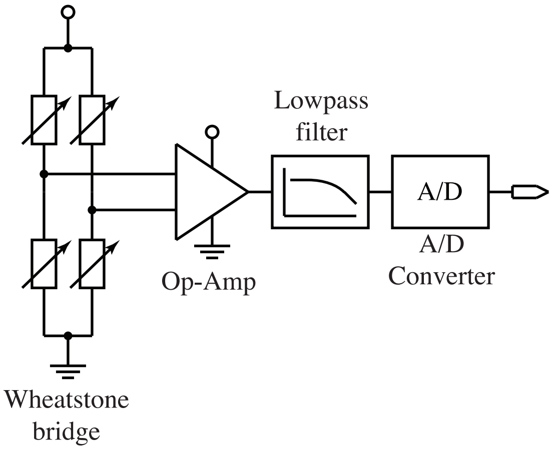

Figure 4.16: Wheatstone bridge strain gauge network, strain gauge amplifier and signal conditioning electronics.

4.3.3 Sensor Geometry

The general monolithic structures shown in Fig. 4.17, including some variations, were considered for the development of the 6 DoF force-torque sensor. Suitable sensor structures are chosen based on sensing properties (isometric sensitivity for all loads, stiffness), transducer type and location, and geometry considerations. Of these properties, the importance of structural stiffness, which is paramount in high dynamic and high load applications, is somewhat less severe in the present application. The FTS is to be placed close to the tip of the MIRS tool with little mass attached and mostly slow, soft tissue interactions.

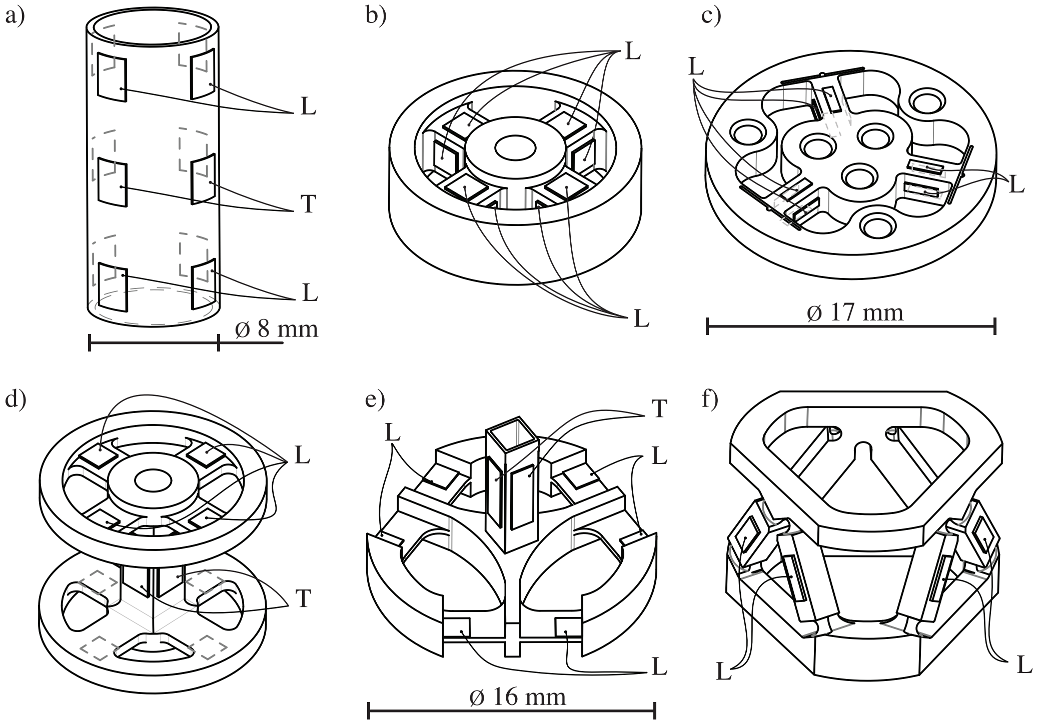

Figure 4.17: Monolithic 6 DoF force/torque sensor structures with ’L’ denoting longitudinal strain transducers, ’T’ denoting shear strain transducers: Tubular shape (a), basic Maltese cross bar (b), ATI nano 17 (c), double spoke design (d), DLR fingertip sensor (e) and Stewart Platform based sensor (f).

Preferably, strain transducers are applied to structures that deform, at the location of highest deformation. The structures shown in Fig. 4.17 (c) and (f) contain elastic flexures that serve the purpose of decoupling load components, which will show high deformations, but with no strain transducers attached. While maximizing the elastic deformation at the transducer locations, care has to be taken that no part of the flexure will be subjected to plastic deformation. Plastic deformation of any part of the sensing structure, strain gauge attached or not, would lead to measurement errors and hysteresis. Ideally the flexures should reach the limit of elastic deformation at the same load that produces maximum elastic strain at the transducer locations.

A qualitative assessment regarding the suitability of the structures shown in Fig. 4.17 is given in the following summary:

- *The tubular shape*, Fig. 4.17 (a), is more suited as a 4 DoF FTS for lateral forces and bending moments. Due to the high axial and torsional stiffness of the tubular structure, sensitivity to the axial force and torsion about the tube axis is very small. This design is commonly used for retrofitting existing MIS instrument shafts for lab experiments. Due to the low sensitivity in 2 DoF it should not be considered for a dedicated sensor design. The structure is fairly long but provides a large hollow central cross-section that allows for the space saving integration of other tool components.
- *The Maltese Cross bar shape*, Fig. 4.17 (b), was proposed in 1987 by Uchiyama et al. [187] as true 6 DoF sensor. The structure can be designed with reasonable sensitivity in all directions, however there is significant cross coupling between forces and moments. Strain transducer elements are placed on all four sides of the four spokes which hinders miniaturization as access to the beam sides becomes more difficult with smaller dimensions. The structure is short but only a small central bore is possible.
- *ATI nano 17*, Fig. 4.17 (c), is a commercially available 6 DoF FTS with an outer diameter of 17 mm and a height of 12 mm. The actual sensing structure is a steel disc of only about 2 mm height. It is derived from the Maltese cross bar structure, however, thin flexures at the end of the tree spokes provide effective decoupling of load components. It provides good sensitivity for all load components. However, similar to the Maltese Cross bar, strain transducers are applied to all four sides of the three spokes, making further miniaturization next to impossible, a central bore is not available with the 17 mm diameter size (ATI [188]).
- *The double spoke shape*, Fig. 4.17 (d), is derived from the Maltese Cross by sepa-

rating it into top and bottom sections connected by a torsion bar. This has several advantages: cross coupling is reduced, torsional sensitivity and the ability to distinguish between lateral forces and bending moments are improved. Also, transducer elements are not required on the sides of the two sets of spokes. Still, the central bore is small and the structure is fairly long.

- *The DLR Fingertip*, Fig. 4.17 (e) is used in the tip of the DLR hand's fingers. In contrast to the double spoke design, in the Fingertip the spokes are rigid and strain transducers are arranged on thinned out sections on the circumference of the structure basis. Torsional loads are measured similarly to the double spoke design by a torsion bar. Sensitivity is high for all moments and the axial force. Sensitivity for lateral forces is somewhat reduced. The central bore is small and the structure fairly long due to the torsion bar. Due to the location of transducers in close proximity to the mounting points of the structure basis, without decoupling flexure between transducer and mounting point, this structure is very sensitive to mounting conditions and the design of connecting parts.

- *The Stewart Platform* based structure, see Fig. 4.17 (f). Stewart Platforms are a class of 6 DoF parallel robotic structures first described and investigated by Stewart [107]. The kinematic arrangement has been analyzed and used as 6 DoF FTS in larger structures, usually consisting of individual linear force transducers connected to two rigid platforms by individual spherical joints (see Kerr [189], Byun et al. [190], Ferraresi et al. [191], Sorli and Pastorelli [192]). Miniaturization is possible when the discrete joints are replaced with elastic flexures (as described by Li [193]). Advantages of the Stewart Platform include high stiffness, sensitivity to individual load components that can be tailored over a wide range, annular shape with large central hollow, and scalability. Furthermore, only linear strain transducers are required, eliminating the need for shear transducers. All transducers are placed on a roughly hexagonal cross-section, in a generally longitudinal direction. This placement facilitates the future use of measurement systems other than electrical strain gauges. However, while all previously introduced structures utilize strain transducers placed in locations where beam bending occurs, with the Stewart Platform only linear tension/compression occurs at the transducer locations. The strain caused by tension/compression is often lower than the strain caused by bending for the same beam dimensions. Also, careful layout is required to suppress parasitic bending effects introduced by the flexural joints (this will be discussed in more detail in Sec. 5.1.3).

The forward kinematics of a generic Stewart Platform takes the from of an 20^{th} order equation. Using some restrictions, such as non-intersecting links and symmetry, this equation can be reduced to 8^{th} order. However, if a Stewart Platform based sensor is assumed to be rigid under the desired load, only the inverse kinematics for the undeformed case is required. A derivation using a force balance approach has been presented by Sorli and Pastorelli [192] and takes the form of a system of six linear equations. Using this solution, much of the guesswork can be eliminated from the traditionally iterative process of force sensor design. Tailoring the sensor properties to the load requirements for the MIRS tool can be accomplished analytically rather than by repetitive Finite Element Analyses (FEA). For this reason, the Stewart Platform type structure instrumented with resistive strain gauges is chosen for the force-torque sensor to be developed. The implementation will be presented in detail in Sec. 5.1.

4.4 Generic Functional Tip

A large number of MIS tools (grasper, scissors, needle holder) mainly differ in the shape and size of the end effector jaws. Exact details of the jaw design depend on tool manufacturer, target application and surgeon preference. It is not the goal of the present work to create the large tool variety commonly available during surgical interventions, but rather the implementation of one generic end effector mechanism that includes two jaws of generic shape that can later be adapted to different requirements. Furthermore, it was decided in Sec. 4.3 to place the manipulation sensor (FTS) between end effector and wrist rather than inside the jaws due to size constraints. Designating the jaws as passive component without any sensor components simplifies the design and manufacture of various jaw shapes. Placing the gripping force sensor (GFS) inside the jaws would negate that advantage.

While the current concept is focused on an end effector with two symmetrically actuated jaws, further tool variations containing no active movable parts are easily realized. Examples are palpation tools to record tissue stiffness, dissection hooks as well as irrigation and suction tools. Actuation of the end effector follows similar considerations as wrist actuation, with the addition that the end effector actuation energy is required to pass through the wrist and force-torque sensor. Available concepts include:

- *Translatory* motion transmitted either by cable or rod (see Fig. 4.18 (a-c)). Two cables can be used in a fully active pull-pull mechanism for active opening and closing of the end effector (as described by Cooper et al. [69] for the 5 mm EndoWrist® and by Ishii and Kobayashi [91]), or a single cable can be used in a semi-active pull mechanism counteracted by a spring (shown in Fig. 4.18 (a) and (b)). The spring in both cases is a torsion spring located between the end effector jaws on the jaw axis (not shown in figures). In Fig. 4.18 (a) the cables are directly terminated at the end effector jaws, whereas in Fig. 4.18 (b) the jaws are connected to the actuation cable by a link mechanism. Fig. 4.18 (c) shows a rod actuated mechanism found in many conventional MIS tools. The rod is used in a push-pull configuration to actively open and close the jaws.

- *Rotatatory* motion using a flexible torque shaft and a thread or worm gear mechanism for opening and closing the jaws. Fig. 4.18 (d) shows a direct-drive concept using a micro-motor placed directly inside the tool tip. This example is shown as reference only. The decision against the use of direct-drive actuation has been explained in Sec. 4.1. A similar mechanism could be realized by using a torque shaft to transmit the actuating energy from the EMU. With all rotatory transmissions, self locking of the thread or gear mechanism – which would limit the backdrivability – has to be considered. A change in grasping state due to tissue movement for example is not detectable. As a side note, the concepts shown in Fig. 4.18 (b) and (c) might alternatively also be actuated by a rotatory shaft and thread mechanism, rather than by cable as shown.

Generating the gripping force to securely hold a needle requires large actuation forces due to the transmission ratio being limited by the tool diameter and jaw lengths. Using the kinematics example shown in Fig. 4.19 (a), generating a gripping force f_g of 10 N will require a cable force F_c of 60 N, assuming a gripper pulley radius r_g of 3.25 mm and an active jaw length l_g of 9.75 mm. This actuation force is delivered from the motor unit past the manipulation load sensor, and the force loop is closed by the FTS. Fig. 4.19 (b) shows the resulting force acting inside the FTS according to the method of sections. This will affect the loads measured by the FTS by introducing a significant error of -60 N in f_z.

While it seems straightforward to use a measurement of the gripper actuation force F_c to mathematically compensate for the error caused in the FTS reading, there are a number of disadvantages. The FTS sensor is now required to withstand not only the external manipulation loads, but also the large actuation force, greatly reducing usable sensor resolution.

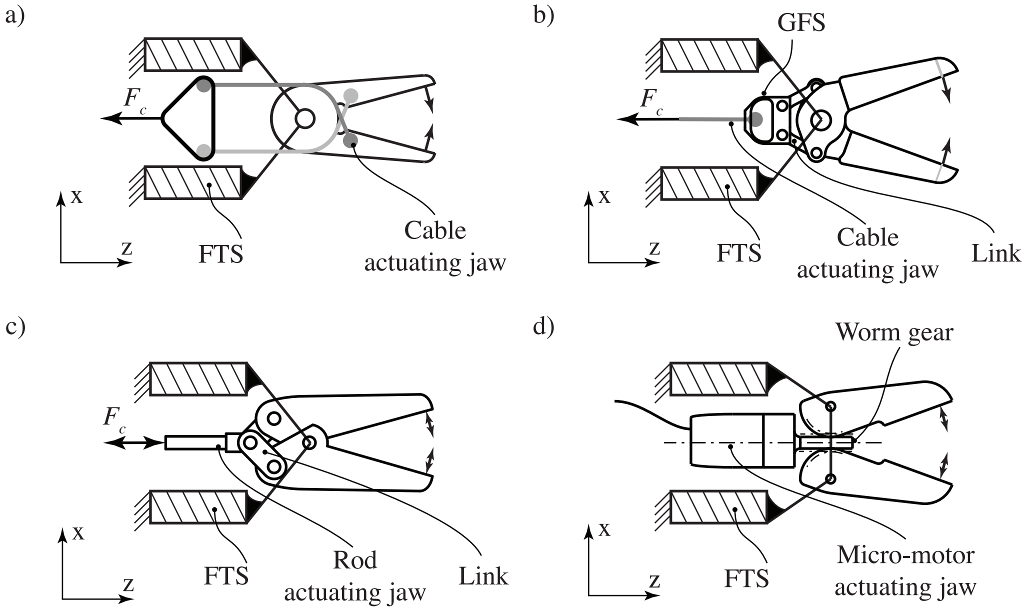

Figure 4.18: (a) Cable driven end effector mechanism. Jaws are closed by a cable strand attached to each jaw and opened by a spring (not shown). (b) Cable actuated link mechanism. Jaws are closed by a cable attached to a link-type mechanism and opened by a spring (not shown). (c) Link-type end effector mechanism found in many conventional MIS instruments. Jaws are closed by pushing on a drive rod and opened by pulling. (d) Motor-driven end effector mechanism. A micro-motor drives a worm gear opening and closing the jaws.

Moreover, any remaining sources of error in the drive train (friction in the drive mechanism, stick-slip effects and play) cannot be accounted for and will introduce large errors in the measurement. To avoid this limitation, a mechanical decoupling system has to be integrated in the gripper actuation path. The goal is to effectively support the gripper actuation force F_c at the base of the FTS and creating a decoupled force loop at the tip of the FTS.

Direct-drive actuation of the end effector by micro-motor (as shown in Fig. 4.18 (d)) or SMA actuator at the tip of the FTS would provide a mechanically less complicated solution for avoiding manipulation force measurements being affected by end effector actuation. Only electrical energy would be transmitted through the FTS and the end effector actuation force would be generated distal of the FTS. However, as outlined previously, available actuator work density would require the end effector to be extremely long in order to accommodate

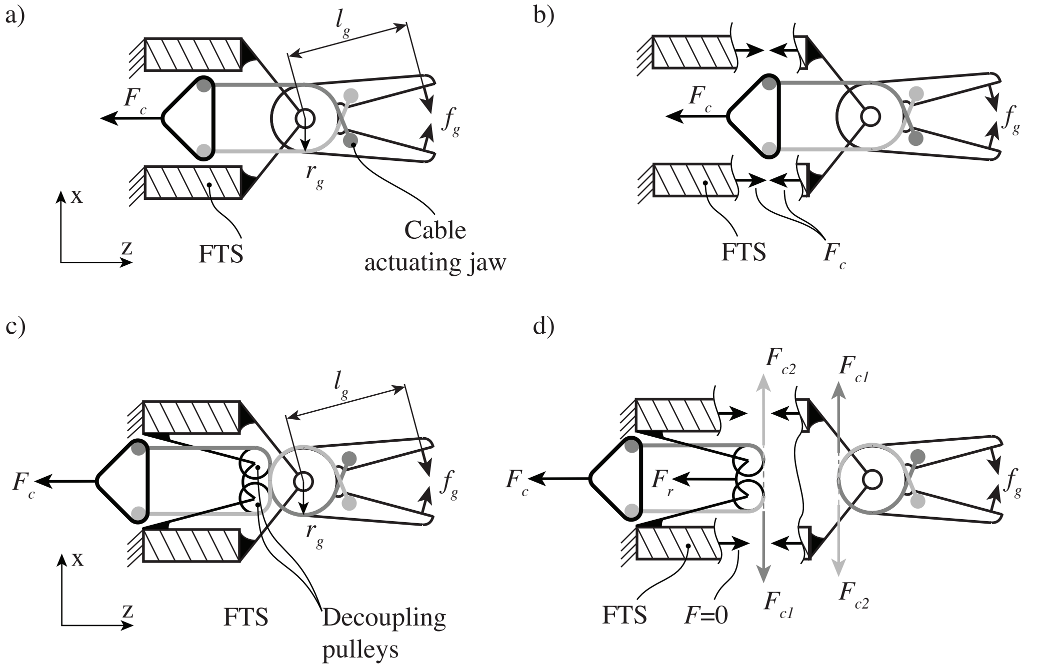

Figure 4.19: The end effector is actuated by a cable strand attached to each jaw (a). The actuation cable force F_c loop is closed through the FTS. (b) shows the force flow according to the method of sections, it can be seen that the FTS is subjected to the full force flow of F_c. Decoupling of actuation cable forces is achieved by guiding the two actuation cable strands over decoupling pulleys that are supported at the FTS base (c). (d) shows the decoupled force flow. The FTS is not subjected to F_c.

the necessary electric actuators. Hydraulic actuation would present an elegant solution as well, as the force generated by a hydraulic system is dependent on the active cross-section subjected to hydraulic pressure. A thin hydraulic tube running through the FTS will only generate a small parasitic force on the sensor due to the tube's small cross-section. Using a larger diameter cylinder attached to the distal side of the FTS to generate the jaw motion will provide a large end effector force without compromising the FTS.

One example of a mechanical force decoupling mechanism is shown in Fig. 4.19 (c). This example is tailored towards end effector actuation by a single semi-active cable mechanism, counteracted by a spring which opens the gripper jaws. Similar decoupling mechanisms can be devised for push-pull rod actuation. The mechanical decoupling of the actuation force in the cable driven example is achieved by routing the gripper actuation cable strands around decoupling pulleys supported at the base of the FTS. In the sectional view Fig. 4.19 (d), the left section shows that two cable force components are created. The components in z-direction combine to reaction force F_r in axial (z)-direction which is supported at the base of the FTS and, therefore, does not affect the manipulation load measurement. The components in x and $-\mathrm{x}$ direction (F_{c1} and F_{c2}) created at the output of the pulley system, are of equal but opposing size. These contain no component in (z)-direction and do not exert an axial load on the FTS. Therefore, the force flow through the FTS caused by the actuation cable force F_c is 0. Only a small amount of parasitic moment (m_z) is transmitted onto the sensor as the cable strands cannot both run in the xz-plane, but are offset by a small amount in y-direction. In the right section of Fig. 4.19 (d), the equal and opposing cable force components F_{c1} and F_{c2} actuate the end effector jaws. A gripping force sensor, measuring the gripper actuation force is integrated into the decoupling pulley support. Calibration of the FTS and GFS together as combined 7 DoF sensor will account for the interaction and thereby compensate for residual errors. The calibration method is described in more detail in Sec. 6.1. Clearly, this type of decoupling mechanism is only applicable for tools with two symmetrically moving jaws and cannot be used for tools with one stationary and one moving jaw.

4.5 Tool Interface Unit

Earlier in this chapter it was postulated that from a system point of view, it would be reasonable to structure the instrument into a generic extra-corporal motor unit required for all tools, and into an interchangeable, task specific tool aimed at a distinct therapeutic functionality. The separation of the MIRS instrument into these components (see Fig. 4.1) requires the definition of an electro-mechanical interface between the two. This *tool interface unit* provides suitable mechanical transmission of actuation energy to the tool, as well as standardized digital communication with any sensors located in the tool. Based on the *MiroSurge* framework, the *MIRO* provides a hollow axis wrist design with the instrument mounted above the robot wrist and tool shaft extending downwards through the wrist (as shown in Fig. 3.1). The *MIRO* wrist provides a hollow diameter of 11.4 mm, large enough only for tool shaft insertion. For the shaft to extend through the *MIRO* wrist, the tool interface unit needs to be placed above the wrist. This placement between the *MIRO* wrist and the instrument extra-corporal motor unit requires the tool interface unit to incorporate a second interface, connecting the instrument and *MIRO* robot.

The tool interface unit (shown in Fig. 4.1), therefore, combines several functional components:

- *A system specific* interface to the *MIRO* arm ('Robot interface' in Fig. 4.1) on the side facing the tool shaft. This interface provides secure mechanical attachment of the *MICA* to the *MIRO*.
- *A system specific* interface to the EMU on the side facing away from the tool shaft. This interface mechanically and electrically connects the tool to the EMU creating the instrument. The transmission design needs to be free of mechanical play, provide a secure connection, but also needs to be easy to connect and disconnect.
- *A tool specific* linkage or pulley system translating the linear motion of the EMU actuator rods into the motion required for articulating the tool, thereby transmitting the actuation energy from the EMU into the tool shaft.

The EMU provides mechanical motion for the tool's 3 DoF. Therefore, the reconnection between tool and EMU is greatly facilitated if all 3 DoF can be connected simultaneously, independent of the respective actuator and tool position. Fig. 4.20 shows four possible approaches for the simultaneous connection of several actuator motions (rotational in (a) and (b) and linear in (c) and (d)). Those concepts in particular are:

- *The daVinci® tool interface*, Fig. 4.20 (a) (Cooper et al. [194], Devengenzo et al. [197]), consists of four axially spring loaded disks, each containing two mating pegs. The individual position of the tool wrist – and, therefore, the rotational alignment of the mating disks – is unknown. On connection of the tool, the counterparts of these tool disks, located on the surface of the robot arm, perform a position finding rotary motion until the tool mating disks snap into place securing the connection. A certain amount of tool wrist movement needs to be accepted during the position finding phase. The daVinci® tool interface couples the rotary motion of the actuator to a rotary motion of a cable pulley inside the tool. The mating direction of the interface is parallel to the axis of rotation of the interface disk. After connection, the tool is locked into place by spring loaded levers.
- *The EMU implemented by Kübler [166]* used an interface also coupling rotary actuator motion to the rotary motion of a cable pulley. In contrast to the daVinci® interface,

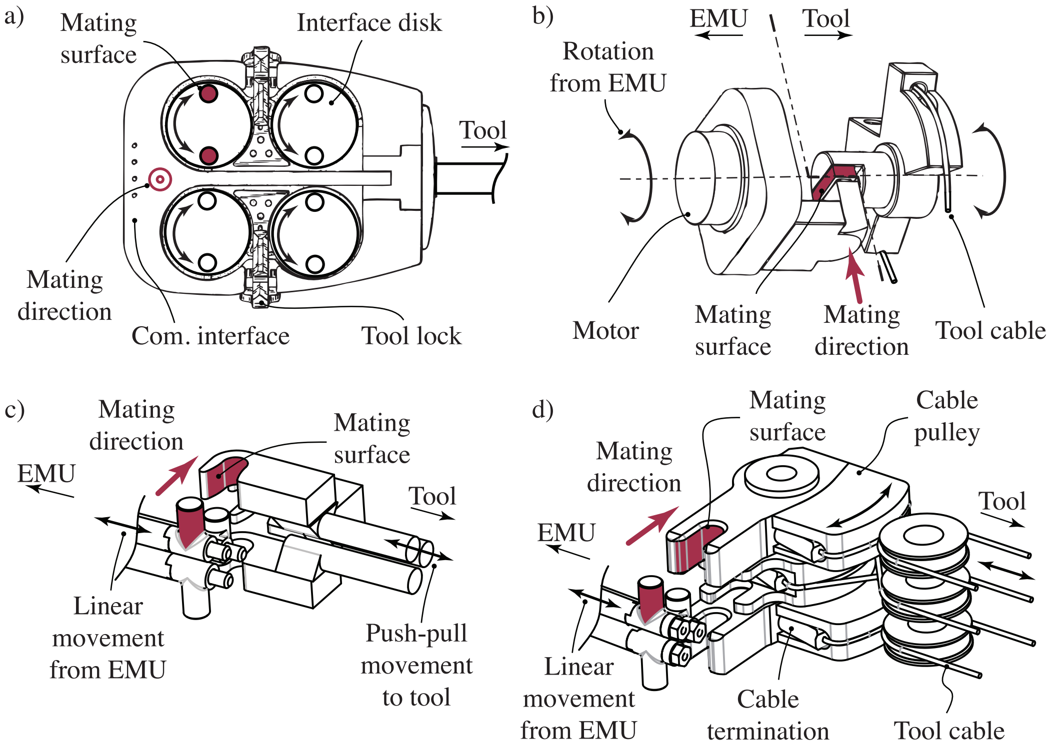

Figure 4.20: Tool specific interface unit motion transmission concepts. Intuitive Surgical® tool interface (a) with rotary disk drive to cable pulley transmission with axial mating direction (*Image from Cooper et al. [194]*). Rotary shaft drive (b) to cable pulley transmission with normal to rotation axis mating direction (*Image from Kübler et al. [195]*). Translatory rod drive (c) to translatory tool transmission with mating direction normal to drive movement. Translatory drive (d) to cable pulley transmission with mating direction normal to drive motion (Seibold et al. [196]).

however, the mating direction was normal to the axis of rotation. The range of rotation for the mating surfaces (see Fig. 4.20 (b)) was limited to $\pm 15^\circ$ in order to guarantee that mating surfaces for all 3 DoF would connect properly independent of actuator and tool wrist position (Kübler et al. [195]). However, the arrangement of mating surfaces directly on the axis of rotation, together with the limited range of rotation, rendered this concept extremely susceptible to even small misalignments between the mating surfaces, causing unwanted mechanical play or mating difficulties.

- *The EMU implemented by Thielmann [167]* provides 3 DoF of linear movement as output of the EMU section. The 3 push-pull rods have a rod diameter of 2.5 mm and are arrayed in circular pattern within a diameter of 7 mm. Fig. 4.20 (c) shows a concept for coupling the 3 linear movements provided by the EMU to 3 linear rod movements for the tool (for more details, refer to Seibold et al. [198]). Fig. 4.20 (d) shows a concept for coupling the 3 linear movements provided by the EMU to 3 cable loop movements for the tool. Mating surfaces take the shape of key-and-slot joints with a mating direction normal to the direction of movement. The slots of the mating surfaces open up towards the front in order to allow coupling even with small misalignment between key and slot (Seibold et al. [196]).

Due to the fact, that the EMU implemented by Thielmann [167] provides 3 DoF of linear movement as output of the EMU section and the articulated wrist described in Sec. 4.2 is driven by stainless steel cables, the connection mechanism concept shown in Fig. 4.20 (d) will be implemented.

4.6 Summary of Concepts

The current chapter has introduced five discrete modules of the *MICA* instrument: extra-corporal motor unit (Sec. 4.1), wrist (Sec. 4.2), force-torque sensor (Sec. 4.3), end effector (Sec. 4.4), and tool interface unit (Sec. 4.5). Solution concepts have been described and evaluated for each module. Selecting from all introduced ideas, the following concepts are chosen for implementation of the advanced force feedback tool for MIRS:

- *The extra-corporal motor unit* is based on rotatory BLDC motors, generating either rotatory or linear motion. Through mechanical transmission this motion is providing a wrist movement frequency of greater than 5 Hz at manipulation forces of greater than 10 N.
- *The intra-corporal articulated wrist* is based on a single stage, cable actuated universal joint with intersecting axes. It provides a range of motion of $\pm 45°$ in 2 degrees of freedom. Advantages include compact size and low parts count.
- *The intra-corporal force-torque sensor* is based on a Stewart Platform geometry, instrumented with strain gauges and capable of measuring manipulation loads in 6 DoF up to 10 N and 150 Nmm.
- *The generic functional tip* provides a single DoF for end effector actuation with symmetrically opposing jaws, either forceps or scissors, actuated by cable. The actuation will include a mechanism to reduce parasitic forces acting on the manipulation load sensor.
- *The tool interface unit* provides an electromechanical interface between generic drive unit and tool, allowing for the separation of the two. It also provides the system specific interface between *MICA* and *MIRO*.

5

Implementation

In this chapter the dimensioning and design of the force sensors, wrist, end effector (shown in Fig. 5.1) and interface unit of the minimally invasive tool will be described in detail.

Figure 5.1: Closeup view of the minimally invasive tool tip in the form of a short needle holder with centimeter scale in the background. Diameter of the tool is 10 mm.

5.1 Force Sensor

In Sec. 4.3 a number of feasible force sensing concepts for the application in a minimally invasive instrument have been discussed. A major advantage of the specific Stewart Platform based structure is the existence of a simple, linear solution to its inverse kinematics (see Sec. 5.1.1). Rather than using a trial and error approach using finite element analysis (FEA) for dimensioning the sensor, the overall geometry of the sensor structure is tailored to the desired loadset using analytical inverse kinematics (see Sec. 5.1.2). Fine tuning of the flexural joints and transducer placements using FEA analysis is still necessary (see Sec. 5.1.3), but a lot of guesswork is removed from the process. Structural elements for the final force-torque sensor design are shown in Fig. 5.2.

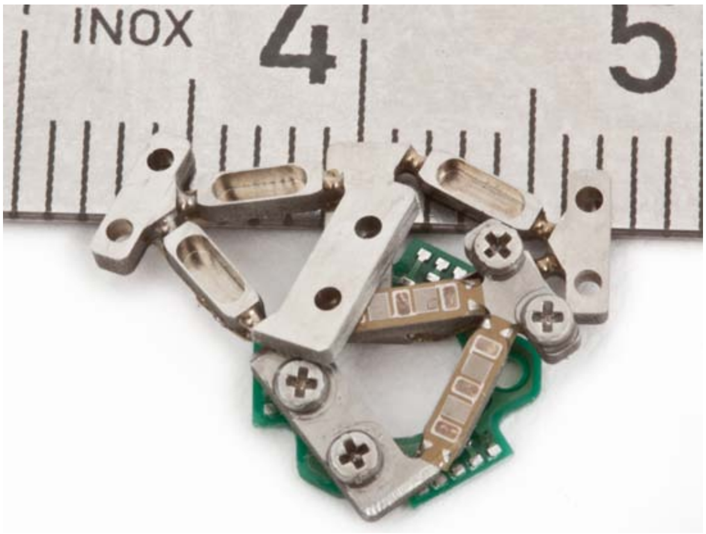

Figure 5.2: Closeup view of sensor components with centimeter scale (small graduation equals 1 mm) in the background. Shown are the 3 V-shaped structural segments of the force-torque sensor with strain gauges attached to the front and C-shaped link section at the back.

5.1.1 Sensor Inverse Kinematics

Labeling of geometric parameters and the development of the inverse kinematics shown in this section is a recap of the work published by Sorli and Pastorelli [192]. Structure and labeling are shown in Fig. 5.3. The original structure of a six DoF parallel robot as

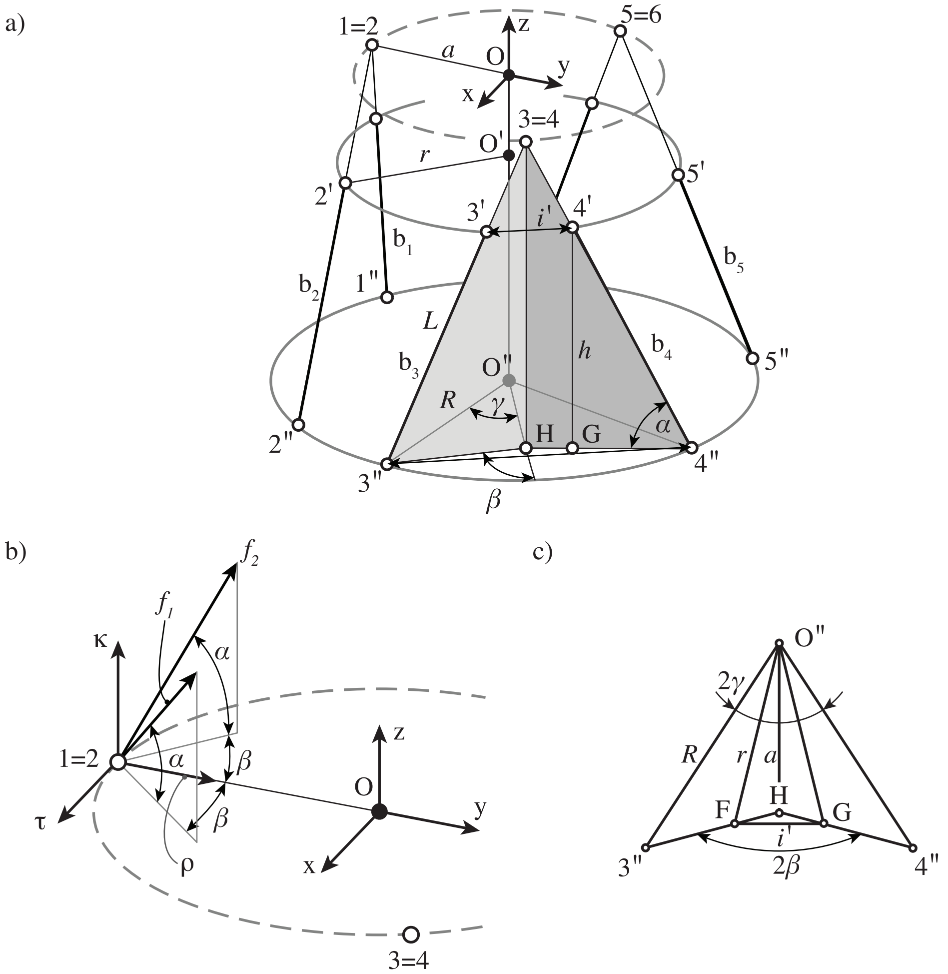

Figure 5.3: Geometrical parameters of Stewart Platform adapted from Sorli and Pastorelli [192]: General structure, joint and link arrangement (a), force decomposition with link forces f_1 and f_2 acting on links b_1 and b_2 (b) and detailed view of one link pair projected in $-z$ direction (c).

developed by Stewart [107] calls for two infinitely stiff platforms, one fixed, one moving with six arbitrarily arranged ideal spherical joints (frictionless, no play, unlimited RoM) each. Those joints are connected by infinitely stiff links. Each link, due to the spherical joints, is able to transmit a force only in link direction. No restriction is placed on the shape and orientation of the platforms, the arrangement of joints or the length and direction of the links. For practical reasons, only a very specific subset of the general Stewart Platform structure will be investigated:

- Links $b_{1..6}$ connecting the spherical joints $1''..6''$ on the lower (fixed) platform to the spherical joints $1'..6'$ on the upper (moving) platform are of equal length and non intersecting.
- Joints $1''..6''$ on the lower platform are arranged on a concentric circle with radius R and center O$''$. The center O$''$ is located on the z-axis which is normal to the plane containing joints $1''..6''$.
- Similarly, joints $1'..6'$ on the upper platform are arranged on a concentric circle with radius r and center O$'$. The center O$'$ is located on the z-axis which is normal to the plane containing joints $1'..6'$.
- Joint pairs $1'', 2''$ and $1', 2'$ for adjacent links $b_{1,2}$, $3'', 4''$ and $3', 4'$ for adjacent links $b_{3,4}$ and $5'', 6''$ and $5', 6'$ for adjacent links $b_{5,6}$ are distributed symmetrically along their respective circles.

These conditions ensure that link pairs $b_{1,2}$, $b_{3,4}$ and $b_{5,6}$ will intersect in three virtual points $1 = 2$, $3 = 4$ and $5 = 6$. Those virtual intersections span a circle with center 0 and radius a, concentric to the circles spanned by joints $1''..6''$ and $1'..6'$. For all further investigations, the sensor coordinate system is placed at the center O of this virtual circle with the z-axis pointing away from O$''$ and O$'$ as shown in Fig. 5.3 (a). Using this geometry, the set of parameters (R, L, α, β, γ), denoting the radius of the lower platform (R), the link length (L), the distribution angle of lower joints (γ) and the link direction (α, β) sufficiently describe the geometry, and thus, the properties of the sensor. Derived from these parameters are the upper platform radius r, the radius of virtual link intersections a, the structure height h, and the linear separation of joint pairs on the lower platform i'' and upper platform i'.

The characteristic matrix of the sensor is developed as described by Sorli and Pastorelli [192] by investigating the forces acting on the three individual link pairs at the point of intersection. An example for links b_1 and b_1 is shown in Fig. 5.3 with link forces f_1 and f_2 broken down into a radial component (direction ρ), a tangent component (direction τ) and a normal component (direction κ). Summing the projections of the $\rho\tau\kappa$ force components onto the xyz reference system for all links and creating the static equilibrium yields the characteristic matrix $\mathbf{A} \in \mathbb{R}^{(6\times6)}$. $\mathbf{A} \in \mathbb{R}^{(6\times6)}$ describes the transformation of internal link forces into external loads acting on the virtual platform (for the complete derivation refer to Sec. A.1 and Sorli and Pastorelli [192]).

$$[f_x, f_y, f_z, m_x, m_y, m_z]^T = \mathbf{A} \cdot [f_1, f_2, f_3, f_4, f_5, f_6]^T \tag{5.1}$$

with

$$\mathbf{A} = \frac{1}{2}\begin{bmatrix} -2n & 2n & \sqrt{3}m+n & \sqrt{3}m-n & -\sqrt{3}m+n & -\sqrt{3}m-n \\ -2m & -2m & m-\sqrt{3}n & m+\sqrt{3}n & m+\sqrt{3}n & m-\sqrt{3}n \\ -2q & -2q & -2q & -2q & -2q & -2q \\ 2aq & 2aq & -aq & -aq & -aq & -aq \\ 0 & 0 & aq\sqrt{3} & aq\sqrt{3} & -aq\sqrt{3} & -aq\sqrt{3} \\ -2an & 2an & -2an & 2an & -2an & 2an \end{bmatrix} \tag{5.2}$$

where

$$\begin{aligned} m &= \cos(\alpha)\cos(\beta) \\ n &= \cos(\alpha)\sin(\beta) \\ q &= \sin(\alpha) \\ a &= R\left(\cos(\gamma) - \frac{\sin(\gamma)}{tan(\beta)}\right) \\ i' &= 2(R\sin(\gamma) - L\cos(\alpha)\sin(\beta)) \end{aligned}$$

The upper half of $\mathbf{A}$, relating link forces to external forces is dimensionless, while the lower half, relating link forces to external moments is scaled by the radius a of virtual link intersections. The inverse kinematics shown above is used to find a set of parameters R, L, α, β, γ fully describing a sensor geometry that is well suited for the measurement of tissue manipulation loads expected during surgery. Geometrically valid combinations (non intersecting links) of R, L, α, β, γ are used to calculate $\mathbf{A}$. For assumed values of R and

L, geometrically valid combinations of the parameters α, β, γ are given by:

$$0^\circ \leq \gamma \leq 60^\circ \tag{5.3}$$

$$\gamma + 1^\circ \leq \beta \leq 90^\circ \tag{5.4}$$

$$\arccos\left(\frac{R\sin(\gamma)}{L\sin(\beta)}\right) \leq \alpha \leq 90^\circ \tag{5.5}$$

5.1.2 Analytical Dimensioning

$\mathbf{A}$ is inverted numerically to yield the sensor Jacobian, the transformation of externally applied loads to link forces $\mathbf{J} \in \mathbb{R}^{(6\times6)}$. Sets of maximally expected external loads $\mathbf{F}_{extern} = [\mathbf{f}_{extern\ 1}..\mathbf{f}_{extern\ n}]$ with $n \geq 6$ are selected. $\mathbf{F}_{extern}$ must have a rank of six, containing six linearly independent load vectors. An example for a external load set is:

$$\mathbf{F}_{extern} = \begin{bmatrix} f_x & 0 & 0 & 0 & 0 & 0 \\ 0 & f_y & 0 & 0 & 0 & 0 \\ 0 & 0 & f_z & 0 & 0 & 0 \\ 0 & 0 & 0 & m_x & 0 & 0 \\ 0 & 0 & 0 & 0 & m_y & 0 \\ 0 & 0 & 0 & 0 & 0 & m_z \end{bmatrix} \tag{5.6}$$

Every member of the external load set is pre-multiplied by $\mathbf{J} = \mathbf{A}^{-1}$, yielding the corresponding set of internal leg forces:

$$\mathbf{F}_{intern} = \begin{bmatrix} \mathbf{f}_{intern\ 1} \\ .. \\ \mathbf{f}_{intern\ n} \end{bmatrix} = \mathbf{J}\mathbf{F}^T_{extern} \tag{5.7}$$

The condition number of the internal leg force set $\kappa(\mathbf{F}_{intern})$, which is shown in Fig. 5.4 and Fig. 5.5, is a measure of the isotropy of the sensor structure with respect to the external load set. This, however, is not an isotropy in the classical definition, since the external loads in the principal directions need not be equal. The definition of isotropy is ambiguous for the described structure because of the scaling of moment sensitivity dependent on the size a. Usually this problem is tackled by calculating isotropy separately for forces and moments. By contrast, in the current document, the *structural or unity isotropy* $\kappa_{unity}(\mathbf{F}_{intern})$ will be defined as equal sensitivity to principal external unit forces $f_{xyz} = 1$ N and principal external unit moments, which are unit forces applied at the radius a, yielding $m_{xyz} = a$ Nmm. Fig. 5.4 shows the *structural or unity isotropy* for these principal unit loads, dependent on the parameters α and γ. Values of R and L were initially also varied, however in the MIS tool they are governed by the tool diameter and strain transducer size. Fixed values of $R = 4.3$ and $L = 4.3$ are assumed for the following calculations. More limitations will be placed on the structure by manufacturing considerations, e.g. real joints have finite size and cannot overlap, therefore, the separation of adjacent joints i'' and i' need to be greater than zero as well.

Fig. 5.4 shows examples only for $\beta = 60°$ and $\beta = 90°$, similar results can be generated for all other valid values of β (see Eq. 5.5). However, it has been found that for unit loads on a transducer of a diameter and length to fit into a MIRS tool, $\beta = 90°$ consistently yielded the lowest condition numbers.

Finding the *structural isotropy* $\kappa_{unity}(\mathbf{F}_{intern})$ is of little help for the real world application as the sensor in the minimally invasive tool will be subjected to more specific conditions. To find a sensor geometry that is well conditioned and optimized for the force range expected in a surgical application, the external load set will consist of the loads expected at the tool tip. This measure will be called *load isotropy*. Fig. 5.5 shows the *load isotropy* for the load set that was determined in Sec. 3.1.4 as requirements for the sensor: $f_x, f_y, f_z = 10$ N, $m_x, m_y = 150$ Nmm and $m_z = 100$ Nmm.

Similar to the *structural isotropy* shown in Fig. 5.4, *load isotropy* is shown in Fig. 5.5 dependent on the parameters α and γ for fixed values of $R = 4.3$ and $L = 4.3$ as governed by the tool diameter and transducer size. Only $\beta = 90°$ is plotted as $min(\kappa_{load}(\mathbf{F}_{intern})) \geq 10$ for $\beta = 60°$, and, therefore, not visible on the plotted scale. Again, it has been found that for the selected loads on a transducer of this diameter and length, $\beta = 90°$ consistently yielded the lowest condition numbers. An upper joint distance of $i' = 1.1\text{mm}$ has been determined as minimum distance that allows manufacturing of the sensor structure by milling.

Table 5.1: Parameters for overall Stewart Platform geometry.

Stewart Platform Geometry and Design Loads					
$R = 4.3$ mm	$L = 4.3$ mm	$\alpha = 65°$	$\beta = 90°$	$\gamma = 36°$	
$f_x = 10$ N	$f_y = 10$ N	$f_z = 10$ N	$m_x = 150$ Nmm	$m_y = 150$ Nmm	$m_z = 100$ Nmm

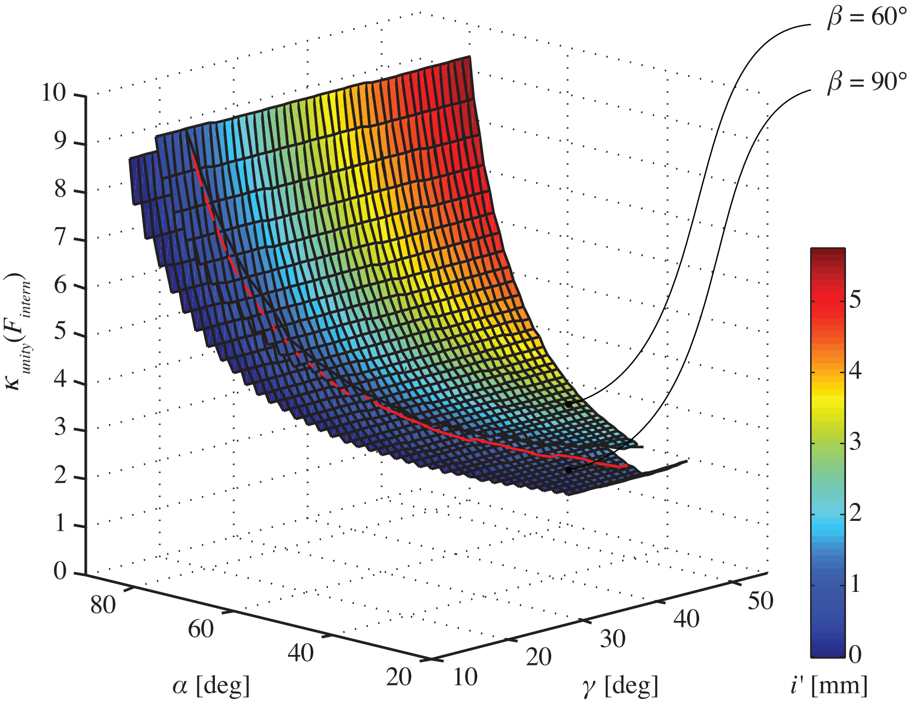

Figure 5.4: Condition number $\kappa_{unity}(\mathbf{F_{intern}})$ for *structural isotropy* (loadset $f_{xyz} = 1$ N and $m_{xyz} = a$ Nmm) dependent on α and γ. Two examples are shown for $\beta = 60°$ and $\beta = 90°$, with $R = 4.3\text{mm}$ and $L = 4.3\text{mm}$ in all cases. Colors denote the distance of upper joint pairs i' in mm. Red and black lines show the $i' = 1.1\text{mm}$ for $\beta = 90°$ and $\beta = 60°$, respectively.

Following these simulations for the load set $f_{xyz} = 10$ N, $m_{xy} = 150$ Nmm and $m_z = 100$ Nmm, the following parameters were selected as optimal sensor geometry using the analytical dimensioning process: $R = 4.3$ mm, $L = 4.3$ mm, $\alpha = 65°$, $\beta = 90°$, $\gamma = 36°$ (see Tab. 5.1), yielding a conditioning number of $\kappa_{load}(\mathbf{F_{intern}}) = 6.17$ and a joint separation of $i' = 1.1$ mm. Using Sec. 5.7 the internal link forces of the described Stewart Platform caused by above external loadset can be calculated (see Tab. 5.2).

5.1.3 Numerical Dimensioning

The analytical model developed in Sec. 5.1.1 is based on assumptions that cannot fully be satisfied in practice. Therefore, after establishing the sensor geometry by analytical

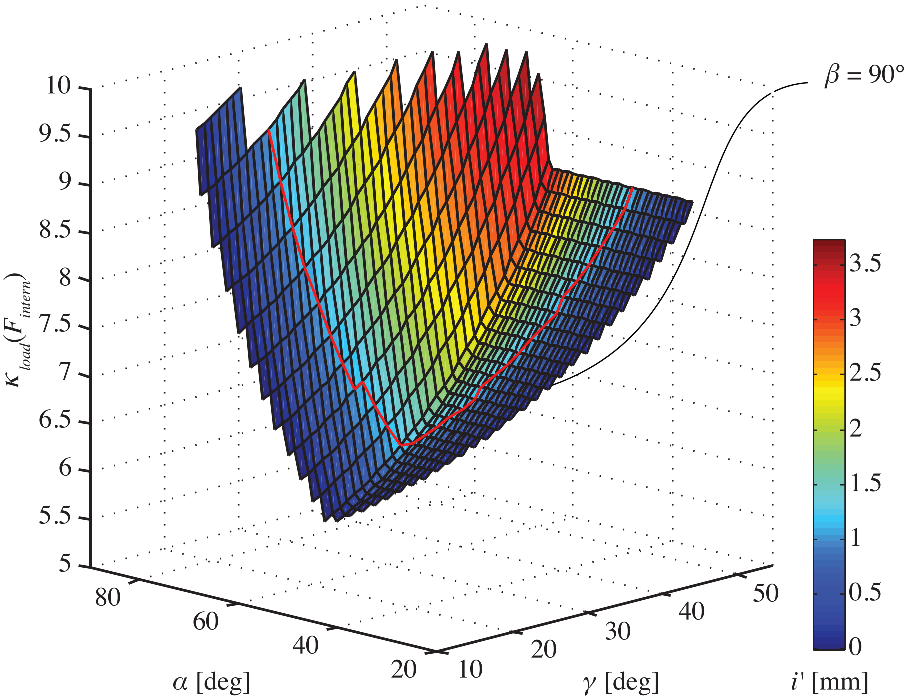

Figure 5.5: Condition number $\kappa_{load}(\mathbf{F_{intern}})$ for *load isotropy* (loadset $f_{xyz} = 10$ N, $m_{xy} = 150$ Nmm and $m_z = 100$ Nmm) dependent on α and γ for $\beta = 90°$, $R = 4.3$ mm and $L = 4.3$ mm in all cases. Colors denote the distance of upper joint pairs i' in mm. The red line shows $i' = 1.1$ mm.

Table 5.2: Link forces calculated with Sec. 5.7 and geometry $R = 4.3$ mm, $L = 4.3$ mm, $\alpha = 65°$, $\beta = 90°$, $\gamma = 36°$. The condition number of the link force matrix is $\kappa_{load}(\mathbf{F_{intern}}) = 6.17$.

f_n	$f_x = 10$ N	$f_y = 10$ N	$f_z = 10$ N	$m_x = 0.15$ Nm [N]	$m_y = 0.15$ Nm	$m_z = 0.1$ Nm
f_1	7.89	0	1.84	-15.86	0	11.34
f_2	-7.89	0	1.84	-15.86	0	-11.34
f_3	-3.94	6.83	1.84	7.93	-13.73	11.34
f_4	3.94	-6.83	1.84	7.93	-13.73	-11.34
f_5	-3.94	-6.83	1.84	7.93	13.73	11.34
f_6	3.94	6.83	1.84	7.93	13.73	-11.34

analysis, further refinement of the sensor structure is necessary. The following assumptions in particular need to be revisited:

- *Rigid Platforms*. The top and bottom platform are necessarily ring shaped to accommodate wrist and tip mechanics in the MIRS tool. These rings will deform under load. The deformation has to be minimized or compensated for.
- *Ideal spherical joints*. Top and bottom platform are connected to six links by ideal spherical joints. For a sensor of less than 10 mm diameter it is not possible to manufacture spherical joints that provide an absence of mechanical play or friction but sufficient load bearing capability. Ideal spherical joints will, therefore, be approximated by flexural joints. The conflicting goals of high load bearing capability and low bending resistance require a compromise in flexure design.
- *Ideally stiff links*. The analytical model assumes that links only transmit compressive or tensional loading in the direction of each link. However, flexural joints also transmit bending moments into the links.

In order to minimize the bending resistance of the flexural joints, and, therefore, the transmission of parasitic moments into the links, the cross sectional area of the flexural joints should be as small as possible. However, the flexural joints are also subject to the full load transmitted by the links, increased by notch stress in the flexure. Therefore, thinning down the cross section of the flexure to facilitate bending has to be limited. At the same time, the links should exhibit large resistance against bending. At the same time the links need to exhibit large deformations for longitudinal loading in order to provide measurable changes in longitudinal strain. Ideally, the cross section of the links would be tubular with thin walls (cross sectional area A_{lo}), narrowed down to a preferably thin cylindrical cross section (cross sectional area A_{jo}) at the flexural joints as shown in Fig. 5.6. An according link shape of the required size would have to be assembled from a number of individual components.

In order to keep parts and assembly to a minimum, a link shape is suggested that enables the complete sensor structure to be manufactured as monolithic component. At the same time the proposed link shape provides a good compromise for the requirements of load bearing capability of the flexure, and bending resistance of the link. The link cross section is a rectangular C-shape, open outwards so it can be manufactured by milling, and providing a

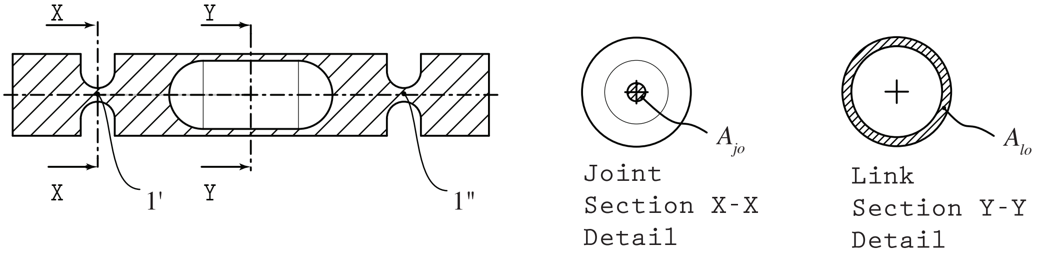

Figure 5.6: Cross sections of an ideal circular link geometry with flexural hinges. $1''$ and $1'$ denote analytical joint locations, A_{lo} and A_{jo} denote cross sectional areas of link and joint respectively. Unfortunately this structure cannot be machined in one piece.

flat bonding surface for strain gauges on the inwards side. A good trade-off for the C-shaped link is to have a cross sectional area A_{lc} similar to the cross sectional area of the flexural joint A_{jc}, making the best use of the strain carrying capacity of the link material. The first generation sensor prototype (see Sec. 5.1.3.1) was based on these rough assumptions only. The exact geometry of link and joint sections were established by repeated FEA.

Link deformation under a force acting along the projection from analytical joint locations $1''$ and $1'$ should be purely compressive or tensile. Bending deformation and buckling of the link sidewalls have to be minimized to avoid erroneous strain measurements. Therefore, the neutral axis of bending of the flexural joints and the neutral axis of the C-shaped links are required to be coincident with the line connecting the joint locations $1''$ and $1'$ of the analytical model. A suitable geometry satisfying these requirements is shown in Fig. 5.7. The distance of the neutral bending axes from the inside face is denoted by e_{jc} for the flexural joint and e_{lc} for the C-shaped link section, respectively. The positions of the neutral axes can be calculated using the centroid of compound shapes (see Eq. 5.9 for C-shape and Eq. 5.11 for compound shape consisting of rectangle and semicircle).

$$A_{lc} = ah + bd \tag{5.8}$$

$$e_{lc} = \frac{1}{2}\frac{ah^2 + bd^2}{A_{lc}} \tag{5.9}$$

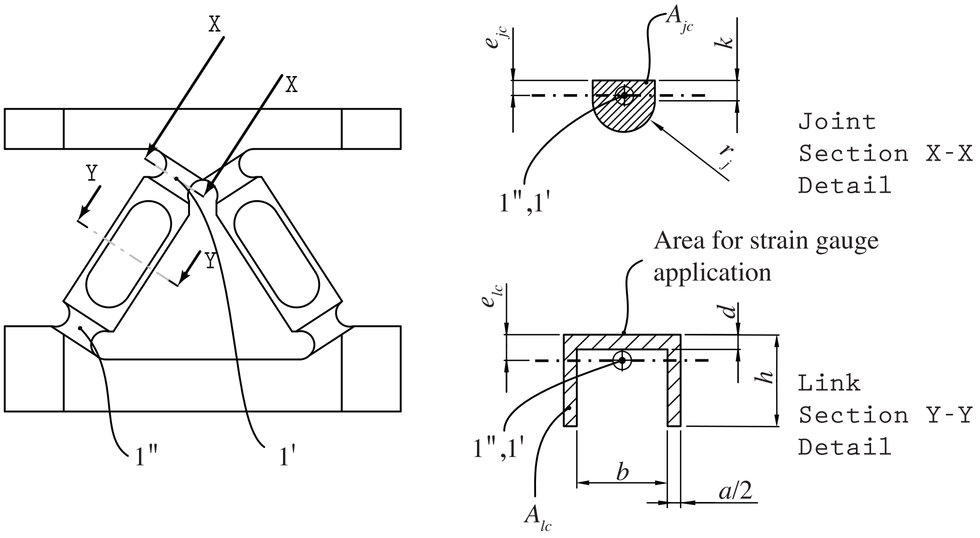

Figure 5.7: Actual link and joint geometry. $1''$ and $1'$ denote analytical joint locations. Cross sections of flexural joint (X-X) with area A_{jc} and transducer section (Y-Y) with area A_{lc}. Distance of the neutral bending axes from the inside surface is shown for the joint e_{jc}, described in Eq. 5.11 and C-shaped link section e_{lc}, described in Eq. 5.9.

$$A_{jc} = A_{rect} + A_{semic} = 2r_j k + \frac{1}{2} r_j^2 \pi \tag{5.10}$$

$$e_{cj} = \frac{\frac{k}{2} A_{rect} + (k + \frac{4r_j}{3\pi}) A_{semic}}{A_{rect} + A_{semic}} = \frac{k^2 r_j + \frac{1}{2} r_j^2 \pi (k + \frac{4r_j}{3\pi})}{A_{jc}} \tag{5.11}$$

Requiring coincidence of the neutral bending axes ($e_{jc} = e_{lc}$) and roughly similar cross sectional areas ($A_{jc} = c \cdot A_{lc}$) allows solving for k and r_j. The cross-section of the flexural joint should not be considerably smaller than the link to account for notch stress. However, to reduce the bending stiffness and therefore, the transmission of parasitic bending moments into the links causing cross talk, the proportional factor c was chosen to be $c = 0.75$.

The maximum link forces claculated in Tab. 5.2 can be used to determine the required cross sectional area of the link A_{lc}. At the Robotics and Mechatronics Center force sensor structures made from AlCuMg1.5 (F55) aluminum or 1.4542 (17-4PH) stainless steel are generally designed to exhibit a maximum of 1‰ strain under nominal load. In the following sections the measure microstrain (μe) will be used to denote strain values ($1000\ \mu\text{e} = 1000\frac{\mu\text{m}}{\text{m}} = 1\text{‰}$). This strain limit has been found to be a good compromise for avoiding the material's limit of elastic deformation and providing a large enough strain for foil backed strain gauges.

Table 5.3: Parameters for Stewart Platform joint and link geometry according to Fig. 5.7.

Stewart Platform Joint and Link Geometry	
First Prototype	$h = 0.97$ mm $b = 1.0$ mm $a = 0.3$ mm $d = 0.22$ mm $k = 0.34$ mm $r_j = 0.35$ mm $A_{jc} = 0.43\ \text{mm}^2$ $e_{jc} = 0.31$ mm $A_{lc} = 0.51\ \text{mm}^2$ $e_{lc} = 0.32$ mm
Final Prototype	$h = 0.9$ mm $b = 1.2$ mm $a = 0.2$ mm $d = 0.15$ mm $k = 0.31$ mm $r_j = 0.26$ mm $A_{jc} = 0.27\ \text{mm}^2$ $e_{jc} = 0.26$ mm $A_{lc} = 0.36\ \text{mm}^2$ $e_{lc} = 0.26$ mm

5.1.3.1 First Generation Sensor Prototype

The first generation sensor is designed as monolithic aluminum structure fabricated from AlCuMg1.5 (F55), based on the parameters shown in Tab. 5.1. A FEA was performed subjecting the structure to the principal load set of $f_{xyz} = 10$ N, $m_{xy} = 150\ \text{Nmm}$ and $m_z = 100\ \text{Nmm}$. Results for f_z (top) and m_y (bottom) are shown in Fig. 5.8. Maximum strain levels in $[\frac{\text{mm}}{\text{mm}}]$ (regardless of strain component) are shown using color fringes on the deformed structure. Deformation is scaled by a factor of 2000 in the case of f_z and 155 in the case of m_y. It can be seen that strains exceed the postulated limit of $1000\ \mu\text{e}$ in the flexural joints for an external load of $m_y = 150\ \text{Nmm}$. The onset of plastic deformation in the flexural joint and therefore, hysteresis has to be expected in this case.

The maximal principal strain depicted in the FEA results (Fig. 5.8) gives a quick overview of the overall strain level and highlights potential overload locations. In order to evaluate predicted sensor performance in more detail, however, the principal strain in transducer (link) direction at each future transducer location is required. These results can be obtained by creating separate link coordinate systems (CSY), placed at the center of each link on the inward surface, x-axis aligned with each link direction, z-axis normal to the surface. During post processing of the FEA analysis, the xx-strain (longitudinal strain, (ε_{xx})) at the origin of each of the link coordinate systems is evaluated and recorded for every load component. Based on the simulated strain values (presented in Tab. 5.4) the Jacobian of the sensor can be calculated and the condition number can be compared to the analytical prediction (see Tab. 5.2). It has to be noted that for the analytical design (Sec. 5.1.2, Tab. 5.2) the Jacobian relates internal link forces to external loads. In the FEA (Sec. 5.1.3, Tab. 5.4) the Jacobian relates internal principal strains to external loads. The condition number of the Jacobian is $\kappa_{Load}(\epsilon_{\mathbf{xx}}) = 6.03$.

Table 5.4: Link strains ε_{xx} $[\mu\mathrm{e}]$ for each link and six loadsets at the simulation CSY locations calculated by FEA for the first prototype. The condition number of the Jacobian is $\kappa_{Load}(\varepsilon_{\mathbf{xx}}) = 6.03$.

$\varepsilon_{xx,n}$	$f_x = 10$ N	$f_y = 10$ N	$f_z = 10$ N	$m_x = 0.15$ Nm $[\mu\mathrm{e}]$	$m_y = 0.15$ Nm	$m_z = 0.1$ Nm
$\varepsilon_{xx,1}$	205.9	46.8	71.1	-566.4	68.1	296.3
$\varepsilon_{xx,2}$	-205.8	44.7	70.2	-556.4	-66.2	-298.5
$\varepsilon_{xx,3}$	-137.8	151.8	69.4	213.0	-504.7	290.6
$\varepsilon_{xx,4}$	63.8	-200.7	70.5	336.8	-450.2	-300.9
$\varepsilon_{xx,5}$	-62.4	-195.0	68.5	327.7	437.3	287.2
$\varepsilon_{xx,6}$	141.2	154.6	70.3	218.0	511.5	-294.5

This first generation sensor prototype was machined from AlCuMg1.5 (F55) aluminum with an overall diameter of $9.4\ \mathrm{mm}$ and was instrumented with $350\ \Omega$ linear strain gauges, arranged in a Wheatstone quarter bridge configuration. Due to the monolithic sensor structure no assembly of the sensor itself was required. Parasitic effects, such as hysteresis of the links (caused by adhesive creep), nonlinearities (caused by internal stress due to mechanical tolerances and misalignment or welding) are absent. As a drawback, however, the C-shaped link structure is necessarily open towards the outside to facilitate machining. This destines the inside surfaces of the links for placement of strain transducers. While the basic sensor concept could be proven with this setup, bonding and contacting the strain gauges on the inside of the links proved difficult and unreliable.

The strain gauges used are BLH FAE-02W-35-S13E (350 Ω), creep adapted for aluminum, Vishay Precision Group [199] with the polyimide carrier matrix cut to fit the sensor links. For a description of the strain gauge bonding process, please refer to Sec. A.2. Only one active strain gauge and three precision resistors are used in a Wheatstone bridge arrangement. Small precision resistors with values between $1\ \Omega$ and $10\ \Omega$ are soldered into the ground

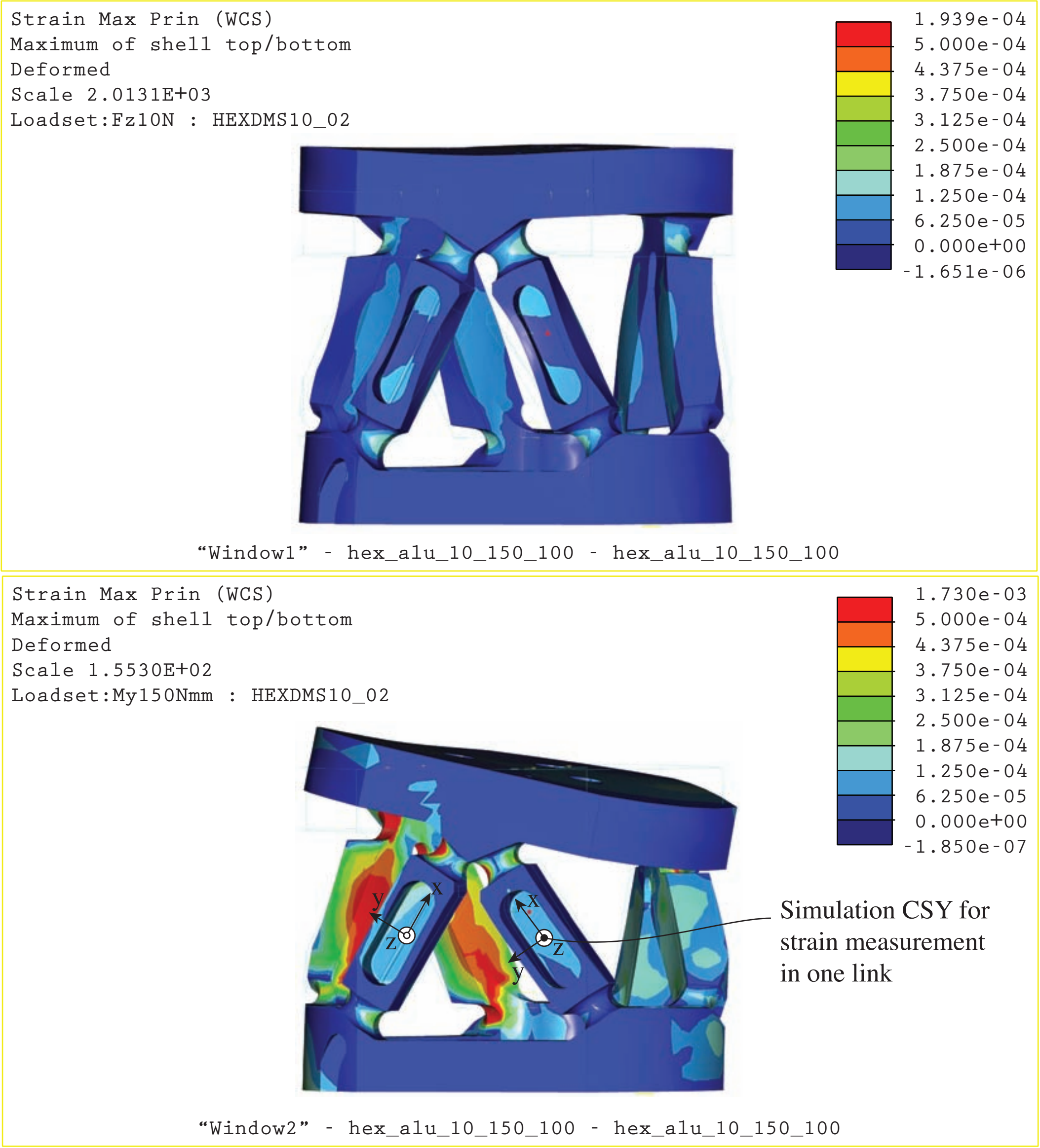

Strain Max Prin (WCS)
Maximum of shell top/bottom
Deformed
Scale 2.0131E+03
Loadset:Fz10N : HEXDMS10_02

“Window1” - hex_alu_10_150_100 - hex_alu_10_150_100

Strain Max Prin (WCS)
Maximum of shell top/bottom
Deformed
Scale 1.5530E+02
Loadset:My150Nmm : HEXDMS10_02

“Window2” - hex_alu_10_150_100 - hex_alu_10_150_100

Figure 5.8: Screenshot of ProMechanica FEA of monolithic aluminum sensor geometry with loading of $f_z = 10$ N (top) and $m_y = 150$ Nmm (bottom). Colors denote maximal principal strains in $[\frac{\mathrm{mm}}{\mathrm{mm}}]$, it can be seen that strains in the flexural joints exceed 1000 μe in the case of $m_y = 150$ Nmm. For measuring the principal strain in every link (ε_{xx}), simulation coordinate systems (CSY) are placed on every link.

Figure 5.9: Image of first generation monolithic sensor geometry fabricated by milling from Al-CuMg1.5 (F55) aluminum with a diameter of 9.4 mm.

path of the Wheatstone bridge to balance the bridge output (as shown in Fig. 5.10).

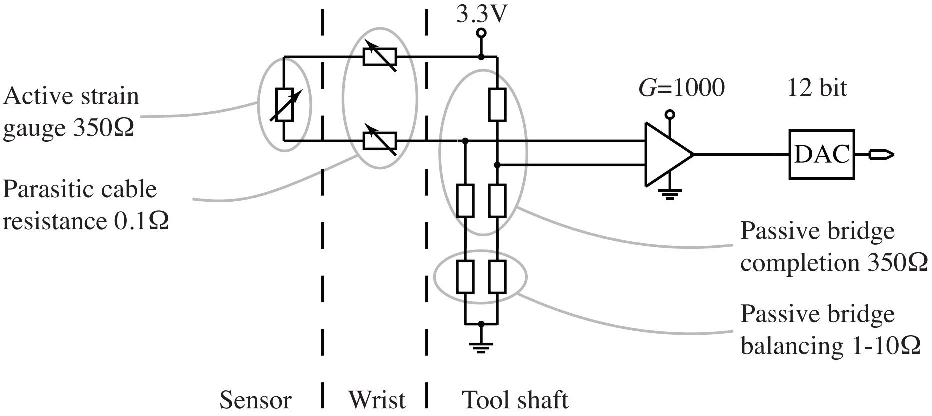

Figure 5.10: Simplified schematic of signal conditioning electronics used in first sensor prototype with Wheatstone quarter bridge configuration and 350 Ω strain gauges.

The signal conditioning electronics used with this sensor were developed at the Robotics and Mechatronics Center and modified versions are being used with various sensors. The circuitry is based on the Burr Brown INA337 precision instrumentation amplifier [200]. The simplified schematic is shown in Fig. 5.10. More details on sensor conditioning electronics in general can be found in Stefanescu [173], Fraden [176], Tietze and Schenk [201]. The output voltage to the Wheatstone bridge U_O can be calculated using Eq. 4.2:

$$U_O = U_B \cdot \frac{N}{4} \cdot K \cdot \epsilon \tag{5.12}$$

from the bridge excitation voltage $U_B = 3.3$ V. The bridge factor N equals 1 in the case of a quarter bridge configuration with one strain gauge aligned to the longitudinal strain (see Measurements Group [183]), the gauge factor of the strain gauge $K = 2.05$. A mechanical strain of $\varepsilon = \pm 600\ \mu\mathrm{e}$ (compare Tab. 5.4), will yield a bridge output voltage of $U_O = \pm 1\ \mathrm{mV}$. The noise level of the INA337 instrumentation amplifier, referenced to the output is given in the data sheet [200] as:

$$V_N = G \cdot 33 \frac{\mathrm{nV}}{\sqrt{\mathrm{Hz}}} \cdot \sqrt{f} + (800 \frac{\mathrm{nV}}{\sqrt{\mathrm{Hz}}} \cdot \sqrt{f}) \tag{5.13}$$

With a sampling frequency $f = 1$ kHz and the amplification $G = 1000$ the output side amplifier noise is $1069\ \mathrm{mV}$. To this should be added the thermal noise of the strain gauge resistor which is given by Tietze and Schenk [201] as:

$$V_R = \sqrt{4 \cdot k \cdot T_0 \cdot B \cdot R} \tag{5.14}$$

with the Boltzmann constant $k = 1.38 \cdot 10^{-23} \frac{\mathrm{J}}{\mathrm{K}}$, the absolute temperature T_0, the signal bandwidth B and the resistance R. However, for the small strain gauge resistance used in this sensor, the thermal noise is lower than the amplifier noise by a factor of 25 and will, therefore, be neglected.

The bridge output voltage multiplied by the amplifier gain of $G = 1000$ yields an output signal of ± 1 V with a noise level of $1.069\ \mathrm{mV}$. The output voltage of the INA337 is sampled by a 12-bit analog to digital converter (ADC), which for a supply voltage of 3.3 V translates to an increment of roughly 0.8 mV. Fig. 5.11 (b) shows that the measured noise level is far greater than the expected $\frac{1.069\ \mathrm{mV}}{0.8\ \mathrm{mV}} = 1.3$ increments. Noise in the power supply and inadequate shielding were suspected as additional noise sources.

Fig. 5.11 (a) shows thermal drift of the sensor output signal. Thermal drift is caused by a combination of factors. The strain gauge acts as resistive heater driven by the bridge excitation voltage. Not only will the resistivity of the strain gauge change with temperature, thermal expansion will also cause an apparent strain in the sensor structure. The individual

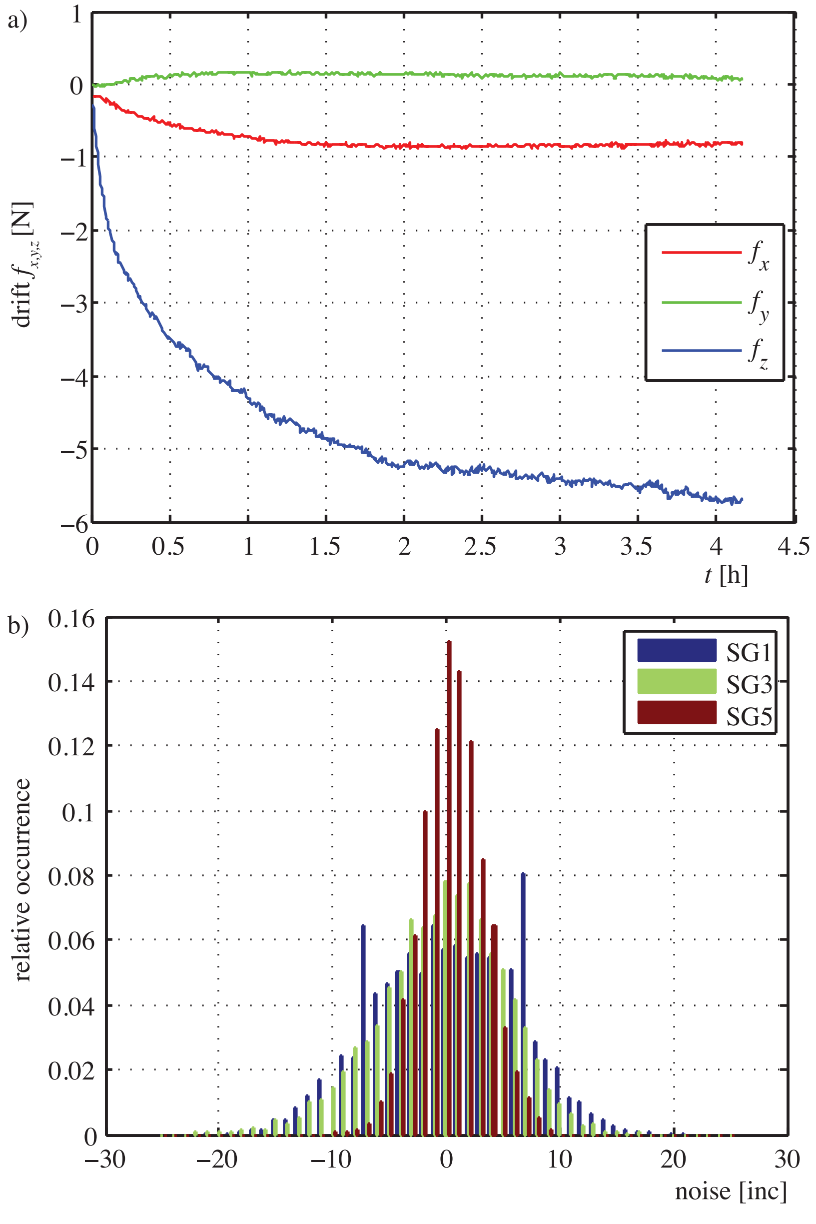

Figure 5.11: Measurements of output drift and noise of first generation sensor with Wheatstone quarter bridge configuration and 350 Ω strain gauges. The strain gauges act as resistive heating elements causing thermally induced strain. All six links are affected equally, the effect causes apparent loading in f_z (a). Noise is shown for three of the six strain gauges and shows a nearly normal distribution (b). Noise level is far larger than the 1.3 increments caused by amplifier noise.

resistors in the bridge completion network exhibit a change of resistivity different from the strain gauge, adding to thermal drift. It can be expected that these factors are roughly similar for every strain gauge and amplifier portion. The thermal drift will, therefore, cause an apparent loading in the f_z force component of the sensor output. The output of the sensor has not reached an equilibrium state even after four hours.

This sensor was used in a scalpel tool for the phantom dissection experiments reported by Deml et al. [202]. The physical sensor and signal conditioning electronics are shown in Fig. 5.17, image (a). While it was possible to show the validity of a small 6 DoF sensor concept based on a Stewart Platform with this sensor design, the actual sensor performance is not adequate.

A number of further prototypes were built to address the identified shortcomings:

- Large thermal drift.
- Large signal noise.
- Difficult mounting of strain gauges to the inside of the sensor structure.
- Large deformation of lower and upper platform of the sensor structure.

5.1.3.2 Final Sensor Prototype

Aside from thermal drift and noise problems, it was found that the soft aluminum structure of the first generation prototype is easily damaged in the area of the C-shaped link section due to its thin wall thickness. Furthermore, the top and bottom platforms undergo large unwanted deformations due to the low modulus of elasticity of aluminum, leading to measurement errors. Therefore, 1.4542 (17-4PH) stainless steel in annealing condition 1070 (minimum tensile strength 1070 $^{\mathrm{N}}/_{\mathrm{mm}^2}$) was used for all subsequent sensor structures due to its low creep tendency and high tensile strength. To facilitate bonding and connection of strain gauges, the link structure was turned inside-out with strain gauge application areas facing outwards and C-shaped sections opening inwards. Fabrication of the entire sensor structure as monolithic component is no longer possible, so the sensor structure is assembled from three triangular link pairs and an upper and lower platform component. Geometry parameters and loads are identical to Tab. 5.1. The final, currently used sensor geometry, integrated with upper and lower platforms is shown in Fig. 5.12 and Fig. 5.13.

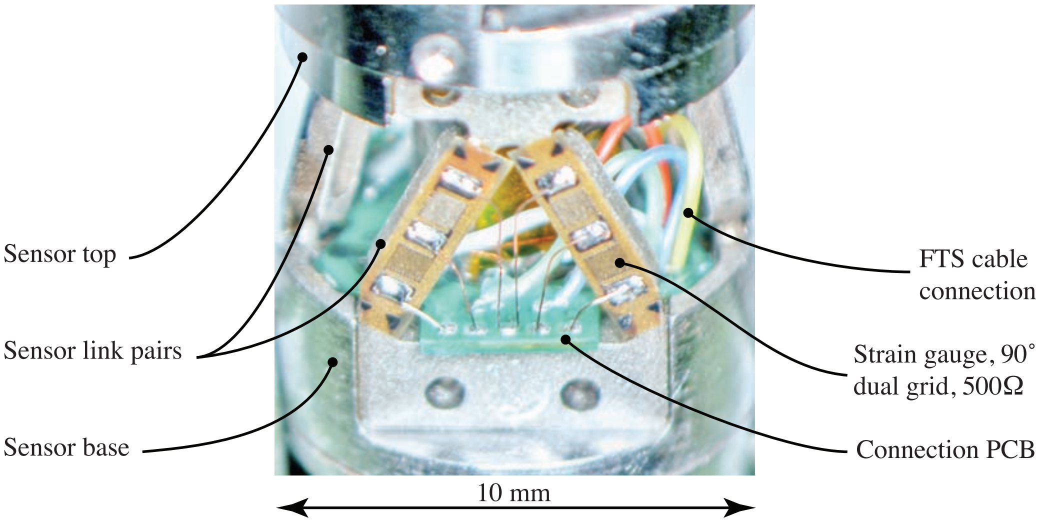

Figure 5.12: Closeup of final sensor prototype during fabrication without cover. Two of six links instrumented with dual element strain gauges can be seen in the foreground. Strain gauges are wired to a connection PCB attached to the lower platform.

A FEA identical to the first prototype was performed subjecting the structure to the principal load set of $f_{xyz} = 10$ N, $m_{xy} = 150$ Nmm and $m_z = 100$ Nmm. Results for f_z (top) and m_y (bottom) are shown in Fig. 5.13. Maximum strain levels in $[\frac{\mathrm{mm}}{\mathrm{mm}}]$ (regardless of strain component) are shown using color fringes on the deformed structure (color scaling is identical to the first prototype). Deformation is scaled by a factor of 1600 in the case of f_z and 66 in the case of m_y. It can be seen that strains exceed the postulated limit of $1000\ \mu\mathrm{e}$ in the flexural joints for an external load of $m_y = 150\ \mathrm{Nmm}$. The onset of plastic deformation in the flexural joint and therefore, hysteresis has to be expected in this case also.

Again the FEA results include measures of the longitudinal strain (ε_{xx}) at the center of each link simulation CYS. Tab. 5.5 shows that strain levels are lower by a factor of 2 for the steel sensor compared to aluminum, although thinner walls were used in the links (0.1 mm for sidewalls and 0.15 mm for strain gauge application surface as compared to 0.15 mm and 0.22 mm respectively in the aluminum monolithic structure). A further reduction in thickness would lead to buckling of the walls during machining. All sensor structural components are bonded using EPO-TEK® (Epoxy Technology) 353ND [203]. The sensor assembly forms the entire distal section of the MIRS tool as the distal section of the tool wrist and end effector carrier are integrated with the top and bottom platforms of the sensor.

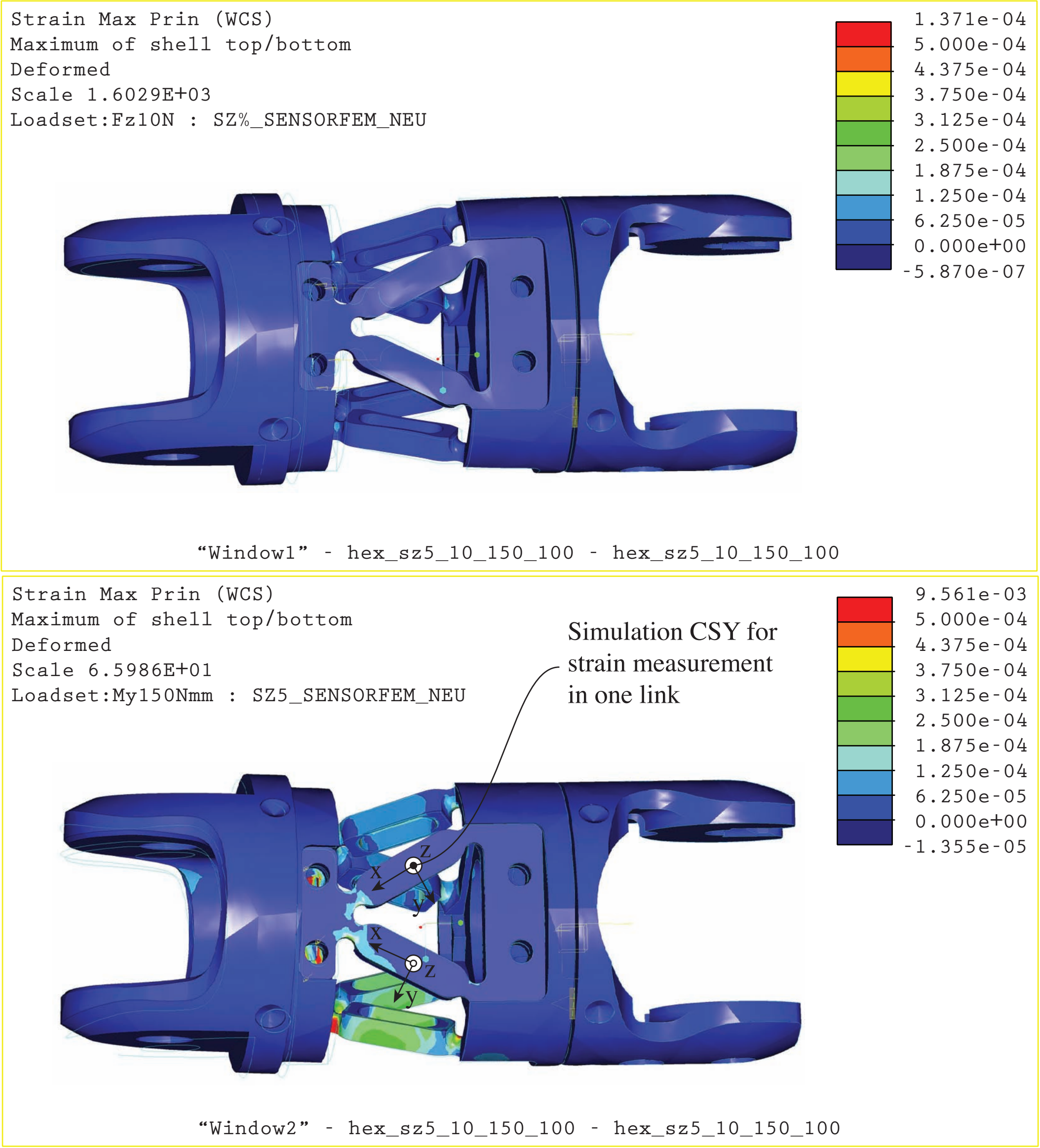

Strain Max Prin (WCS)
Maximum of shell top/bottom
Deformed
Scale 1.6029E+03
Loadset:Fz10N : SZ%_SENSORFEM_NEU

“Window1” - hex_sz5_10_150_100 - hex_sz5_10_150_100

Strain Max Prin (WCS)
Maximum of shell top/bottom
Deformed
Scale 6.5986E+01
Loadset:My150Nmm : SZ5_SENSORFEM_NEU

Simulation CSY for strain measurement in one link

“Window2” - hex_sz5_10_150_100 - hex_sz5_10_150_100

Figure 5.13: Screenshot of ProMechanica FEA of bonded steel sensor with loading of $f_z = 10$ N (top) and $m_y = 150$ Nmm (bottom). Colors denote maximal principal strains in $[\frac{\mathrm{mm}}{\mathrm{mm}}]$, it can be seen that strains in the flexural joints exceed $1000\ \mu e$ in the case of $m_y = 150$ Nmm. For measuring the principal strain in every link (ε_{xx}), simulation coordinate systems (CSY) are placed on every link. The maximum strain value of 1% for m_y is caused by a meshing artifact on a sharp edge.

Based on the simulated longitudinal strain values (see Tab. 5.5) the Jacobian of the sensor is calculated and the condition number is compared to the analytical prediction (see Tab. 5.2). Similar to the previous FEA analysis, the Jacobian relates internal principal strains to external loads. The condition number of the Jacobian is $\kappa_{Load}(\epsilon_{\mathbf{xx}}) = 5.62$.

Table 5.5: Link strains ε_{xx} [μe] for each link and six loadsets at the simulation CSY locations calculated by FEA for the final prototype. The condition number of the Jacobian is $\kappa_{Load}(\epsilon_{\mathbf{xx}}) = 5.62$.

$\varepsilon_{xx,n}$	$f_x = 10$ N	$f_y = 10$ N	$f_z = 10$ N	$m_x = 0.15$ Nm [μe]	$m_y = 0.15$ Nm	$m_z = 0.1$ Nm
$\varepsilon_{xx,1}$	105.2	10.5	31.2	-297.4	23.8	178.0
$\varepsilon_{xx,2}$	-104.6	10.1	31.3	-297.2	-25.2	-177.8
$\varepsilon_{xx,3}$	-62.7	86.5	31.3	128.6	-271.7	179.9
$\varepsilon_{xx,4}$	42.6	-93.3	30.4	166.6	-239.8	-175.1
$\varepsilon_{xx,5}$	-42.1	-92.9	30.2	165.0	239.3	173.0
$\varepsilon_{xx,6}$	55.8	77.5	28.2	115.3	247.3	-163.0

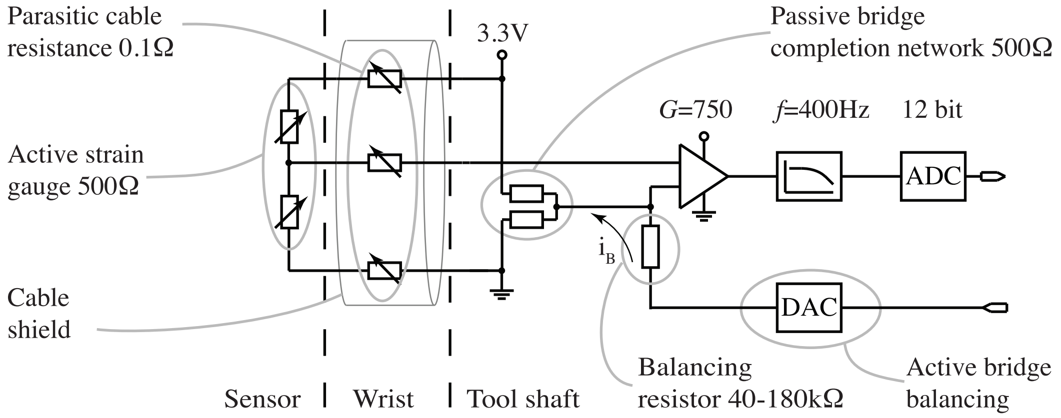

Figure 5.14: Simplified schematic of signal conditioning electronics used in final sensor prototype with Wheatstone half bridge configuration and 500 Ω strain gauges.

The sensor signal conditioning electronics used for the final prototype was also developed by the Robotics and Mechatronics Center. It is again based on the INA337 precision instrumentation amplifier [200], using the simplified schematic shown in Fig. 5.14. The following changes over the original sensor and signal conditioning electronics have been made:

- *Connection and strain relief printed circuit board (PCB).* Connections between sensor and signal conditioning electronics run through the wrist joint. In order to provide shielding against environmental influences and noise, a six core, 38 AWG (American Wire Gauge), Teflon® insulated, shielded cable (Vishay, STC-38T-6) [204] is used. Despite a cable diameter of only 1.3 mm, the cable is comparatively stiff. Therefore, the cable connections have to be protected from mechanical stress induced by articulating the wrist joint. A connection PCB (visible in Fig. 5.12) is used as mechanically fixed termination point between cable and strain gauges. Strain gauge connections to the PCB are made with $50\ \mu m$ copper filaments.

- *Custom fabricated dual strain gauge.* Initially two individual single element strain gauges were bonded to each link, one linear grid, one transverse grid. These were identical to the strain gauges used in the first prototype, except being matched to the thermal expansion of steel (BLH FAE-02W-35-S06E, 350 Ω, creep compensation for steel). The Wheatstone half bridge arrangement resulted in a gain in output signal and the benefit of temperature compensation compared to the quarter bridge used in the first prototype. But it was found that measurement errors due to misalignment of the two individual strain gauge elements and plastic deformation of solder joints negated the advantages of the half bridge. Therefore, custom dual element gauges with higher electrical resistance and an overall size of 3.5 mm by 1.2 mm were commissioned from Vishay. These contain one linear and one transverse grid with a resistance of 500 Ω each on a single matrix (see Fig. 5.12). The grids are matched in resistance and creep compensation, providing a far smaller thermal drift, while the higher resistance reduces the resistive self-heating effect.

- *Wheatstone half bridge arrangement.* The cable connecting the sensor to the signal conditioning electronics is subjected to movement when the tool wrist is articulated. The cable itself will act as variable resistance in this configuration. The half bridge arrangement ensures that the trace leading from the midpoint of the strain gauge matrix to the high impedance input of the instrumentation amplifier will not carry any current. Therefore, any change in trace resistance should not affect the sensor signal. Bridge excitation and ground path carry current but are subjected to identical movement, so the variable resistance in these traces will have a symmetric effect, largely cancelling itself and not affecting the midpoint voltage.

- *Thermally matched bridge completion network.* The individual bridge completion resistors of earlier prototypes are replaced by a thermally matched dual resistor network. Again, changes in temperature will have a much smaller effect on the midpoint voltage and therefore, reduce thermal drift.

- *Reduced signal amplification.* While signal amplitude is increased by higher gain, noise is increased as well (as can be seen from Eq. 5.13). The amplifier output voltage is sampled by an ADC. Ideally the noise level should remain below the least significant bit (LSB) level of the ADC.

- *Active bridge balancing.* While placing individual resistors in the ground path of the Wheatstone bridge to balance the bridge output is a commonly used approach, it requires an additional measurement and assembly step. Furthermore, should the sensor be slightly deformed by a drop or crash during use it might still be structurally usable, but is now electrically unbalanced. Using active bridge balancing circuitry, bridge balance can now be adjusted through software commands. A digital to analog converter (DAC) provides a variable voltage, which, by using a balancing resistor of $40\ \mathrm{k}\Omega - 180\ \mathrm{k}\Omega$ injects a small current i_B (compare Fig. 5.14) into one of the bridge branches. Assuming bridge resistors of $500\ \Omega$, the branch midpoint voltage can be adjusted by about $\pm 4.5\ \mathrm{mV}$ with a balancing resistor of $180\ \mathrm{k}\Omega$ up to $\pm 20\ \mathrm{mV}$ with a balancing resistor of $40\ \mathrm{k}\Omega$.

- *A 400 Hz low pass filter* was added at the amplifier output to reduce signal noise.

- *Supply line filters* were added to reduce supply line noise and a multi-level PCB design allows strain gauge signals to be shielded between top and bottom ground layers.

The $500\ \Omega$ custom dual strain gauges are used in a half bridge with one linear and one transverse gauge (yielding a bridge factor of $N = 1.3$). The amplifier is set to a gain of $G = 750$ and is followed by a 400 Hz low pass filter. The maximum expected strain value of 300 $\mu\mathrm{e}$ (compare Tab. 5.5) allows an updated calculation of bridge output voltage using Eq. 5.12 and noise level using Eq. 5.13.

The final sensor prototype provides a maximum output voltage swing of $\pm 495\ \mathrm{mV}$ and a noise level of 554 μV is expected. These values are roughly half of the output voltage swing and noise level of the first aluminum prototype sensor. Reasons for the lower output voltage is the reduction in amplifier gain from $G = 1000$ to $G = 750$ and the stiffer sensor structure fabricated from steel rather than aluminum. Based on the amplifier gain and strain gauge properties, the incremental resolution of the sensor was determined as $f_{inc}(x, y) = 0.07$ N, $f_{inc}(z) = 0.16$ N, $m_{inc}(x, y) = 0.4$ Nmm, and $m_{inc}(z) = 0.28$ Nmm.

The lower noise level is caused in part by the reduced amplifier gain and in part by the addition of the 400 Hz low pass filter. The output voltage of the INA337 is sampled again by a 12-bit ADC, translating to an increment size of roughly 0.8 mV. Fig. 5.15 (b) shows that the measured noise level is greater than the estimated $\frac{554\ \mu\mathrm{V}}{0.8\ \mathrm{mV}} = 0.7$ increments, however, it is drastically reduced over previous prototypes. Thermally induced drift is reduced both in magnitude and in duration during warm up (Fig. 5.15 (a)), reaching thermal equilibrium after only 600 seconds.

5.1.4 Stress Relief

One of the assumptions of the Stewart Platform (compare Sec. 5.1) states that the top and bottom platform of the force-torque sensor are completely rigid and will not deform under load. This assumption is violated in the current sensor structure due to size constraints.

The output side of the tool wrist, the distal wrist component, which includes joint bearing, actuation cable termination, and lower sensor platform are formed by a single mechanical component. The link sections are directly bonded to this distal wrist component, forming the force-torque sensor (see Fig. 5.16). Cable forces and friction in the tool wrist lead to deformations in the distal wrist component that affect force torque measurements. The deformations propagate through the flexural joints into the links of the sensor. Fig. 5.16 (top) shows maximal principal strains caused by a simulated cable force of $f_c = 50$ N acting at the actuation cable attachment point. Deformations are magnified by a factor of 700. The joint bearing surface to the left of the cable attachment is subjected to a fixed boundary condition for this FEA, preventing the distal wrist component from rotating around the pin joint. The structure to the right of the cable attachment point can move freely in space and should not be subjected to any strain.

However, due to the deformation of the distal wrist component, a strain of up to $\varepsilon = 6\ \mu\mathrm{e}$ is induced in one of the links. By comparison, a manipulation force of $f_y = 1$ N (acting upwards in Fig. 5.16) would cause approximately similar strain levels. This cross-coupling between actuation force and manipulation load measurement should clearly be avoided.

One possible solution has been introduced in the final sensor prototype. A circular, 0.3 mm

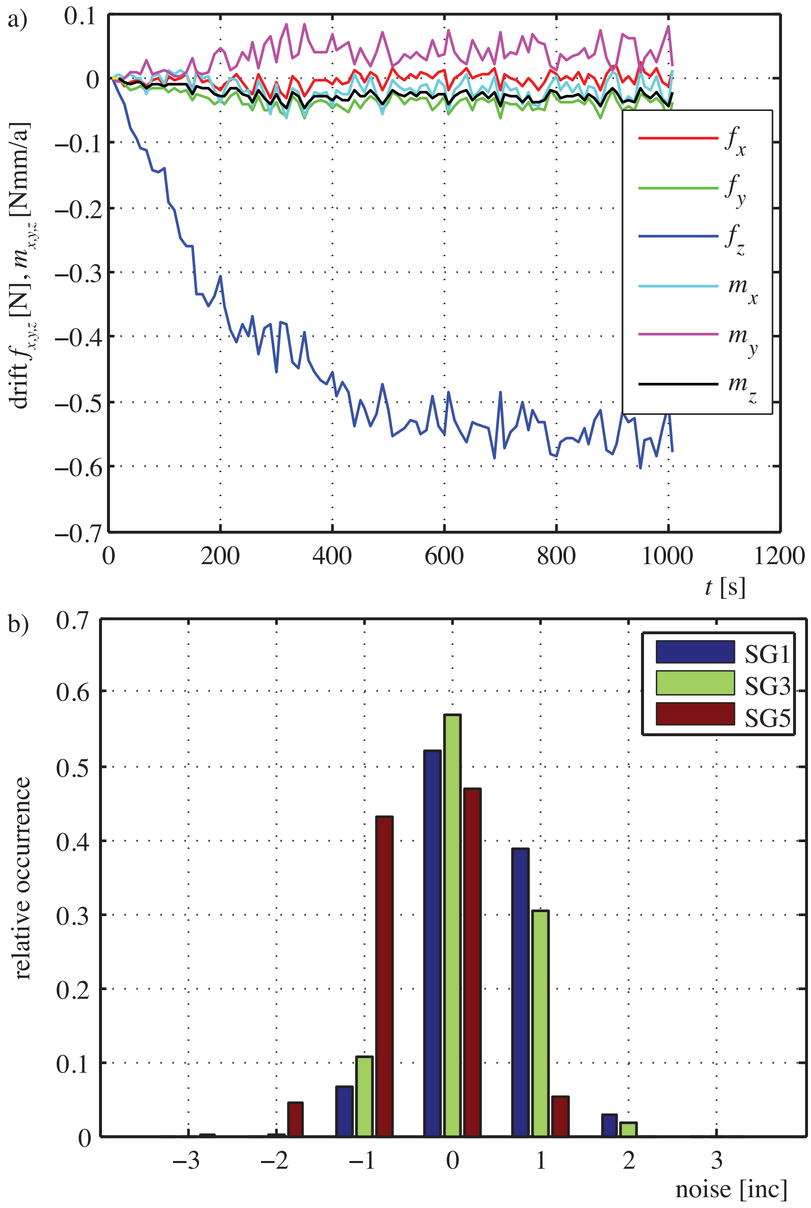

Figure 5.15: Measurements of thermal drift (a) and noise (b) of the last generation sensor with Wheatstone half bridge configuration and 500 Ω strain gauges. Thermally induced strain is drastically reduced compared to the first generation prototype (compare Fig. 5.11). Thermal equilibrium is reached after roughly 600 seconds. Noise is shown for three of the six strain gauges and shows a nearly normal distribution. Noise level is only slightly larger than the 0.7 increments caused by amplifier noise.

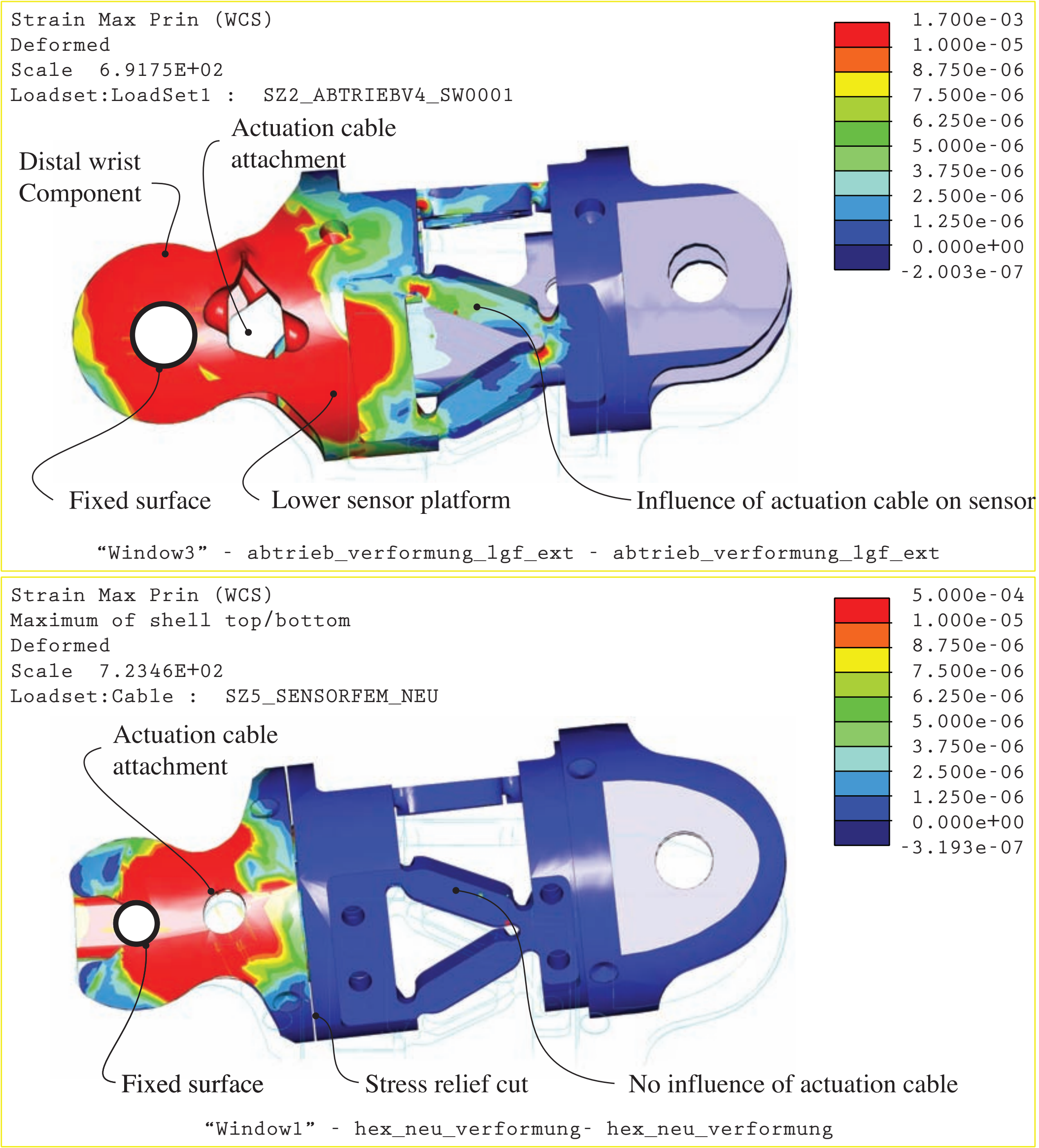

Figure 5.16: FEA of the influence of a cable actuation force of $f_c = 50$ N on the sensor structure. The top image denotes strain propagation from the tool wrist into the sensor links causing roughly 1 N measurement errors. The bottom image shows strain isolation by relief cut. Colors denote maximal principal strains in $[\frac{\text{mm}}{\text{mm}}]$.

wide stress relief cut (shown in Fig. 5.16 (bottom)) is fabricated by electrical wire discharge machining (EWDM) down to a diameter of $5\ \mathrm{mm}$. This cut diverts the force flow from the cable attachment towards the center of the component and increases the path length to the force-torque sensor links. Fig. 5.16 (bottom) shows that this cut effectively isolates the links from most tool wrist deformations, reducing the induced strain to near $0\ \mu\mathrm{e}$. While the stress relief cut slightly reduces stiffness of the sensor assembly, no hysteresis is introduced, and measurement errors are reduced by a large margin. To avoid contaminants gathering in this gap, the cut is later sealed with biocompatible elastomer.

This last section perfectly illustrates why a force feedback tool for MIRS cannot be built from off-the-shelf components. Due to size constraints wrist, force-torque sensor, and end effector need to be closely integrated and their seemingly separate functions will invariably interfere. While avoiding this interaction is impossible, parallel design of all components can help to limit unwanted interaction.

5.2 Tool Wrist

The previous section described the development of a force-torque sensor for placement between wrist and functional tip. That location was determined in Sec. 4.3.1 in order to balance the quality of manipulation load measurements with design constraints. Based on the sensor location, a tool with coinciding axes for θ_9 and θ_{10}, similar to the EndoWrist® seems not possible as two sets of actuation cables would have to be routed through the force-torque sensor, rather than just the end effector actuation.

During surgery the allowable length of the tool assembly distal to the wrist axis (the distal portion) is restricted by the distance between insertion point and operation site and also by manipulability considerations. For abdominal procedures the distance can be increased through a pneumoperitoneum[1]. However, due to the rigidity of the ribcage, the distance between the patient's ribs and the operation site can not be increased during procedures on the heart. The wrist and gripper mechanics should, therefore, be kept as short as possible.

Furthermore, a simulation during early stages of the tool development, on the optimal link lengths for a surgical robot carried out by Konietschke et al. [146] indicated that the distance l_d between axes A_9 and A_{10} (compare Fig. 4.4) should be kept as short as possible. No

---

[1] insufflating the abdomen with inert gas to expand the workroom

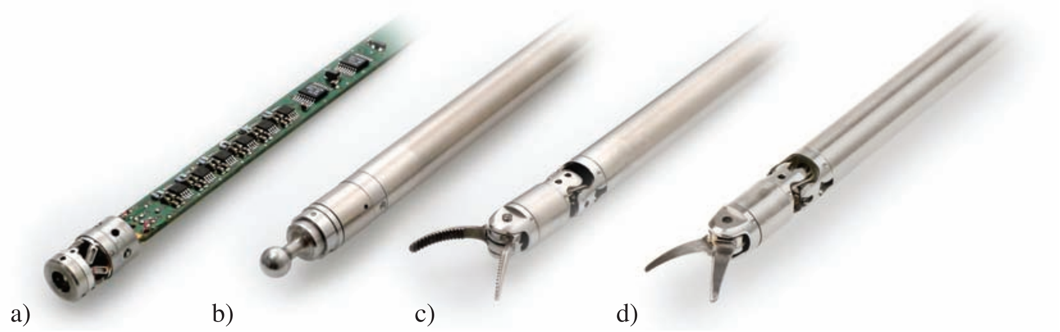

Figure 5.17: Three generations of tools. First generation monolithic aluminum sensor and electronics for scalpel (a), 6 DoF palpation tool (b), and latest generation MIRS tool including 2 DoF wrist and 7 DoF force sensing (Maryland grasper (c) and Metzenbaum scissors (d)).

clear indication on the required joint range of motion (RoM) was included in the simulation results.

In 2011 Zacharias [149] established a reachability measure for planning robotic manipulation tasks. For this evaluation the entire reachable workspace is filled with small virtual spheres. A reachability index of 100 would indicate that any point on any sphere surface can be reached with any tool orientation. Fig. 5.18 (a) shows the reachability index distribution for the current tool geometry. Colors denote the reachability index. Red spheres (index equals zero) cannot be reached at all (directly around the trocar point) and reachability increases with distance from the point of insertion to a maximum index of 22 (dark blue spheres), with an average over the entire workspace of 15.75.

Fig. 5.18 (b,c) indicate the change in the reachability index averaged over the entire workspace with different wrist RoM (b) and distal length (c). It can be seen from these new simulation results that the length of the distal portion has only a minor influence when averaged over the entire workspace, whereas an increase in wrist RoM will drastically improve reachability. As these new simulation results have only become available after the conclusion of the tool development described in this thesis, they have not yet been incorporated in the present wrist design, but clearly point to the direction of future research.

It is expected, however, that while the length of the distal portion does not show a large influence on the reachability index averaged over the entire workspace, the unreachable volume around the point of insertion will grow proportionally. In confined workspaces this unreachable volume will occupy a larger portion of the entire workspace. Also, an increase in the length of the distal portion will increase the required *MIRO* elbow joint movements and dynamics during manipulation.

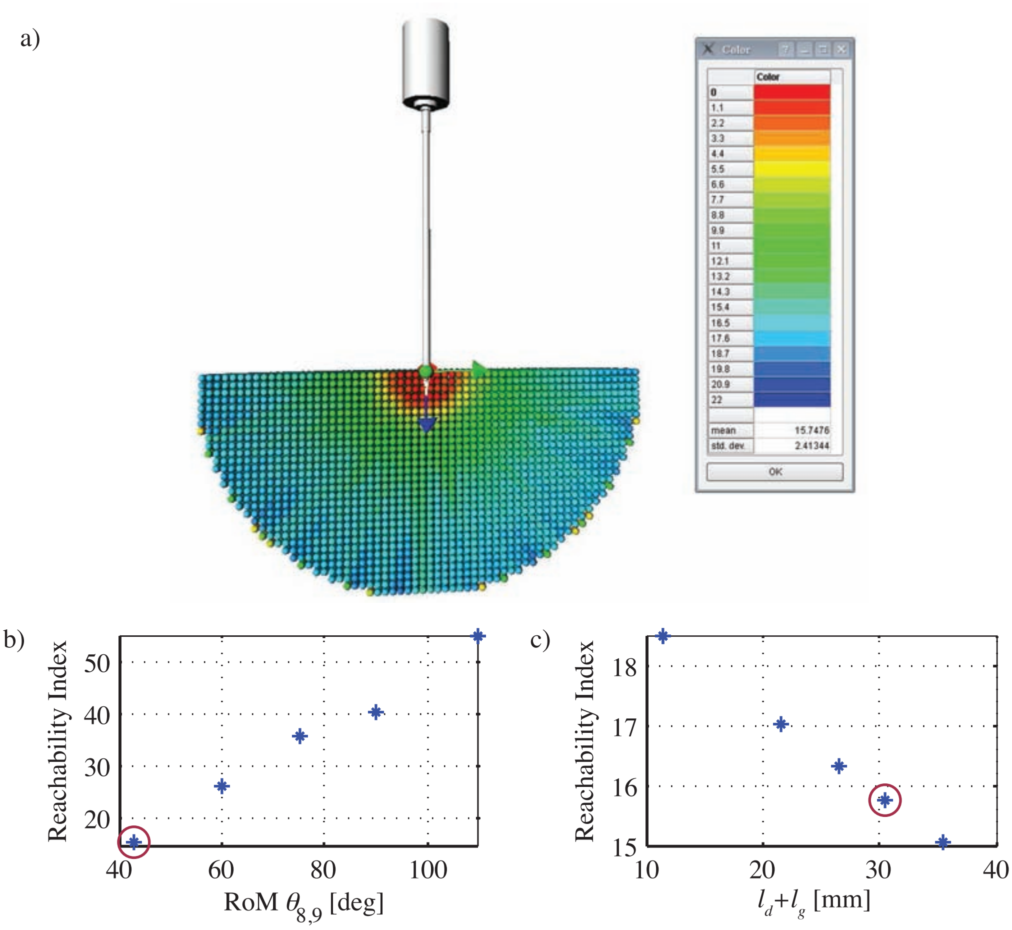

Figure 5.18: Simulation of reachability percentage (a) for current wrist kinematics (wrist $\mathrm{RoM} = 43\,\mathrm{deg}$ and distal portion length $l_d + l_g = 30.5\mathrm{mm}$, compare Fig. 4.4) and change with wrist RoM (b) and length of distal portion (c).

As described in Sec. 4.2 the single stage universal joint wrist (Fig. 4.7 (g)) was chosen despite its workspace limitation for being compact and rugged. It is also preferred for having intersecting axes. Intersecting wrist axes allow for rotating the end effector about its longitudinal axis without the need for pivoting the instrument shaft about the point of insertion (similar to the drive shaft movement in a front-wheel driven car). The unrestricted rotation of the end effector could equally be accomplished by a roll-pitch-roll kinematic, however, there the rotating distal portion would complicate the integration of force-torque sensor cable connections into the tool wrist.

Universal joints have a limited spherical workspace. Exceeding that workspace is possible along the two principal directions θ_8 and θ_9, however, in the intermediary directions ($\theta_8 = \theta_9$) the proximal and distal joint portions will start to interfere. In order to avoid a lock-up of the wrist, the range of motion was restricted to about ±43° for both θ_8 and θ_9 resulting in a rectangular workspace (as shown in Fig. 5.20 (c) for ($\theta_8 = \theta_9 = \pm 40°$)) ensuring that all points in the workspace can be reached by straight line movements.

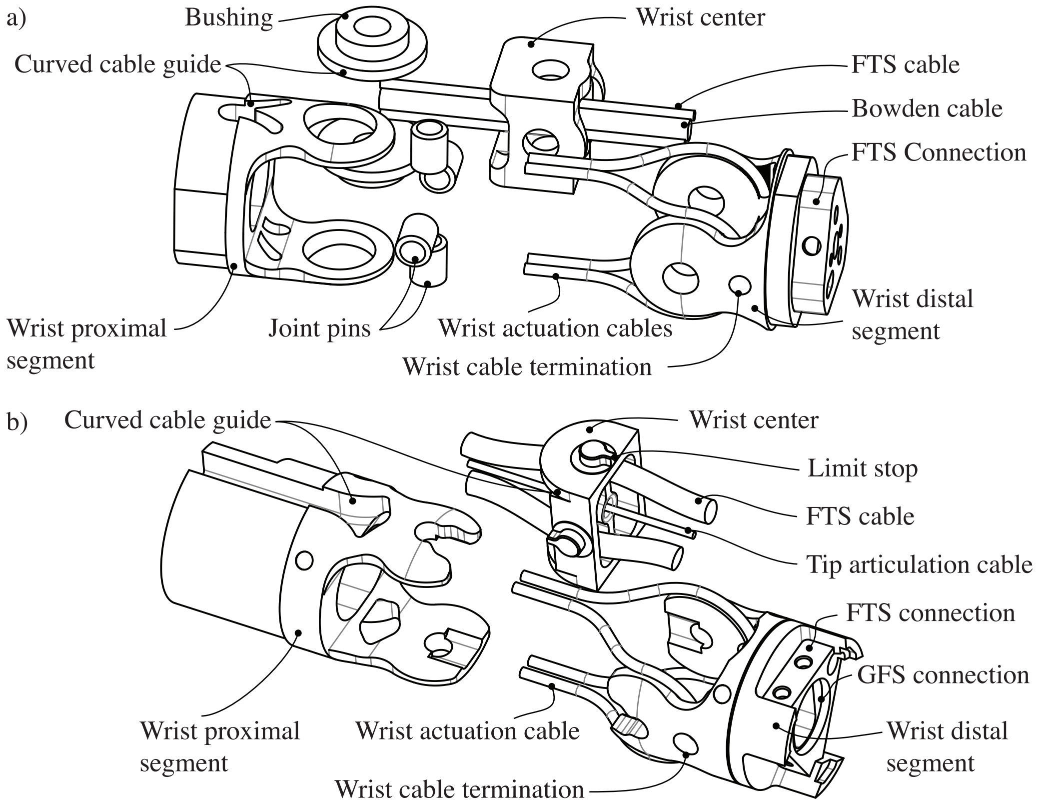

Figure 5.19: Two generations of wrist designs. Both have identical RoM of ±43° and cable actuation. The first generation (a) consists of more parts and tip actuation is transmitted by bowden cable. The latest generation (b) consists of only three parts and the tip actuation cable is guided in a nozzle.

All generations of tool wrist designs share the basic design and cable actuation. Also, all designs share the three part layout of proximal, center, and distal segment. All wrist components as well as the actuation cables are made from surgical stainless steel. The first generation (see Fig. 5.19 (a)) contained individual joint pins, creating the danger of components coming loose and getting lost. A further breakdown of the wrist proximal segment into three separate parts was evaluated in an intermediary design. The three part proximal section allowed a prefabricated sensor and electronics assembly to be integrated with the wrist instead of threading cables through the proximal wrist segment during wrist assembly and establishing electrical connections last. However, the larger part count made assembly of wrist itself much more complicated, so that design was abandoned. In the latest design the joint pins are integrated with the wrist center. The three wrist components (proximal, center and distal) fit together by snap fit and are secured by the cable tension. Also integrated into the wrist center are mechanical limit stops that physically restrict the wrist RoM to $\pm 43^\circ$ and so safeguard the FTS connection cables against mechanical damage.

The FTS electrical connection consists of Teflon® insulated, shielded cable (Vishay, STC-38T-6). Compared to individual single strand enamel insulated copper leads, the Teflon® cable provides better signal quality due to shielding and allows for a higher number of wrist movement cycles before cable damage occurs due to embrittlement. Still, the Teflon® cables show some disadvantages. While Teflon® is autoclavable, and especially Teflon® (PFA)[2] shows excellent performance for all sterilization processes according to Massey [205], due to the difficulties of bonding Teflon®, it is almost impossible to seal the cable termination inside the FTS against environmental influences. Furthermore,due to the relative softness of the Teflon®, after repeated use the insulation of individual cable strands will be penetrated by the shielding braid causing a short between shield and signal. Custom manufactured cables overcoming these restrictions are available, however, at prohibitively high cost for an experimental evaluation. These cables use an outer jacket made from steam sterilizable thermoplastic elastomer (e.g. flexible PVC) and additional Teflon® tape separating inner signal strands and shield (e.g. adapted from 10 x AWG36 TPU by Industrifil [206] with modified jacket).

All wrist components contain curved (circular) surfaces acting as guide pulleys for the actuation cables (see Fig. 5.19). There is no relative movement between the actuation cables and the wrist distal segment, on the proximal and center component, the actuation cables slide across the curved guides. The circular guide surfaces ensure that the instantaneous

---

[2] perfluoroalkoxy copolymer

pulley diameter is constant over the entire workspace. Therefore, the transmission ratio is also constant and wrist motion is directly proportional to the cable movement over the entire workspace, greatly simplifying wrist motion control.

The actuating cables consist of two separate cable loops (red and blue in Fig. 5.20 (a)). The middle of each cable loop is fitted with a crimped stainless steel ball terminal that is attached to the distal wrist component. At their proximal end the cable loops are connected crosswise to the two actuators (p_1 and p_2 in Fig. 5.20 (a)). Using the crosswise layout only two fixed rotary drives are needed to fully actuate the joint, yielding linear transmission characteristics. Driving only one actuator results in a tilting motion of the instrument tip at 45° angle to the principal axes of the joint (see inverse kinematics Eq. 5.15 and direct kinematics Eq. 5.16):

$$\begin{pmatrix} p_1 \\ p_2 \end{pmatrix} = r_{pulley} \begin{bmatrix} -1 & -1 \\ 1 & -1 \end{bmatrix} \begin{pmatrix} \theta_8 \\ \theta_9 \end{pmatrix} \tag{5.15}$$

$$\begin{pmatrix} \theta_8 \\ \theta_9 \end{pmatrix} = \frac{1}{r_{pulley}} \begin{bmatrix} -0.5 & 0.5 \\ -0.5 & -0.5 \end{bmatrix} \begin{pmatrix} p_1 \\ p_2 \end{pmatrix} \tag{5.16}$$

with r_{pulley} : radius of joint pulley (2.95 mm), θ_8, θ_9 [rad] : joint angles and p_1, p_2 [mm] : actuator positions.

Due to the motion coupling of the universal joint, the expected manipulation force at the tool tip for an actuation cable force of 100 N would be 7 N in the 45° direction (only one motor actuating the wrist) and 10 N along the θ_8 or θ_9 direction (both motors actuating the wrist). The drive cable loops are pre-stressed to guarantee backlash free operation. While the cable tension is necessary to improve the accuracy of wrist motion movements, it adds static friction between the sliding cable and proximal joint component. Since the actuation cable inside the shaft acts as a 300 mm long spring with a friction element at the end, some stick-slip or delayed motion is likely to occur. The amount of cable stretch due to the actuation force is calculated with Eq. 5.17. A more detailed evaluation on the relationship between cable tension, friction losses and wrist motion tracking accuracy will be conducted in the near future.

At a cable force of 100 N and with a free cable length inside the tool shaft of 300 mm, and a cable cross-sectional area of $0.16\mathrm{mm}^2$, the cables will stretch by:

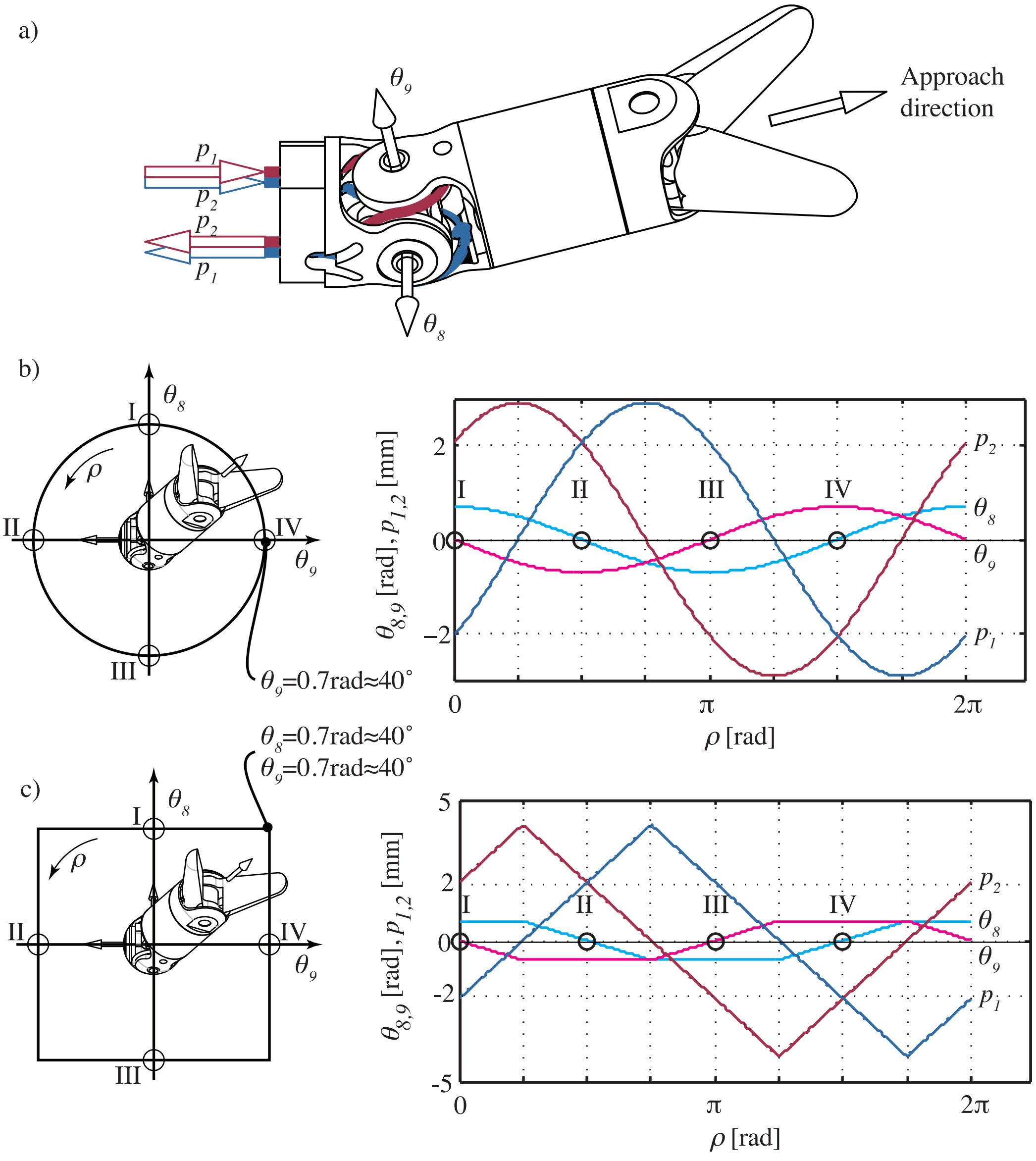

Figure 5.20: Wrist Kinematics. Two continuous actuation cable loops attach to the distal portion of the wrist (a). Note that cables are connected crosswise to the actuators. One end of the red cable loop is connected to the push side of actuator p_1, the other end is connected to the pull side of actuator p_2. Actuator linear positions (b) required to move the wrist along a circular path. Actuator linear positions (c) required to move the wrist along a rectangular path. Actuator positions p_1 and p_2 are given in [mm], wrist angles θ_8 and θ_9 in [rad].

$$\Delta l_c = \frac{F_c \cdot l_c}{E \cdot A} = \frac{100\ \mathrm{N} \cdot 300\ \mathrm{mm}}{65\frac{\mathrm{kN}}{\mathrm{mm}^2} \cdot 0.16\ \mathrm{mm}^2} = 2.88\ \mathrm{mm} \tag{5.17}$$

The effective modulus of elasticity of the steel cable is lower than that of bulk steel due to the rope construction. Measurements provided by CarlStahl [207] show that the effective modulus of elasticity for this cable is only $65000\frac{\mathrm{N}}{\mathrm{mm}^2}$. The cable used in this joint is a stainless steel wire rope made from 1.4401 stainless steel with a 7x19 construction and a diameter of 0.45 mm. The minimal breaking strength is 153 N and the weight is $0.810\frac{\mathrm{g}}{\mathrm{m}}$ (CarlStahl [208]).

The relatively large elastic deformation of the actuation cables is dependent on the acting cable force and, therefore, on the manipulation forces. Implementing a feed forward control scheme based on the manipulation forces measured by the force-torque sensor to improve the positioning accuracy of the wrist is planned for the near future.

5.3 Generic Functional Tip

Figure 5.21: Closeup view of the tool tip with short jaws which are used as needle holder. Centimeter scale to the left.

A large variety of surgical tool functionality can be realized with an end effector that can be actuated in up to 1 DoF. Ultrasonic and high frequency scalpels, dissection hooks, and remote palpation tools require no actuation and can, therefore, be attached to the FTS top platform directly. No actuation cable through the wrist and no gripping force sensor are necessary. Scissors, needle holders, and graspers, each consisting of two symmetrically movable, opposing jaws can all be actuated by a single DoF.

It was shown in Sec. 4.4 that the actuation mechanisms commonly used in MIS tools close the force loop through the instrument shaft, and if used in the present tool, through the force-torque sensor. This would lead to large actuation forces having to be supported by the FTS. With an active jaw length of $l_g = 9.75 \text{ mm}$ as defined in Fig. 4.4, a gripper pulley radius of $r_g = 3.25 \text{ mm}$, and the two jaws being actuated symmetrically, the ratio between gripping force and actuation cable force is $1 : 6$. Therefore, an actuation cable force F_c of 60 N is required to generate a gripping force of 10 N. The Stewart platform described in Sec. 5.1.2) exhibits a larger load capability in the f_z direction versus f_{xy} directions, and the load capability could be further increased to support the actuation cable force of 60 N by altering the geometry. However, any friction present in the gripper actuation mechanism will affect the FTS measurement proportionally to the actuation cable force. Assuming that all parasitic effects (e.g. friction and sensor signal noise) account for only 2% error in the FTS signal, a manipulation force of 1 N would be smaller than the error level. Clearly this is undesirable. Avoiding a reduction in sensitivity and large measurement errors is only possible by *mechanically* decoupling the gripper actuation force from the manipulation forces.

The functional principle of this mechanical decoupling mechanism has been introduced in Fig. 4.19 (d) and is briefly reiterated here with the help of Fig. 5.22 in order to illustrate the technical implementation presented in Fig. 5.23. The gripper actuation cable is split into two strands which are supported by two guide pins at the base of the FTS and directed outwards and around the decoupling cable pulleys (see Fig. 5.22 and Fig. 5.23). In contrast to Fig. 4.19 the two decoupling pulleys are arranged collinear to allow for a larger pulley diameter. The decoupling cable pulleys are supported at the base of the FTS and all reaction forces F_r exerted on the gripper pulleys are, therefore, not measured by the FTS. The two actuation cable strands form opposing S-loops intersecting between decoupling cable pulleys and jaw cable pulleys. In the ideal case the approach direction of the cable segment actuating each jaw would be radial to the tool axis, not containing a force component in the tool z-direction. However, jaw cable pulleys and decoupling cable pulleys should not touch. The small axial separation (in the range of $0.3\ \mathrm{mm}$) causes both cable strands (F_{c1} and F_{c2} to exert a small axial force component onto the jaw cable pulleys and, therefore, a small f_x component on the FTS. Additionally, physical intersection of the two cable strands is not possible. In the actual assembly the strands are offset from the center plane along the y-axis (see Fig. 5.22 Section B-B), creating a small torque about the tool axis, visible as m_x component on the FTS signal. The functional tip is actuated by one cable counteracted by a spring (active closing, passive opening). The cable based decoupling mechanism in its present form is limited to symmetrically actuated jaws as it relies on the cancellation of opposing force components.

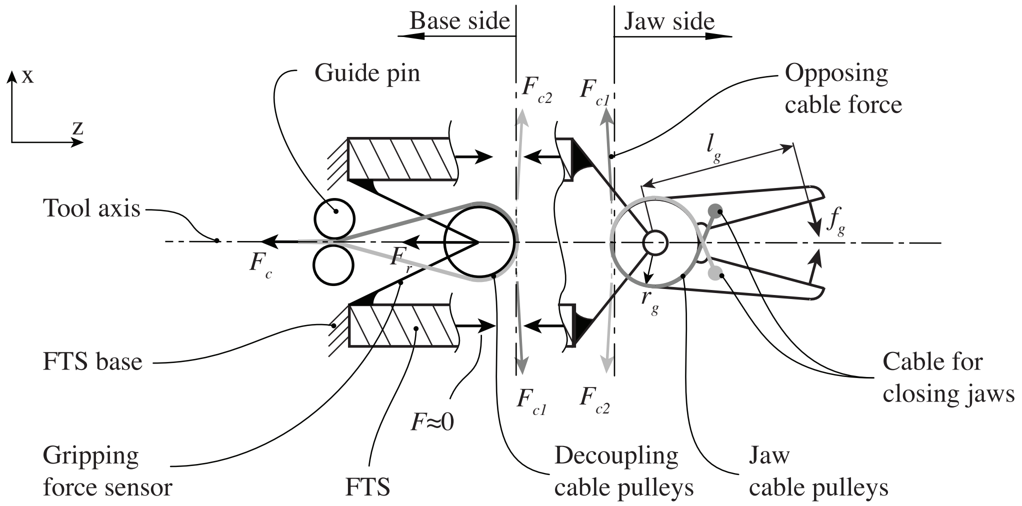

Figure 5.22: Gripping force decoupling principle (recap from Sec. 4.4). Two actuation cable strands are routed around the gripper cable pulleys. The resulting reaction force F_r is supported at the base of the FTS, while cable forces F_{c1} and F_{c2} create a pure torque for actuating the gripper jaws.

Fig. 5.23 gives a more detailed view of the internal construction and integration of force-torque sensor and end effector. Gripper actuation cable strands and respective jaw are colored in red and blue. FTS links are colored grey with the connection PCB colored green. The mechanical component carrying the decoupling cable pulleys is designed as gripping force sensor (GFS). It connects the decoupling cable pulleys to the base of the FTS. A FEA simulation of the GFS component is shown in Fig. 5.24 with a cable force of 5 N. The cable force acting on the pulley is simulated by area loads representing the force components of each cable running onto and off the pulley on cutouts in both pulleys (cutouts are visible for cables running off the pulleys and hidden inside the structure for cables running onto the pulleys). The large strains at the force application area are simulation artifacts due to the small area. A sketch shows the location for strain gauges with shear pattern.

The strain gauges are mounted on the outside surface of the gripping force sensor and are connected to the same connection PCB used in the FTS shown in Fig. 5.12. A dual pattern grid is placed each on the front and back surface of the sensor component, allowing the creation of a full bridge Wheatstone bridge circuit. The small circular gap between the sensor component and the top of the FTS is sealed with silicone or similar biocompatible elastomer, thereby creating a sealed cylindrical space containing all sensor elements. At the same time, the center of the end effector mechanics containing the actuation cable strands is open along the tool axis and can be flushed with cleaning fluid during sterilization.

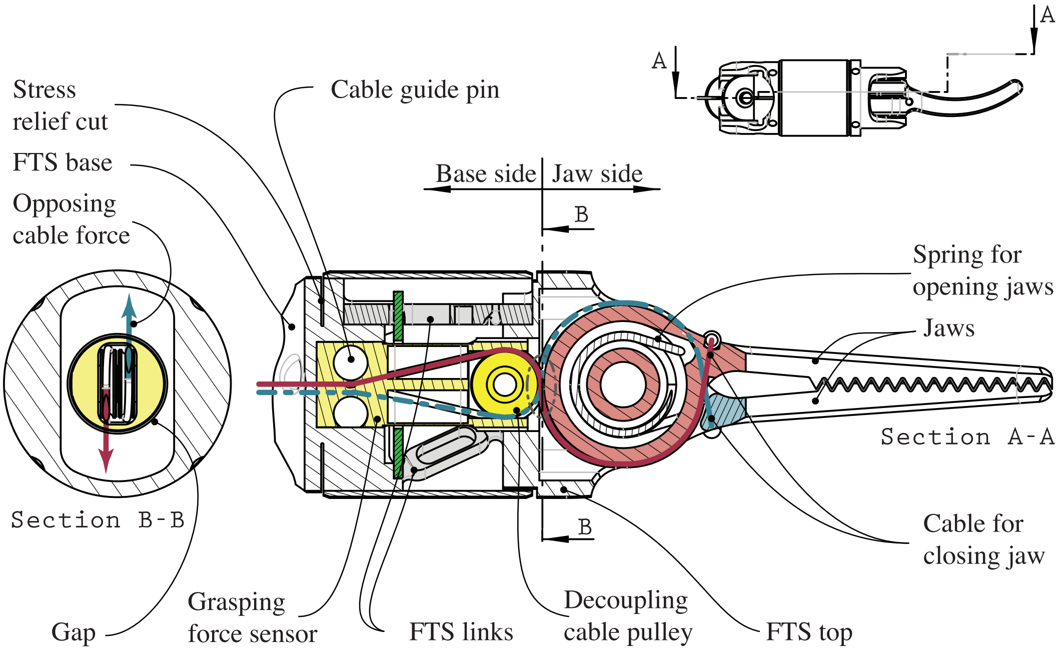

Figure 5.23: Functional tip internal construction with FTS (grey) with connection PCB (green), gripper jaws and respective actuation cables (red and blue) and decoupling pulleys held by the GFS (yellow).

A bowden cable was used to transmit the functional tip actuation force through the first generation wrist (compare Fig. 5.19 (a)) in order to keep the cable length constant and in-

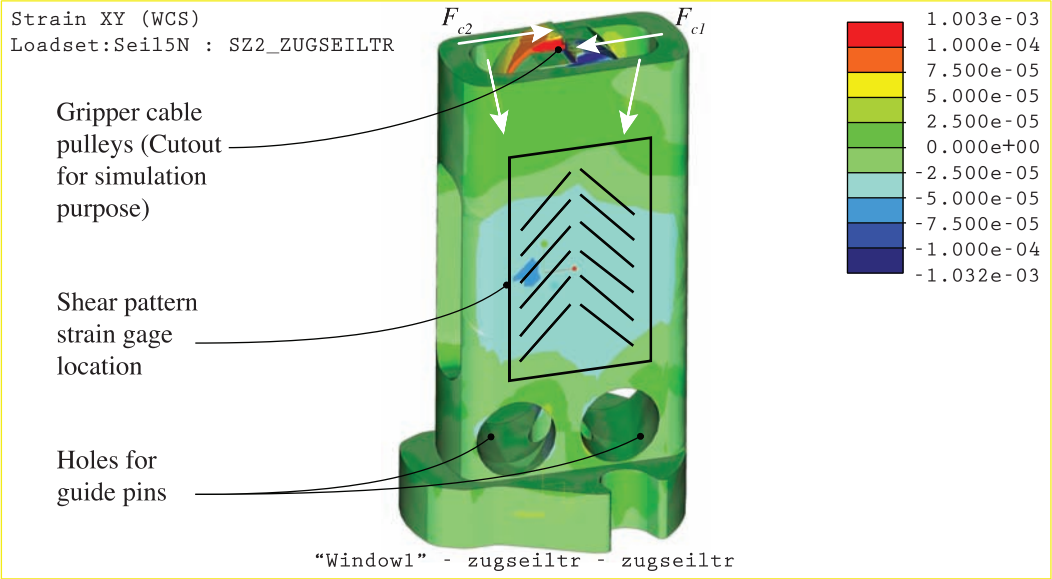

Figure 5.24: Gripping force sensor with location of dual grid shear strain gauge shown. The simulated cable force is 5 N for each strand in the case shown.

dependent of the wrist articulation. Unfortunately, for the available diameter no bowden cable with sufficient strength to support the tip actuation could be found. In the last generations end effector actuation is achieved by an open cable guided by a nozzle-shaped bore in the wrist center component (compare Fig. 5.19 (b) and Fig. 5.25). Since the cable cannot follow the neutral axis of the joint, the length of cable path segments will change due to wrist articulation. Fig. 5.25 shows the simulated cable shape under tension for a given wrist articulation about θ_8 and Tab. 5.6 shows the according numerical change Δs in cable path length, together with the change in jaw opening angle $\Delta\ \theta_{10}$. If the jaws are completely closed or grasping an object, the user will, therefore, feel a change in gripping force when articulating the wrist. Changes in cable path length are similar for θ_9. For articulation about both DoF simultaneously, the geometric sum of $\theta_{combined} = \sqrt{\theta_8^2 + \theta_9^2}$ yields a good estimate to be used for the lookup table Tab. 5.6.

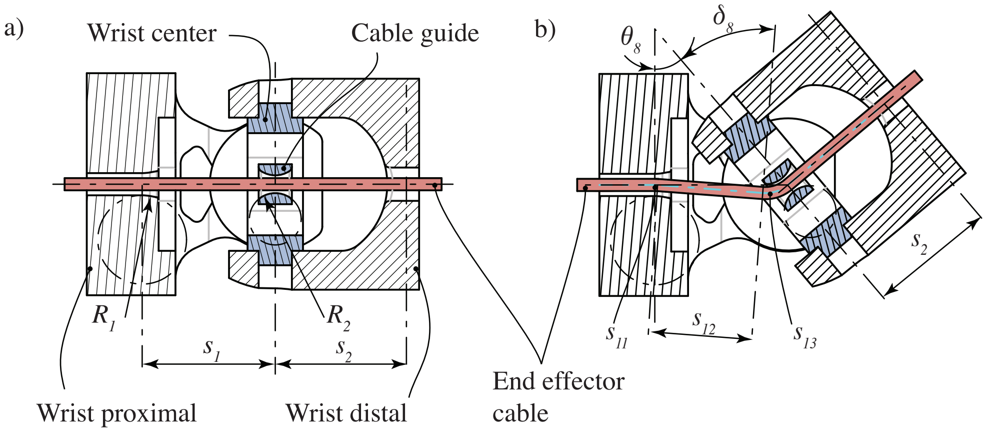

Figure 5.25: Elongation of end effector actuator cable path due to wrist articulation, shown about θ_8. The straight case is shown in (a) with cable length $s_1 + s_2$. The deflected case is shown in (b) with new cable path length $s_{11} + s_{12} + s_{13} + s_2$. Radius $R_1 = 2$ mm, radius $R_2 = 1.2$ mm. Simulation results are shown in Tab. 5.6.

Table 5.6: Simulated elongation and friction of functional tip articulation cable due to wrist deflection about θ_8. $\Delta s = (s_1 + s_2) - (s_{11} + s_{12} + s_{13} + s_2)$ (according to Fig. 5.25). $\Delta\theta_{10}$ is the resulting closure of the gripper and F_{frict}/F_c shows the added friction due to the cable running over the curved nozzle surface with $\mu_{\text{Steel(wet)}} = 0.15$.

θ_8 [°]	δ_8 [°]	Δs [mm]	$\Delta\ \theta_{10}$ [°]	$\frac{F_{frict}}{F_c}$
0	0	0	0	0
10	10.31	0.01	0.33	0.03
20	21.31	0.02	0.65	0.06
30	33.14	0.06	1.96	0.10
40	45.93	0.13	4.26	0.15

Figure 5.26: Closeup view of the interface unit.

5.4 Interface Unit

The *MICA* drive unit provides actuation in 3 DoF and an electrical sensor bus connections to all tools. Actuation is provided by 3 push-pull rods of $2.5\ \mathrm{mm}$ diameter arranged in $120°$ increments on a circle of $3.5\ \mathrm{mm}$ diameter. Total rod travel is limited to $10.5\ \mathrm{mm}$ per rod and maximum rod velocity is $120\ {}^{\mathrm{mm}}/_{\mathrm{s}}$. The sensor interface is a high speed differential bus adhering to the open industry sensor bus standard BiSS C-Mode described by iC-Haus [209]. It is a reliable bidirectional cascadeable serial bus, capable of transferring upstream and downstream data in the same cycle with data rates up to 10 Mbit/s.

An interface unit is necessary to adapt this generic actuation mode provided by the EMU to the requirements of specific tools and also to enable quick tool changes during clinical use. It combines several functional components:

- A *system specific* interface to the EMU. This interface mechanically connects the tool frame to the EMU creating the instrument. The connection is realized by radially sliding and locking the interface unit into place. It can be easily dis/connected for tool changes. An electrical connector is provided, establishing a digital interface for any additional (sensing) functionality of the tool. While sliding the interface unit into place, a peg-in-groove connection is established with the actuator rods of the drive unit. The mating parts and mating process are shown in Fig. 5.27. Proper alignment and secure connection is guaranteed by four guide pins. Mechanical play is avoided by machining the connecting surfaces to close tolerances from high-grade surgical stainless steel. Still, due to careful design of the mating surface geometry, connection is possible even if the mating surfaces do not initially line up exactly. Mating surfaces are designed to withstand Hertzian contact stress under full load.

- A *system specific* interface to the *MIRO* arm. This interface provides secure mechanical attachment of the interface unit, and thereby the entire instrument to the robotic system. *MIRO* is equipped with a magnetic coupling device which can be disabled on command for tool changes. This interface also includes connectors supplying any instrument with power and a connection to the system bus for communication. This interface also denotes the location of the sterile barrier between *MIRO* and *MICA*.
- A *tool specific* linkage or pulley system translating the linear motion of the drive unit's actuator rods to the motion required for articulating the tool. Currently the three linear motions ($p_{(1,2,3)}(mica)$) are translated with a transmission ratio of roughly 1:1 (see Eq. 5.18) into the rotation of pulley segments, which are in turn driving steel cable loops ($p_{(1,2,3)}(cable)$) actuating the tool wrist and end effector. The radius of the pulley segments is $r_{1,2} = 13.25 \text{ mm}$ for the wrist actuation and $r_3 = 9.5 \text{ mm}$ for the functional tip actuation (see Fig. 5.27 (c)).

$$p_n(cable) = \arctan\left(\frac{p_n(mica)}{r_n}\right) r_n \tag{5.18}$$

While not strictly linear, the linearity error is less than 5% over the range of actuation. The cable termination and pre-stressing mechanism is also integrated into these pulley segments (see Fig. 5.27 (c)). By changing transmission ratio and principle, a wide variety of tools with zero to three DoF based on cables, push-pull rods and rotating shafts can be adapted to the EMU.

- A *sealed electronics compartment*. All sensor signal conditioning is provided inside the interface unit so that only digital signals adhering to the BiSS standard are transmitted between instrument components, providing better immunity against noise and interference. The electronic connection between EMU and interface unit is established by a spring loaded contact matrix which is discarded after each use. Gold plated contacts on both the drive unit and interface unit (matrix of gold dots on green surface visible in Fig. 5.28) provide a flat landing grid for the spring loaded contacts. All necessary electronic components inside the interface unit are sealed (see Fig. 5.28) to withstand cleaning and autoclaving. Still, the integrated electronic components have to withstand the sterilization temperatures at least in a disconnected power state.

The design of the interface unit has been kept as open as possible (aside from the sealed electronics compartment) to facilitate flushing the entire mechanism with sterile cleaning solution and sterilization of the tool.

5.5 Summary of Implementations

The current chapter has described the practical implementation of the four major functional modules of the *MICA* dedicated tool section: force-torque sensor (Sec. 5.1), wrist (Sec. 5.2), functional tip (Sec. 5.3), and tool interface unit (Sec. 5.4). The details of design and implementation have been described for each module. Module level simulations and initial measurements have been provided. For a more comprehensive evaluation of the entire tool, the integration into the *MiroSurge* system is necessary. System level experiments and results that validate the functionality for the entire advanced tool are described in the following Sec. 6.

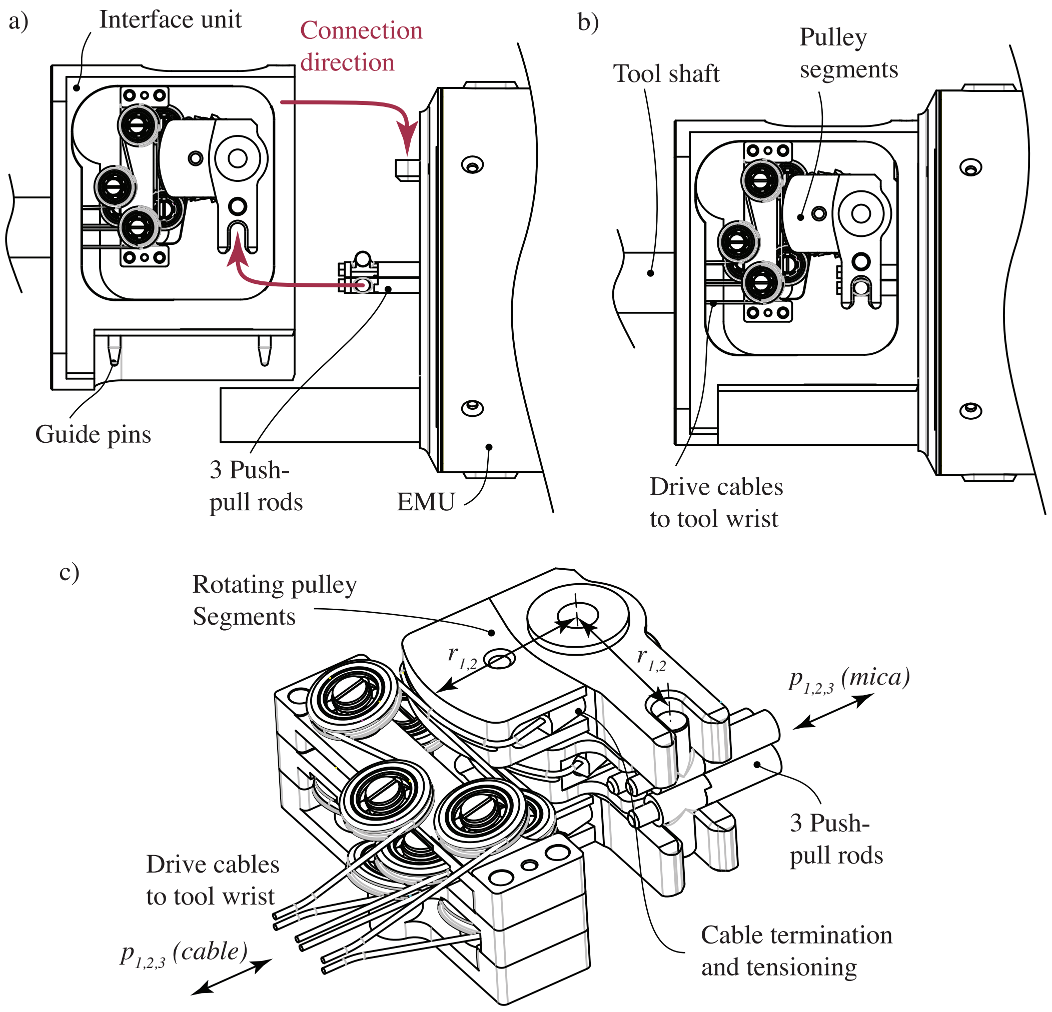

Figure 5.27: Tool connection process to the drive unit (a) and coupled position (b).

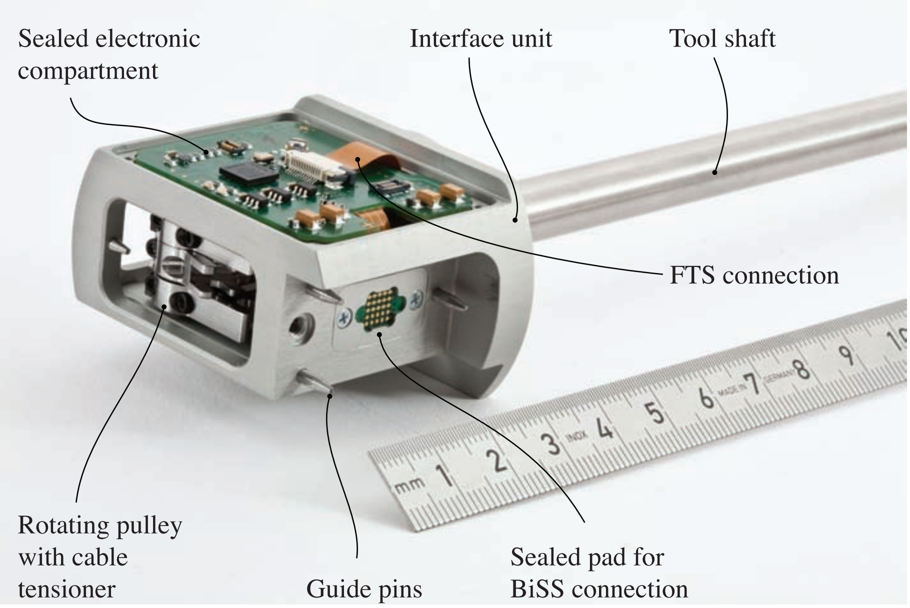

Figure 5.28: Components of interface unit and electronics connections (lid of electronics compartment removed).

6

Results

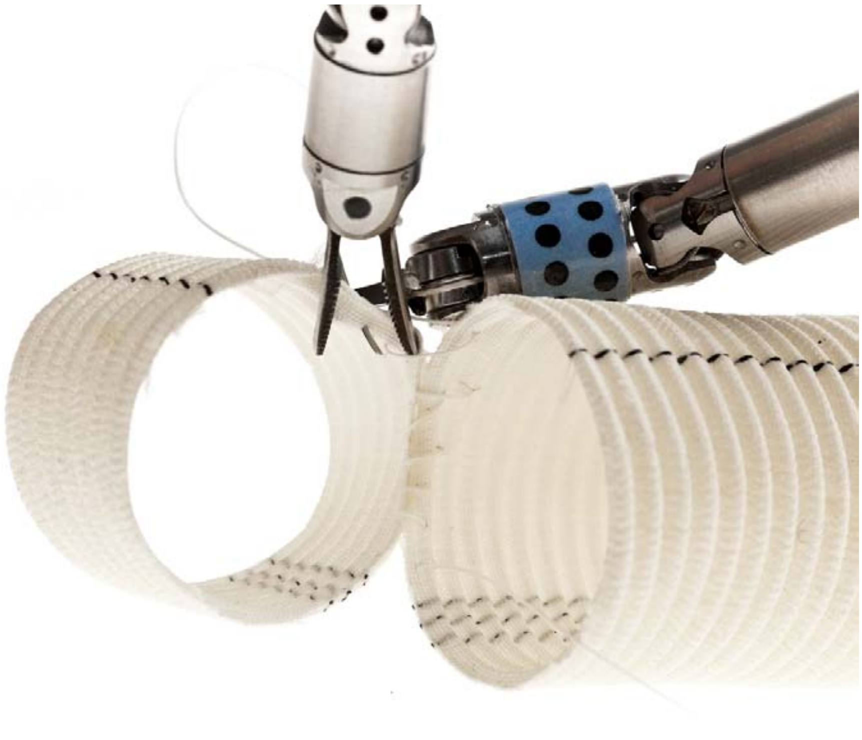

Figure 6.1: Suturing hollow tissue phantom with running stitch.

This chapter describes a series of experiments aimed towards verifying the design specifications of the MIRS tool, beginning with the calibration of the 6+1 DoF force sensor

(Sec. 6.1), followed by accuracy measurements of the wrist motion (Sec. 6.2). The ability to discern the elasticity of various tissues is then shown using the palpation tool with user interaction (Sec. 6.3) and in autonomous mode (Sec. 6.3). All of these experiments are aimed at evaluating the performance of the *MICA* tool only, however a large part of the *MiroSurge* infrastructure (see Fig. 2.2) is necessary for the presented experiments.

6.1 Force Sensor Calibration

After fabrication and assembly of the strain gauges, the sensor is calibrated using a set of known weights applied in the six principal directions using a calibration jig. The sensor is subjected to at least one loading/unloading cycle in positive and negative directions to check for hysteresis. Currently 14 values are recorded for each of the principal force directions and 5 values are recorded for the gripping force, resulting in a 89x14 matrix relating the externally applied loads to the 12-bit output values of the sensor signal conditioning electronics. The origin of applied loads is placed between the jaws of the gripper at a distance of $l_d + l_g = 28.5$ mm as defined in Fig. 4.4.

For calibration purposes, the raw sensor data is transmitted using a custom DSP board as SPI to Serial converter which is connected directly to the sensor conditioning electronics. The serial data stream is then recorded directly with a Matlab script using the built-in set of serial port functions. The performance of Matlab's built-in serial port functions is relatively poor, allowing for a data rate of 25 to 50 Hz only, which is, however, sufficient for the current static calibration process (all other experiments are conducted at the *MiroSurge* system clock rate of 3 kHz).

A linear least square estimate (LLSE) is then calculated using the data of applied loads and resulting sensor response, assuming that the sensor response is linear for the desired measurement range. The result of the LLSE is the calibration matrix $\mathbf{C} \in \mathbb{R}^{(7\times 7)}$ of the force-torque sensor including the gripping force sensor, calculating the externally applied force in N and torque in Nmm from the digitized strain gauge output. Clearly the calibration matrix $\mathbf{C}$ is different from matrix $\mathbf{A}$ calculated in Sec. 5.1 which relates internal link forces to loads applied externally at the analytical origin 0 of the sensor (see Fig. 5.3 and Eq. 5.2). $\mathbf{C}$ contains the mapping of raw strain gauge values to forces for 7 DoF, the shift of the force application point from the sensor origin to the point defined by $l_d + l_g$, the effects of manufacturing tolerances, strain gauge misalignment, and amplifier gain inaccuracies.

Results of the calibration of one sensor (FTS 1, see Tab. 6.1) are shown in Fig. 6.3 to Fig. 6.6. Each figure shows the externally applied load on the abscissa and the force-torque sensor response on the ordinate with forces denoted by solid lines and moments denoted by dotted lines. The force-torque sensor response shows all principal directions in order to determine any parasitic cross coupling. Ideally the output relating to the applied load should appear as unity line with all remaining outputs being zero. The bisector is shown in every graph for reference. Measured sensor data for the according DoF is denoted by star symbols. The force-torque sensor response for moments is displayed in Ncm rather than Nmm or the previously introduced measure of $^{\mathrm{Nmm}}/_{\mathrm{a}}$. The scaling factor was chosen arbitrarily, however the scaled results convey a more accurate representation of the error perceived by the user (for this sensor).

Fig. 6.3 to Fig. 6.6 confirm the linearity assumption. It can be seen in Fig. 6.3 and Fig. 6.4 that the force-torque sensor output follows the expected unity response very closely for f_x, f_y, m_x m_y, and m_z loads. Performance is worse for f_z and f_g forces. Using the calibration jig shown in Fig. 6.2, the accurate application of forces in the z direction is very difficult. Small alignment errors will result in large cross coupling resulting in larger errors for the LLSE. Also, higher stiffness of the sensor structure in the f_z direction leads to a smaller strain gauge output and, therefore, larger corresponding entries in the calibration matrix $\mathbf{C}$ for the f_z direction amplifying any errors. The same is true for the gripping force f_g. Accurate application of only the gripping force without any other load component is only possible by substituting the gripper cable force for the gripping force. The cable force is larger than the gripping force by a factor of 6 (see Sec. 5.3). Therefore, a cable force F_c of up to 15 N was applied for calibration purposes. This leads to a proportionally larger influence of friction and other errors. With the current calibration setup the application of higher cable forces is not possible, however, during instrument operation gripping forces of up to 8.5 N (requiring a cable force F_c of more than 50 N) were measured with an external force sensor located between the tip of the gripper jaws, validating the design goal of a gripping force of 10 N at the l_g (effective gripper length) point.

The current calibration procedure, using a LLSE of 14 data points for each of the 6 principal manipulation loads and only 5 data points for the gripping force, is heavily favoring the accuracy of manipulation loads over the gripping force, explaining the poor results for the gripping force shown in Fig. 6.6. However, for the calculation of residuals shown in Tab. 6.1 all recorded data points are taken into account, which heavily favors the gripping force sensor. Manipulation load measurements are affected by the gripping force due to residual errors in the force decoupling mechanism. However, the reverse is not true. The gripping force sensor is mechanically independent of manipulation loads and therefore residuals of the gripping force are zero for most data points resulting in the very low average residuals reported in Tab. 6.1.

Therefore, the results shown Tab. 6.1 can be used to define the accuracy of the manipulation force sensor as mean residual plus one standard deviation for each principal load. The accuracy of the gripping force sensor can be estimated from Fig. 6.6 as having a mean residual of 0.19 N and a standard deviation of 0.23 N.

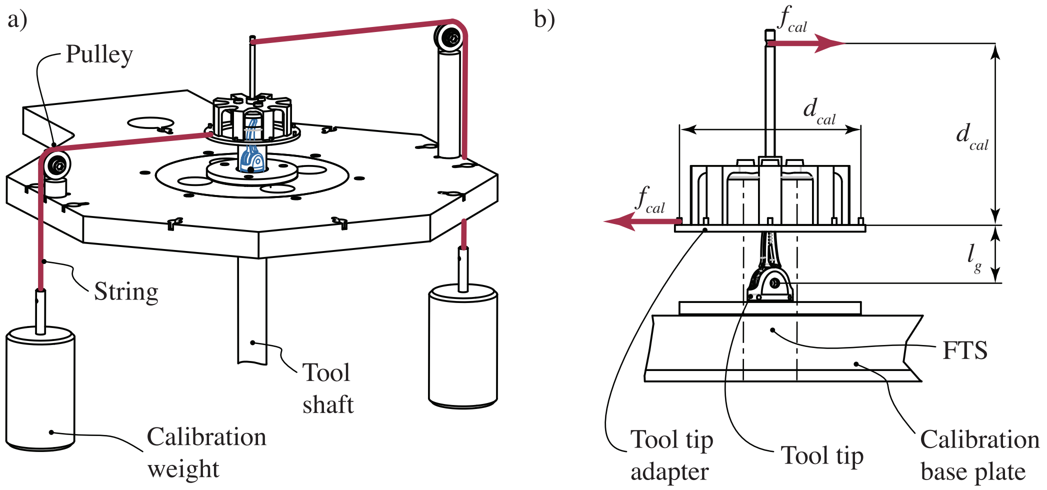

Figure 6.2: Force sensor calibration jig overview (a). The FTS is subjected to specific loads by attaching weights in different directions. Weights are placed so that the sensor origin is placed between gripper jaws, at a distance of l_g from θ_{10}. Moments are created as shown in detail (b) by attaching two identical weights in opposite directions, separated by a distance of d_{cal}.

a) f_x

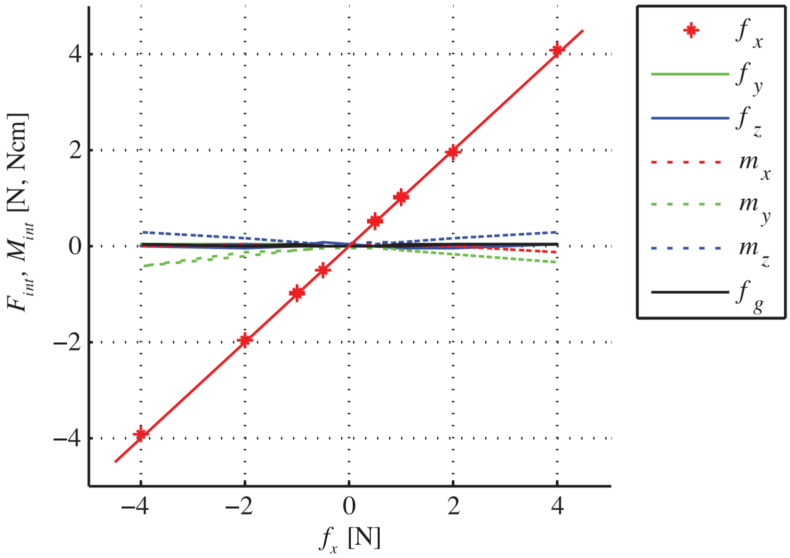

b) m_x

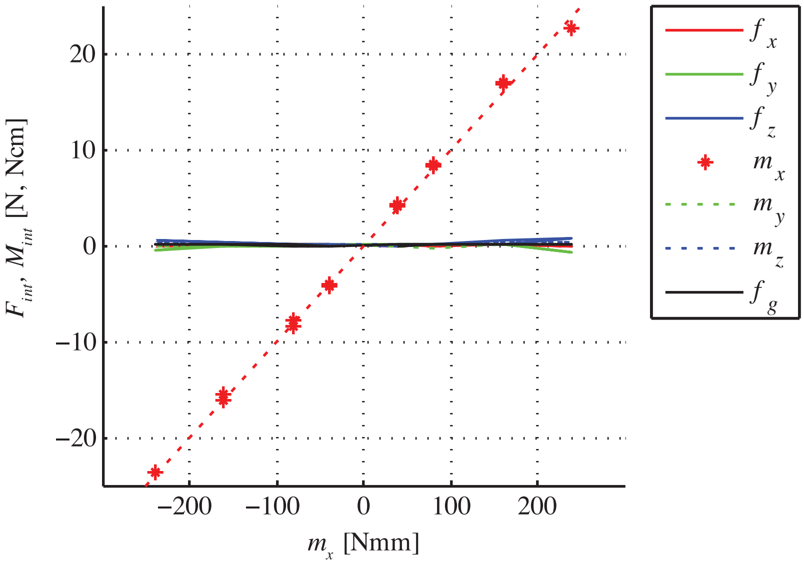

Figure 6.3: Calibration response of FTS 1 to externally applied force and moment in x-direction. Linear unity response is indicated by red solid line in (a) and red dashed line in (b), actual measures are indicated by red stars.

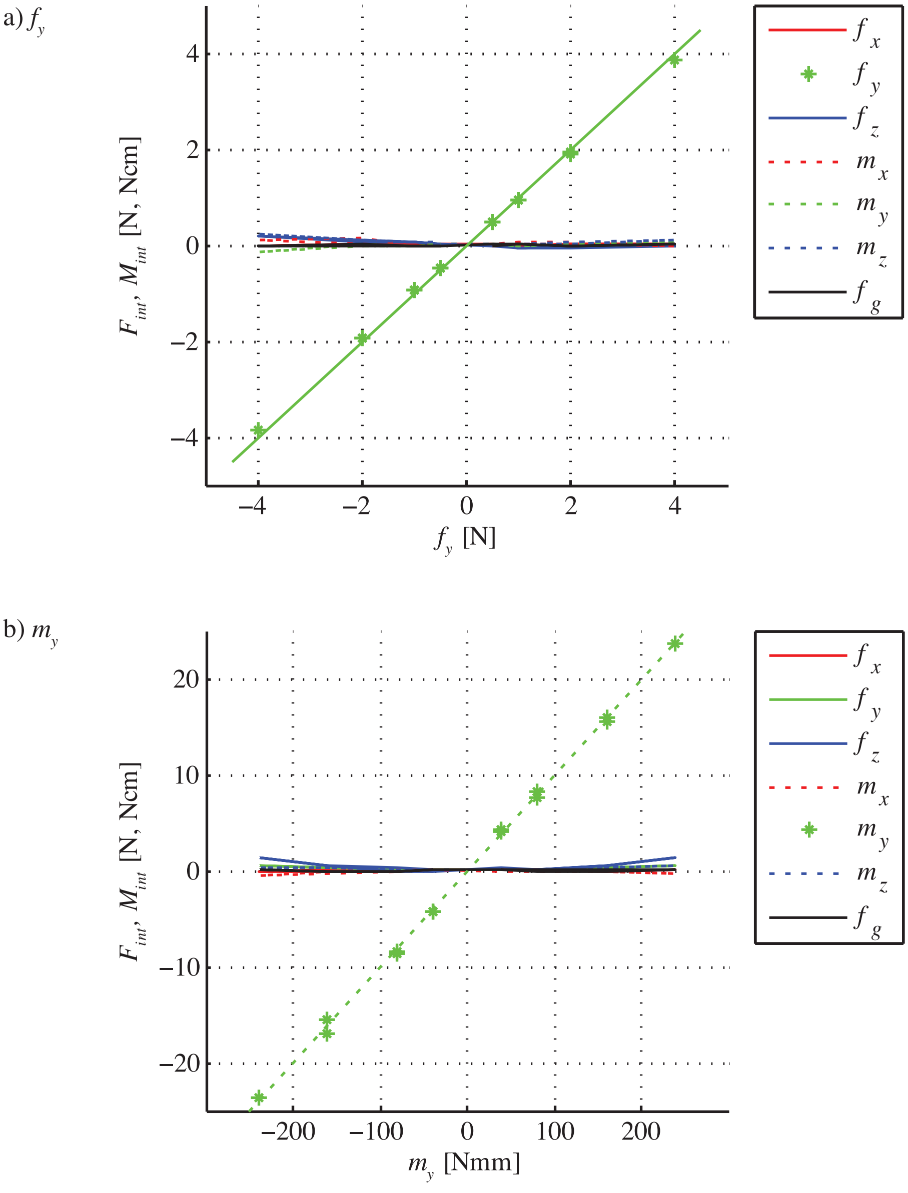

Figure 6.4: Calibration response of FTS 1 to externally applied force and moment in y-direction. Linear unity response is indicated by green solid line in (a) and green dashed line in (b), actual measures are indicated by green stars.

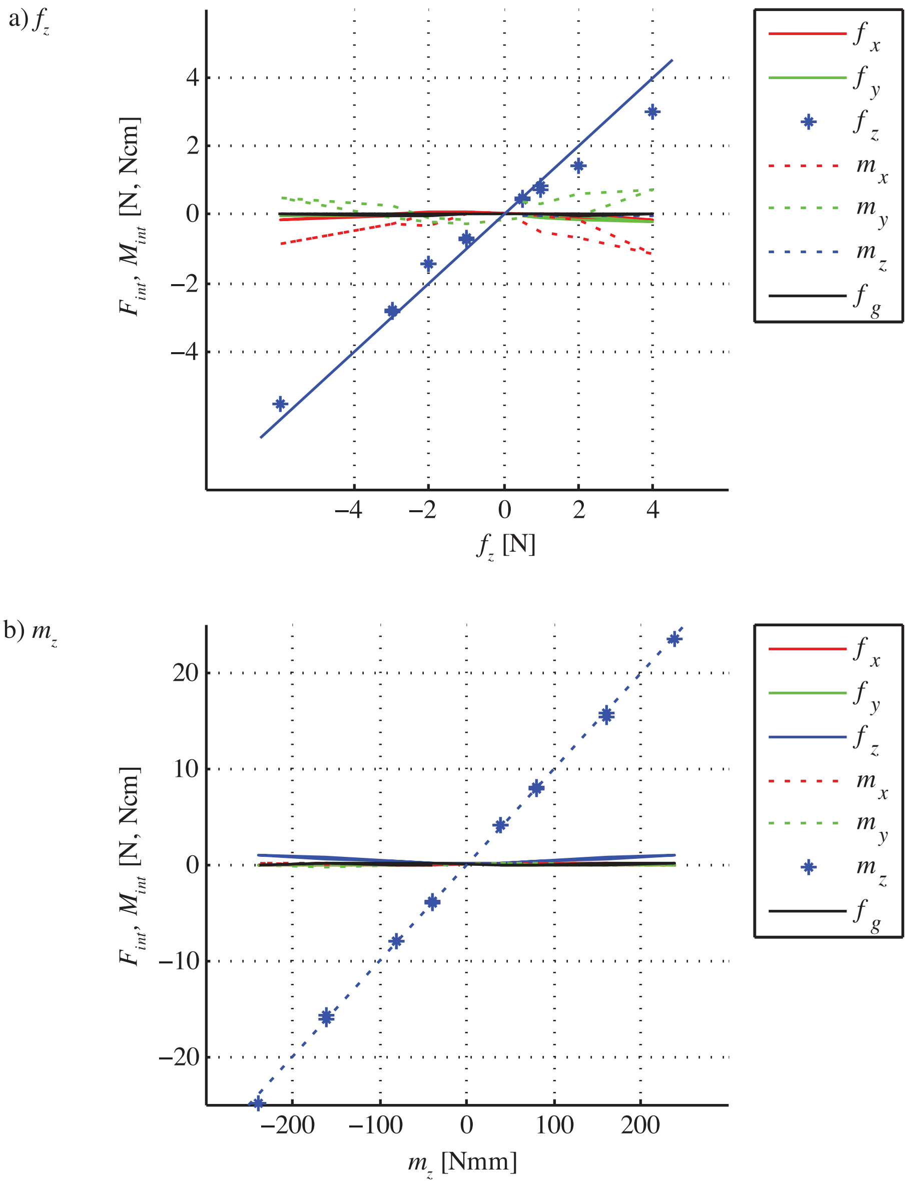

Figure 6.5: Calibration response of FTS 1 to externally applied force and moment in z-direction. Linear unity response is indicated by blue solid line in (a) and blue dashed line in (b), actual measures are indicated by blue stars.

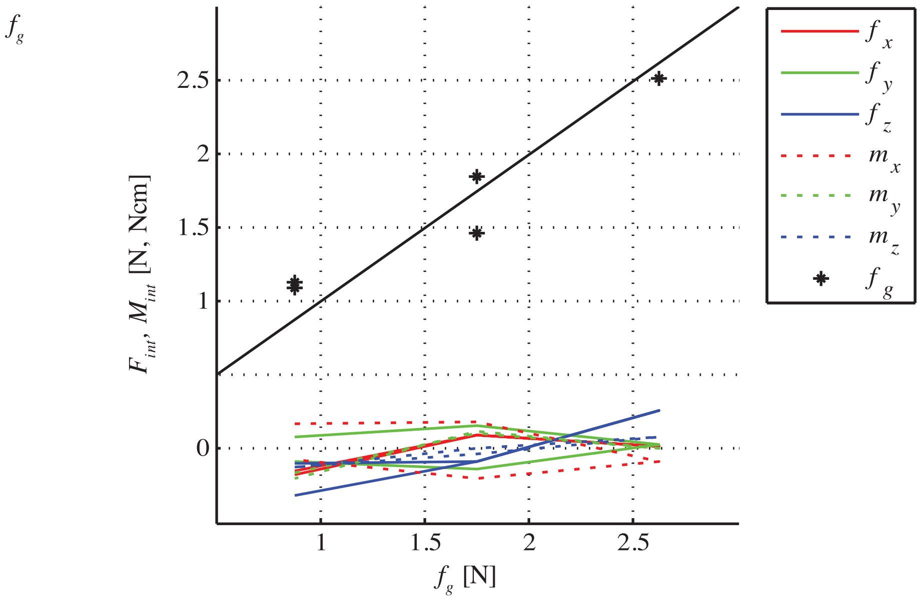

Figure 6.6: Calibration response of FTS 1 to gripping force. Gripper is actuated by cable. Linear unity response is indicated by black solid line in, actual measures are indicated by black stars.

Table 6.1: Residuals of least square estimate (mean | standard deviation) for FTS calibration of five different sensors. The palpation tool does not contain a gripping force sensor.

Sensor	f_x	f_y [N]	f_z	m_x	m_y [Nmm]	m_z	f_g [N]
FTS 1	0.03 | 0.04	0.03 | 0.04	0.07 | 0.07	2.2 | 3.1	2.5 | 3.6	2.3 | 2.6	0.02 | 0.05
FTS 2	0.07 | 0.12	0.09 | 0.12	0.15 | 0.27	1.9 | 3.0	1.4 | 2.6	0.3 | 0.5	0.07 | 0.10
FTS 3	0.09 | 0.13	0.13 | 0.18	0.35 | 0.64	2.6 | 3.9	1.3 | 2.1	0.4 | 0.6	0.01 | 0.02
FTS 4	0.05 | 0.07	0.10 | 0.15	0.25 | 0.36	1.7 | 3.1	1.6 | 2.4	1.3 | 2.0	0.02 | 0.05
Palpation 1	0.03 | 0.04	0.03 | 0.05	0.06 | 0.07	2.0 | 4.0	1.4 | 2.7	2.8 | 1.3	
Average	0.05 | 0.08	0.08 | 0.10	0.18 | 0.28	2.1 | 3.4	1.6 | 2.7	1.4 | 1.4	n.s.

6.2 Wrist Motion Tracking

In order to measure the tracking accuracy of the wrist, magnetic encoders (US Digital, MA3-A10-125-B) are attached to the wrist, which provide a single turn absolute voltage signal proportional to the wrist angle. The external encoder resolution in this setup is $0.35°$. The encoders are mounted in a 2 DoF bracket (see Fig. 6.8) which is connected to the tool, parallel to and aligned with the wrist. The encoder provides a 10-bit analog voltage signal which is converted using a National Instruments NI-6220 AD data acquisition card located in the QNX joint control PC. Data acquisition is synchronized with the Simulink model execution. Data is available inside the model at a rate of 1 kHz and also logged to file at a rate of 100 Hz.

Control of the *MICA* is accomplished by an S-function block within the external mode of Simulink Realtime Workshop (see Fig. 6.7). The S-function block takes status and torque commands as input and provides status and sensor data as output. Details of the underlying hardware interface are described in Thielmann et al. [168]. Position control and trajectory generation was implemented using a very basic P-controller. Nevertheless, for the sinusoidal trajectories (up to 4 Hz at wrist deflections of up to $40°$) used in the wrist tracking experiments, performance of the P-controller was sufficient.

Fig. 6.10 and Fig. 6.11 show counterclockwise circular trajectories at 0.5 Hz (one complete circle every two seconds) and 4 Hz (4 circles per second) respectively. Wrist deflection is increased from 5° (a), 10° (b), 20° (c) to 40° (d) at both velocities. Red and green dashed traces show actuation cable positions (measured by the *MICA* motor encoder) converted to wrist angles θ_{8c} and θ_{9c}, red and green solid traces show actual wrist angles measured by the external magnetic encoder θ_{8j} and θ_{9j}. The black traces shows the error between cable and wrist angle, solid for θ_8 and dashed for θ_9. Evaluation of the position controller performance itself is not part of the experiments shown here, which are limited to the tool kinematics, therefore, the desired motor position is not plotted. However, previous experiments evaluating the *MICA* drive unit alone have shown that position accuracy is good for sinusoidal trajectories even at 7.5 Hz.

These diagrams show that the maximum tracking error remains fairly consistent at $\pm 2.5°$ for θ_8 and slightly larger for θ_9 for 5° and 10° articulation and increase to $\pm 4.5°$ for 20° and 40° articulation. These errors are similar for all articulation speeds. The observed error characteristic is consistent with a serial spring and damper arrangement formed by the free

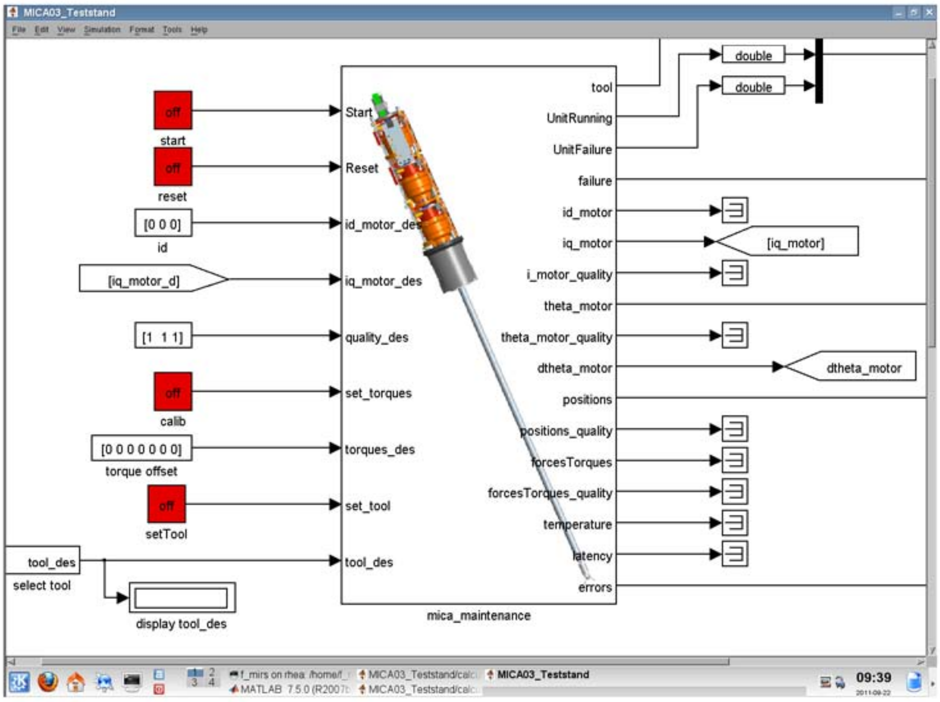

Figure 6.7: S-function block in Simulink to control *MICA*. Desired motor current and status signals are inputs to the block, actual motor current, motor position and status signals are outputs of the block. A P-type position controller is built around this block.

length of elastic cable in the shaft followed by a sliding contact over a stationary pulley in the wrist. The error is larger for θ_9 as the angle of contact between cable and curved surface is larger. It can be seen from Fig. 5.19 (b), for θ_8 the actuation cable slides over the curved cable guide of the proximal segment only, whereas for θ_9 the cable guide segment of the wrist center is added.

Fig. 6.12 shows wrist motion tracking (a and c) as well as parasitic force measurements (b and d) at 2 Hz movement about θ_8 (vertical movement, a and b), and θ_9 (horizontal movement, c and d) at 40° wrist deflection. Red and green dashed traces show measured cable position converted to wrist angles θ_{8c} and θ_{9c}, red and green dash-dot traces show measured wrist angles θ_{8j} and θ_{9j}. Solid traces in force diagrams (b) and (d) refer to the right ordinate and show parasitic forces and moments in N and Ncm. Wrist tracking accuracy and parasitic forces were measured in two separate experiments as the external encoder as-

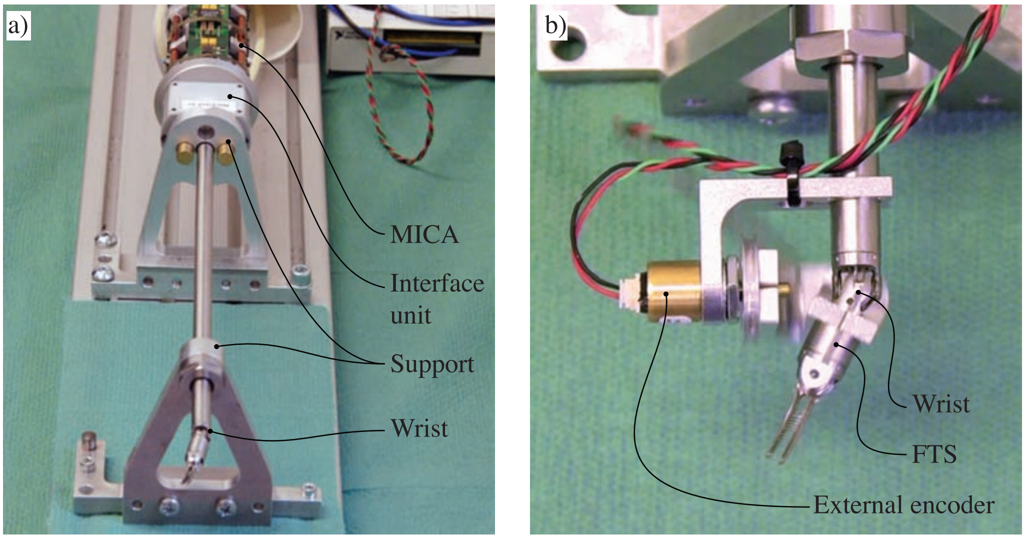

Figure 6.8: Setup for measuring wrist motion tracking. Overview (a) and detail of encoder assembly (b). In this setup articulation about θ_8 yields vertical tip motion, θ_9 yields horizontal tip motion.

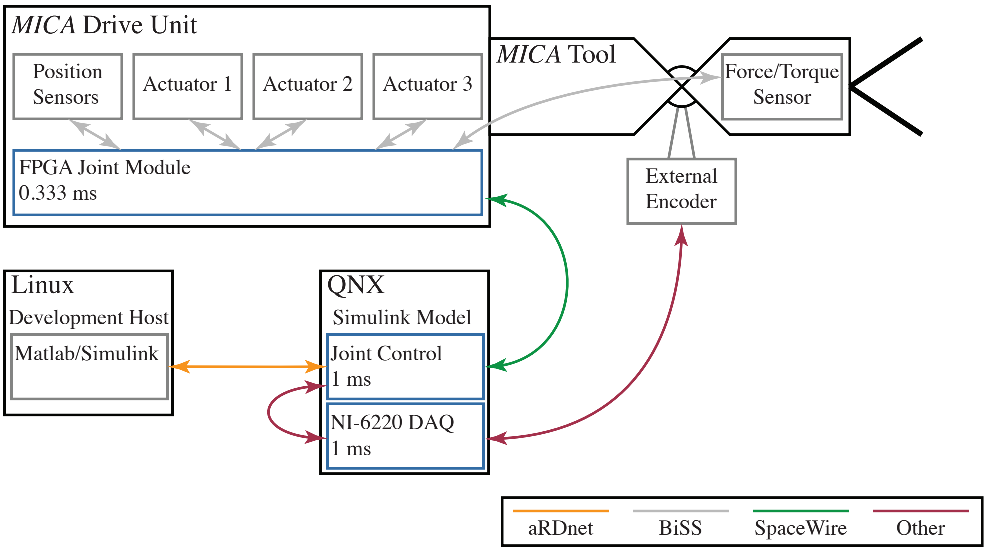

Figure 6.9: Setup topology for wrist motion measurements. The infrastructure is similar to the *MiroSurge* topology (see Fig. 2.2), reduced to the components necessary for controlling a single *MICA*.

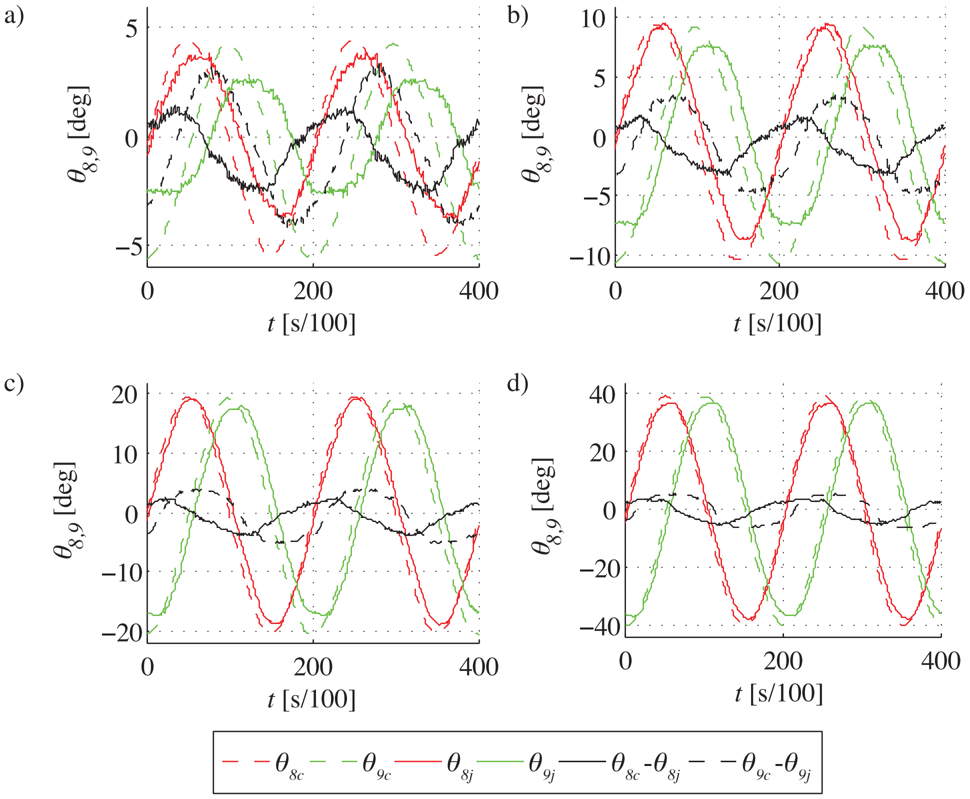

Figure 6.10: Wrist motion tracking at 0.5 Hz for a circle of 5° (a), 10° (b), 20° (c) and 40° (d) wrist deflection. Red and green dashed traces show measured cable position converted to wrist angles θ_{8c} and θ_{9c}, red and green solid traces show measured wrist angles θ_{8j} and θ_{9j}. Black trace shows error between cable and wrist angle, solid for θ_8 and dahsed for θ_9.

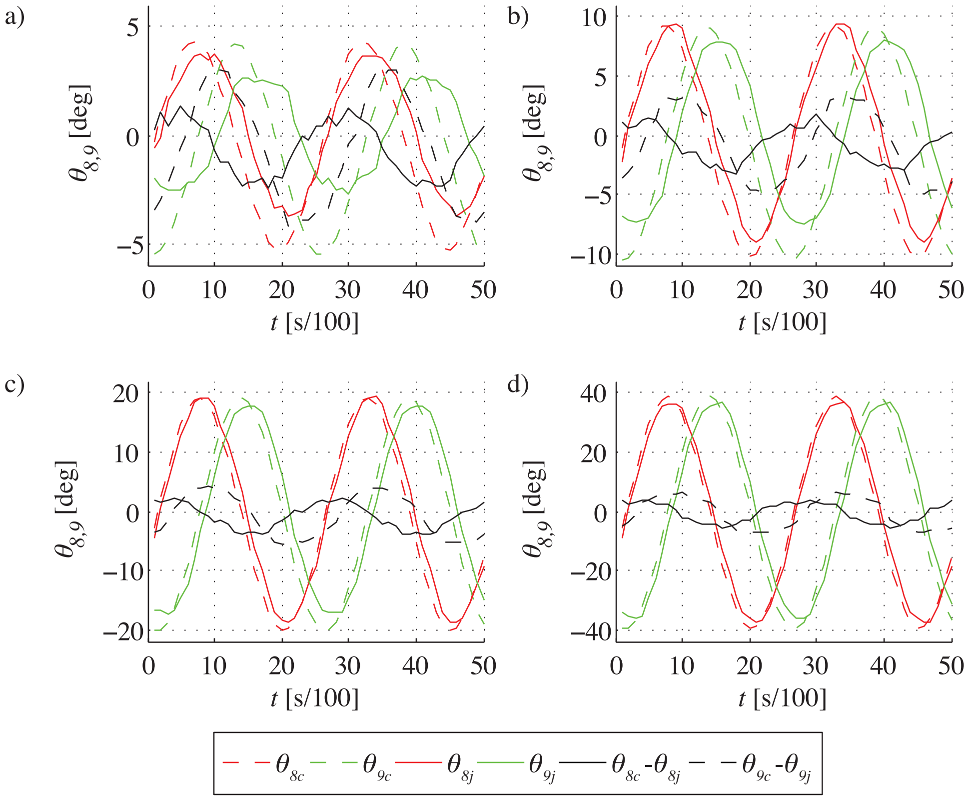

Figure 6.11: Wrist motion tracking at 4 Hz for a circle of 5° (a), 10° (b), 20° (c) and 40° (d) wrist deflection. Red and green dashed traces show measured cable position converted to wrist angles θ_{8c} and θ_{9c}, red and green solid traces show measured wrist angles θ_{8j} and θ_{9j}. Black trace shows error between cable and wrist angle, solid for θ_8 and dahsed for θ_9.

sembly necessary to measure the actual wrist deflection (shown in Fig. 6.8) interferes with the force-torque sensor and increases the force measurement error, so the encoder assembly was removed during force measurements. Fig. 6.12 shows moderate parasitic forces of up to 0.3 N for wrist motion in the θ_8 direction, with f_y, f_z and f_g being most prominent. Force measurement errors increase drastically for wrist motion about θ_9. While f_z shows a similar error magnitude as before, errors for f_x and f_g increase to beyond 0.5 N.

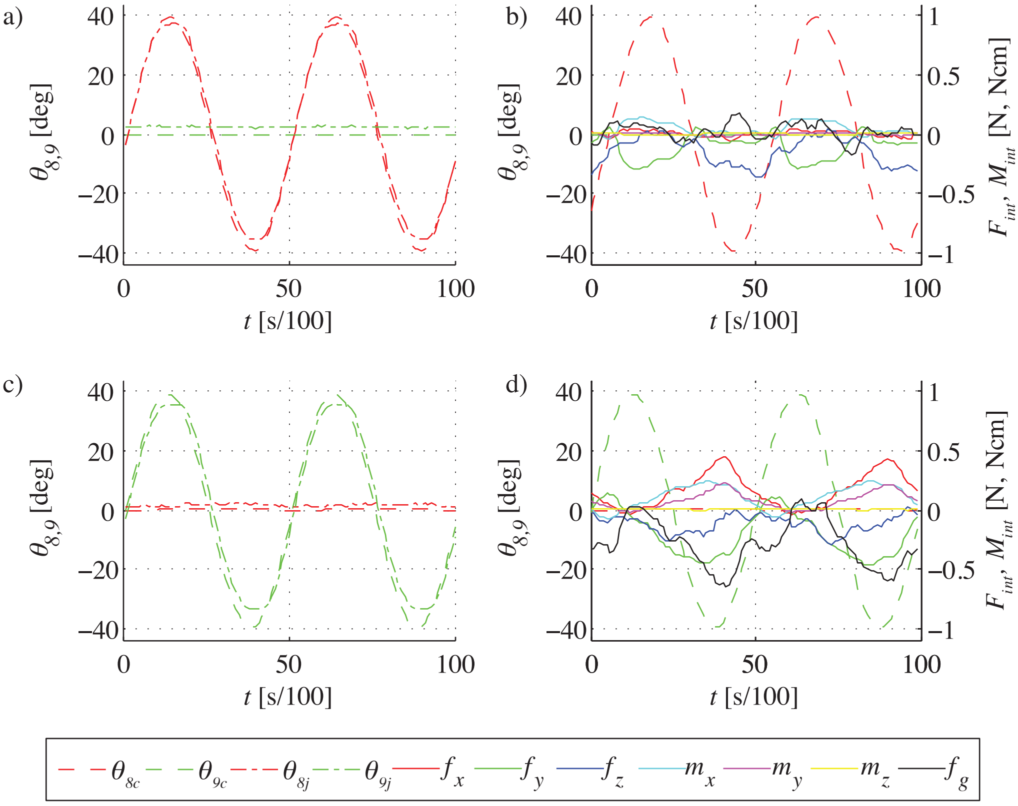

Figure 6.12: Wrist motion tracking (left) and parasitic force measurements (right) at 2 Hz movement about θ_8 (vertical movement (top)), and θ_9 (horizontal movement (bottom)) at 40° wrist deflection. Red and green dashed traces show measured cable position converted to wrist angles θ_{8c} and θ_{9c}, red and green dash-dot traces show measured wrist angles θ_{8j} and θ_{9j}. Solid traces in force diagrams (b) and (d) refer to the right ordinate and show parasitic forces and moments in N and Ncm.

One possible source for these parasitic forces is an inadequate function of the stress relief cut (see Sec. 5.1.4) which would propagate deformations of the wrist distal component caused by articulation into the force-torque sensor base. Errors could also be introduced by the FTS cables connecting the sensor electrically to the signal conditioning electronics. Movement of the cables could cause a change of resistance inside the cable, or could deform and stress the sensor base including the connection PCB.

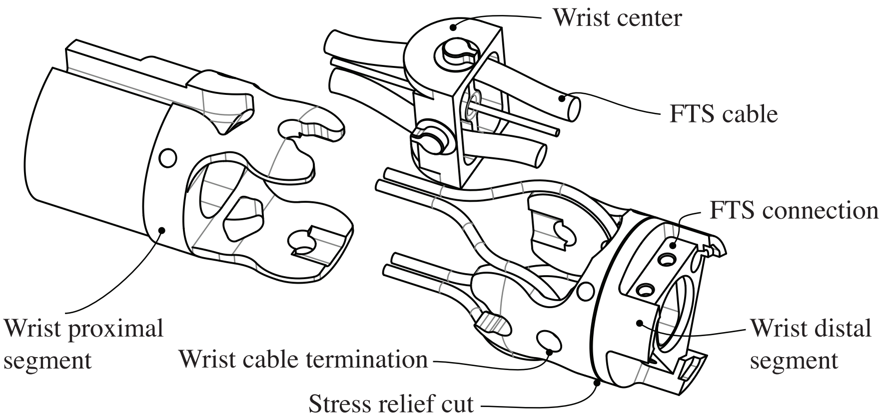

Figure 6.13: Recap of wrist components from Fig. 5.19. Two likely causes for the occurrence of parasitic manipulation forces while articulating the wrist are inadequate decoupling of deformations by the stress relief cut and deformations of FTS cables.

In order to attribute the parasitic forces seen by the force-torque sensor to either cause, a modified tool was built omitting the FTS cables and instead connecting the sensor to the signal conditioning electronics with long, extremely flexible single strands (shown in Fig. 6.14). The wrist motion tracking experiment shown in Fig. 6.12 at 2 Hz articulation frequency was repeated with the modified tool. Results are shown in Fig. 6.15. The force error in f_y is still present for θ_8, but greatly reduced for θ_9. All remaining force components remain below 0.15 N, showing a great reduction in parasitic force components over the initial experiment. It can be concluded, therefore, that a major portion of the original force errors was caused by the FTS cable. A more flexible cable and improved cable strain relief will be included in future designs.

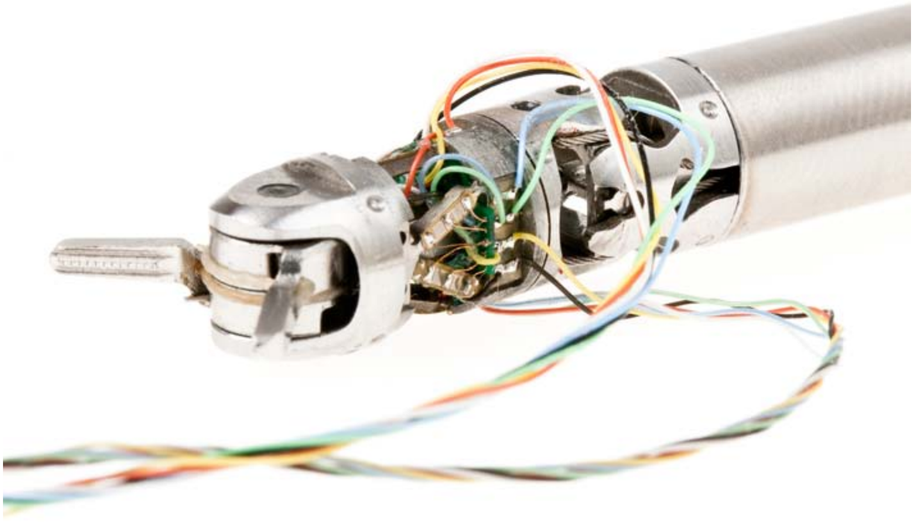

Figure 6.14: Image of modified tool with external sensor connections used in wrist tracking and parasitic force measurement experiments. Rather than routing the sensor connections through the wrist joint, they are realized with thin 38 AWG lead wires in order to reduce the deformation of, and caused by sensor cables. Results are shown in Fig. 6.15.

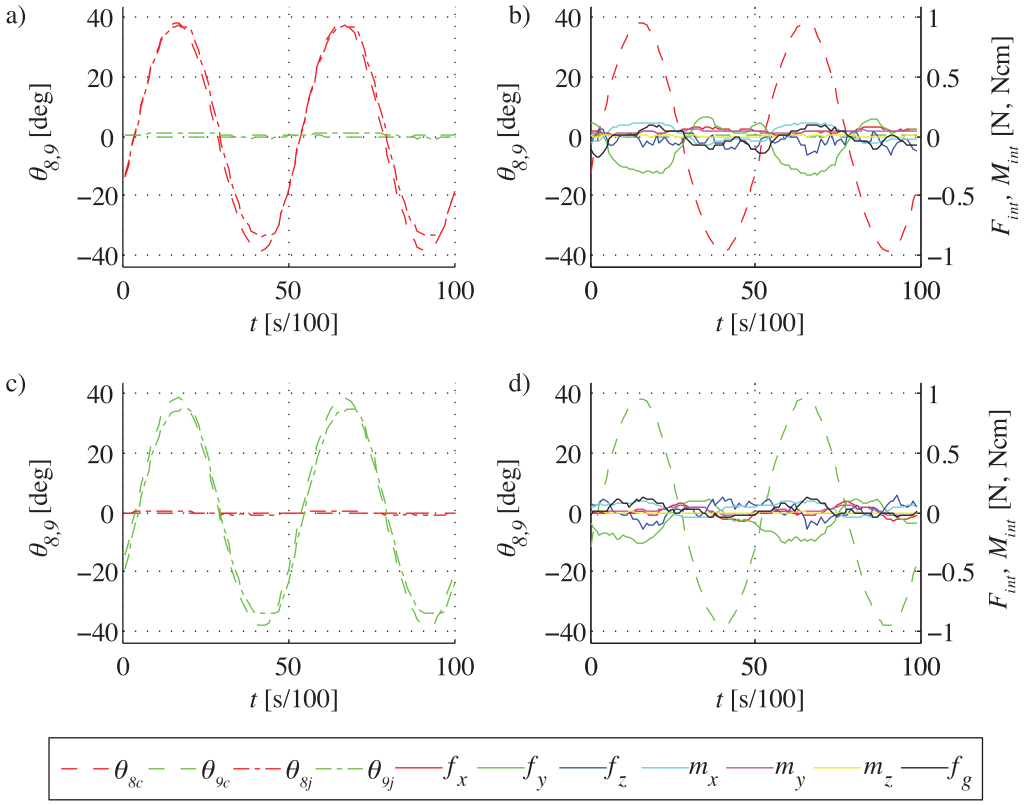

Figure 6.15: Same experiment as Fig. 6.12. However, in this case the force-torque sensor is connected externally with thin 38 AWG lead wires. Wrist motion tracking (left) and parasitic force measurements (right) at 2 Hz movement about θ_8 (vertical movement (top)), and θ_9 (horizontal movement (bottom)) at 40° wrist deflection. Red and green dashed traces show measured cable position converted to wrist angles θ_{8c} and θ_{9c}, red and green dash-dot traces show measured wrist angles θ_{8j} and θ_{9j}. Solid traces in force diagrams (b) and (d) refer to the right ordinate and show parasitic forces and moments in N and Ncm.

6.3 Tissue Palpation

Discerning tissue types and finding inclusions in surrounding tissue are two of the many tasks surgeons perform during open surgical procedures by palpating tissue with their fingers. Two sets of experiments were performed with *MICA* in order to assess the performance of the force-torque sensor while remotely palpating tissue samples. However, commercial artificial samples containing inclusions surrounded by bulk tissue are normally targeted at ultrasound elastography rather than exhibiting specific mechanical properties, and only limited information on mechanical properties is available. Therefore, the in-house manufacturing of artificial tissue samples was investigated, starting from a review of published tissue elasticities.

Direct palpation is used frequently for early cancer screening in mammarian and prostate tissue, therefore a large number of studies Matsumura et al. [210], Samani et al. [211], Krouskop et al. [212], Egorov and Sarvazyan [213], Ahn et al. [214] are concerned with quantifying the Young's modulus for bulk tissue as well as benign and cancerous inclusions in these two fields. Most of these studies are based on force/strain measurements from indention tests using ex-vivo tissue samples to determine the Young's modulus of the tissue. Comparing these studies, it quickly becomes apparent that a large variation in the reported elastic moduli exists. Even results reported in studies with closely matching experimental conditions (strain, strain rate, indenter shape) vary greatly.

The large variation in reported tissue properties makes it difficult to choose specific tissue properties to be simulated during palpation experiments. The most universal statement regarding the range of tissue elasticity was made by Samani et al. [211] relating to mammarian tissue, postulating that "... data indicated that high-grade invasive ductal carcinomas were the stiffest tumors exhibiting a Young's modulus approximately 13 fold larger than either fat or fibroglandular tissue with most other tumors demonstrating a 3-6-fold increase in tissue stiffness".

Manufacturing of artificial tissue samples from commercially available elastomers is further complicated by elastomer properties commonly being stated on the Shore scale and conversion between Young's modulus and Shore Hardness not being straight forward. Kunz and Studer [215] developed a conversion model based on indention tests and experimentally determined model parameters for the Shore A scale only, while tissue elasticities of interest, correspond to Shore 0/C and Shore 00 scales.

Table 6.2: Comparison of tissue Young's modulus measured in several studies for fat, glandular tissue, ductal carcinoma in situ (DCIS) and invasive ductal carcinoma (IDC). All except Egorov and Sarvazyan [213] who used a tactile pressure array were determined by indentation tests.

	Fat	Gland	DCIS	IDC
Reference	Young's modulus [kPa]: $\mathrm{mean} \pm \mathrm{STD}$			
[210] Ind. 0.01 Hz, $\varepsilon = 6\%$, $\varnothing 3\mathrm{mm}$	0.7 ± 0.2	0.8 ± 0.2	3.4 ± 1.3	11.5 ± 8.4
[210] Ind. 0.01 Hz, $\varepsilon = 30\%$, $\varnothing 3\mathrm{mm}$	17.3 ± 4.8	15.4 ± 3.9	15.6 ± 2.0	27.0 ± 9.2
[211] Ind. 0.1 Hz, $\varepsilon = 5\%$, $\varnothing 5\mathrm{mm}$	3.25 ± 0.91	3.24 ± 0.61	16.38 ± 1.55	10.4 ± 2.6– 42.52 ± 12.47
[212] Ind. 0.1 Hz, $\varepsilon = 5 - 30\%$, $\varnothing 4.83\mathrm{mm}$	18 ± 7	28 ± 14	22 ± 8	106 ± 32
[213] Tactile pressure array.	6.9 ± 1.4			95.5 ± 38.89

Furthermore, although silicone itself has good long term stability, that does not necessarily apply to compounds of silicone mixed with plasticizer to create varying mechanical properties. A liver model was created for a previous study at the Robotics and Mechatronics Center containing three lesions of different sizes. Each lesion was created using a silicone composition with Young's modulus twice that of the bulk material. The moduli were adjusted to tissue properties given by surgeons and confirmed using indention testing. After six months, the initially harder lesions had turned far softer than the bulk material. Silicone oils used to adjust the material properties likely had diffused between the different materials, rendering any original specifications obsolete.

The variation in real tissue data and the lack of realistic, reproducible, long term stable tissue phantoms creates a limitation for the experiment design. It was decided, therefore, to limit palpation experiments to the comparison of relative stiffness only, albeit still ensuring that absolute stiffness values are within the previously reported range for real tissue.

- *A subjective evaluation* was carried out, involving users ranking 4 samples of varying mechanical properties according to perceived stiffness. Relative stiffness values of 1, 3, 6 and 13, representing the relative variation in tissue properties found by Samani et al. [211] were selected.
- *An objective evaluation*, autonomously creating a stiffness map of a silicone sample containing areas of varying mechanical properties.

- *An objective evaluation*, autonomously creating a stiffness map of an ex-vivo porcine liver section.

Subjective Evaluation

In this study, users were asked to compare samples of different elasticities and rank them in ascending order. To provide reproducible test conditions, tissue stiffness was simulated by metal leaf springs of varying spring rates. The spring rates are based on the observation by Samani et al. [211], and relative stiffness values of 1, 3, 6 and 13 were chosen to represent the variation in tissue properties observed in mammarian tissue.

Three out of four studies mentioned in Tab. 6.2 show force/strain curves indicating viscoelastic properties. Still, the studies used a linear elastic approximation to calculate a mean Young's modulus over the indention pass, neglecting damping and relaxation effects, assuming that indention rate is slow and there is no dwell time. For the calculation of the Young's modulus, all studies assumed tissue to be incompressible and elastic. Given the large variation in tissue properties found in literature, it was decided to follow the linear approximation and use steel leaf springs to represent four distinct stiffness values for the present evaluation.

Hertzian contact theory between a rigid cylinder and elastic half space (see Fig. 6.16 (a)) is used to determine the indention force and calculate a mean tissue spring rate $\frac{F}{d}$ from the reported Young's modulus and indenter shape. Tissue properties in Samani et al. [211] were determined by indention testing with a cylindrical indenter of $R = 2.5\ \mathrm{mm}$ and assuming tissue Poission's ratio of $\nu = 0.495$:

$$F = 2E^{\star}Rd \tag{6.1}$$

with

$$E^{\star} = \frac{E}{(1-\nu^2)} \tag{6.2}$$

In the case of a rigid sphere and elastic half space (see Fig. 6.16 (b)), the indention force is given by:

$$F = \frac{4}{3}E^{\star}\sqrt{R}\sqrt{d^3} \tag{6.3}$$

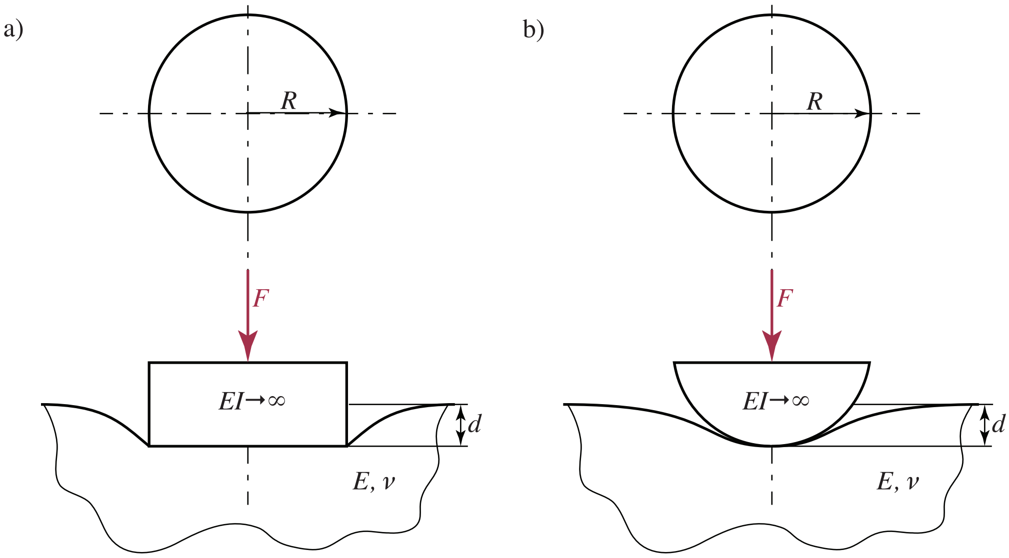

Figure 6.16: Indention based on Hertzian contacts (Kunz and Studer [215], Popov [216]). Rigid cylinder (a) and rigid sphere (b) with elastic half space.

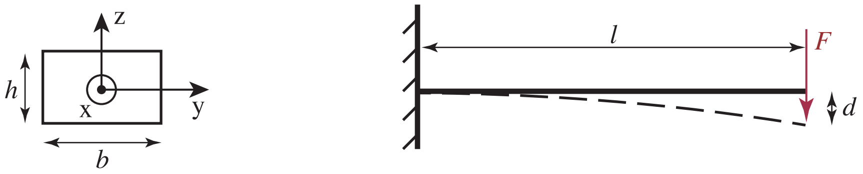

Figure 6.17: Deformation of single sided rigidly supported beam under point load.

The spring rate calculated with either Eq. 6.1 or Eq. 6.3 is then simulated by a leaf spring acting as single sided rigidly supported beam under point loading (see Fig. 6.17) using linear elastic theory. Flat leaf springs were chosen for this experiment as they obviate the necessity for mechanical guides and allow for much lower spring rates to be displayed successfully.

Flat steel leaf springs of constant width $b = 10\mathrm{mm}$ and Young's module of $E = 205000\,\frac{\mathrm{N}}{\mathrm{mm}^2}$, were available in thickness h increments of 0.05 mm. The end point deflection force for a single sided, rigidly supported beam (see Fig. 6.17) is given by:

$$F = 8\frac{E}{l^3}\frac{bh^3}{12}d \tag{6.4}$$

By matching the spring rate $\frac{F}{d}$ of a particular tissue to the spring rate of the leaf spring, the leaf thickness h and clamp length l required to represent a linear approximation of that particular tissue can be calculated, resulting in the following parameters:

Table 6.3: Spring dimension and spring rate corresponding to the four selected tissue elasticities.

Young's modulus [kPa]	10	30	60	130
Tissue spring rate $\frac{F}{d}$ $[\frac{\mathrm{N}}{\mathrm{m}}]$	66.2	198.7	397.4	861.0
Leaf spring thickness h [mm]	0.3	0.4	0.55	0.7
Clamp length l [mm]	82	76	83	82

The experimental setup is shown in Fig. 6.18. Springs are mounted underneath a cover plate to hide relative spring dimensions from the user. Only short pegs attached to the free end of the leaf spring are protruding through four holes in the plate and define the force application location. The peg arrangement was completely covered with a thin flexible membrane to avoid direct comparison of peg movement within each hole, which gave quite a strong indication of the stiffness. Using a bright blue membrane, only the deformation of the membrane was clearly visible. Only the peg location and four symbols (circle, rectangle, triangle, star), assigned to the four locations are marked on top of the membrane. Mapping between symbols and elasticities was chosen randomly. The four elasticity values shown in Tab. 6.3 were chosen, starting with a Young's modulus of 10 kPa and steps of factors 3, 6, and 13. The number of elasticity samples and the close proximity of peg locations was selected to match the workspace of the palpation tool. Users could reach all four pegs without the need for repositioning the tool. During a preliminary experiment using six samples and larger spacing, users indicated that the need for tool repositioning interfered severely with comparing the different elasticities. During the actual experiment, users were asked to compare the four elasticities by pressing down on the pegs and rank them in ascending order.

Four separate palpation experiments were compared, in the following order:

- *Remote robotic palpation without force feedback* using the palpation tool in the *MiroSurge* scenario with force feedback turned off.
- *Remote robotic palpation with force feedback* using the palpation tool in the *Miro-*

Surge scenario with force feedback turned on.

- *Direct manual palpation* by depressing the pegs with one finger.
- *Indirect manual palpation* by depressing the pegs with a plastic rod as 'ideal' telemanipulator.

For the two remote robotic palpation experiments, the complete *MiroSurge* scenario was used (see Fig. 2.2) with users controlling the palpation tool by using the Force Dimension omega.7 haptic input device. A 3D view of the scene was provided by a 3D endoscope image displayed on an autostereoscopic monitor. In the case without force feedback, only the built-in gravity compensation of the Force Dimension omega.7 devices was used. In the force feedback case, the three force components measured by the palpation tool were displayed to the user. No moments were displayed, assuming a point contact between the spherical tip of the palpation tool and the circular flat area of the pegs' tops. Force amplification was set to unity and the motion was scaled by a factor of $^1/_3$, matching impedance of *MIRO* and Force Dimension omega.7.

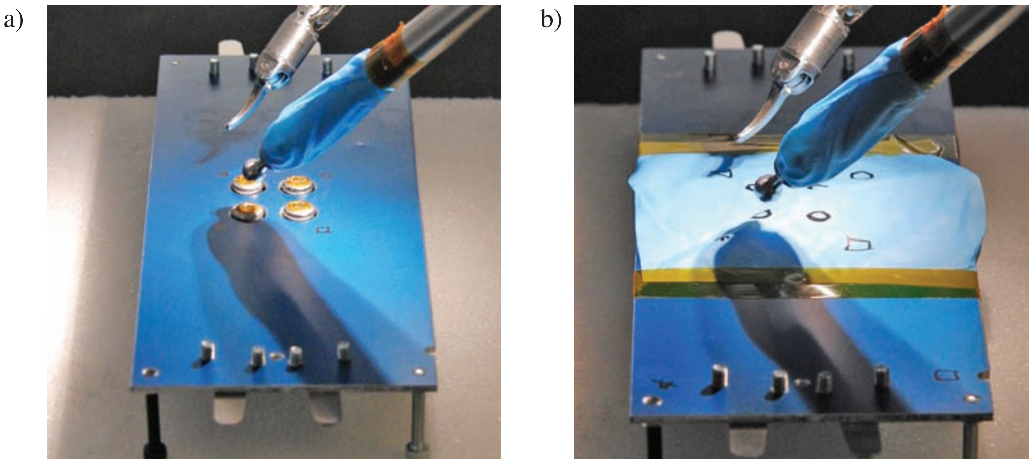

Figure 6.18: Palpation test bed without membrane cover (a) and with cover (b).

As participants for this experiment, 15 volunteers were recruited among RMC staff, 8 of which had previous experience using the *MiroSurge* setup (ranging from only having moved the tools to tying surgical sutures), 7 were using the setup for the first time during this experiment. Participants were given a few minutes to familiarize themselves with the operation of the *MiroSurge* setup and on how to clutch and recenter the palpation tool prior to the experiments. No further instructions were given, users could take as much time as needed and were allowed to follow any or no pattern when exploring elasticities. While novice participants focused only on the given task and generally reached a conclusion quickly (between 40 seconds and 1:30 minutes), experienced users spent some time evaluating and discussing system performance and characteristics unrelated to the palpation experiment. Answers were scored on an error scale from 0 (all correct), 1 (one mix-up of stiffness values, regardless of neighboring or distant), 2 (two mix-ups), to 3 errors (all wrong).

In the case of robotic palpation without force feedback, only 8 participants gave an answer (scoring from 0 to 3 errors), while 7 participants (from both the experienced and novice groups) declined to guess on a stiffness order. In general, there was no observable difference in performance between both groups. In the case of robotic palpation with force feedback 8 participants rated all samples in the correct order and 7 participants scored with one error each.

Table 6.4: Result of subjective palpation experiment showing the average number of errors in sorting tissue stiffness.

Test	Direct	Ideal	Tele noFFB	Tele FFB
Average errors	0	0.07	1.75	0.43
Standard Deviation	0	0.27	0.89	0.51

Table 6.5: Statistical significance of average palpation errors.

Direct vs. Ideal	Ideal vs. Tele noFFB	Ideal vs. Tele FFB	Tele noFFB vs. Tele FFB
0.336	0.002*	0.055	0.028*

In the case of direct manual palpation all participants rated the order correctly, and in the case of indirect manual palpation (using a plastic rod as ideal telemanipulator), 14 participants rated the order correctly, one participant scored with one error. The average number of errors, including the standard deviation for all experiments is shown in Tab. 6.4. Using a student's t-test, significance of the results was evaluated (see Tab. 6.5 with significant difference within a 95% confidence interval denoted by an asterisk). Obviously, there was no difference between the direct manual and ideal telemanipulation results. Although performance using the robotic setup with force feedback is visibly worse than both the direct and indirect manual cases, the difference in error rates failed to reach a significant level by a tiny fraction. Robotic palpation without force feedback showed significantly worse results compared to both the robotic case with force feedback as well as the indirect manual case.

It can be concluded from the experimental outcome that although robotic palpation performance using the force feedback tool was worse than both direct and indirect manual palpation performance, it was significantly better than using a robotic tool without force feedback.

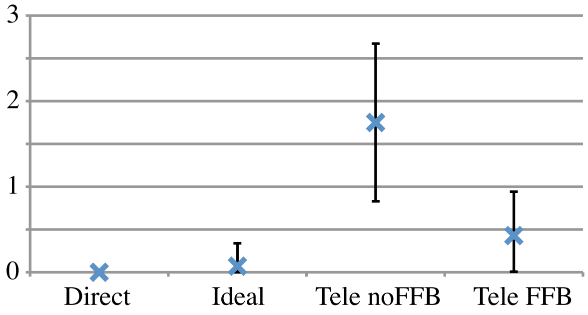

Figure 6.19: Result of subjective palpation experiment showing the average number of errors in sorting tissue stiffness.

Objective Evaluation

The palpation tool was used in an objective (no user involvement) setup to generate stiffness maps of simulated and ex-vivo tissue samples. The experiments required most of the *MiroSurge* infrastructure (see Fig. 2.2) except the user input console. One of the *MIRO* arms is used to move the *MICA* with attached palpation tool along a grid pattern with a grid spacing of 3 mm in a plane parallel to the OR table while moving vertically down towards the table and back up at every grid point. Tissue contact is detected by a rise in force along the z-axis of the tool. A force of 0.15 N was selected as threshold for tissue detection. The tool then continues penetrating the tissue until either a predetermined depth threshold of 32 mm or force threshold of 2 N was reached, and then reverses direction. The z-coordinates of both tissue detection and direction reversal were recorded along with all tissue interaction forces. Infrastructure and software models for this experiment were provided by [217].

In post processing, the tissue spring rate is calculated as maximum penetration depth divided by maximum penetration force along the tool axis (f_z). Fig. 6.20 shows the experimental setup (a) and resulting map of tissue spring rates (b) for a liver phantom placed on an elastic surface. The silicone liver phantom was discussed at the top of Sec. 6.3. Bulk stiffness was modelled after real tissue properties, and three hardened lesions (locations marked as 1 to 3 in Fig. 6.20) were introduced below the surface consisting of silicone with a stiffness twice that of the bulk tissue. However, over time the silicone used in the lesions softened, likely by diffusion, and at the time of the experiment were much softer than the surrounding material. The result plot (Fig. 6.20 (b)) shows the detected tissue surface as solid surface with colours denoting the measured spring rate. The buried mesh surface shows the reversal locations. It can be seen that in regions of softer material, penetration was deeper than in stiffer areas. The variation in spring rate can clearly be seen in the resulting map, with a minimal spring rate of $113\frac{\mathrm{N}}{\mathrm{m}}$ at the location of the lesions and maximal spring rate of $355\frac{\mathrm{N}}{\mathrm{m}}$ in between. The elastic underground shows a spring rate of $230 - 250\frac{\mathrm{N}}{\mathrm{m}}$.

The objective palpation experiment was repeated with an ex-vivo section of porcine liver. The liver was obtained from a butcher shop the same day the animal was killed and had been refrigerated prior to the experiments. The liver section used for the palpation experiment was placed on a surgical drape on a hard surface with the liver surface facing upward (seeFig. 6.21). An identical 20 by 20 grid using the same force and penetration thresholds as above was used for generating the stiffness map. Minimal spring rate was recorded as $149\frac{\mathrm{N}}{\mathrm{m}}$ in location (1) (see Fig. 6.21 (a) and Fig. 6.22) where the palpation tool broke through

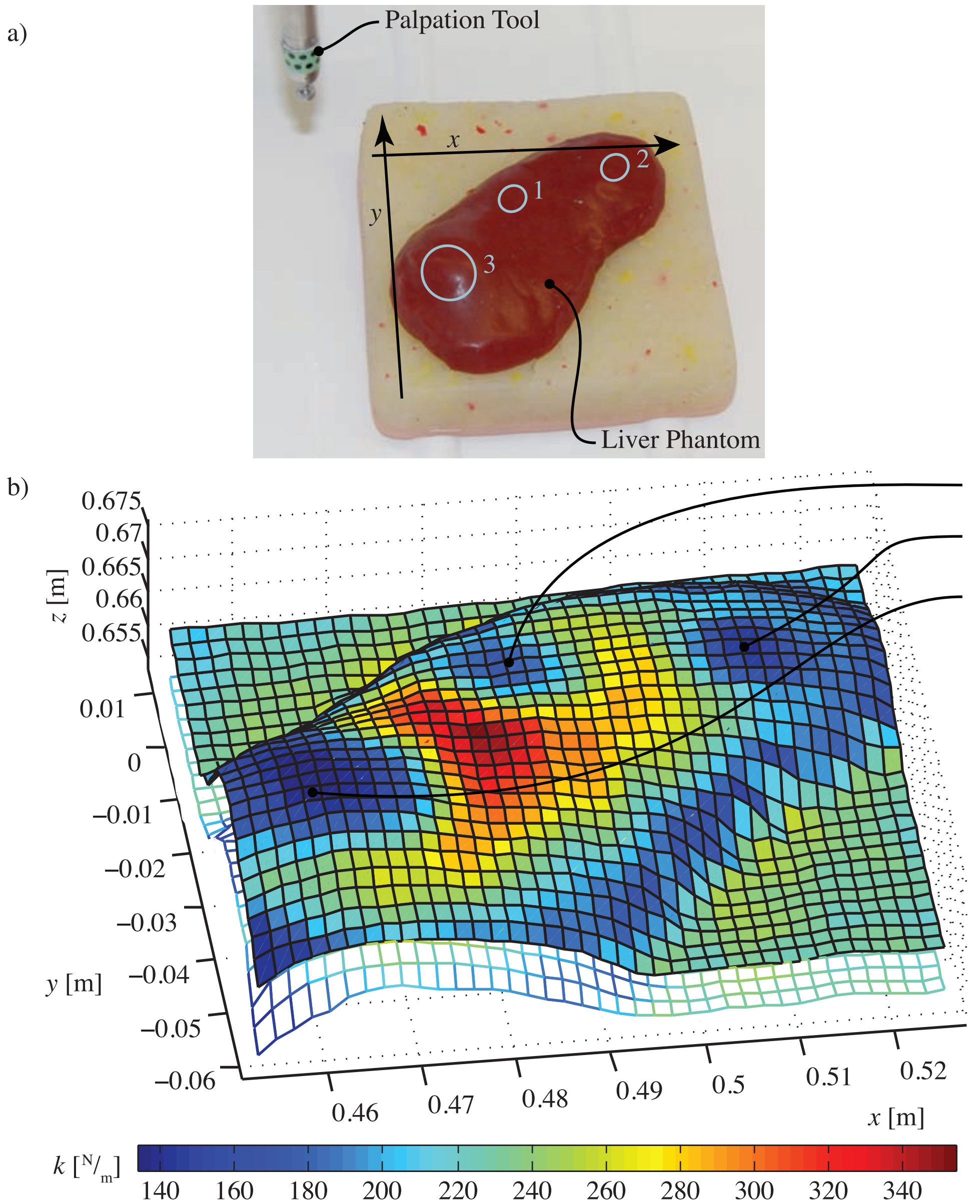

Figure 6.20: Test setup (a) and results (b) for phantom liver palpation. Minimal spring rate of $113\,\frac{\mathrm{N}}{\mathrm{m}}$ and maximal spring rate of $355\,\frac{\mathrm{N}}{\mathrm{m}}$. Locations 1, 2 and 3 correspond to the original locations of lesions which can clearly be identified by lower spring rate.

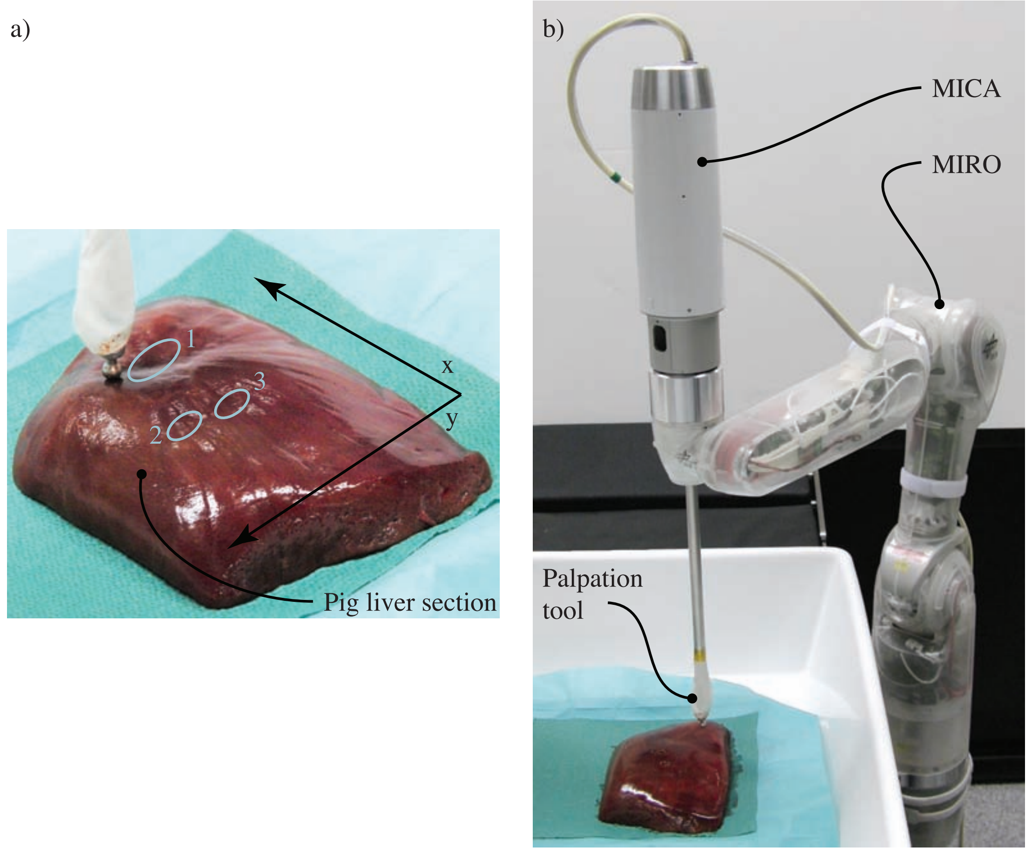

Figure 6.21: Test setup for pig liver palpation. Closeup view of palpation tool (a) and overview of *MICA* attached to *MIRO* arm (b).

the tissue surface into a cavity just below the surface. Tool penetration can clearly be seen in the meshed surface of Fig. 6.22 at location (1). The maximal spring rate was recorded as $650\frac{\mathrm{N}}{\mathrm{m}}$. Locations 2 and 3 on the stiffness map (see Fig. 6.21) were visible as lesions on the liver surface due to a difference in appearance, however, they could not be further classified.

The values reported for the Young's modulus of liver tissue determined by compression tests range from between 0.64 kPa to 20 kPa in Yeh et al. [218] to 640 kPa in Burdick and Mauck [219]. Using Eq. 6.3 the Young's modulus for the liver in the current experiment can be estimated. Results show an average penetration depth of 4.0 mm and an average spring rate of $485.5\frac{\mathrm{N}}{\mathrm{m}}$ over the entire grid during the palpation experiment. Assuming a tissue

Poission's ratio of $\nu = 0.495$ and using the radius of the spherical indenter of $R = 3\ \mathrm{mm}$, the Young's modulus equates to $0.079\ \frac{\mathrm{N}}{\mathrm{mm}^2}$ or 79 kPa. Given the range of reported values the experimental result appears to be reasonable.

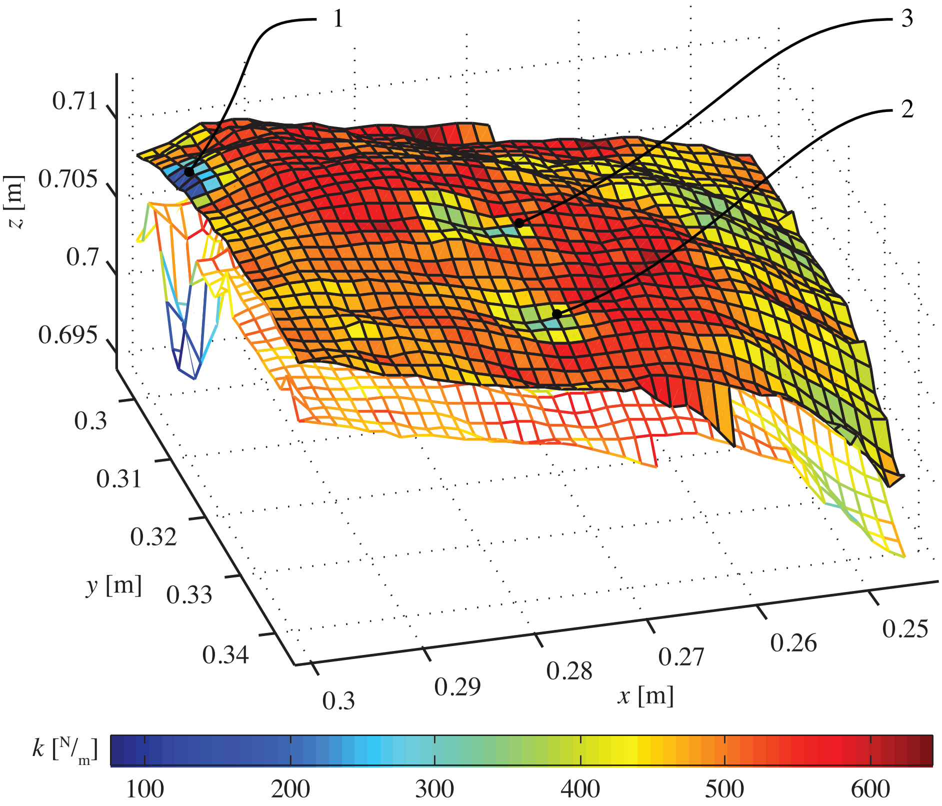

Figure 6.22: Pig liver palpation results. Minimal spring rate of $149\frac{\mathrm{N}}{\mathrm{m}}$ and maximal spring rate of $650\frac{\mathrm{N}}{\mathrm{m}}$. At location (1) the palpation tool penetrated the surface resulting in lowest spring rate values. Locations (2) and (3) (see Fig. 6.21) could be visually identified on the surface due to a different appearance.

These results conclude the experimental section presented in this thesis. Component level experiments have shown that the tool fulfills the functional requirements laid out in Sec. 3.1. System level experiments provided a first glimpse at the whole system performance of the presented force feedback tool within the *MiroSurge* scenario.

7

Conclusion

7.1 Discussion

A review of research in the field of force feedback for minimally invasive surgery has shown that the benefit of dexterity has been established while the impact of force feedback on the surgeon's task performance is still being debated. Individual components – tools, articulated wrist designs and full-DoF force-torque sensor – exist, however the combination of all these components into one dexterous tool that provides full (7 DoF) force feedback has been lacking.

It has been shown in this thesis that such a tool requires more than just a combination of off-the-shelf components, but that the interaction and interdependence of these components needs to be addressed in the tool design. Still, such a tool is possible. A tool concept has been proposed, implemented and tested in this thesis combining a 2 DoF articulated wrist with a 6 DoF force-torque sensor. The wrist and force-torque sensor components have been integrated with an end effector, which was implemented in the shapes of a generic needle holder, Maryland grasper, and Metzenbaum scissors. In addition to the manipulation forces, gripping forces are measured by an additional single degree force sensor.

The 2 DoF wrist is based on an universal joint with intersecting axes and has a range of motion of 43° . Actuation is accomplished by stainless steel cables and can reach full range motion up to 5 Hz (translating to $700°\frac{1}{s}$). Dynamics and according wrist accuracies have been reported in this thesis. Tracking errors remain consistent over the entire dynamic range with $\pm 2.5°$ at up to $10°$ wrist articulation, growing to $\pm 4°$ at up to $40°$ wrist articulation.

The force-torque sensor for measuring interaction forces and torques between the tool tip and manipulated tissue is based on a Stewart platform with flexural joints. The measurement range is up to 10 N for forces and up to 150 Nmm for torques. It is currently the smallest 6 DoF force-torque sensor with a measurement range of several Newton. Smaller 6 DoF force-torque sensor have been reported, however they are micro-machined from single crystal silicon and have measurement ranges in the fractional Newton range.

It has also been shown that high quality force feedback can only be achieved if force-torque sensors are accounted for in the overall design concept right from the beginning. Experiments have shown that wrist and end effector actuation cause large measurement errors. It is, therefore, absolutely crucial that the force measurement is isolated from the actuation forces of wrist and end effector as well as from the wrist motion. In case of the end effector, friction in the tip actuation mechanism alone can exceed the tissue manipulation forces that are to be measured. These errors cannot be compensated for by software. Mechanical isolation principles for both wrist articulation, and end effector actuation have been proposed and successfully implemented.

The tool has been fully integrated into the DLR Robotics and Mechatronics Center's *MiroSurge* system for minimally invasive robotic surgery as the self-sufficient dedicated instrument *MICA*. Aside from experiments to test individual components, two system wide studies have been conducted.

In a subjective evaluation of perceived tissue stiffness, a number of users were asked to order four stainless steel leaf springs according to increasing stiffness by touching them with a finger, with a plastic rod (representing an ideal telemanipulator), using robotic palpation without force feedback, and finally using robotic palpation with force feedback. For the robotic experiments users were controlling the *MICA* instrument from the *MiroSurge* surgeon console. Steel leaf springs were used in place of tissue samples to generate repeatable data. Robotic palpation with force feedback significantly reduced the error rate over robotic palpation without force feedback, and while robotic palpation with force feedback showed a higher error rate compared to direct palpation with the ideal telemanipulator, the difference did not reach statistical significance.

In an objective evaluation the surface stiffness maps of a liver phantom made from silicone and of an ex-vivo porcine liver were generated without user interaction. The *MiroSurge* system was used to palpate a grid of surface points with the *MICA* instrument. Depth of indentation and according force levels were recorded and converted into a linear approximation of tissue spring rates. This autonomous palpation tool generates colored stiffness maps that show differences in much more detail than the human users were able to identify in the subjective evaluation. The functionality of the advanced force feedback tool design proposed in this thesis could, thereby, be proven convincingly.

At this point, the intra-corporal wrist and force-torque sensor can be entered into the state of the art. Tab. 7.1 and Tab. 7.2 showcase the new entries into the survey tables presented in Sec. 2.3.

7.2 Outlook

Based on the articulated, force feedback integrated surgical tool presented in this thesis, a number of future development and research topics are envisioned or are already in progress. The tool and *MICA* instrument have successfully been integrated into the *MiroSurge* scenario and evaluated in a number of phantom based lab experiments with engineers and surgeons. Reactions have been overall positive.

Recent research presented by Zacharias [149] has shown that extending the wrist range of motion of a surgical tool has a much greater impact on reachability than shortening the distal portion of the wrist. Still, the distal length will have to stay below the maximum number of 30 mm reported by Konietschke [145] during his work on kinematics optimization of the *MIRO* arm. A wrist RoM extension through a two stage universal joint design has been proposed in Fig. 4.7 (h) and will be revisited in the near future.

Currently *MICA* is a robotic instrument aimed towards medical applications. In order to make the transition towards a medical instrument, an evaluation in a realistic clinical setting is indispensable. Consequently, an animal trial of the entire *MiroSurge* system in a realistic clinical setting is planned for the near future. Two important work packages will have to be concluded prior to these animal tests:

First, one of the most important surgical tool functionalities in minimally invasive surgery is electrosurgery. An efficient dissection of blood perfused tissue or the quick sealing of capillary blood vessels is not possible without electro-surgical coagulation and cauterization. The electrical isolation of each jaw in the end effector from the tool body and sensor components is currently under way. The connection of either one or two electrical leads

Table 7.1: Wrist result specifications.

DoF	RoM [°]	Size $d \cdot l$ [mm]	Kinem.	Segm.	Joint	Trans.	Actuation	F_{Tip} [N]	Dynamics	Accuracy [°]	FTS
2+1	±43, 60	⌀10x18.75	pys	1	univ	c	BLDC 100 W	10,10	$560^\circ \frac{1}{s}$	±4	6+1

Table 7.2: Sensor result specifications at rest. Resolution after amplifier noise calculated from Tab. 5.5 with Eq. 5.13, accuracy data calculated from Tab. 6.1.

DoF	Load	Range	Size	Method	Location	Bandw.	Sampling	Resolution		Accuracy		Wrist DoF
			[mm]			[Hz]	[Hz]	[N,Nmm]	[eq. bit]	[N,Nmm]	[eq. bit]	
6+1	$\mathrm{f_{xy}}$	10 N	⌀10	SG, HB	Tip	400	3000	0.07 N	8.2	0.16 N	7	2+1
	$\mathrm{f_z}$	10 N						0.16 N	7.1	0.45 N	5.5	
	$\mathrm{m_{xy}}$	150 Nmm						0.4 Nmm	9.6	4.9 Nmm	5.9	
	$\mathrm{m_z}$	100 Nmm						0.3 Nmm	9.3	2.8 Nmm	6.2	
	$\mathrm{f_g}$	10 N						0.1 N	7.6	0.4 N	5.6	

through the tool shaft, terminated in the interface unit will allow the application of the tool in mono and bipolar cautery.

Second, the instrument is designed for multiple uses, therefore, cleaning and sterilization of the tool prior and following contact with real tissue is absolutely paramount. So far the seals and encapsulations of individual components have been taken into account during the component design stage, but not implemented during tool assembly to allow for subsequent disassembly, component wear evaluation and repairs. Tools coming into contact with tissue and fluids, and requiring subsequent cleaning will need all those safeguards in place. Cleaning and sterilization procedures will have to be established and evaluated.

Providing a tool that will allow the assessment of the impact and possible benefit of haptic feedback during surgery was one of the stated goals of this thesis. This assessment requires the integration of the entire system: robotic arms, instruments, surgeon workstation, vision system, control infrastructure. The *MiroSurge* system has now reached a maturity where meaningful experiments can be conducted. The initial evaluation of simplified and standardized tasks will lead to better understanding of the whole system performance. Future requirements for further testing as well as for tool designs can be gained from these tests. Evaluating the task benefit of a force feedback integrated MIRS system on precisely quantifiable system specific measures alone (tool path length, exerted forces, time) is difficult as these measures do not directly relate to an overall benefit. Subjective impressions e. g. usability, immersion, user-friendliness play an important role. Motion analysis and the recognition of target oriented movements as well as auxiliary motions can be performed. A performance metric has to be developed to account for e. g. the trade-off between task completion time and error rate. An effort to identify meaningful tasks or task primitives as well as to define a useful performance metric is currently under way at the Robotics and Mechatronics Center with the help of surgeons and psychologists.

The sensor technology developed in this thesis need not be limited to applications in the medical field. Various applications for small and stiff multi-DoF force-torque sensor can be found in the field of robotics alone, e. g. in the finger tips of robotic hands or in the toes of small multi-legged autonomous crawling robots. Especially the application in autonomous crawlers, where the force-torque sensors have to support the robot's body weight, is predestined for the Stewart platform based sensor described in this thesis. Lower sensitivity in the direction normal to the ground helps to support the weight while preserving higher sensitivity in all other directions, allowing for accurate prediction of ground slope and surface consistency.

In conclusion, the *MICA* instrument transfers the benefit of light-weight advanced robotic technology into the operating room, and places additional functionality at the surgeons fingertips. This thesis has proven the feasibility of combining articulation and high quality force feedback in a minimally invasive tool for robotic surgery. It is the opinion of the author that this advance in robotic technology will increase the immersion and user-friendliness of robotic surgery for the benefit of surgeon and patient.

List of Figures

List of Tables

Bibliography

[1] M.-T. Huang, P.-L. Wei, C.-C. Wu, I.-R. Lai, R. J. Chen, and W.-J. Lee, “Needlescopic, laparoscopic, and open appendectomy: A comparative study,” *Surgical Laparoscopy, Endoscopy & Percutaneous Techniques*, vol. 11, no. 5, pp. 306–312, Oct. 2001.

[2] S. Sauerland, R. Lefering, and E. Neugebauer, “Laparoscopic versus open surgery for suspected appendicitis,” *Cochrane Database of Systematic Reviews*, vol. 4, p. Art. No.: CD001546, 2002, DOI: 10.1002/14651858.CD001546.pub2.

[3] C. Wullstein, M. Golling, and W. O. Bechstein, “Telerobotics in laparoscopic general surgery,” *European Journal of Surgery*, vol. 36, no. 4, pp. 233–238, 2004.

[4] U. A. Hagn, “The Aspect of Versatility in the Design of a Lightweight Robot for Surgical Applications,” Ph.D. dissertation, University of Hannover, 2011, iSBN: 978-3-86853-797-0.

[5] T. Ortmaier, U. Seibold, U. Hagn, D. Boehm, H. Reichenspurner, and G. Hirzinger, “Autonomy and Haptic Feedback in Minimally Invasive Robotic Surgery,” in *4th Annual Meeting of the International Society for Minimally Invasive Cardiac Surgery (ISMICS), Munich - Germany*, 2001. [Online]. Available: http://www.hsforum.com

[6] J. M. Sackier and Y. Wang, *Computer-Integrated Surgery*. MIT Press, 1995, ch. Robotically Assisted Laparoscopic Surgery: From Concept to Development, pp. 577–580.

[7] T. Ortmaier, H. Weiss, and G. Hirzinger, “Minimally Invasive Robotic Surgery: Foundations and Perspectives,” in *ICRA - Proc. of the IEEE Int. Conf. on Robotics and Automation*, Taipei, Taiwan, Sep. 2003.

[8] J. Rosen, B. Hannaford, and R. M. Satava, Eds., *Surgical Robotics*. New York, Dordrecht, Heidelberg, London: Springer, 2011, DOI: 10.1007/978-1-4419-1126-1.

[9] VDI, “Methodik zum Entwickeln und Konstruieren technischer Systeme und Produkte (Systematic approach to the development and design of technical systems and products),” VDI-Gesellschaft Produkt- und Prozessgestaltung (GPP), Fachbereich Produktentwicklung und Mechatronik, Richtlinie VDI 2221, May 1993, iCS: 03.100.40.

[10] N. Frei, “Der Konstruktionsprozess: Wirkmodelle basierend auf Constraints,” Dissertation, ETH Zürich, 2002.

[11] T. Ortmaier, H. Weiss, U. Hagn, M. Grebenstein, M. Nickl, A. Albu-Schäffer, C. Ott, S. Jörg, R. Konietschke, L. Le-Tien, and G. Hirzinger, “A Hands-On-Robot for Accurate Placement of Pedicle Screws,” in *ICRA - Proc. of the IEEE Int. Conf. on Robotics and Automation*, Orlando, Florida, USA, 2006.

[12] U. A. Hagn, M. Nickl, S. Jörg, G. Passig, T. Bahls, A. Nothhelfer, F. Hacker, L. Le-Tien, A. Albu-Schäffer, R. Konietschke, M. Grebenstein, R. Warpup, R. Haslinger, M. Frommberger, and G. Hirzinger, “The DLR MIRO: a versatile lightweight robot for surgical applications,” *Industrial Robot: An International Journal*, vol. 35, no. 4, pp. 324–336, 2008, DOI: 10.1108/01439910810876427.

[13] U. Hagn, T. Ortmaier, R. Konietschke, B. Kübler, U. Seibold, A. Tobergte, M. Nickl, S. Jörg, and G. Hirzinger, “Telemanipulator for Remote Minimally Invasive Surgery,” *IEEE Robotics & Automation Magazine*, vol. 15, no. 4, pp. 28–38, Dec. 2008, DOI: 10.1109/MRA.2008.929925.

[14] U. Hagn, R. Konietschke, A. Tobergte, M. Nickl, S. Jörg, B. Kübler, G. Passig, M. Gröger, F. Fröhlich, U. Seibold, L. Le-Tien, A. Albu-Schäffer, A. Nothhelfer, F. Hacker, M. Grebenstein, and G. Hirzinger, “DLR MiroSurge: a versatile system for research in endoscopic telesurgery,” *International Journal of Computer Assisted Radiology and Surgery*, vol. 5, no. 2, pp. 183–193, 2009, DOI: 10.1007/s11548-009-0372-4.

[15] Force Dimension, “Force Dimension,” Website, 2011, [Link accessed 8-October-2011]. [Online]. Available: http://www.forcedimension.com/

[16] ESA, “ECSS E-50-12A SpaceWire - Links, nodes, routers and networks,” European Space Agency, Tech. Rep., 2003, [Link accessed 13-August-2011]. [Online]. Available: http://spacewire.esa.int

[17] RIM, “QNX Real Time Operating System,” Research in Motion, Website, 2011, [Link accessed 13-August-2011]. [Online]. Available: http://www.qnx.com

[18] B. Bäuml and G. Hirzinger, “When hard realtime matters: Software for complex mechatronic systems,” *Robototics and Autonomous Systems*, vol. 56, pp. 5–13, Jan. 2008, dOI: 10.1016/j.robot.2007.09.017.

[19] G.-Q. Wei, K. Arbter, and G. Hirzinger, “Real-time visual servoing for laparoscopic surgery,” *IEEE Engineering in Medicine and Biology*, vol. 16, no. 1, pp. 40–45, Jan. 1997, DOI: 10.1109/51.566151.

[20] K. Omote, H. Feussner, A. Ungeheuer, K. Arbter, G.-Q. Wei, J. R. Siewert, and G. Hirzinger, “Self-Guided Robotic Camera Control for Laparoscopic Surgery Compared with Human Camera Control,” *The American Journal of Surgery*, vol. 117, pp. 321–324, Apr. 1999.

[21] U. Hagn, M. Nickl, S. Jörg, A. Tobergte, B. Kübler, G. Passig, M. Gröger, U. Seibold, R. Konietschke, T. Ortmaier, and G. Hirzinger, “DLR MiroSurge – Towards Versatility in Surgical Robotics,” in *CURAC - Jahrestagung der Deutschen Gesellschaft für Computer- und Roboterassistierte Chirurgie*, D. Bartz, S. Bohn, and J. Hoffmann, Eds., Leipzig, Germany, 2008, pp. 143–146.

[22] F. Roeske, “Entwurf und Implementierung einer Architektur fr die Anbindung von Nutzerschnittstellen an die Steuerung eines Robotiksystems fr die Chirurgie,” Masterarbeit, Hochschule Mannheim, Aug. 2011, DLR Institut für Robotik.

[23] D. B. Camarillo, T. M. Krummel, and J. K. Salisbury, “Robotic technology in surgery: past, present and future,” *The American Journal of Surgery*, vol. 188, pp. 25–155, 2004.

[24] H. L. Kim and P. Schulam, “The PAKY, HERMES, AESOP, ZEUS, and daVinci robotic systems,” *Urologic Clinics of North America*, vol. 31, no. 4, pp. 659 – 669, 2004, DOI: 10.1016/j.ucl.2004.06.008.

[25] V. Dotzel, D. Wetzel, D. Wilhelm, A. Schneider, G. Wessels, and H. Feusner, “Roboter- und Navigationssysteme: Praktikabilität für den Operateur - Nutzen für den Patienten?” *Zentralblatt Chirurgie*, vol. 128, pp. 227–231, 2003.

[26] R. Taylor and D. Stoianovici, “Medical Robotics in Computer-Integrated Surgery,” *IEEE Transactions on Robotics and Automation*, vol. 19, no. 5, pp. 765–781, 2003.

[27] K. Cleary and C. Nguyen, “State of the art in surgical robotics: clinical applications and technology challenges,” *Computer Aided Surgery*, vol. 6, no. 6, pp. 312–328, 2001.

[28] B. Davies, "A Review of Robotics in Surgery," *Proc. of the Institution of Mechanical Engineers: Journal of Engineering in Medicine*, vol. 214, pp. 129–140, 2000.

[29] M. Ghodousssi, S. Butner, and Y. Wang, "Robotic Surgery – The Transatlantic Case," in *ICRA - Proc. of the IEEE Int. Conf. on Robotics and Automation*, 2002.

[30] Intuitive Surgical, "Company profile of Intuitive Surgical, Inc., Sunnyvale, CA, USA," Website, 06 2011, [Link accessed 13-August-2011]. [Online]. Available: http://www.intuitivesurgical.com

[31] G. Guthart and J. Salisbury, "The Intuitive Telesurgery System: Overview and Application," in *ICRA - Proc. of the IEEE Int. Conf. on Robotics and Automation*, vol. 1, San Francisco, CA, USA, Apr. 2000, pp. 618–621, DOI: 10.1109/ROBOT.2000.844121.

[32] G. T. Sung and I. S. Gill, "Robotic Laparoscopic surgery: A Comparison of the daVinci and Zeus Systems," *Adult Urology*, vol. 58, no. 6, pp. 893–898, 2001.

[33] E. C. Lee, A. Rafiq, R. Merrell, R. Ackerman, and J. T. Dennerlein, "Ergonomics and human factors in endoscopic surgery: a comparison of manual vs. telerobotic simulation systems," *Surgical Endoscopy*, vol. 19, pp. 1064–1070, 2005, DOI: 10.1007/s00464-004-8213-6.

[34] P. Desgranges, A. Bourriez, I. Javerliat, O. VanLaere, F. Losy, A. Lobontiu, D. Melliere, and J. Becquemin, "Robotically Assisted Aorto-femoral Bypass Grafting: Lessons Learned from our Initial Experience," *European Journal of Vascular and Endovascular Surgery*, vol. 27, pp. 507–511, 2004.

[35] R. Trimlett, A. Souza, A. Coonar, K. Jurgens, R. Kuenzler, and J. Pepper, "Toward totally endoscopic coronary artery surgery," *Surgical Endoscopy*, vol. 18, pp. 319–322, 2004.

[36] S. M. Prasad, C. T. Ducko, E. R. Stephenson, C. E. Chambers, and R. J. Damiano, "Prospective Clinical Trial of Robotically Assisted Endoscopic Coronary Grafting With 1-Year Follow-Up," *Annals of Surgery*, vol. 223, no. 6, pp. 725–732, 2001.

[37] A. J. Hodgson, R. A. Pantazopol, M. D. Visser, S. E. Salcudean, and A. G. Nagy, "Assessing potential benefits of enhanced dexterity in laparoscopic surgery," Chicago, IL, October 1997 1997, pp. 1966–1969.

[38] M. Braun, M. Schurr, V. Hausam, and G. Buess, “Erweiterte Freiheitsgrade mechanischer Manipulatoren für die minimalinvasive Chirurgie,” *Biomedizinische Technik*, vol. 49, no. 2, pp. 126–127, 2004.

[39] T. Frede, A. Hammadya, J. Klein, D. Teber, N. Inaki, M. Waseda, G. Buess, and J. Rassweiler, “The Radius Surgical System – A New Device for Complex Minimally Invasive Procedures in Urology?” *European Urology*, vol. 51, no. 4, pp. 1015–1022, Apr. 2007, DOI: 10.1016/j.eururo.2006.11.046.

[40] G. Dakin and M. Gagner, “Comparison of laparoscopic skills performance between standard instruments and two surgical robotic systems,” *Surgical Endoscopy*, vol. 17, pp. 574–579, 2003.

[41] J. Hernandez, S. Bann, Y. Munz, K. Moorthy, V. Datta, S. Martin, A. Dosis, F. Bello, A. Darzi, and T. Rockall, “Qualitative and quantitative analysis of the learning curve of a simulated surgical task on the daVinci system,” *Surgical Endoscopy*, vol. 18, no. 3, pp. 372–378, Mar. 2004, DOI: 10.1007/s00464-003-9047-3.

[42] S. Lederman and R. Klatzky, “Haptic perception: A tutorial,” *Attention, Perception, & Psychophysics*, vol. 71, pp. 1439–1459, 2009, DOI: 10.3758/APP.71.7.1439.

[43] O. S. Bholat, R. S. Haluck, W. B. Murray, P. J. Gorman, and T. M. Krummel, “Tactile Feedback Is Present During Minimally Invaisve Surgery,” *Journal of American College of Surgeons*, vol. 189, no. 4, pp. 349–355, 1999.

[44] D. Salle, P. Bidaud, and G. Morel, “Optimal Design of High Dexterity Modular MIS Instrument for Coronary Artery Bypass Grafting,” in *ICRA - Proc. of the IEEE Int. Conf. on Robotics and Automation*, vol. 2, Apr. 2004, pp. 1276–1281, DOI: 10.1109/ROBOT.2004.1308000.

[45] J. Peirs, J. Clijnen, P. Herijgers, D. Reynaerts, H. V. Brussel, B. Corteville, and S. Boone, “Design of an Optical Force Sensor for Force Feedback during Minimally Invasive Robotic Surgery,” in *Eurosensors XVII, The 17th European conference on Solid-State Transducers*, Guimaraes, Portugal, 2003.

[46] M. Kitagawa, “Indirect Feedback of Haptic Information for Robot-Assisted Telemanipulation,” Master’s thesis, Johns Hopkins University, Sep. 2003.

[47] L. Verner, K. Jeung, and A. Okamura, “The Effects of Gripping and Translational Forces on Teleoperation,” in *ICRA - Proc. of the IEEE Int. Conf. on Robotics and Automation, Workshop on Multi-point Interaction in Robotics and Virtual Reality*, 2004.

[48] E. Braun, C. Gaertner, H. Mayer, C. Staub, A. Knoll, R. Lange, and R. Bauernschmitt, “Features in Telemanipulation for Heart Surgery: Haptic Tasks,” in *World Congress on Medical Physics and Biomedical Engineering*, ser. IFMBE Proceedings, O. Dössel and W. C. Schlegel, Eds., vol. 25/VI. Springer, Sep. 2009, pp. 6–7.

[49] I. Brouwer, J. Ustin, L. Bentley, A. Sherman, N. Dhruv, and F. Tendick, “Measuring In Vivo Animal Soft Tissue Properties for Haptic Modeling in Surgical Simulation,” in *MMVR - Annual Medicine Meets Virtual Reality Conference*, J. W. et al., Ed. IOS Press, 2001.

[50] G. Picod, A. C. Jambon, D. Vinatier, and P. Dubois, “What can the operator actually feel when performing a laparoscopy?.” *Surgical Endoscopy*, vol. 19, no. 1, pp. 95 – 100, 2005.

[51] C. Wagner, N. Stylopoulos, and R. Howe, “The Role of Force Feedback in Surgery: Analysis of Blunt Dissection,” in *Proc. of the 10th Symposium on Haptic Interfaces for Virtual Environment and Teleoperator Systems (HAPTICS)*, Mar. 2002, pp. 68–74. [Online]. Available: http://biorobotics.harvard.edu/research/ff_surgery.html

[52] J. Müller, “Charité, Klinik für Allgemein-, Visceral-, Gefäß- und Thoraxchirurgie, Campus Mitte,” discussion, 2004.

[53] M. Kitagawa, D. Dokko, A. M. Okamura, B. T. Bethea, and D. D. Yuh, “Effect of Sensory Substitution on Suture Manipulation Forces for Surgical Teleoperation,” in *MMVR - Annual Medicine Meets Virtual Reality Conference*, Newport Beach, CA, USA, Jan. 2004, submitted.

[54] T. Akinbiyi, C. E. Reiley, S. Saha, D. Burschka, C. J. Hasser, D. D. Yuh, and A. M. Okamura, “Dynamic Augmented Reality for Sensory Substitution in Robot-Assisted Surgical Systems,” in *Proc. of the 28th IEEE EMBS Annual Int. Conf.*, New York City, NY, USA, Aug. 2006, pp. 567–570, DOI: 10.1109/IEMBS.2006.259707.

[55] M. E. Hagen, J. J. Meehan, I. Inan, and P. Morel, “Visual clues act as a substitute for haptic feedback in robotic surgery.” *Surgical Endoscopy*, vol. 22, no. 6, pp. 1505 – 1508, 2008.

[56] C. R. Wagner, “Force Feedback In Surgery: Physical Constraints and Haptic Information,” Ph.D. dissertation, Harvard University, Division Of Engineering and Applied Sciences, Cambridge, Massachusetts, USA, Jun. 2006.

[57] B. Deml, T. Ortmaier, and H. Weiss, “Minimally Invasive Surgery: Empirical Comparison of Manual and Robot Assisted Force Feedback Surgery,” in *Proc. of EuroHaptics*, Jun. 2004.

[58] C. R. Wagner and R. D. Howe, “Force Feedback Benefit Depends on Experience in Multiple Degree of Freedom Robotic Surgery Task,” *IEEE Transactions on Robotics*, vol. 23, no. 6, pp. 1235–1240, Dec. 2007, DOI: 10.1109/TRO.2007.904891.

[59] M. Tavakoli, R. Patel, and M. Moallem, “Haptic interaction in robot-assisted endoscopic surgery: a sensorized end-effector,” *International Journal on Medical Robotics and Computer Assisted Surgery*, vol. 1, no. 2, pp. 53–63, Nov. 2005, DOI: 10.1581/mrcas.2005.010205.

[60] S. Saha, “Appropriate Degrees of Freedom of Force Sensing in Robot-Assisted Minimally Invasive Surgery,” Master’s thesis, Johns Hopkins University, Baltimore, Maryland, USA, May 2005.

[61] I. Brouwer, “Cost-performance trade-offs in haptic hardware design,” Master’s thesis, University of British Columbia, 2004.

[62] C. Basdogan, S. De, J. Kim, M. Muniyandi, H. Kim, and M. Srinivasan, “Haptics in Minimally Invasive Surgical Simulation and Training,” *IEEE Computer Graphics and Apllications*, vol. 24, no. 2, pp. 56–64, Mar. 2004, DOI: 10.1109/MCG.2004.10021.

[63] P. J. Fager, “The use of haptics in medical applications,” *International Journal of Medical Robotics and Computer Assisted Surgery*, vol. 1, no. 1, pp. 36–42, Apr. 2004.

[64] O. A. J. van der Meijden and M. P. Schijven, “The value of haptic feedback in conventional and robot-assisted minimal invasive surgery and virtual reality training: a current review.” *Surgical Endoscopy*, vol. 23, no. 6, pp. 1180 – 1190, 2009.

[65] B. Bethea, A. Okamura, M. Kitagawa, T. Fitton, S. Cattaneo, V. Gott, W. Baumgartner, and D. Yuh, “Application of Haptic Feedback to Robotic Surgery,” *Journal of Laparoendoscopic & Advanced Surgical Techniques*, vol. 14, no. 3, pp. 191–195, 2004.

[66] R. Feller, C. Lau, C. Wagner, D. Perrin, and R. Howe, “The effect of force feedback on remote palpation,” in *ICRA - Proc. of the IEEE Int. Conf. on Robotics and Automation*, vol. 1, 2004, pp. 782– 788, DOI: 10.1109/ROBOT.2004.1307244.

[67] M. Tavakoli, R. Patel, M. Moallem, and A. Aziminejad, *Haptics for Teleoperated Surgical Robotic Systems*, 1st ed., ser. New Frontiers in Robotics. Singapore: World Scientific Publishing, Apr. 2008, vol. 1.

[68] A. J. Madhani and J. K. Salisbury, “Articulated Surgical Instrument for performing minimally invasive surgery with enhanced dexterity and sensitivity,” U.S. Patent US 5,792,135, Aug., 1998.

[69] T. G. Cooper, D. T. Wallace, S. C. Anderson, D. Williams, and S. Manzo, “Surgical tool having positively positionable tendon-actuated multi-disk wrist joints,” U.S. Patent Application Publication US 2003/0 036 748 A1, 2003.

[70] W. Lee and D. L. Brock, “Surgical instrument,” U.S. Patent US 6,554,844 B2, Apr., 2003.

[71] K. Grace, “Rigidly-linked Articulating Wrist with Decoupled Motion Transmission,” U.S. Patent US 6,132,441, Nov., 2000.

[72] M. E. Rosheim, *Robot Wrist Actuators*. New York, Chichester, Brisbane, Toronto, Singapore: John Wiley and Sons, 1989.

[73] F. Cepolina and R. Michelini, “Review of robotic fixtures for minimally invasive surgery,” *The International Journal of Medical Robotics and Computer Assisted Surgery*, vol. 1, no. 1, pp. 43 – 63, 2005, DOI: 10.1002/rcs.5.

[74] J. Catherine, C. Rotinat-Libersa, and A. Micaelli, “Comparative review of endoscopic devices, articulations, technologies developed for minimally invasive medical procedures,” *Applied Bionics and Biomechanics*, vol. 8, no. 2, pp. 151–171, Jan. 2011, DOI: 10.3233/ABB-2011-0018.

[75] D. Abbott, C. Becke, R. Rothstein, and W. Peine, “Design of an endoluminal NOTES robotic system,” in *IROS - Proc. of the IEEE/RSJ Int. Conf. on Intelligent Robots and Systems*, Nov. 2007, pp. 410 –416, DOI: 10.1109/IROS.2007.4399536.

[76] P. Dario, M. Carrozza, M. Marcacci, S. D’Attanasio, B. Magnami, O. Tonet, and G. Megali, “A novel mechatronic tool for computer-assisted arthroscopy,” *IEEE Transactions on Information Technology in Biomedicine*, vol. 4, no. 1, pp. 15 –29, Mar. 2000, DOI: 10.1109/4233.826855.

[77] J. Arata, M. Mitsuishi, S. Warisawa, K. Tanaka, T. Yoshizawa, and M. Hashizume, “Development of a dexterous minimally-invasive surgical system with augmented force feedback capability,” in *IROS - Proc. of the IEEE/RSJ Int. Conf. on Intelligent Robots and Systems*, 2005.

[78] M. Piccigallo, F. Focacci, O. Tonet, G. Megali, C. Quaglia, and P. Dario, “Hand-held robotic instrument for dextrous laparoscopic interventions,” *The International Journal of Medical Robotics and Computer Assisted Surgery*, vol. 4, no. 4, pp. 331–338, 2008, DOI: 10.1002/rcs.214.

[79] M. Piccigallo, U. Scarfogliero, C. Quaglia, G. Petroni, P. Valdastri, A. Menciassi, and P. Dario, “Design of a Novel Bimanual Robotic System for Single-Port Laparoscopy,” *IEEE/ASME Transactions on Mechatronics*, vol. 15, no. 6, pp. 871 –878, Dec. 2010, DOI: 10.1109/TMECH.2010.2078512.

[80] A. L. Trejos, R. V. Patel, and M. D. Naish, “Force sensing and its application in minimally invasive surgery and therapy: a survey,” *Proc. of the Institution of Mechanical Engineers, Part C: Journal of Mechanical Engineering Science*, vol. 224, no. 7, pp. 1435–1454, 2010, DOI: 10.1243/09544062JMES1917.

[81] P. Puangmali, K. Althoefer, L. D. Seneviratne, D. Murphy, and P. Dasgupta, “State-of-the-Art in Force and Tactile Sensing for Minimally Invasive Surgery,” *IEEE Sensors Journal*, vol. 8, no. 4, pp. 371–381, Apr. 2008, DOI: 10.1109/JSEN.2008.917481.

[82] E. P. W. van der Putten, R. H. M. Goossens, J. J. Jakimowicz, and J. Dankelman, “Haptics in minimally invasive surgery - a review,” *Minimally Invasive Therapy and Allied Technologies*, vol. 17, no. 1, pp. 3–16, Jan. 2008.

[83] A. M. Okamura, “Haptic feedback in robot-assisted minimally invasive surgery.” *Current Opinion In Urology*, vol. 19, no. 1, pp. 102 – 107, 2009, DOI: 10.1097/MOU.0b013e32831a478c.

[84] A. Melzer, K. Kipfmüller, and B. Halfar, “Deflectable endoscopic instrument system DENIS,” *Surgical Endoscopy*, vol. 11, pp. 1045–1051, 1997, DOI: 10.1007/s004649900523.

[85] R. Nakamura, E. Kobayashia, K. Masamunea, I. Sakumab, T. Dohib, T. Tsujib, and D. Hashimotoc, “Development of forceps manipulator system for laparoscopic surgery,” in *CARS - Computer Assisted Radiology and Surgery*, 2000, pp. 105–110.

[86] F. Focacci, M. Piccigallo, O. Tonet, G. Megali, A. Pietrabissa, and P. Dario, “Lightweight Hand-held Robot for Laparoscopic Surgery,” in *ICRA - Proc. of the IEEE Int. Conf. on Robotics and Automation*, Rome, Italy, Apr. 2007, pp. 599–604, DOI: 10.1109/ROBOT.2007.363052.

[87] H. Yamashita, D. Kim, N. Hata, and T. Dohi, “Multi-slider linkage mechanism for endoscopic forceps manipulator,” in *IROS - Proc. of the IEEE/RSJ Int. Conf. on Intelligent Robots and Systems*, 2003, DOI: 10.1109/IROS.2003.1249258.

[88] J. Müglitz, G. Kunad, P. Dautzenberg, B. Neisius, and R. Trapp, “Modular, Miniaturized Articulated Mechanism Symmetrically Pivotable in One Plane, for Medical Applications,” World Patent WO 94/17 965, Aug., 1994.

[89] K. Harada, K. Tsubouchi, M. G. Fujie, and T. Chiba, “Micro Manipulators for Intrauterine Fetal Surgery in an Open MRI,” in *ICRA - Proc. of the IEEE Int. Conf. on Robotics and Automation*, 2005, pp. 502– 507.

[90] P. Berkelman and J. Ma, “A Compact Modular Teleoperated Robotic System for Laparoscopic Surgery,” *The International Journal of Robotics Research*, vol. 28, no. 9, pp. 1198–1215, Sep. 2009, DOI: 10.1177/0278364909104276.

[91] C. Ishii and K. Kobayashi, “Development of a New Bending Mechanism and Its Application to Robotic Forceps Manipulator,” in *Proc. of the IEEE Int. Conf. on Robotics and Automation*, Roma, Italy, Apr. 2007, pp. 238–243, DOI: 10.1109/ROBOT.2007.363793.

[92] C. Ishii, K. Kobayashi, Y. Kamei, and Y. Nishitani, “Robotic Forceps Manipulator With a Novel Bending Mechanism,” *IEEE/ASME Transactions on Mechatronics*, vol. 15, no. 5, pp. 671 –684, Oct. 2010, DOI: 10.1109/TMECH.2009.2031641.

[93] V. R. C. Kode, M. C. Cavusoglu, and M. T. Azar, “Design and Characterization of a Novel Hybrid Actuator using Shape Memory Alloy and D.C Motor for Minimally Invasive Surgery Applications,” in *Proc. of the IEEE Int. Conf. on Mechatronics & Automation*, Jul. 2005.

[94] A. Zahraee, J. Paik, J. Szewczyk, and G. Morel, “Toward the Development of a Hand-Held Surgical Robot for Laparoscopy,” *IEEE/ASME Transactions on Mechatronics*, vol. 15, no. 6, pp. 853 –861, 12 2010, DOI: 10.1109/TMECH.2010.2055577.

[95] J. Arata, Y. Saito, and H. Fujimoto, “Outer shell type 2 DoF bending manipulator using spring-link mechanism for medical applications,” in *ICRA - Proc. of the IEEE Int. Conf. on Robotics and Automation*, May 2010, pp. 1041 –1046, DOI: 10.1109/ROBOT.2010.5509705.

[96] G. Darbemamieh, S. Najarian, and S. Mosafer, “Design and analysis of a mechanism for enhanced flexibility in minimally invasive surgical instruments,” in *5th Cairo International Biomedical Engineering Conference*, Dec. 2010, pp. 90 –93, DOI: 10.1109/CIBEC.2010.5716084.

[97] J. Peirs, H. V. Brussel, D. Reynaerts, and G. D. Gersem, “A flexible distal tip with two degrees of freedom for enhanced dexterity in endoscopic robot surgery,” in *MME - Micromechanics Europe Workshop*, 2002, pp. 271–274.

[98] M. Ho and J. Desai, “Towards a MRI-compatible meso-scale SMA-actuated robot using PWM control,” in *BioRob - Proc. of the IEEE/RAS and EMBS Int. Conf. on Biomedical Robotics and Biomechatronics*, Sep. 2010, pp. 361 –366, DOI: 10.1109/BIOROB.2010.5626044.

[99] M. Guckert and M. Naish, “Design of a novel 3 degree of freedom robotic joint,” in *IROS - Proc. of the IEEE/RSJ Int. Conf. on Intelligent Robots and Systems*, Oct. 2009, pp. 5146 –5152, DOI: 10.1109/IROS.2009.5354302.

[100] W. Sieklicki, M. Zoppi, and R. Molfino, “Superelastic compliant mechanisms for needlescopic surgical wrists,” in *ASME/IFToMM - Proc. of the Int. Conf. on Reconfigurable Mechanisms and Robots*, 2009, pp. 392–399.

[101] G. Morel and P. Poignet, "Kinematics, position and force control issue in minimally invasive surgery," in *MICCAI - Medical Image Computing and Computer-Assisted Intervention*, 2004.

[102] T. Kawahara, T. Matsumoto, N. Muramatsu, T. Osada, N. Sakamoto, and F. Arai, "Development of a decoupling wire driven exoskeletal microarm for endoscopic Submucosal Dissection," in *BioRob - Proc. of the IEEE/RAS and EMBS Int. Conf. on Biomedical Robotics and Biomechatronics*, Sep. 2010, pp. 849 –854, DOI: 10.1109/BIOROB.2010.5628027.

[103] K. Ikuta, T. Hasegawa, and S. Daifu, "Hyper Redundant Miniature Manipulator "Hyper Finger" for Remote Minimally Invasive Surgery in Deep Area," in *ICRA - Proc. of the IEEE Int. Conf. on Robotics and Automation*, 2003.

[104] T. Takaki, Y. Omasa, I. Ishii, T. Kawahara, and M. Okajima, "Force Visualization Mechanism Using a Moire Fringe Applied to Endoscopic Surgical Instruments," in *ICRA - Proc. of the IEEE Int. Conf. on Robotics and Automation*, 2010.

[105] F. Beyeler, S. Muntwyler, and B. J. Nelson, "A Six-Axis MEMS ForceTorque Sensor With Micro-Newton and Nano-Newtonmeter Resolution," *Journal of Microelectromechanical Systems*, vol. 18, no. 2, pp. 433–441, Apr. 2009.

[106] J. Dai and D. Kerr, "A six-component contact force measurement device based on the Stewart platforms," in *Proc. of the Institution of Mechanical Engineers, Part C: Journal of Mechanical Engineering Science*, vol. 214. Professional Engineering Publishing, 2000, pp. 687–697, DOI: 10.1243/0954406001523696.

[107] D. Stewart, "A platform with six degrees of freedom," *Proc. of the Institution of Mechanical Engineers*, vol. 180, no. 15, pp. 371–386, 1965.

[108] P. J. Berkelman, L. L. Whitcomb, R. H. Taylor, and P. Jensen, "A Miniature Micro-Surgical Instrument Tip Force Sensor for Enhanced Force Feedback During Robot-Assisted Manipulation," *IEEE Transactions on Robotics and Automation*, vol. 19, no. 5, pp. 917–922, Oct. 2003.

[109] I. Iordachita, Z. Sun, M. Balicki, J. Kang, S. Phee, J. Handa, P. Gehlbach, and R. Taylor, "A sub-millimetric, 0.25 mN resolution fully integrated fiber-optic force-sensing tool for retinal microsurgery," *International Journal of Computer Assisted Radiology*

and Surgery, vol. 4, no. 4, pp. 383–390, Jun. 2009, DOI: 10.1007/s11548-009-0301-6.

[110] T. Akinbiyi, "Intelligent Instruments and Visual Force Feedback in Laparoscopic Minimally Invasive Surgery," Master's thesis, The Johns Hopkins University, Baltimore, Maryland, USA, Oct. 2005.

[111] H. Mayer, I. Nagy, and A. Knoll, "Kinematics and Modelling of a System for Robotic Surgery," in *9th International Symposium on Advances in Robot Kinematics*, 2004, pp. 181–190.

[112] D. Q. Larkin, S. J. Blumenkranz, and R. Kumar, "Modular force sensor," U.S. Patent Application Publication US 2007/0 151 391 A1, Jul., 2007.

[113] S. Perreault, A. Talasaz, A. Trejos, C. Ward, R. Patel, and B. Kiaii, "A 7-DoF haptics-enabled teleoperated robotic system: Kinematic modeling and experimental verification," in *BioRob - Proc. of the IEEE/RAS and EMBS Int. Conf. on Biomedical Robotics and Biomechatronics*, Sep. 2010, pp. 906 –911, DOI: 10.1109/BIOROB.2010.5625949.

[114] S. Shimachi, S. Hirunyanitiwatna, Y. Fujiwara, A. Hashimoto, and Y. Hakozaki, "Adapter for contact force sensing of the daVinci robot." *The International Journal Of Medical Robotics & Computer Assisted Surgery: MRCAS*, vol. 4, no. 2, pp. 121 – 130, 2008.

[115] F. V. Meer, D. Esteve, A. Giraud, and A. M. Gue, "2D Silicon Macro-Force Sensor for Tele-Operated Surgical Instrument," in *Int. Conf. on MEMS, NANO, and Smart Systems*, vol. 0. Los Alamitos, CA, USA: IEEE Computer Society, 2004, pp. 468–472, DOI: 10.1109/ICMENS.2004.1508995.

[116] K. Tadano and K. Kawashima, "Development of 4-DoFs forceps with force sensing using pneumatic servo system," in *ICRA - Proc. of the IEEE Int. Conf. on Robotics and Automation*, May 2006, pp. 2250 –2255, DOI: 10.1109/ROBOT.2006.1642038.

[117] S. Prasad, M. Kitagawa, G. Fischer, J. Zand, M. Talamini, R. Taylor, and A. Okamura, "A Modular 2-DoF Force-Sensing Instrument For Laparoscopic Surgery," in *MICCAI - Medical Image Computing and Computer-Assisted Intervention*, ser. Lecture Notes in Computer Science, vol. 2878. Springer Berlin Heidelberg, 2003, pp. 279–286.

[118] A. Trejos, R. Patel, M. Naish, and C. Schlachta, “Design of a Sensorized Instrument for Skills Assessment and Training in Minimally Invasive Surgery,” in *BioRob - Proc. of the IEEE/RAS and EMBS Int. Conf. on Biomedical Robotics and Biomechatronics*, 2008, p. 965970.

[119] G. Hanna, T. Drew, G. Arnold, M. Fakhry, and A. Cuschieri, “Development of force measurement system for clinical use in minimal access surgery,” *Surgical Endoscopy*, vol. 22, pp. 467–471, 2008.

[120] S. Shimachi, Y. Hakozaki, T. Tada, and Y. Fujiwara, “Measurement of force acting on surgical instrument for force-feedback to master robot console,” in *CARS - Computer Assisted Radiology and Surgery*, vol. 1256, 2003, pp. 538–546, DOI: 10.1016/S0531-5131(03)00356-X.

[121] P. Dubois, Q. Thommen, and A. Jambon, “In vivo measurement of surgical gestures,” *IEEE Transactions on Biomedical Engineering*, vol. 49, no. 1, pp. 49–54, Jan. 2002, DOI: 10.1109/10.972839.

[122] J. Rosen, M. Solazzo, B. Hannaford, and M. Sinanan, “Objective Laparoscopic Skills Assessments of Surgical Residents Using Hidden Markov Models Based on Haptic Information and Tool/Tissue Interactions,” in *MMVR - Annual Medicine Meets Virtual Reality Conference*, 2001.

[123] J. Rosen, J. D. Brown, L. Chang, M. Barreca, M. Sinanan, and B. Hannaford, “The BlueDRAGON – A System for Measuring the Kinematics and the Dynamics of Minimally Invasive Surgical Tools In-Vivo,” in *ICRA - Proc. of the IEEE Int. Conf. on Robotics and Automation*, vol. 2, Washington, DC, USA, May 2002, pp. 1876– 1881, DOI: 10.1109/ROBOT.2002.1014814.

[124] N. Zemiti, G. Morel, T. Ortmaier, and N. Bonnet, “Mechatronic design of a new robot for force control in minimally invasive surgery,” *IEEE/ASME Transactions on Mechatronics*, vol. 12, no. 2, pp. 143–153, 2007.

[125] A. Trejos, A. Lyle, R. Patel, M. Naish, and C. Schlachta, “A Sensorized Instrument for Skills Assessment and Training in Minimally Invasive Surgery,” *Journal of Medical Devices*, vol. 3, pp. 1–12, 2009.

[126] A. Bicchi, G. Canepa, D. D. Rossi, P. Iacconi, and E. P. Scilingo, “A Sensorized Minimally Invasive Surgery Tool for Detecting Tissue Elastic Properties,” in *ICRA -*

Proc. of the IEEE Int. Conf. on Robotics and Automation, Minneapolis, Minnesota, USA, Apr. 1996, pp. 884–888.

[127] S. De, P. Swanson, M. Sinanan, J. Rosen, A. Dagan, and B. Hannaford, "Assessment of Tissue Damage due to Mechanical Stresses," in *BioRob - Proc. of the IEEE/RAS and EMBS Int. Conf. on Biomedical Robotics and Biomechatronics*, Pisa, Tuscany, Italy, Feb. 2006.

[128] M. MacFarlane, J. Rosen, B. Hannaford, C. Pellegrini, and M. Sinanan, "Force-Feedback Grasper Helps Restore Sense of Touch in Minimally Invasive Surgery," *Journal of Gastrointestinal Surgery*, vol. 3, no. 3, pp. 278–285, May-June 1999.

[129] B. Hannaford, J. Trujillo, M. Sinanan, M. Moreyra, J. Rosen, J. Brown, R. Leuschke, and M. MacFarlane, "Computerized Endoscopic Surgical Grasper," in *MMVR - Annual Medicine Meets Virtual Reality Conference*, Jan. 1998.

[130] H. Mayer, I. Nagy, A. Knoll, E. Schirmbeck, and R. Bauernschmitt, "Upgrading Instruments for Robotic Surgery," in *Australasian Conference on Robotics & Automation*, 2004.

[131] H. Mayer, I. Nagy, A. Knoll, E. U. Braun, R. Bauernschmitt, and R. Lange, "Haptic Feedback in a Telepresence System for Endoscopic Heart Surgery," *Presence*, vol. 16, no. 5, pp. 459–470, Oct. 2007, DOI: 10.1162/pres.16.5.459.

[132] A. Trejos, S. Jayaraman, R. Patel, M. Naish, and C. Schlachta, "Force sensing in natural orifice transluminal endoscopic surgery," *Surgical Endoscopy*, vol. 25, pp. 186–192, 2011.

[133] P. Valdastri, K. Harada, A. Menciassi, L. Beccai, C. Stefanini, M. Fujie, and P. Dario, "Integration of a Miniaturised Triaxial Force Sensor in a Minimally Invasive Surgical Tool," *IEEE Transactions on Biomedical Engineering*, vol. 53, no. 11, pp. 2397–2400, Nov. 2006, DOI: 10.1109/TBME.2006.883618.

[134] L. Beccai, S. Roccella, A. Arena, F. Valvo, P. Valdastri, A. Menciassi, M. C. Carrozza, and P. Dario, "Design and fabrication of a hybrid silicon three-axial force sensor for biomechanical applications," *Sensors and Actuators A: Physical*, vol. 120, no. 2, pp. 370 – 382, 2005, DOI: 10.1016/j.sna.2005.01.007.

[135] P. J. Berkelman, L. L. Whitcomb, R. H. Taylor, and P. S. Jensen, “A Miniature Instrument Tip Force Sensor for Robot/Human Cooperative Microsurgical Manipulation with Enhanced Force Feedback,” in *MICCAI - Medical Image Computing and Computer-Assisted Intervention*, ser. Lecture Notes in Computer Science, T. Dohi and R. Kikins, Eds., vol. 2488. Springer, Sep. 2000, pp. 897–906.

[136] J. Peirs, J. Clijnen, D. Reynaerts, H. V. Brussel, P. Herijgers, B. Corteville, and S. Boone, “A micro optical force sensor for force feedback during minimally invasive robotic surgery,” *Sensors and Actuators A*, vol. 115, pp. 447–455, 2004. [Online]. Available: http://people.mech.kuleuven.be/~jpeirs/Papers/Paper_Sensors&Actuators_A115.pdf

[137] J. Rausch and R. Werthschützky, “A Miniaturised Piezoresistive Multi-Component Force Sensor for Minimally Invasive Surgery.” in *Sensor/Test Conference 2009. Proceedings Sensor, Volume I.*, Mai 2009. [Online]. Available: http://tubiblio.ulb.tu-darmstadt.de/45812/

[138] G. Tholey, A. Pillarisetti, W. Green, and J. P. Desai, “Design, Development, and Testing of an Automated Laparoscopic Grasper with 3-D Force Measurement Capability,” in *Proc. of the International Symposium on Medical Simulation (ISMS)*, S. Cotin and D. N. Metaxas, Eds., vol. 3078. Cambridge, MA, USA: Springer Berlin / Heidelberg, Jun. 2004, pp. 38–48, DOI: 10.1007/b98155.

[139] G. Tholey and J. P. Desai, “A Compact and Modular Laparoscopic Grasper With Tridirectional Force Measurement Capability,” *Journal of Medical Devices*, vol. 2, no. 3, p. 031001, 2008, DOI: 10.1115/1.2952817.

[140] M. Stephan, G. Rognini, A. Sengul, R. Beira, L. Santos-Carreras, and H. Bleuler, “Modeling and Design of a Gripper for a Robotic Surgical System Integrating Force Sensing Capabilities in 4 DOF,” in *Int. Conf. on Control, Automation and Systems*, Oct. 2010.

[141] J. Rosen, M. MacFarlane, C. Richards, B. Hannaford, and M. Sinanan, “Surgeon-Tool Force/Torque Signatures – Evaluation of Surgical Skills in Minimally Invasive Surgery,” in *MMVR - Annual Medicine Meets Virtual Reality Conference*, vol. 7, Jan. 1999.

[142] Johns Hopkins University, “Computer Integrated Surgical Systems and Technology (CISST) Engineering Research Center,” Website, 2011, [Link accessed 8-October-2011]. [Online]. Available: http://www.cisst.org/

[143] V. Falk, A. Diegeler, T. Walther, N. Löscher, B. Vogel, C. Ulmann, T. Rauch, and F. W. Mohr, “Endoscopic coronary artery bypass grafting on the beating heart using a computer enhanced Telemanipulation system,” *Heart Surgery Forum*, vol. 2, pp. 199–205, 1999.

[144] T. Ortmaier, *Motion Compensation in Minimally Invasive Robotic Surgery*. VDI Verlag, 2003, phD Thesis.

[145] R. Konietschke, “Planning of Workplaces with Multiple Kinematically Redundant Robots,” Ph.D. dissertation, Technische Universität München, 2007.

[146] R. Konietschke, T. Ortmaier, H. Weiss, R. Engelke, and G. Hirzinger, “Optimal Design of a Medical Robot for Minimally Invasive Surgery,” in *CURAC - Jahrestagung der Deutschen Gesellschaft für Computer- und Roboterassistierte Chirurgie*, Nüernberg, Germany, Nov. 2003.

[147] K. Luttgens and N. Hamilton, *Kinesiology: Scientific basis of human motion*. Brown and Benchmark, Aug. 1997.

[148] K. Abdel-Malek, J. Yang, R. Brand, and E. Tanbour, “Towards Understanding the Workspace of Human Limbs,” *Ergonomics*, vol. 47, no. 13, pp. 1386–1405, 2004.

[149] F. Zacharias, “Knowledge Representations for Planning Manipulation Tasks,” Dissertation, Technische Universität München, München, 2011.

[150] M. J. Lum, D. Trimble, J. Rosen, K. F. II, H. King, G. Sanarayanaranan, J. Dosher, R. Leushke, B. Martin-Anderson, M. N. Sinanan, and B. Hannaford, “Multidisciplinary Approach for Developing a New Minimally Invasive Surgical Robotic System,” in *BioRob - Proc. of the IEEE/RAS and EMBS Int. Conf. on Biomedical Robotics and Biomechatronics*, Pisa, Italy, Feb. 2006.

[151] N. Abolhassani, R. Patel, and M. Moallem, “Needle insertion into soft tissue: A survey,” *Medical Engineering & Physics*, vol. 29, no. 4, pp. 413–431, May 2007, DOI: 10.1016/j.medengphy.2006.07.003.

[152] T. Frick, D. Marucci, J. Cartmill, C. Martin, and W. Walsh, “Resistance forces acting on suture needles,” *Journal of Biomechanics*, vol. 34, no. 10, pp. 1335–40, Oct. 2001.

[153] B. Maurin, J. Gangloff, B. Bayle, M. de Mathelin, O. Piccin, P. Zanne, C. Doignon, L. Soler, and A. Gangi, “A Parallel Robotic System with Force Sensors for Percutaneous Procedures Under CT-Guidance,” in *MICCAI - Medical Image Computing and Computer-Assisted Intervention*, vol. 3217, Saint-Malo, France, Sep. 2004, pp. 176–183.

[154] A. Okamura, C. Simone, and M. O’Leary, “Force modeling for needle insertion into soft tissue,” *IEEE Transactions on Biomedical Engineering*, vol. 51, no. 10, pp. 1707–1716, Oct. 2004, DOI: 10.1109/TBME.2004.831542.

[155] T. Podder, J. Sherman, D. Clark, E. Messing, D. Rubens, J. Strang, L. Liao, R. Brasacchio, Y. Zhang, W. Ng, and Y. Yu, “Evaluation of robotic needle insertion in conjunction with in vivo manual insertion in the operating room,” in *Proc. of the IEEE International Workshop on Robot and Human Interactive Communication (ROMAN)*, Aug. 2005, pp. 66–72, DOI: 10.1109/ROMAN.2005.1513758.

[156] European Economic Community, *93-42-EEC: Council Directive of 14 June 1993 concerning medical devices*, European Economic Community Std.

[157] European Economic Community, *90-385-EEC: Council Directive of 20 June 1990 on the approximation of the laws of the Member States relating to active implantable medical devices*, European Economic Community Std.

[158] G. Chiu, C. Fraser, H. Bansevicius, T. Tolocka, M. Sorli, and S. Pastorelli, *The Mechatronics Handbook*. CRC Press Inc., 2002, ch. 20, ISBN: 0-8493-0066-5.

[159] R. Koller and N. Kastrup, *Prinziplösungen zur Konstruktion technischer Produkte, 2. Auflage*. Springer, 1998, iSBN: 3-540-63060-0.

[160] R. Kornbluh, R. Pelrine, Q. Pei, M. Rosenthal, S. Stanford, N. Bonwit, R. Heydt, H. Prahlad, and S. V. Shastri, *Electroactive Polymer (EAP) Actuators as Artificial Muscles: Reality, Potential, and Challenges*, 2nd ed. SPIE Press, 2004, ch. 16, pp. 529–580.

[161] V. Giurgiutiu and C. A. Rogers, “Power and Energy Characteristics of Solid-State Induced-Strain Actuators for Static and Dynamic Applications,” *Journal of Intel-*

ligent Material Systems and Structures, vol. 8, no. 9, pp. 738–750, 1997, DOI: 10.1177/1045389X9700800903.

[162] V. Giurgiutiu, R. Pomirleanu, and C. A. Rogers, "Energy-Based Comparison of Solid-State Actuators," Laboratory for Adaptive Materials and Smart Structures, University of South Carolina, Columbia, Tech. Rep., 2000. [Online]. Available: http://www.me.sc.edu/Research/lamss/pdf/REPORTS/ActReportFinal.pdf

[163] I. Hunter and S. Lafontaine, "A comparison of muscle with artificial actuators," in *Solid-State Sensor and Actuator Workshop, 1992. 5th Technical Digest., IEEE*, Jun. 1992, pp. 178 –185, DOI: 10.1109/SOLSEN.1992.228297.

[164] J. E. Huber, N. A. Fleck, and M. F. Ashby, "The selection of mechanical actuators based on performance indices," *Proceedings of the Royal Society of London. Series A: Mathematical, Physical and Engineering Sciences*, vol. 453, no. 1965, pp. 2185–2205, 1997, dOI:10.1098/rspa.1997.0117.

[165] N. Troisfontaine, P. Bidaud, and M. Larnicol, "Optimal design of micro-actuators based on SMA wires," *Smart Matter*, vol. 8, pp. 197–203, 1999.

[166] B. Kübler, "Entwicklung einer integrierten Antriebseinheit für ein minimal invasives Zangeninstrument in der robotergestützten Chirurgie," Diplomarbeit, Universität Stuttgart, Apr. 2003, DLR Institut für Robotik.

[167] S. Thielmann, "Antriebseinheit für ein robotergeführtes minimal invasives Instrument," Diplomarbeit, Technische Universität München, Mar. 2008, DLR Institut für Robotik.

[168] S. Thielmann, U. Seibold, R. Haslinger, G. Passig, T. Bahls, S. Jörg, M. Nickl, A. Nothhelfer, U. Hagn, and G. Hirzinger, "MICA -A new generation of versatile instruments in robotic surgery," in *IROS - Proc. of the IEEE/RSJ Int. Conf. on Intelligent Robots and Systems*, Oct. 2010.

[169] M. C. Cavusoglu, I. Villanueva, and F. Tendick, "Workspace Analysis of Robotic Manipulators for a Teleoperated Suturing Task," in *IROS - Proc. of the IEEE/RSJ Int. Conf. on Intelligent Robots and Systems*, 2001.

[170] K. R. Thompson, "Equal angle guide mechanism for double universal joints," U.S. Patent US 6,139,437, 2000.

[171] J. Müglitz, G. Kunad, B. Neisius, and R. Trapp, "Modularer, in einer Ebene symmetrisch schwenkbarer, miniaturisierter Gelenkmechanismus für die Anwendung in der Medizin," Deutsche Offenlegungsschrift DE 43 03 311 A1, Aug., 1993.

[172] R. M. White, "A Sensor Classification Scheme," *Ultrasonics, Ferroelectrics and Frequency Control, IEEE Transactions on*, vol. 34, no. 2, pp. 124 – 126, Mar. 1987, DOI: 10.1109/T-UFFC.1987.26922.

[173] D. M. Stefanescu, "Wheatstone Bridge - The Basic Circuit for Strain Gauge Force Transducers," in *Handbook of Force Transducers*. Springer Berlin Heidelberg, 2011, pp. 347–360, DOI: 10.1007/978-3-642-18296-9_18.

[174] B. Siciliano and O. Khatib, Eds., *Springer Handbook of Robotics*. Springer Berlin Heidelberg, 2008, DOI: 10.1007/978-3-540-30301-5.

[175] R. Pallàs-Areny and J. G. Webster, *Sensors and Signal Conditioning (2nd Edition)*. John Wiley & Sons, 2000.

[176] J. Fraden, *Handbook of Modern Sensors - Physics, Designs and Applications (4th Edition)*. Springer New York Heidelberg Dordrecht London, 2010, DOI: 10.1007/978-1-4419-6466-3.

[177] HBM, "The piezo effect and its applications," HBM (Hottinger Baldwin Messtechnik), Whitepaper,, 2007, [Link accessed 13-August-2011]. [Online]. Available: http://www.hbm.com/fileadmin/mediapool/techarticles/2007/ipc_piezo_en.pdf

[178] A. D. Kersey, M. A. Davis, T. A. Berkoff, D. G. Bellemore, K. P. Koo, and R. T. Jones, "Progress toward the development of practical fiber Bragg instrumentation systems," *Proceedings of the SPIE International Society for Optical Engineering*, vol. 2839, pp. 40–63, 1996, dOI: 10.1117/12.255381.

[179] Wikipedia, "Fiber Bragg grating — Wikipedia, The Free Encyclopedia," 2011, [Link accessed 8-October-2011]. [Online]. Available: http://en.wikipedia.org/w/index.php?title=Fiber_Bragg_grating&oldid=444774974

[180] K. Totsu, Y. Haga, and M. Esashi, "Ultra-miniature fiber-optic pressure sensor using white light interferometry," *Journal of Micromechanics and Microengineering*, vol. 15, pp. 71–75, 2005.

[181] ENDOSENSE, “TACTICATH,” Website, 2011, [Link accessed 8-October-2011]. [Online]. Available: http://www.endosense.com/

[182] K. Hoffmann, “An Introduction to Measurements using Strain Gages,” HBM (Hottinger Baldwin Messtechnik GmbH), Whitepaper, 1989, [Link accessed 13-August-2011]. [Online]. Available: http://www.hbm.com/en/menu/applications/experimental-stress-analysis/reference-book/

[183] Measurements Group, “DMS Messtechnologie Formeln und Tabellen,” Application Notes, 1992, Measurements Group Messtechnik GmbH.

[184] S. Büttgenbach, *Mikromechanik - Einführung in Technologie und Anwendung*, 2nd ed., A. Schlachetzki and M. Schulz, Eds. B.G. Teubner, Stuttgart, 1994, iSBN: 3-519-13071-8.

[185] R. Little, “Silicon or Foil: Which strain gage should be used in Force/Forque transducers,” ATI Industrial Automation, Tech. Rep., 1992.

[186] HBM, “The Route to Measurement Transducers [Technical Article at www.hbm.com, checked Oct 12nd, 2011],” HBM (Hottinger Baldwin Messtechnik), Whitepaper, 2008, [Link accessed 13-August-2011]. [Online]. Available: http://www.hbm.com/hbm_doc/navi/start-en_brochures_(strain-gages).htm

[187] M. Uchiyama, E. Bayo, and E. Palma-Villalon, “A Systematic Design Procedure to Minimize a Performance Index for Robot Force Sensors,” *Journal of Dynamic Systems, Measurement, and Control*, vol. 113, no. 3, pp. 388–394, 1991, DOI: 10.1115/1.2896422.

[188] ATI, “F/T Catalogs and Manuals,” ATI Industrial Automation, Website, 2011, [Link accessed 8-October-2011]. [Online]. Available: http://www.ati-ia.com/products/ft/ft_literature.aspx

[189] D. Kerr, “Analysis, Properties and Design of a Stewart-Platform Transducer,” *ASME Journal Mechanical Transmission Automation and Design*, vol. 111, no. 25, pp. 25–28, Mar. 1989.

[190] Y. K. Byun, D. Kim, and H. Cho, “Analysis of a 6-DoF pose/wrench sensor integrated Stewart platform-based robotic wrist,” in *4th International Symposium on Measurement and Control in Robotics*, Jun. 1995.

[191] C. Ferraresi, S. Pastorelli, M. Sorli, and N. Zhmud, “Static and Dynamic Behavior of a High Stiffness Stewart Platform-Based Force/Torque Sensors,” *Journal of Robotic Systems*, vol. 12, no. 12, pp. 883–893, Mar. 1995, DOI: 10.1002/rob.4620121211.

[192] M. Sorli and S. Pastorelli, “Six-Axis Reticulated Structure Force/Torque Sensor with Adaptable Performances,” *Mechatronics*, vol. 5, no. 6, pp. 585–601, 1995.

[193] F. Li, “Design and analysis of a Fingertip Stewart Platform Force/Torque Sensor,” Master’s thesis, Simon Fraser University, Burnaby, Canada, Mar. 1998.

[194] T. Cooper, C. Julian, and S. J. Blumenkranz, “Interface for a medical instrument,” U.S. Design Patent US D444,555 S, Jul., 2001.

[195] B. Kübler, U. Seibold, and U. A. Hagn, “Chirurgisches Manipulationsinstrument,” Deutsche Offenlegungsschrift DE 10 2006 045 865 A1, Apr., 2008.

[196] U. Seibold, S. Thielmann, and M. Strohmayr, “Chirurgisches Manipulationsinstrument,” Deutsche Offenlegungsschrift DE 10 2009 056 982 A1, 2009.

[197] R. L. Devengenzo, T. G. Copper, J. P. Orban III, B. Schena, A. Loh, and S. Anderson, “Instrument interface of a robotic surgical system,” U.S. Patent Application Publication US 2007/0 119 274 A1, May, 2007.

[198] U. Seibold, S. Thielmann, and M. Strohmayr, “Chirurgisches Manipulationsinstrument,” Deutsche Offenlegungsschrift DE 10 2009 060 987 A1, 2009.

[199] Vishay Precision Group, “Transducer-Class Strain Gages,” Vishay Measurements Group GmbH, Tech. Rep., 2010, [Link accessed 13-August-2011]. [Online]. Available: http://www.blh.de/pdf/tc_e.pdf

[200] Burr-Brown Products, “INA337: Wide-Temperature, Precision Instrumentation Amplifier,” Texas Instruments, Tech. Rep., 2002, [Link accessed 13-August-2011]. [Online]. Available: http://www.ti.com/lit/ds/symlink/ina337.pdf

[201] U. Tietze and C. Schenk, *Electronic Circuits: Handbook for Design and Application*. Secaucus, NJ, USA: Springer-Verlag New York, Inc., 2007.

[202] B. Deml, T. Ortmaier, and U. Seibold, “The Touch and Feel in Minimally Invasive Surgery,” in *HAVE 2005 IEEE International Workshop on Haptic Audio Visual Environments and their Applications*, Oct. 2005, pp. 33–38.

[203] Epo-Tek, “Epo-Tek 353ND Technical Data Sheet,” Epo-Tek, Tech. Rep., 2010, [Link accessed 13-August-2011]. [Online]. Available: http://www.epotek.com/SSCDocs/datasheets/353ND.PDF

[204] Vishay Precision Group, “Miniature Cables,” Vishay Measurements Group GmbH, Tech. Rep., 2010, [Link accessed 13-August-2011]. [Online]. Available: http://www.blh.de/pdf/miniature_cables.pdf

[205] L. K. Massey, *The Effects of Sterilization Methods on Plastics and Elastomers, The Definitive Users Guide and Databook*, 2nd ed. William Andrew, 2005, iSBN: 0-8155-1505-7.

[206] Industrifil, “Wires and Cables,” Industrifil, Tech. Rep., 2011, [Link accessed 13-August-2011]. [Online]. Available: http://www.industrifil.com/Images1/Cable.pdf

[207] CarlStahl, “Modulus of Elasticity for TechnoCables,” 2003, discussion with CarlStahl Tech Support.

[208] CarlStahl, “TechnoCables Edition No. 5,” CarlStahl, Tech. Rep., 2010, [Link accessed 13-August-2011]. [Online]. Available: http://www.carlstahl.de/download/techno.pdf

[209] iC-Haus, “BiSS Interface Protocol Description (C-Mode),” iC-Haus, Tech. Rep., 2008, [Link accessed 13-August-2011]. [Online]. Available: http://www.ichaus.de/upload/pdf/BiSS-C-Protocol_c5es.pdf

[210] T. Matsumura, T. Umemoto, Y. Fujihara, E. Ueno, M. Yamakawa, T. Shiina, and T. Mitake, “Measurement of elastic property of breast tissue for elasticity imaging,” in *Ultrasonics Symposium (IUS), 2009 IEEE International*, Sep. 2009, pp. 1451 – 1454, DOI: 10.1109/ULTSYM.2009.5442044.

[211] A. Samani, J. Zubovits, and D. Plewes, “Elastic moduli of normal and pathological human breast tissues: an inversion-technique-based investigation of 169 samples,” *Physics in Medicine and Biology*, vol. 52, no. 6, p. 1565, 2007.

[212] T. A. Krouskop, T. M. Wheeler, F. Kallel, B. S. Garra, and T. Hall, “Elastic Moduli of Breast and Prostate Tissues Under Compression,” *Ultrasonic Imaging*, vol. 20, pp. 260–274, 1998.

[213] V. Egorov and A. Sarvazyan, “Mechanical Imaging of the Breast,” *IEEE Transactions on Medical Imaging*, vol. 27, no. 9, pp. 1275 –1287, Sep. 2008, DOI: 10.1109/TMI.2008.922192.

[214] B. Ahn, K. Park, H. Lee, E. Lorenzo, K. H. Rha, and J. Kim, “Robotic palpation system for prostate cancer detection,” in *BioRob - Proc. of the IEEE/RAS and EMBS Int. Conf. on Biomedical Robotics and Biomechatronics*, sept 2010, pp. 644 –649, DOI: 10.1109/BIOROB.2010.5626092.

[215] J. Kunz and M. Studer, “Druck-Elastizitätsmodul über Shore-A-Härte ermitteln,” in *Kunststoffe*, no. 6. Carl Hanser Verlag, 2006, pp. 92–96, [Link accessed 13-August-2011]. [Online]. Available: http://www.kunststoffe.de/ku/amf.asp?url=get_doc_free.asp&bin_id=2661311432-69&o_id=251115171124-79

[216] V. L. Popov, *Contact Mechanics and Friction*. Springer Heidelberg, 2010, DOI: 10.1007/978-3-642-10803-7.

[217] F. Fröhlich, “Rastertaster,” 2010, experiments at DLR Robotics and Mechatronics Institute.

[218] W.-C. Yeh, P.-C. Li, Y.-M. Jeng, H.-C. Hsu, P.-L. Kuo, M.-L. Li, P.-M. Yang, and P. H. Lee, “Elastic modulus measurements of human liver and correlation with pathology,” *Ultrasound in Medicine & Biology*, vol. 28, no. 4, pp. 467 – 474, 2002, DOI: 10.1016/S0301-5629(02)00489-1.

[219] J. A. Burdick and R. L. Mauck, Eds., *Biomaterials for Tissue Engineering Applications: A Review of the Past and Future Trends*. Springer Wien New York, 2011, DOI: 10.1007/978-3-7091-0385-2.

[220] Vishay Precision Group, “Tech Note TT-610: Anpressdrucktechniken für DMS-Installationen,” Vishay Measurements Group GmbH, Tech. Rep., 2010, [Link accessed 13-August-2011]. [Online]. Available: http://www.blh.de/german/technote.htm

[221] Vishay Precision Group, “Tech Note TN-505 Auswahl von DMS; Kriterien, Verfahren, Empfehlungen,” Vishay Measurements Group GmbH, Tech. Rep., 2010, [Link accessed 13-August-2011]. [Online]. Available: http://www.blh.de/german/technote.htm

[222] Vishay Precision Group, “M-Bond 200,” Vishay Measurements Group GmbH, Tech. Rep., 2010, [Link accessed 13-August-2011]. [Online]. Available: http://www.vishaypg.com/micro-measurements/list/product-11010/

[223] Vishay Precision Group, “M-Bond 600,” Vishay Measurements Group GmbH, Tech. Rep., 2010, [Link accessed 13-August-2011]. [Online]. Available: http://www.vishaypg.com/micro-measurements/list/product-11014/

[224] M. Sturm, “Entwicklung eines chirurgischen Zangeninstrumentes für die minimal invasive Telechirurgie,” Diplomarbeit, Fachhochschule München, Sep. 2000.

A

Appendix

A.1 Stewart Platform Characteristic Matrix

The characteristic matrix of the Stewart Platform sensor is developed as described by Sorli and Pastorelli [192] by investigating the forces acting on the three individual link pairs at the point of intersection (see Fig. 5.3). An example for links b_1 and b_1 is shown in Fig. 5.3 (b) with link forces f_1 and f_2 broken down into a radial component (direction ρ), a tangent component (direction τ) and a normal component (direction κ). Note that links are numbered in mathematical positive direction here in contrast to Sorli and Pastorelli [192]. Applied to all links this yields the following force components exerted by the links on the top platform:

$$f_{\rho 12} = (f_1 + f_2)\cos(\alpha)\cos(\beta) \tag{A.1}$$

$$f_{\tau 12} = (f_1 - f_2)\cos(\alpha)\sin(\beta) \tag{A.2}$$

$$f_{\kappa 12} = (f_1 + f_2)\sin(\alpha) \tag{A.3}$$

$$f_{\rho 34} = (f_3 + f_4)\cos(\alpha)\cos(\beta) \tag{A.4}$$

$$f_{\tau 34} = (f_3 - f_4)\cos(\alpha)\sin(\beta) \tag{A.5}$$

$$f_{\kappa 34} = (f_3 + f_4)\sin(\alpha) \tag{A.6}$$

$$f_{\rho 56} = (f_5 + f_6)\cos(\alpha)\cos(\beta) \tag{A.7}$$

$$f_{\tau 56} = (f_5 - f_6)\cos(\alpha)\sin(\beta) \tag{A.8}$$

$$f_{\kappa 56} = (f_5 + f_6)\sin(\alpha) \tag{A.9}$$

Summing these components to create the static equilibrium in the xyz reference system yields:

$$
\begin{aligned}
f_x + f_{\tau 12} - \frac{1}{2}(f_{\tau 34} + f_{\tau 56}) - \frac{\sqrt{3}}{2}(f_{\rho 34} - f_{\rho 56}) &= 0 && \text{(A.10)}\\
f_y + f_{\rho 12} - \frac{1}{2}(f_{\rho 34} + f_{\rho 56}) + \frac{\sqrt{3}}{2}(f_{\tau 34} - f_{\tau 56}) &= 0 && \text{(A.11)}\\
f_z + f_{\kappa 12} + f_{\kappa 34} + f_{\kappa 56} &= 0 && \text{(A.12)}\\
m_x - a f_{\kappa 12} + \frac{a}{2}(f_{\kappa 34} + f_{\kappa 56}) &= 0 && \text{(A.13)}\\
m_y - a\frac{\sqrt{3}}{2}(f_{\kappa 34} - f_{\kappa 56}) &= 0 && \text{(A.14)}\\
m_z + a(f_{\tau 12} + f_{\tau 34} + f_{\tau 56}) &= 0 && \text{(A.15)}
\end{aligned}
$$

Substituting Eq. A.1 - Eq. A.9 into Eq. A.10 - Eq. A.15 yields the characteristic matrix $\mathbf{A} \in \mathbb{R}^{(6\times 6)}$ describing the transformation of internal link forces into external loads acting on the virtual platform.

$$[f_x, f_y, f_z, m_x, m_y, m_z]^T = \mathbf{A} \cdot [f_1, f_2, f_3, f_4, f_5, f_6]^T \tag{A.16}$$

with

$$
\mathbf{A} = \frac{1}{2}\begin{bmatrix}
-2n & 2n & \sqrt{3}m + n & \sqrt{3}m - n & -\sqrt{3}m + n & -\sqrt{3}m - n\\
-2m & -2m & m - \sqrt{3}n & m + \sqrt{3}n & m + \sqrt{3}n & m - \sqrt{3}n\\
-2q & -2q & -2q & -2q & -2q & -2q\\
2aq & 2aq & -aq & -aq & -aq & -aq\\
0 & 0 & aq\sqrt{3} & aq\sqrt{3} & -aq\sqrt{3} & -aq\sqrt{3}\\
-2an & 2an & -2an & 2an & -2an & 2an
\end{bmatrix} \tag{A.17}
$$

where

$$
\begin{aligned}
m &= \cos(\alpha)\cos(\beta)\\
n &= \cos(\alpha)\sin(\beta)\\
q &= \sin(\alpha)\\
a &= R\left(\cos(\gamma) - \frac{\sin(\gamma)}{tan(\beta)}\right)\\
i' &= 2(R\sin(\gamma) - L\cos(\alpha)\sin(\beta))
\end{aligned}
$$

A.2 Strain gauge applicaton

Strain gauge application was accomplished according to the application notes published by Vishay Precision Group [220, 221]. The material surface was mechanically prepared for gauge application by fine sanding with 400 grit sandpaper and cleaning with compressed air. Any organic residue was then chemically removed by rinsing with Methyl-Ethyl-Ketone (2-Butanone) and Isopropyl alcohol (2-Propanol) each followed by a compressed air dry. Various adhesives were tested during experiments, including M-Bond 200 [222] (cyanoacrylate based, room temperature curing, maximum operating temperature 100°C), M-Bond 600 [223] (two-component, solvent-thinned, epoxy-phenolic adhesive, high temperature curing, minimal curing temperature 120°C, maximum operating temperature 370°C) and EPO-TEK® (Epoxy Technology) 353ND [203] (two component, high temperature epoxy designed for fiber optic and medical applications, minimal curing temperature 80°C, maximum operating temperature 250°C).

The strain gauge bonding application note calls for pressure to be applied during initial curing to ensure the thinnest possible adhesive layer between substrate and strain gauge. A layer of adhesive as thin as possible will reduce hysteresis due to adhesive creep. The application note calls for the strain gauge to be temporarily fixed with Kapton® tape to prevent misalignment while applying pressure. Due to the small size of the sensor structure, this application method is difficult to follow in the present application. The use of adhesive Kapton® tape to fixate the gauge – while producing desired results in larger area applications – was not possible for the small sensor dimension. Therefore, application of pressure to extremely small strain gauges, which at that point are freely floating on the liquid adhesive layer, will force the strain gauge to drift sideways on the surface of the displaced adhesive layer and render the sensor unusable once the adhesive is cured.

Using EPO-TEK® (Epoxy Technology) as adhesive, aside from creating a strong adhesive interface that shows little hysteresis, provides a convenient solution to the curing problem. This adhesive will exhibit extremely low viscosity at the initial curing stage and – due to the capillary effect – disperse, thereby creating a thin, even layer of adhesive underneath the strain gauge. At the same time, proper design of the link surface will ensure that the surface tension of the adhesive in its liquid state will keep the strain gauge centered and aligned with the link structure during the curing process.

A.3 Needle Insertion Experiments

Cadaveric tissue manipulation trials with porcine heart tissue were performed to generate reliable needle insertion force data. A porcine heart (less than 24 h after slaughter, refrigerated) was chosen for its availability and close analogy to the human heart. On this object four different tissue types were examined: vessel tissue (aortic artery), ring of the heart valve (mitral and aortic valve), muscle tissue (myocardium), and muscle tissue covered with fat (tela subepicardiaca / myocardium). Tissue in each of these locations was penetrated with three different but commonly used needle types:

- Ethicon Prolene 6-0 (0.7 Ph. Eur.) ”C-1” ($\frac{3}{8}$ circle, round body, arc length 13 mm) (see Fig. A.1),
- Ethicon Prolene 7-0 (0.5 Ph. Eur.) ”BV175-8” ($\frac{3}{8}$ circle, round body, arc length 9.3 mm) (see Fig. A.2),
- Ethicon Prolene 8-0 (0.4 Ph. Eur.) ”BV130-5” ($\frac{3}{8}$ circle, round body, arc length 6.5 mm) (see Fig. A.3).

Furthermore, the needles were inserted with three different plausible insertion speeds, $2.3\ \frac{\mathrm{mm}}{\mathrm{s}}$, $4.3\ \frac{\mathrm{mm}}{\mathrm{s}}$, and $7\ \frac{\mathrm{mm}}{\mathrm{s}}$. The following figures show experimental results for 5 insertions for each needle, insertion speed and tissue type. Horizontal axis shows time in $^{1}/_{100}$th of a second and vertical axis shows needle tip force in N.

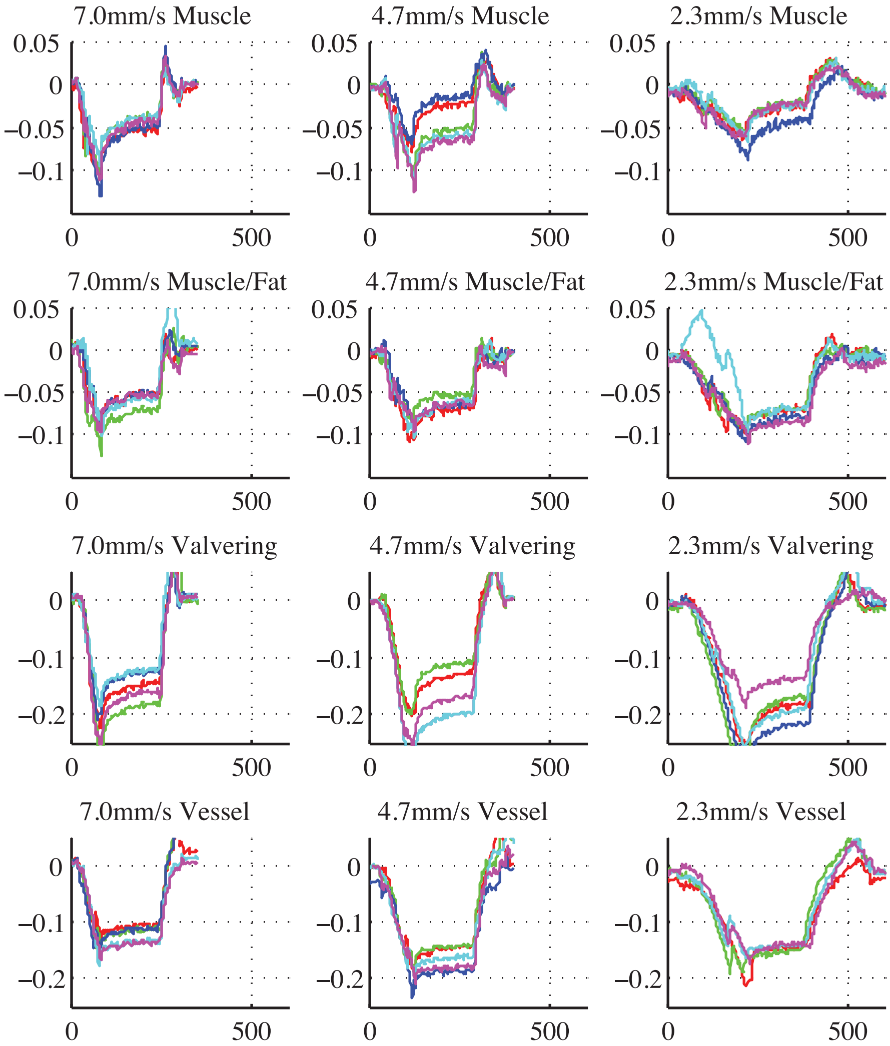

Figure A.1: Needle Insertion Experiments Ethicon Prolene 6-0 (0.7 Ph. Eur.) "C-1" ($\frac{3}{8}$ circle, round body, arc length 13 mm). Tip force in N on vertical axis, time in $^{1}/_{100}$th of a second on horizontal axis.

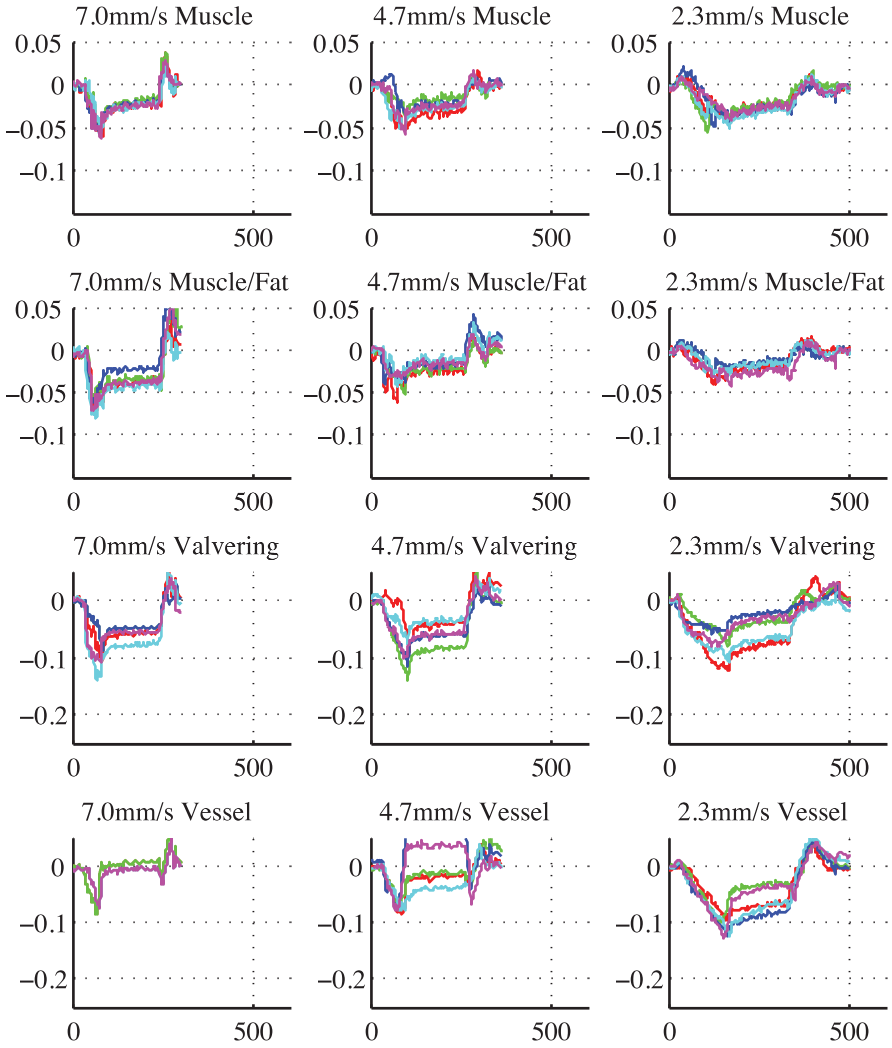

Figure A.2: Needle Insertion Experiments Ethicon Prolene 7-0 (0.5 Ph. Eur.) ”BV175-8” ($\frac{3}{8}$ circle, round body, arc length 9.3 mm). Tip force in N on vertical axis, time in $^{1}/_{100}$th of a second on horizontal axis.

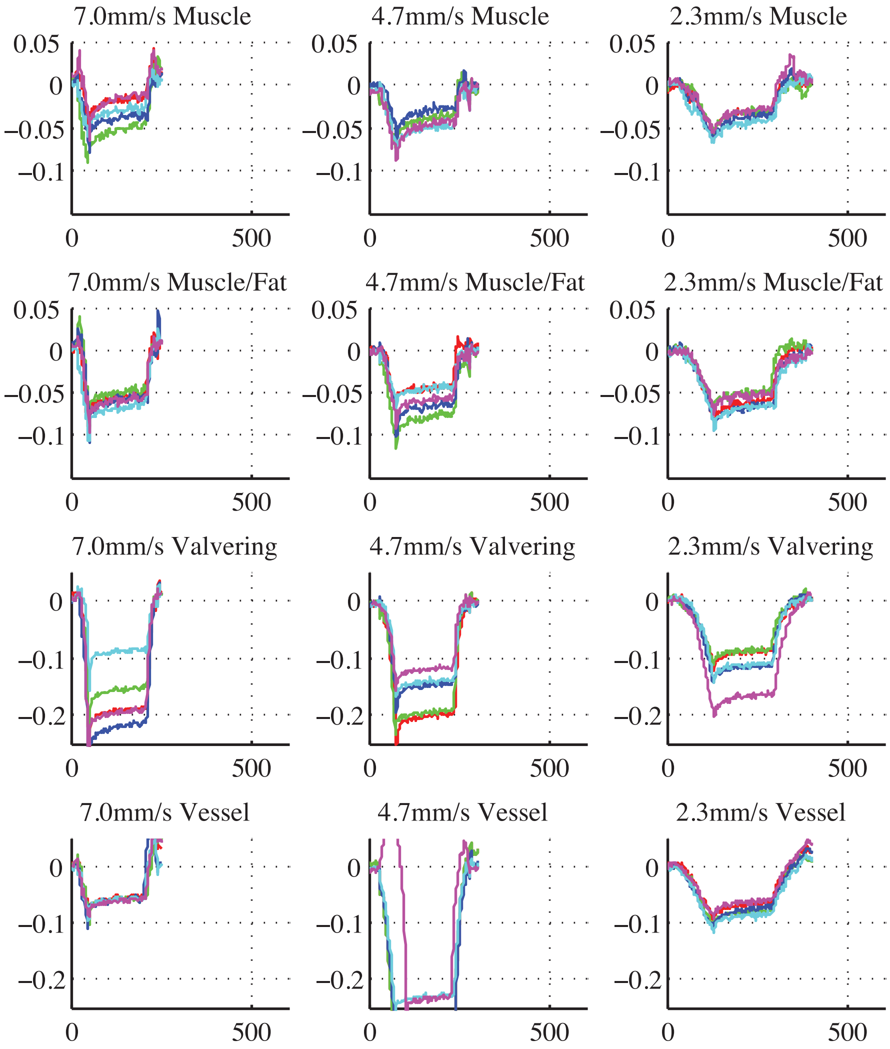

Figure A.3: Needle Insertion Experiments Ethicon Prolene 8-0 (0.4 Ph. Eur.) ”BV130-5” ($\frac{3}{8}$ circle, round body, arc length 6.5 mm). Tip force in N on vertical axis, time in $^{1}/_{100}$th of a second on horizontal axis.

A.4 Selection of Wrist Prototypes

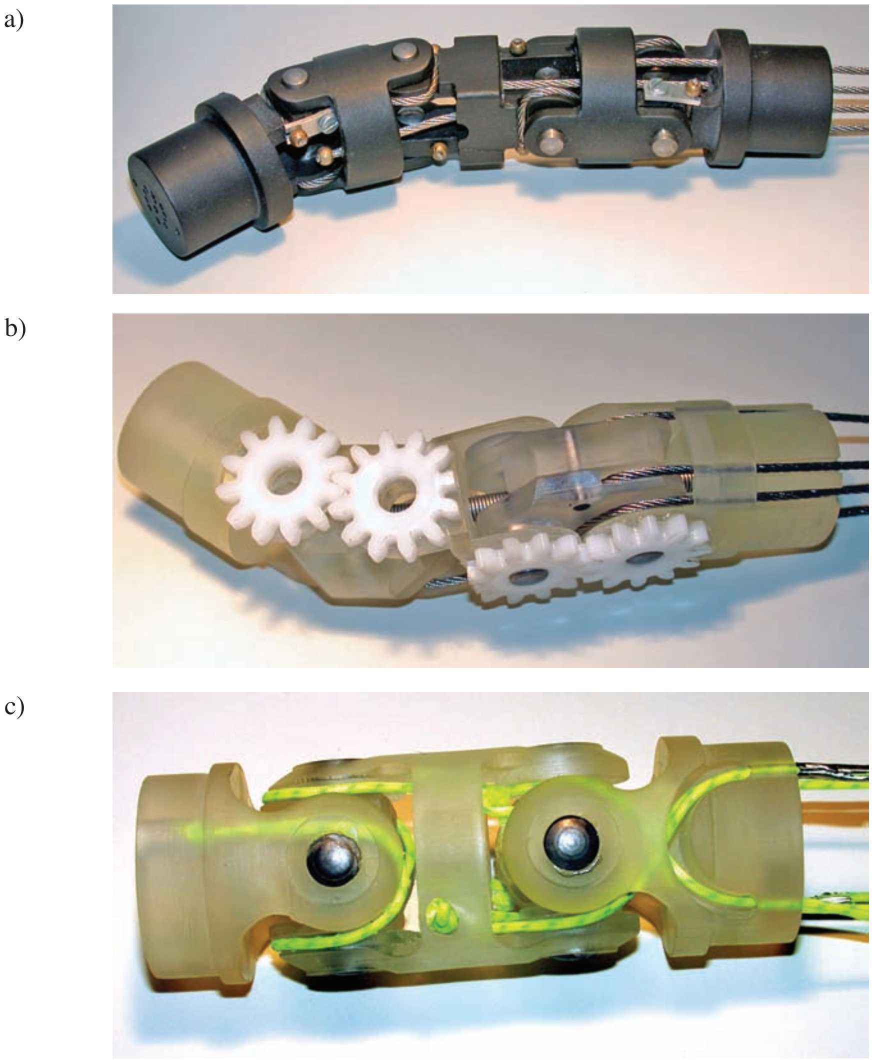

Figure A.4: Wrist prototypes fabricated using stereolithography. Wrist based on the DLR robotic finger (a) using cables for motion coupling, Sturm [224], wrist based on the DLR robotic finger (b) using gears for motion coupling (compare Fig. 4.7 (a)), and coupled double universal joint (c) (compare Fig. 4.7 (f)).